Universität Augsburg
University

Rainfall Estimation with Opportunistic Sensors

Kumulative Dissertation zur Erlangung des Doktorgrades
an der Fakultät für Angewandte Informatik
der Universität Augsburg

vorgelegt von
Maximilian Martin Graf

2024

Erstes Gutachten: Prof. Dr. Harald Kunstmann
Zweites Gutachten: Prof. Dr. Christoph Beck
Tag der mündlichen Prüfung: 15.05.2024

"In investigating the possibility of using millimeter waves for satellite communication and earth-based radio relay, we find that attenuation by rain is the chief cause of unreliability. But much is yet to be learned about the spatial and temporal behavior of rainfall." (Hogg, 1968)

Abstract

Precipitation can impact human security significantly, and its accurate estimation in time and space is vital for various applications, including water management decisions and flash flood forecasting. Traditional observation systems like rain gauges, weather radars, and satellite instruments have individual limitations in capturing precipitation accurately and are not available in all regions of the world. Opportunistic rainfall sensors (OS) like commercial microwave links (CMLs) and personal weather stations (PWS) can provide additional rainfall information, and their numbers have surpassed the ones from traditional sensors. However, dealing with the heterogeneous quality of OS-derived precipitation information remains a scientific problem and limits their use in hydrologic applications. To address this gap, this thesis aims to develop methods for quality control, processing, and spatial reconstruction of OS data. First, data from 4000 CMLs in Germany, which are part of the cellular backhaul network, were used to derive rainfall information based on the attenuation of their microwave signal. CML processing methods were developed and optimized, leading to rainfall estimates with good quality when compared to a rain gauge-adjusted weather radar product used as a reference. To improve CML processing further, a novel method for the crucial step of rain event detection was developed using a convolutional neural network. This method improved the rainfall estimation significantly by reducing falsely classified rainfall by over 50%. With a similar performance for new CMLs and time periods, the method proved its ability to generalize to previously unseen data. CMLs may experience a total loss of signal due to high attenuation during heavy rainfall. These so-called blackouts were investigated using three years of CML and 20 years of weather radar data. Overall, only around one percent of rainfall was missed due to blackouts in the CML data. However, blackouts have to be considered in applications using CML rainfall estimates, as this one percent consisted of the most intense events. Surprisingly, longer CMLs had more blackouts, despite having a higher dynamic range to compensate for more attenuation that is caused by their length. PWS are another source of opportunistically sensed rainfall information. Data from around 20,000 PWS were evaluated individually and in combination with CML and rain gauge data in Germany. Filtering and interpolation methods were developed for these datasets, and the resulting rainfall maps were evaluated against three reference datasets covering different spatial and temporal scales. The OS-based products performed similarly well as operational radar products of the DWD, especially on local and regional scales with hourly resolution, and surpassed the quality of products using conventional rain gauges. In conclusion, this thesis demonstrates the development and evaluation of methods for filtering, processing, and combining CML and PWS data. The evaluation of the OS-based rainfall estimates proves that a quality similar to that of operational rainfall products can be achieved.

Zusammenfassung

Niederschlag kann die Sicherheit und das Wohlbefinden der Menschen erheblich beeinflussen, weshalb eine genaue Erfassung in Raum und Zeit beispielsweise für wasserwirtschaftliche Entscheidungen oder Sturzflutvorhersagen unerlässlich ist. Herkömmliche Beobachtungssysteme wie Niederschlagsmesser, Wetterradare und Satellitenbeobachtungen haben individuelle Nachteile und sind teilweise nicht in allen Regionen der Welt verfügbar. Opportunistische Niederschlagssensoren (OS) wie beispielsweise kommerzielle Richtfunkstrecken und private Wetterstationen bieten zusätzliche Niederschlagsinformationen liefern, und ihre Zahl hat die traditioneller Messgeräte überholt. Der Umgang mit der heterogenen Qualität von aus OS abgeleiteten Niederschlagsschätzungen stellt jedoch ein wissenschaftliches Problem dar und schränkt ihren Einsatz in hydrologischen Anwendungen ein. Ziel dieser Arbeit ist es, robuste Niederschlagsdaten aus OS zu gewinnen. Hierzu wurden Methoden zur Qualitätskontrolle, Verarbeitung und räumlichen Rekonstruktion von OS-Daten entwickelt. Daten von 4000 kommerziellen Richtfunkstrecken (CMLs) in Deutschland, die Teil des Mobilfunknetzes sind, wurden verwendet, um Niederschlagsinformationen auf der Grundlage der Dämpfung ihres Mikrowellensignals abzuleiten. Dafür wurden CML-Prozessierungsmethoden wurden entwickelt und optimiert und die daraus resultierenden Niderschlagsschätzungen zeigten eine gute Qualität im Vergleich zu einem mit Niederschlagsmessern angeeichten Wetterradarprodukt, das als Referenz verwendet wurde. Um die CML-Prozessierung weiter zu verbessern, wurde eine neuartige Methode für den wichtigen Schritt der Detektion von Niederschlagsereignissen in CML-Zeitreihen unter Verwendung eines neuronalen Netzes entwickelt. Diese Methode verbesserte die Niederschlagsschätzung erheblich, da die Zahl der falsch klassifizierten Niederschläge um über 50% reduziert wurde. Für neue betrachtete Zeiträume und CMLs konnten mit dieser Methode ähnlich gute Ergebnisse erzielt werden. Dies unterstreicht die Robustheit der Methode zur Verallgemeinerung auf unbekannte Daten. Ein bisher nicht berücksichtigtes Phänomen ist der vollständige Signalverlust eines CMLs durch sehr hohe Dämpfung bei sehr starkem Niederschlag. Diese sogenannten Blackouts wurden an drei Jahren CML- und 20 Jahren Wetterradardaten analysiert. Insgesamt wurde durch Blackouts nur ein Prozent der Niederschläge in den CML-Niederschlagsdaten nicht erfasst. Für die Verwendung dieser Daten in hydrologischen Anwendungen sind Blackouts jedoch äußerst relevant, da dieses eine Prozent aus den intensivsten Ereignissen besteht. Überraschenderweise wurden für längere CMLs mehr Blackouts beobachtet, obwohl diese mit einem größeren Dynamikbereich ausgestattet sind, um die längenbedingt größere Dämpfung auszugleichen. Eine weitere Quelle für opportunistisch erfasste Niederschlagsdaten sind Private Wetterstationen (PWS). Daten von rund 20,000 PWSs wurden individuell und in Kombination mit Daten von CMLs und Niederschlagsmessern in Deutschland ausgewertet. Für die PWS und CML

Datensätze wurden Filter- und Interpolationsmethoden entwickelt, und die daraus resultierenden Niederschlagskarten wurden anhand von drei Referenzdatensätzen auf unterschiedlichen räumlichen und zeitlichen Skalen evaluiert. Die OS-basierten Produkte erzielten dabei insbesondere auf lokaler und regionaler Skala mit stündlicher Auflösung ähnlich gute Metriken ab wie operationelle Radarprodukte des DWDs und übertrafen die Qualität der Produkte die herkömmliche Niederschlagsmesser nutzen. Zusammenfassend zeigt diese Arbeit die Entwicklung und Evaluierung von Methoden zur Filterung, Prozessierung und Kombination von CML- und PWS-Daten. Die Auswertung der so erzeigten OS-basierten Niederschlagsinformationen zeigt, dass eine Qualität ähnlich der von operationellen Niederschlagsprodukten erreicht werden kann.

Contents

List of Figures

List of Tables

Chapter 1

Introduction

1.1 The importance of precipitation and its measurement

Water is essential for mankind and its global distribution is determined by the hydrological cycle. Precipitation is a key variable in the hydrological cycle and its excess, or absence, can lead to extreme events like floods (Merz et al., 2021) or droughts (Blauhut et al., 2022). Even moderate precipitation events determine human activities on a daily basis. A variety of applications rely on accurate quantitative precipitation estimates to support decision making for example in flood forecasting, civil protection, agriculture, and urban planning. Further, climatological analysis and the validation of earth system models rely on observational data. Therefore, the correct estimation of precipitation is highly relevant, especially in the context of climate change which likely is responsible for an increase in the occurrence of heavy precipitation events (Calvin et al., 2023).

However, accurately estimating precipitation is not a trivial task due to its highly stochastic character. Its non-stationarity is reflected in its high variability in both space and time. A variety of devices have been developed to measure precipitation. The most commonly used ones are bucket-type rain gauges, disdrometers, weather radars, and active or passive sensors on satellites. While each of these devices has specific advantages justifying their usage, their individual disadvantages can lead to uncertainties in their precipitation estimates which propagate into products and applications using their data.

An even greater issue for applications requiring accurate precipitation information is the lack of dense hydrometeorological measurement networks in many regions of the world. The United Nations has emphasized the need for climate observation systems to provide sufficient information for early warning systems which are not accessible for one-third of the world's population, mainly in the least developed countries (UNFCCC, 2022). A prominent example of such early warning systems are flood forecasts which highly depend on the available precipitation information.

Rainfall estimates from opportunistic sensors (OS) offer a presently scarcely exploited source of rainfall information. OS can potentially be used to both reduce measurement uncertainties of

traditional precipitation sensors through merged products and improve the coverage in regions with sparse observation density. OS are devices that are not intended to deliver high-quality observations of rainfall or other meteorological variables and sometimes do not even measure these parameters directly. OS can be found in everyday products. Examples of direct OS include temperature or pressure sensors used in smartphones, while indirect measurements can be found in infrared-based rainfall sensors utilized for car windshield wipers. OS are often associated with the Internet of Things and their number is increasing with global connectivity. The main scientific limitation of using OS data is their heterogeneous quality. This thesis aims to prove that certain OS can provide high-quality rainfall estimates.

1.2 Traditional precipitation sensors: A brief overview

Rain gauges

Rain gauges are the oldest and most common form of precipitation measurement. They consist of an orifice of a defined size above a measurement unit quantifying the collected amount of precipitation. While early instruments were operated with a height scale to read the amount of precipitation called accumulation gauges, nowadays, mostly tipping-bucket, weighing, and optical gauges are used.

The first evidence of the use of rain gauges can be dated back to the fourth century BC in India and the second century BC in Palestine (Strangeways, 2010). The longest consistent time series from rain gauge rainfall observation is around 300 years long (e.g. Prohom et al., 2016). To date, rain gauges are one of the major sources of rainfall information and the worldwide number of professionally operated rain gauges is around 250,000 (Kidd et al., 2017). They are used to adjust weather radar and satellite products and their information is assimilated into weather and hydrological model systems.

The main advantages of rain gauges are their comparatively low cost, easy setup, and maintenance. Rain gauges measure precipitation at the point scale and depending on the device, their accuracy and temporal resolution can be very high. The lack of spatial representativeness is their major drawback. The combined area of all rain gauges used within global rain gauge-based rainfall datasets (e.g. GPCC) is smaller than the area of a football pitch. Other uncertainties in precipitation observation from rain gauges stem from underestimation due to wind drift and under-catch of snow for unheated rain gauges (Sevruk, 2006).

The global distribution of rain gauges is varying in space and over time. Data sparse regions are Africa, South America, and parts of Asia, especially in deserts and mountain ranges (Lorenz and Kunstmann, 2012). After a steady increase in the number of rain gauges in the 20th century, their number has decreased mainly in North America and Europe since the turn of the millennium. Another challenge is that even when rain gauges are present, data availability is often restrained by national data protection regulations. This is true for example in West African countries and it takes researchers great effort to get access to such data (Bliefernicht et al., 2021).

Disdrometers

Similar to a rain gauge, a disdrometer measures precipitation at the point scale. Precipitation is measured indirectly via the size and vertical velocity of hydrometeors. Therefore, a disdrometer is the main instrument to characterize drop size distribution (DSD). Typically, the drop sizes are counted in bins of increasing width. Invented by Joss and Waldvogel (1967), disdrometers nowadays use optical measurements like lasers or cameras, or acoustic measurements from the impact of raindrops to record the individual hydrometeors within the sampling volume. Some disdrometers are able to automatically distinguish between rain, snow, hail, or graupel. A common application of disdrometer data is to fit the Z-R relation of a weather radar to the local rainfall climatology derived from the DSD (Sheppard and Joe, 1994; Uijlenhoet et al., 2003). Their high accuracy and precise technical complexity make disdrometers an expensive instrument in comparison to rain gauges. That is the main reason why only a few countries (e.g. Canada, Germany, and Great Britain) have operational disdrometer networks (Pickering et al., 2019).

Weather radar

The first efforts to derive precipitation estimates from radar echos were made in the 1930s and 1940s. The measurement principle is that a part of a pulsed radar beam gets reflected back to the radiating source by hydrometeors. By measuring that backscatter and the travel time, a rainfall estimate at a certain distance is obtained. Marshall and Palmer (1948) developed the Z–R relation

$$Z = aR^b \tag{1.1}$$

where Z is the radar reflectivity (mm^6m^{-3}), R is the rain rate (mm^{h-1}) and the parameters a and b depend on the drop size distribution.

Weather radars can capture the spatio-temporal characteristics of precipitation by using a scan pattern with a sub-kilometer and sub-hourly resolution. However, their data is still not used as widely as one could expect in hydrological applications mainly because of errors and uncertainties (Berne and Krajewski, 2013): Weather radars measure precipitation indirectly and thus can suffer from ground clutter, beam blockage, and their measurement high above the ground. Their main source of uncertainty however stems from the Z-R relation, as the drop size distribution varies with local climate but also within each individual rainfall event. The uncertainties of radar estimates and their potential usage in hydrological applications are summarised in a detailed review by Villarini and Krajewski (2010). These uncertainties can lead to low correlations between weather radar data and precipitation measurements on the ground, especially at sub-hourly resolutions (Bárdossy and Pegram, 2017). Efforts have been made to reduce errors and uncertainties for example by using polarimetric radar data, facilitating horizontal and vertical polarized radar beams allowing for example a hydrometeor classification. Nevertheless, a study by Schleiss et al. (2020) has shown that weather radar products, polarimetric as well as gauge-adjusted ones, still tend to underestimate heavy precipitation. This is especially true when considering the sub-pixel variability for heavy, short-duration events (Peleg et al., 2018).

Satellites

Rainfall can also be observed from space with active and passive sensors on earth-observation satellites. The major advantage of these measurements is that they can cover the whole planet, delivering rainfall estimates over areas where no ground-based observation networks are established. While satellite rainfall products, in general, have the drawback of low spatial resolution, specific sensors, and products have individual advantages and disadvantages.

Geostationary satellites with an orbit of 36,000 km continuously observe one region of the earth and can therefore provide a high temporal sampling rate. However, they typically use visible or infrared channels to estimate rainfall based on cloud height and temperature with sophisticated highly parameterized algorithms.

Satellites with low earth or polar orbit can provide a higher spatial resolution of up to 0.1 degree and some are equipped with active microwave sensors which deliver more accurate rainfall estimates. However, their typical revisit times are in the order of hours to days. Many satellite products combine data from geostationary and low-earth orbit satellites to combine their advantages (Kidd et al., 2021). Still, merged multi-satellite products have a latency of several hours. For example, the Integrated Multi-satellite Retrievals (IMERG) early run of the Global Precipitation Measurement Mission (GPM) has a latency of 6 hours, while potentially missing or severely misjudging rainfall events and dynamics on scales below the revisit time of the low earth satellites (Huffman et al., 2015). Further potential error sources are the employed retrieval algorithms which rely on several calibration and correction stages (Adler et al., 2001; Maggioni et al., 2016).

Combination of rainfall sensors

Data from these four sensors are merged into precipitation products by national meteorological services and research institutions. A common combination is the adjustment of weather radar data with rain gauges. The German Weather Service (DWD) operates RADOLAN (Radar Online Adjustment), a radar-based quantitative precipitation estimation that combines the data from 17 weather radars and more than 1000 rain gauges to various products (Bartels et al., 2004; Winterrath et al., 2018). Two of these products which are repeatedly used as references in this thesis are RADOLAN-RW, a real-time product with an hourly resolution used for example for operational flood forecasting, and RADKLIM-YW, a climatologically corrected version issued once a year. Other common combinations consist of satellite and rain gauge measurements (e.g. GPM) or disdrometer measurements which are used for the fitting of the Z-R relation of weather radars.

1.3 Opportunistic rainfall sensing: State of the art

Opportunistic sensing and crowd sourcing

Opportunistic sensing is a fairly new approach to gathering meteorological information from devices that are not intended to deliver high-quality observations in a scientific context. These devices, whether they measure meteorological variables like temperature, pressure, or rainfall directly or indirectly, will here be called opportunistic sensors (OS). Liberman and Messer (2014) were the first to use the term *opportunistic sensor* in the context of rainfall measurements with commercial microwave links. OS are often connected to the internet which gives the opportunity for real-time data transfer. Data from some OS are crowd-sourced which describes the idea of outsourcing observations to the crowd (Howe, 2006). Examples of crowd-sourced data are the collection of meteorological variables from private weather stations (de Vos et al., 2020), smartphones (Guo et al., 2019; Hintz et al., 2019; Madaus and Mass, 2017; Overeem et al., 2013b), connected vehicles (Mahoney and O'Sullivan, 2013; Rabiei et al., 2013) or from social media posts (de Vasconcelos et al., 2016). A summary of crowd-sourced meteorological data is given by Zheng et al. (2018). For other OS, typically the ones that are operated by the private sector, data streams from the sensors to researchers have to be established. Depending on the sensor type and company this can be cumbersome work (Chwala et al., 2016) or related to costs (Andersson et al., 2022).

For rainfall, the feasibility and potential of the following OS were tested: The potential to use the attenuation of CML signals for rainfall estimation has been a research topic for over 15 years (e.g. Messer et al., 2006). Similarly, the rainfall-induced attenuation along satellite-earth connections for TV reception was exploited (Barthès and Mallet, 2013; Mercier et al., 2015). Rainfall data from private weather stations was analyzed in several studies (e.g. de Vos et al., 2020; Bárdossy et al., 2021). Binary rainfall information was derived from windshield wiper frequencies as they are regulated by the optical rainfall sensor of a car (Mahoney and O'Sullivan, 2013; Rabiei et al., 2013). Finally, camera footage of rain was used to derive rainfall estimates (Allamano et al., 2015; Jiang et al., 2019). In the future, the number of potential OS will increase with the growing number of devices connected to the *Internet of Things* (Balsamo et al., 2018; McCabe et al., 2017; Tauro et al., 2018). A first study on multiple OS for the hydrometeorological monitoring for the city of Amsterdam by de Vos et al. (2020) showed their combined potential for applications like the tracking of a frontal system and the observation of urban heat island effects. Within this thesis, data from two OS are analyzed, namely from commercial microwave links (CMLs) and private weather stations (PWSs). In the following two sections, a description and the state of the art for rainfall estimation from CMLs and PWSs will be given.

Commercial Microwave Links

CMLs are part of the global communication infrastructure and constitute large parts of the cellular backhaul network. They use highly directional antennas to transmit data within a line of sight with frequencies typically ranging from 7 to 90 GHz over a few hundred meters to tens of kilometers. They consist of a transmitter and a receiver using radio waves in the microwave frequency

range to transmit data. Applications using similar technology and frequencies are communication between satellites and base stations, wireless local area networks, and other short-range communication devices.

Precipitation affects the propagation of microwave transmission used e.g. by CMLs through scattering and absorption. The fraction of attenuation from scattering and absorption due to raindrops depends heavily on the rain rate. Other hydrometeors have different influences: Dry snow causes far less scattering and absorption than rainfall, while semi-solid hydrometeors like melting snow or hail result in heavily increased attenuation (Paulson and Al-Mreri, 2011).

The history of microwave link communication started in the 1940s when the usage of radio frequencies between 3 and 30 GHz (centimeter waves) for radio communication. The relation between rainfall and attenuation of microwave radiation was already a research subject considered in conferences like the "Meteorological factors in radio-wave propagation" (Physical Society and Royal Meteorological Society, 1947). In the following decades, the usage of centimeter wave bands increased with refined manufacturing processes of radio hardware in the 1960s and to avoid interference, the usage of higher frequencies (millimeter waves, 30 - 300 GHz) bands was investigated. These frequencies have wavelengths more similar to the size of raindrops which therefore cause more attenuation. Engineers saw rainfall as a main challenge for the usage of higher frequency bands and expected that a better knowledge of the spatio-temporal properties of rainfall would be necessary to overcome outages due to rainfall (Hogg, 1968). One decade later, Atlas and Ulbrich (1977) chose a different perspective by using microwave links to measure precipitation for the first time and formulated the k-R relation:

$$k = aR^b \tag{1.2}$$

This relation links the specific attenuation of a microwave beam k in dB/km to a rain rate R in mm/h. The parameters a and b depend on the CMLs frequency and polarization and only to a minor extent on the raindrop temperature and DSD. For frequencies in the range of 20 to 40 GHz, the parameter b is nearly 1. This results in an almost linear relation between rain rate and attenuation. Until the early 2000s, several microwave link experiments for rainfall observation were conducted (e.g. Upton et al., 2005). At the same time, cellular networks grow by the large-scale deployment of CMLs. These were and still are operated mainly with frequencies of 10 to 40 GHz which offer the possibility of information transfer over tens of kilometers. The growing demand for bandwidth has led to the increased deployment of CMLs with frequencies of around 80 GHz in the fifth generation of cellular networks (5G) during the last few years. These frequencies are more sensitive to rainfall and their lengths are accordingly shorter (¡¡ 5 km).

The usage of CMLs, and therefore the opportunistic usage of data from cellular networks for rainfall estimation, was first suggested independently by Messer et al. (2006) and Leijnse et al. (2007). Both showed that the world's 4 million CMLs (Ericsson, 2016) could be used for rainfall estimation. This was the starting point of the research topic of CML-based rainfall estimation. A schematic representation of a CML and the attenuation caused by rainfall is shown in Fig. 1.1.

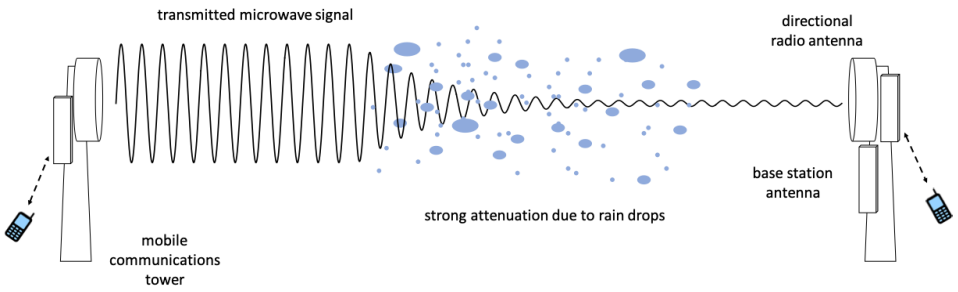

Figure 1.1: Schematic representation of a CML.

The main motivation for CML-based research stems from the large number of potential rainfall sensors from which a variety of hydrological and meteorological applications could benefit.

The state-of-the-art on the way toward reliable CML-derived rainfall estimates and the existing research gaps can be categorized into individual steps:

(a) **Data acquisition**

The acquisition of CML data is more a technical than a scientific task. Researchers depend on cellular network operators to either provide them with a dataset or grant them direct access to measured signal levels from their network. In order to estimate rainfall, information on the signal strength, as well as metadata of the CMLs properties like frequency, length, and polarization are necessary.

Commonly, CML data is acquired by researchers in two different types which define requirements for the retrieval of rainfall information. The first one comprises minimal and maximal signal levels (min-max sampling) over a certain time period which network operators store internally for network monitoring. This min-max sampled data often has a temporal resolution of 15 minutes. This type of CML data was used for rainfall estimation e.g. in the Netherlands (Overeem et al., 2013a) and in Sri Lanka (Overeem et al., 2021) where network operators provided researchers with historical datasets.

The second option is the instantaneous measurement of transmitted and received signal levels (TSL and RSL). The sampling rate can vary between 10 Hz and 15 minutes. Instantaneously sampled data can be retrieved by installing data loggers directly at CML antennas (Chwala et al., 2012), by a simple network management protocol based within the networks operators IP network containing the CMLs (Chwala et al., 2016), or by data sampling by the operator itself. Such systems have the ability to pol data with high temporal frequency in near real-time.

Ericsson, the DWD, and researchers from KIT set up such a system recently, where Ericsson delivers attenuation data from thousands of CMLs with a 10 s resolution once per minute. This development took more than 10 years, which highlights the cumbersome task of CML data acquisition for rainfall estimation. After more than 15 years of CML-based research, there are still only a few public CML datasets available (Andersson et al., 2022; Špačková et al., 2021). The main reasons are the long process of getting data in the first place and because network providers often are restrictive with the geographic locations of the CMLs in their network.

Both min-max and instantaneously measured signal levels are expressed in dBm which relates to the power P where $0\ dBZ = 1\ mW$. Typically, signal levels are quantized which leads to uncertainty, especially during light rain with such an intensity that it causes attenuation in the magnitude of the quantization.

(b) **Quality control**
Rainfall is not the only source of disturbance of a CML's signal. Refraction or reflection causing multi-path propagation of the signal can lead to signal fluctuations (Upton et al., 2005). A largely unexplored source of signal fluctuations is caused by meteorological variables like wind, temperature, or solar radiation, which can influence the CML beam or its antennas. The alignment of two opposing antennas on freestanding masts can be disturbed by wind. Ericsson (2021) analyzed data from 500 E-band CMLs from which a third showed mast sways. They also reported a complete loss of signal due to mast sway for individual CMLs. Temperature and solar radiation can influence the CML electronics in the transmitting and receiving antenna (Chwala and Kunstmann, 2019), but no quantitative investigation in the context of CML rainfall estimation has been conducted so far. Other sources of disturbance can be found in human activity (temporally) blocking the line of sight of a CML for example by a construction crane or by growing vegetation. Fluctuations compared by water vapor and oxygen which have absorption bands within the typical CML frequencies are typically minor compared to attenuation caused by rainfall (Uijlenhoet et al., 2018).

These disturbances have to be considered when using CMLs for rainfall estimation. Due to different data acquisition systems, network configurations, and sampling strategies, each CML dataset has been filtered individually. Overeem et al. (2013a) for example presented a filter based on the spatial correlation of precipitation events of CMLs which suited their dense CML network located in the Netherlands. This would not be possible for mountainous regions where orographic effects can interrupt the spatial correlation of rainfall. For accurate CML-derived rainfall estimates and their future use in (operational) applications, robust filters have to be developed (Chwala and Kunstmann, 2019).

Besides such specifically developed filters, other CML processing steps that are described hereafter are related to quality control or to fluctuations of the signal not caused directly

by rain. The rain event detection and baseline estimation are to a certain degree able to remove fluctuations from other sources than rain and the uncertainty of CML-derived rainfall estimates due to wet antenna attenuation is often considered a non-rain disturbance of the signal and mitigated with specific compensation methods.

(c) **Rain event detection**
Independent of being instantaneously or min-max sampled, each attenuation time series has to be classified in rainy and dry periods. This step is necessary because only then a baseline of the dry signal level can be extrapolated for each rainy period in order to calculate the attenuation caused by rainfall. Two major concepts for this task were developed, the near-by-link approach and time series-based approaches.

The near-by-link approach considers a period as wet when the time series of neighboring CMLs correlate during a signal increase (Overeem et al., 2011). This approach worked better with 15-minute min-max data than with 15-minute instantaneously sampled data (de Vos et al., 2019b). It was used for CML studies in the Netherlands (Overeem et al., 2013a), Brazil (Rios Gaona et al., 2018) and Sri Lanka (Overeem et al., 2021).

A variety of time series-based methods using individual TRSL time series to classify wet and dry periods were developed. A simple yet practicable method used a threshold to separate the rolling standard deviation of TRSL in wet and dry periods (Schleiss and Berne, 2010). Recent studies still used this method (e.g. Kim and Kwon, 2018; Fencl et al., 2020). Other approaches developed for the detection of rainy periods are a Markov switching model (Wang et al., 2012), Fourier transformations on a rolling window of TRSL (Chwala et al., 2012), random forest classifiers and Gaussian factor graphs (Kaufmann and Rieckermann, 2011), decision trees (Cherkassky et al., 2014), and a Multilayer Perceptron (Đorđević et al., 2014). Another approach that classified 15-minute min-max data and a time series-based approach used a Long Short-Term Memory network (Habi and Messer, 2018).

The classification between wet and dry periods can also rely on meteorological data. Schip et al. (2017) proposed the use of rainfall products from the geostationary satellite Meteosat for this task which could show its biggest potential in regions with a lack of radar data and a limited number of traditional ground-based observations.

A main challenge for the development of rain event detection methods is the trade-off between being too liberal and too conservative (Chwala and Kunstmann, 2019). More liberal methods are able to detect more low-intensity events close to the detection limit of the CML but also easily mistake small fluctuations from other sources than rainfall for rainfall. Vice versa, conservative methods reduce this error at the cost of detecting fewer low-intensity events. This trade-off was not analyzed in the evaluation of previous rain event detection methods. Additionally, with a growing number of CMLs in datasets, this trade-off has to be automatically optimized for many CMLs with various properties and error sources.

(d) **Baseline estimation**
For each detected rainy period a baseline of the CMLs' signal has to be estimated to derive the rain-induced attenuation. There is no possibility to measure the baseline directly, which leads to a remaining uncertainty in all baseline estimation methods. Most commonly, a constant baseline based on the last or an average of the last TRSL values before the rain event is assumed. This is reasonable and fairly accurate, especially for CMLs which show stable signal levels over long periods. A few different approaches were proposed to determine the baseline during rain events, for example, a local smoothing with daily quasi-periodicity (Reller et al., 2011), a low-pass filter modeling the baseline (Fenicia et al., 2012) or a simple rolling mean over TRSL (Ostrometzky and Messer, 2018).

(e) **Wet antenna attenuation**
Water droplets on the radome of CML antennas cause attenuation of the CML's signal. The droplets can be caused by rain, melting snow covering the radome, or dew. This effect is called wet antenna attenuation (WAA) and can result in a large uncertainty of rainfall estimates when it is not compensated for (Chwala and Kunstmann, 2019; Pastorek et al., 2022). The most promising way to investigate WAA for a single CML is to set up an experiment where the antennas' properties (hydrophobic or hydrophilic radome material, radome thickness, age, etc.), as well as environmental parameters, can be measured. Moroder et al. (2019) set up such an experiment and developed a model based on the dynamic antenna parameters reflectivity, efficiency, and directivity with a full-wave simulation (Moroder et al., 2020). This setup allowed for the measurement of the WAA contribution through a continuous recording of the CML antenna properties and parameters. Tiede et al. (2023) continued these experiments and was able to record previously unknown temporal dynamics by comparing WAA and camera footage of the antennas. They found delayed wetting events as well as cases of strong decrease of WAA during rainfall events due to the sudden wash-off of large drops.

However, in reality, a CML network is equipped with a variety of hardware with varying antenna properties and the ambient atmospheric conditions are mostly unknown. Therefore, methods to compensate for WAA are often simple and use parameterizations. The simplest models subtract a fixed quantity from the attenuation during rain events (Overeem et al., 2016a; Schleiss et al., 2013). Others consider a wetting and drying dynamic over time (Kharadly and Ross, 2001; Valtr et al., 2019), antenna properties like radome thickness, and the dependency between WAA and the rain rate (Leijnse et al., 2008; Pastorek et al., 2022). The question of which compensation method with which parameters should be used lacks a large-scale analysis to date.

The effect of dew and melting snow on WAA is not investigated in detail. As dew typically forms continuously over several hours the resulting attenuation will typically not be classified as a rain event from a rain event detection method. Melting snow on antennas on the other hand can cause significant attenuation in a short period adding up to the problem of strong attenuation of melting hydrometeors in winter.

(f) **Rainfall retrieval from attenuation**
When for each detected rain event the attenuation above baseline level is calculated and compensated for WAA, it can be used to derive the path-averaged rain rate via the k-R relation (Eq. 1.2). The parameters a and b can either be derived from a local rainfall climatology using e.g. a disdrometer, or, as they are more dependent on the CMLs frequency and length, it is also possible, and common practice, to use universal values from an ITU recommendation (ITU-R, 2005).

(g) **Spatial reconstruction and merging**
Since rainfall can be highly variable in space and time, high-resolution rainfall maps with a high spatiotemporal resolution are the best source of rainfall information for many hydrological applications. Rainfall fields can be spatially reconstructed from path-averaged rainfall information derived from CMLs. Well-known interpolation techniques like inverse distance weighting (IDW) and Kriging (e.g. Overeem et al., 2016b) were used, considering each CML observation as a synthetic point observation at its center. The geometrical property of CML rainfall estimates was considered in several studies using the stochastic reconstruction approach Random Mixing (Haese et al., 2017), tomographic algorithms (D'Amico et al., 2016; Zinevich et al., 2010) or an iterative IDW approach (Goldshtein et al., 2009; Eshel et al., 2021).

CML-derived rainfall information was also used to derive combined rainfall products from the combination with rain gauges (Fencl et al., 2017) and weather radar (Liberman et al., 2014; Trömel et al., 2014). When merging CML rainfall estimates with other rainfall products, CMLs can offer two advantages. First, they outnumber rain gauges both in regions with high hydrometeorological observation coverage like in Europe, and even more so in regions like West Africa, South America, or parts of Asia with a limited number of rainfall observations. Second, they also fill the gap in spatial representativeness between the pointwise observation of rain gauges and spatial integrated measurements from weather radar or satellite observations.

(h) **Application**
Parallel to the development of processing methods, CML-derived rainfall estimates were used in a number of hydrological applications. In most cases, hydrological models were used to compare rainfall input from CMLs to rain gauges. Fencl et al. (2013) conducted such a comparison with an urban rainfall-runoff model. They found an increased performance of the model with the CML rainfall input, albeit some underestimation was caused by smoothed rainfall maxima. Smiatek et al. (2017) and Cazzaniga et al. (2022) conducted a similar comparison using (semi-)distributed hydrological models for two catchments in Germany and Italy, respectively. While in the German case, a better spatial representation of CMLs compared to rain gauges led to an improved hydrograph, in the Italian case the CML networks' layout was unfavorable, and rain gauge data produced a better runoff. The influence of CML positioning and length were investigated with an urban rainfall-runoff model by Pastorek et al. (2019) with the result that shorter CMLs within the catchment boundary lead to

better runoff prediction than CMLs reaching over the catchment boundaries. CML-derived rainfall estimates were also tested as input for rainfall nowcasting (Imhoff et al., 2020).

Personal Weather Stations

Personal weather stations (PWSs) are privately owned weather stations. People buy them out of interest in meteorology or to supply their smart homes with meteorological data. PWSs can consist of indoor and outdoor units measuring for example temperature, pressure, humidity, or CO_2 concentration and can be acquired from different manufacturers. Often a complementing rain gauge, typically tipping bucket-style, can be purchased. Compared to instruments of national meteorological services or research institutions, PWSs are low-cost sensors with acquisition costs from 50 to 500 Euros. In the following, the term PWS will only refer to personal weather stations which measure rainfall. As PWS, in contrast to CMLs, measure rainfall directly, there are fewer processing steps required to evaluate or use PWS data in applications:

(a) **Data acquisition**
The focus here is set on PWS which are connected to the internet. A variety of companies are offering such PWS (e.g. Netatmo, Sainlogic, Ecowitt, Dostmann). Netatmo operates a website where users can upload their data automatically when their PWS is connected to the internet via WLAN. Their own upload enables the use of the data of others in exchange (e.g. `https://weathermap.netatmo.com`). The download is possible via an API that has currently no restrictions on the number of SQL calls. Weather Underground is a platform where PWS data from different PWS manufacturers can be uploaded to (`https://www.wunderground.com/wundermap`). Similar to Netamo their weather maps can be viewed online and data access is also possible via an API, but limited to ten SQL calls per minute and 500 per day. Users can upgrade to a business plan allowing more access. Companies like Netatmo sell their data to researchers to researchers and meteorological services. Depending on negotiations this allows researchers to publish PWS data. de Vos et al. (2019a) were the first to publish a larger PWS dataset for the Amsterdam region. EUMETNET released a dataset containing data of PWSs for the whole of Europe for 2020 from Met Office WOW and Netatmo to support the development of PWS quality control tools (Met Office and Netatmo, 2021). Access to this dataset is, however, restricted at the moment.

(b) **Quality control**
Compared to other variables like temperature or pressure, the quality of PWS rainfall measurements is even more sensitive to the care of their owners. An important step in the setup of a PWS is the choice of location. The distance to buildings and vegetation will in most cases not meet the standards for the setup of rain gauges defined by the World Meteorological Organisation (WMO). The manual for the setup of Netatmos' rain gauges suggests for example a setup height of 0.5 to 1.5 m and a distance of either 3 m or a distance equal to the height of the next building or tree (Netatmo, 2022) which is only half of the distance the WMO recommends. Additionally, careful calibration and regular checks of whether the orifice and tipping bucket are free and functioning are necessary to obtain accurate data.

For the quality control of PWS, de Vos et al. (2019a) defined three filters that remove faulty zeroes, high influx, and station outliers as well as a bias correction. The filters and bias correction are based on the comparison among spatially close CMLs. While removing around 12 % of the data, a Pearson correlation of 0.58 compared to a gauge-adjusted radar product was achieved. Bárdossy et al. (2021) used data from DWD rain gauges as a primary network to filter PWS data (secondary network). Their filters were based on rank statistics between the two networks and consisted of an indicator correlation filter, a bias correction, and an event-based filter. Their results showed that thorough quality control becomes more important for shorter temporal aggregations of PWS data. Some error sources like battery failures or inconsistent Wi-Fi connections are not easily detectable and therefore lead to faulty time series.

(c) **Evaluation and application**
Besides studies focusing on the quality control of PWSs, several studies evaluated or applied PWS data using manual quality checks or routines developed for well-maintained rain gauges. Chen et al. (2018) investigated the trustworthiness of PWSs in the USA for a small urban area. Golroudbary et al. (2018) analyzed the difference between PWSs located in urban and rural areas in the Netherlands. Đorđević et al. (2014) investigated the ability of PWSs to capture heavy and local rainfall events for an urban area near Katowice in Poland and concluded that information from PWSs can be very useful for observing local extremes. In an experimental application Mapiam et al. (2022) used PWSs to adjust radar data from one weather radar in Thailand with a bias correction and found improved results compared to the usage of a sparse traditional rain gauge dataset.

1.4 Research questions

The potential of CMLs and PWSs for rainfall estimation has been shown for various regions. A common limitation of almost all previous studies is that they were based on data from a few OS and often covered short time periods. The methods used to process CML data were like-wise developed on such small datasets. Only Overeem et al. (2016b) conducted a large-scale analysis that covered 2.5 years of 15-minute sampled min-max data from 2044 CMLs in the Netherlands. Nevertheless, their study was limited to a certain extent: They compared CML-derived rainfall maps with a gridded reference without evaluating the performance of individual CMLs. They also used a heavily parameterized processing routine which still is subject to optimization (Wolff et al., 2022). In order to provide reliable rainfall maps from CMLs, robust and generally applicable processing methods have to be developed and tested (Uijlenhoet et al., 2018). The fact that many methods were developed with only a few CMLs leaves the question open whether these methods are robust and transferable to new CMLs and new regions. This thesis could build on a growing dataset of more than 4000 CMLs covering Germany with a temporal resolution of one minute. This dataset fits the challenge of testing and developing a robust processing routine. Hence, the testing and optimization of processing methods with this dataset led to the first research question:

1. How do state-of-the-art processing methods perform, and how can they be optimized to provide high-quality CML rainfall estimates?

Within the processing of CML data, rain event detection is the single most important step. It defines the periods for which a baseline is calculated and subsequently when rain rates are derived from attenuation with respect to that baseline. Equally important, it also serves as a filter to remove fluctuations caused by other factors than rain. The main challenge is to distinguish between noise and signal fluctuations caused by rain. A wrong classification can lead to an over- or underestimation of the rainfall amount. The two most prominent rain event detection algorithms feature critical limitations. The near-by-link approach depends on CML network density, which may be highly variable (e.g. Overeem et al., 2016a)). The rolling standard deviation method (Schleiss and Berne, 2010)) and similarly other time series-based methods are limited in their ability to adapt to differences in the amount of signal fluctuation and do not consider the signal pattern. Improved results could be expected from a method that evaluates the specific patterns in the CML time series such as a machine learning technique for pattern recognition. This leads to the second research question:

2. Can an artificial neural network for rain event detection improve CML-derived rainfall estimates?

Besides the improvement of processing methods for CML data, the actual limitations given by the properties of the CML network and its individual CMLs have to be understood to interpret the derived rainfall estimates correctly. One of the limitations is that heavy rainfall can cause the total loss of signal, here called a blackout. Because of such blackouts, CML rainfall estimates might miss peak rainfall intensities. For hydrological applications like flood forecasting or extreme values statistics, heavy rainfall events are of the highest relevance. Hence, the third research question is formulated to quantify the potential error caused by blackouts:

3. How many blackouts from heavy rainfall can be observed in CML data and how does this affect rainfall estimation?

In contrast to CMLs, PWSs measure rainfall directly. Nevertheless, they are prone to a variety of errors which have to be considered in a filtering routine to ensure data quality (de Vos et al., 2019a). An evaluation of their performance over large spatial and temporal scales is missing to date. Furthermore, no combination of two OS has been conducted so far. To evaluate the quality of rainfall maps from combined CML and PWS data the fourth question is raised:

4. How good is the performance of PWS and combined CML and PWS rainfall estimates considering various spatial scales in a large-scale evaluation?

The overall goal of this thesis is to generate rainfall products from two types of opportunistic sensors and to achieve a quality comparable to rainfall products from traditional rainfall observation. To reach this goal, methods for quality control, processing, and combination of CML and

PWS data have to be developed and limitations have to be investigated. To answer the research questions above and to evaluate the performance of the proposed methods, large-scale evaluations of OS-derived rainfall products will be conducted.

1.5 Outline

This thesis consists of four peer-reviewed articles answering the research questions and is structured as follows:

Chapter 1: Introduction. This chapter gives an overview of traditional and opportunistic rainfall sensors and motivates the research questions of this thesis.

Chapter 2: Rainfall estimation from a German-wide commercial microwave link network: Optimized processing and validation for one year of data (Graf et al., 2020a). The first article can be seen as an introduction to precipitation estimation with CMLs. It presents a CML data set with 4000 CMLs in Germany which is also used in the subsequent chapters. This dataset was used for the development and optimization of CML processing methods. For one year of data, both path-averaged rainfall estimates, as well as IDW-interpolated rainfall maps from CMLs, were computed. These results were evaluated with a gauge-adjusted radar product from the DWD over a period of one year. The CML rainfall estimates achieved good agreement with the reference dataset except for the winter months. The results of this article serve as a benchmark for subsequent developments and analyses.

Chapter 3: Rain event detection in commercial microwave link attenuation data using convolutional neural networks (Polz et al., 2020). The second article describes one of these developments. It presents the use of convolutional neural networks (CNNs) for the detection of rain events by classifying the fluctuations in the CML signals that are caused by precipitation. This is a crucial step for further precipitation estimation and is at the same time challenging, because of factors other than rain which can cause attenuation or signal fluctuations. This classification further serves as part of the quality control, as fluctuations caused by other factors than rain are not classified as wet periods. The main focus of the classification was to minimize the trade-off between false wet and missed wet prediction. Compared to the previously used classification method, the CNN-based method showed a significant improvement.

Chapter 4: Missing rainfall extremes in CML data due to total loss of signal (Polz et al., 2023b). This analysis deals with failures of CMLs that can be caused by complete signal attenuation during extremely heavy rainfall, called blackouts. Their occurrence was analyzed using three years of CML data from Germany as well as 20 years of synthetic CML data derived from a weather radar product. It was found that for yearly rainfall sums, around one percent was missing due to blackouts. Surprisingly, the outages were found particularly in longer CMLs,

despite network operators providing them with higher signal strength. From the comparison of CML and synthetic blackouts, it was found that there are 8.5 times more blackouts in the CML data. These findings have implications both for CML precipitation estimation and CML network planning which are discussed.

Chapter 5: Rainfall estimates from opportunistic sensors in Germany across spatio-temporal scales (Graf et al., 2021b). The previous approach of deriving rainfall maps from CMLs was extended by the usage of PWS in the fourth article. Data from 4000 CMLs and more than 20,000 PWSs were combined for the first time. The main challenges were to ensure the OS data quality and the correct combination of their spatial representativeness for interpolation. Two filters and a bias correction, based on rank statistics between the OS and automated rain gauge from the DWD, ensured the OS data quality. For the combination of OS, a Kriging framework was developed, which incorporates the CMLs' integral characteristic and the uncertainty of OS measurements. The results of a two-year evaluation showed that the combination of CMLs and PWSs was able to outperform the DWDs' measurement network of rain gauges and provided results similar to the ones from two weather radar products on regional and local scales.

Chapter 6: Summary and synthesis. The main objective of this thesis was to derive high-quality precipitation estimates from CML and PWS. The contribution of the individual articles to this overall objective is summarized and discussed in this chapter. The overall framework of this thesis is given in Figure 1.2. It shows the chapters consisting of the publications as well as the overlap of the underlying data and the progressive development and usage of methods in this thesis. Finally, key results and combined innovations connect the chapters and lead to the main outcome of this thesis.

1.6 Innovation of the thesis

The main innovations of this thesis are:

- The first large-scale analysis of country-wide CML data for rainfall estimation in Germany which facilitates a fast parallel workflow on HPC infrastructure.
- The improvement of existing CML processing methods and the development of filtering routines.
- The development of a CNN-based rain event detection which significantly improves the rainfall estimates on large scales.
- The quantification of missing values in CML rainfall estimates due to rainfall-induced blackouts both from CML and radar-based synthetic CML data.
- The development of a framework for quality control and the combination of CML and PWS data with an emphasis on their specific errors and geometrical characteristics.
- The first combined rainfall estimates from CML and PWS data with a country-wide, multi-year evaluation.

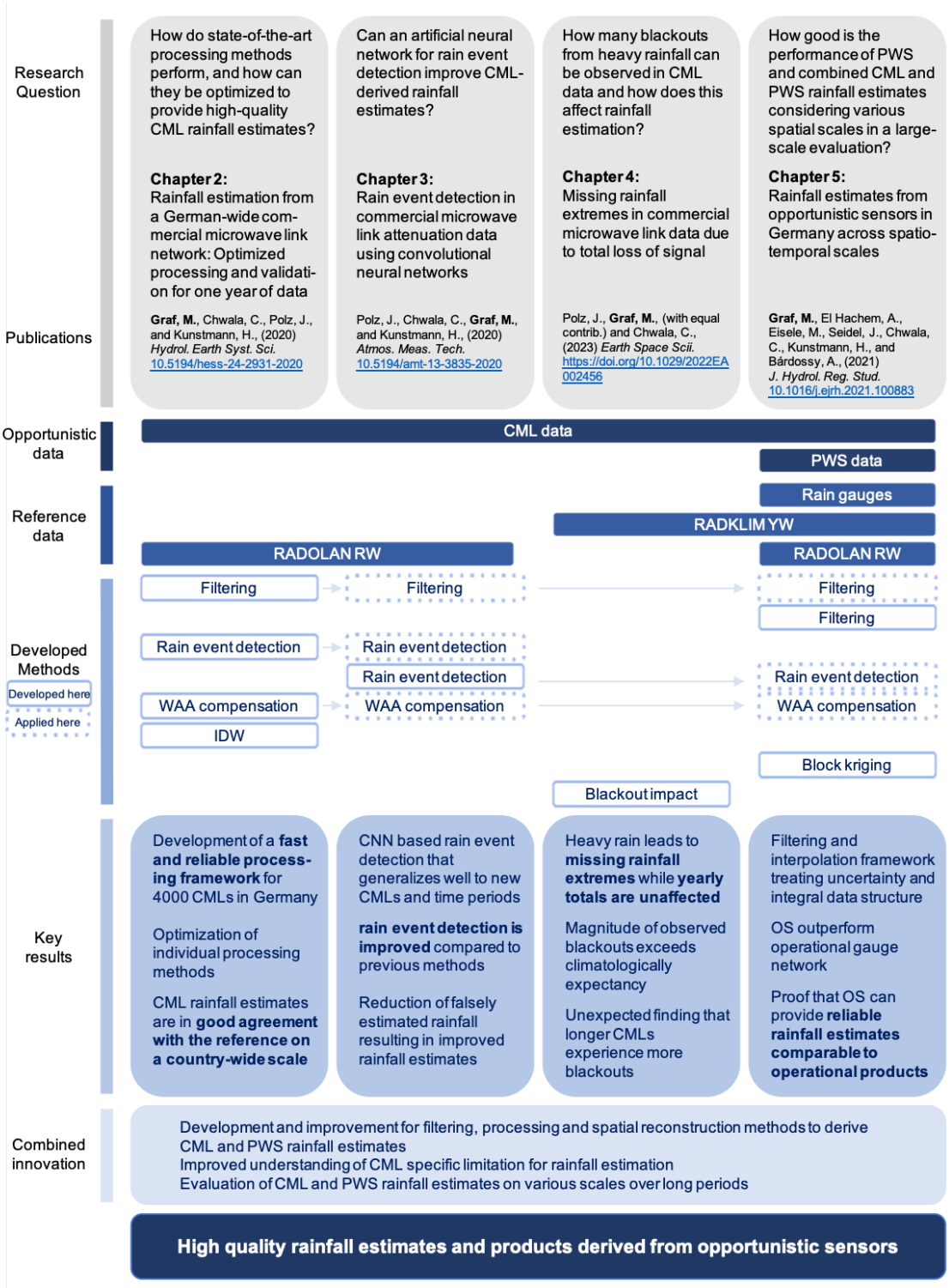

Figure 1.2: Framework, key results and combined innovation of this thesis

1.7 Contribution of the author to the different articles

Chapter 1 and **Chapter 6** were written by Maximilian Graf.

Chapter 2: ***Rainfall estimation from a German-wide commercial microwave link network: Optimized processing and validation for one year of data***

Graf, M., Chwala, C., Polz, J., and Kunstmann, H.: Rainfall estimation from a German-wide commercial microwave link network: optimized processing and validation for 1 year of data, *Hydrol. Earth Syst. Sci.*, 24, 2931–2950, `https://doi.org/10.5194/hess-24-2931-2020`, 2020.

The concept of this study was designed by Maximilian Graf, Christian Chwala, and Harald Kunstmann. Maximilian Graf and Christian Chwala designed the analysis and Maximilian Graf carried it out with contributions from Christian Chwala and Julius Polz. Christian Chwala set up the data acquisition to provide the raw CML data. Maximilian Graf further prepared the CML data and set up a parallelized processing routine which sped up the process of method development. The optimization of the individual processing steps was conducted by Maximilian Graf. He also evaluated the results against a reference CML-wise and map-based. The results were presented by Maximilian Graf and were discussed with all co-authors. The code both for the CML processing and the evaluation was developed by Maximilian Graf with contributions from Christian Chwala and Julius Polz. All figures were prepared by Maximilian Graf. The manuscript was written by Maximilian Graf with contributions from and discussions with all co-authors.

Chapter 3: ***Rain event detection in commercial microwave link attenuation data using convolutional neural networks***

Polz, J., Chwala, C., **Graf, M.**, and Kunstmann, H.: Rain event detection in commercial microwave link attenuation data using convolutional neural networks, *Atmos. Meas. Tech.*, 13, 3835–3853, `https://doi.org/10.5194/amt-13-3835-2020`, 2020

Julius Polz, Christian Chwala, and Harald Kunstmann designed the study layout and Julius Polz carried it out with contributions from Christian Chwala and Maximilian Graf. Christian Chwala set up the data acquisition to provide the raw CML data. Maximilian Graf provided pre-processed CML data for the training and validation including the quality filter from Chapter 2. Julius Polz developed the CNN-based rain event detection model and trained and validated this model. Maximilian Graf provided the data of the reference rain event detection which was used by Julius Polz to evaluate the CNN-based model. Maximilian Graf also used the CNN-based rain event detection to derive CML rainfall estimates with this new method. The code was developed by Julius Polz with the contributions of Christian Chwala and Maximilian Graf. All figures were prepared by Julius Polz. Julius Polz prepared the manuscript with contributions from all co-authors.

Chapter 4: ***Missing rainfall extremes in commercial microwave link data due to total loss of signal***

Polz, J., **Graf, M.**, Chwala, C.: Missing rainfall extremes in commercial microwave link data due to total loss of signal, *ESS*, 10(2), e2022EA002456. `https://doi.org/10.1029/2022EA002456`, 2023. (Julius Polz and Maximilian Graf share the first authorship)

Julius Polz, Maximilian Graf, and Christian Chwala designed the study layout. Julius Polz and Maximilian Graf carried out the analysis in equal parts with contributions from Christian Chwala. The data was provided and prepared by all authors. In general, Julius Polz conducted all analyses related to the synthetic CML data based on RADKLIM-YW and Maximilian Graf conducted all analyses related to the observed CML data with respective contributions and discussion with Christian Chwala. Accordingly, Figures 1 and 2 were prepared by Maximilian Graf who provided CML-based statistics and developed a blackout gap detection algorithm while Figures 3 and 4 were prepared by Julius Polz who provided synthetic CML-based statistics and compared the blackout frequency in real and synthetic CML observation. Figures 5 and 6 were prepared by Maximilian Graf and Julius Polz. Christian Chwala contributed and discussed various stages of the analysis. Accompanying example software of the blackout gap detection algorithm and example data were prepared and published by Maximilian Graf within the python software package *pycomlink*. Julius Polz and Maximilian Graf prepared the manuscript with contributions and discussions of Christian Chwala. Finally, Julius Polz and Maximilian Graf share the authorship of this publication with equal contributions.

Chapter 5: ***Rainfall estimates from opportunistic sensors in Germany across spatio-temporal scales***

Graf, M., El Hachem, A., Eisele, M., Seidel, J., Chwala, C., Kunstmann, H., Bárdossy, A:. Rainfall estimates from opportunistic sensors in Germany across spatio-temporal scales, *J. Hydrol. Reg. Stud.*, 37, 100883. `https://doi.org/10.1016/j.ejrh.2021.100883`, 2021

Maximilian Graf initiated the cooperation behind this article and conceptualized the study together with Jochen Seidel, Christian Chwala, Harald Kunstmann, and András Bárdossy. Maximilian Graf, Abbas El Hachem, Micha Eisele, and András Bárdossy developed the methodology and software and carried out the analysis. The CML data and the reference data from the DWD were prepared by Maximilian Graf. The PWS data was prepared by Micha Eisele. The filtering routine for PWS data and CML-derived rain rates was taken from Bárdossy et al. (2021) and applied by Abbas El Hachem. András Bárdossy and Micha Eisele developed the interpolation framework. Maximilian Graf and András Bárdossy conducted and analyzed the leave-one-out cross-validation and created and evaluated the rainfall products on different scales and for high-intensity rainfall. Maximilian Graf managed the data flow between the different authors. All figures were prepared by Maximilian Graf, except for Figure 2 which was prepared by Abbas El Hachem and Micha Eisele. Maximilian Graf wrote the manuscript with contributions from and discussions with all co-authors.

1.8 Further articles

Besides the four articles described above, the author of this thesis contributed to three peer-reviewed articles, two peer-reviewed conference proceedings, and two non-peer-reviewed articles during the time of his doctorate. These articles have a varying degree of thematic overlap with the topic of this thesis and are presented in the following section.

Peer reviewed articles

The author contributed to two peer-reviewed articles in the context of land surface-atmosphere interaction, more precisely, to the soil moisture precipitation feedback in Graf et al. (2021a) (a) and Arnault et al. (2021) (b). Both articles focused on the use of coupled hydrological and atmospheric models. Nevertheless, a thematic overlap between their simulation-derived results and the conclusions from this thesis can be drawn: accurate rainfall estimates are crucial for the development and validation of weather and climate models. The author also contributed to Graf et al. (2023) (c) and Polz et al. (2023a) (d) which are conference proceedings for the International Conference of Acoustics, Speech and Signal Processing 2023 and cover topics closely related to this thesis. The first one (c) used the findings on blackouts from Polz et al. (2023b) and analyzed three different ways to mitigate blackout gaps. The approach to use the all-time minimum of RSL observed at each CML to fill its blackout gaps proved to be the best method. The rainfall estimates were improved with this approach compared to no and to other mitigation measures. The second conference contribution (d) focused on anomalies in raw CML attenuation data. Four experts (from the author list) manually flagged CML time series which then were processed and compared to a reference. Agreement between experts varied quite strongly but rainfall estimates were improved nevertheless. Finally, the author contributed to the first ever published CML-based rainfall maps in Africa (Djibo et al., 2023a) in (e). A CML processing routine close to the one in **Chapter 2** was used on more than 100 CMLs covering Ouagadougou, the capital of Burkina Faso. As ground-based reference data was scarce, with only one rain gauge with daily resolution available in the city, also satellite data was used. The CML rainfall maps with a resolution of five minutes matched the daily sums of the rain gauge and their temporal correctness could be verified with sub-hourly satellite data.

(a) ***Is the soil moisture precipitation feedback enhanced by heterogeneity and dry soils? A comparative study***

Graf, M., Arnault, J., Fersch, B., & Kunstmann, H. (2021). Is the soil moisture precipitation feedback enhanced by heterogeneity and dry soils? A comparative study. *Hydrological Processes*, 35(9), e14332. `https://doi.org/10.1002/hyp.14332`

Abstract: The interaction between the land surface and the atmosphere is a crucial driver of atmospheric processes. Soil moisture and precipitation are key components in this feedback.

Both variables are intertwined in a cycle, that is, the soil moisture–precipitation feedback for which involved processes and interactions are still discussed. In this study the soil moisture–precipitation feedback is compared for the sempiternal humid Ammer catchment in Southern Germany and for the semiarid to subhumid Sissili catchment in West Africa during the warm season, using precipitation datasets from the Climate Hazards Group InfraRed Precipitation with Station data (CHIRPS), from the German Weather Service (REGNIE) and simulation datasets from the Weather Research and Forecasting (WRF) model and the hydrologically enhanced WRF-Hydro model. WRF and WRF-Hydro differ by their representation of terrestrial water flow. With this setup we want to investigate the strength, sign and variables involved in the soil moisture–precipitation feedback for these two regions. The normalized model spread between the two simulation results shows linkages between precipitation variability and diagnostic variables surface fluxes, moisture flux convergence above the surface and convective available potential energy in both study regions. The soil moisture–precipitation feedback is evaluated with a classification of soil moisture spatial heterogeneity based on the strength of the soil moisture gradients. This allows us to assess the impact of soil moisture anomalies on surface fluxes, moisture flux convergence, convective available potential energy and precipitation. In both regions the amount of precipitation generally increases with soil moisture spatial heterogeneity. For the Ammer region the soil moisture–precipitation feedback has a weak negative sign with more rain near drier patches while it has a positive signal for the Sissili region with more rain over wetter patches. At least for the observed moderate soil moisture values and the spatial scale of the Ammer region, the spatial variability of soil moisture is more important for surface-atmosphere interactions than the actual soil moisture content. Overall, we found that soil moisture heterogeneity can greatly affect the soil moisture–precipitation feedback.

(b) ***Lateral terrestrial water flow contribution to summer precipitation at continental scale – A comparison between Europe and West Africa with WRF-Hydro-tag ensembles***

Arnault, J., Fersch, B., Rummler, T., Zhang, Z., Quenum, G. M., Wei, J., **Graf, M.**, Laux, P., & Kunstmann, H. (2021). Lateral terrestrial water flow contribution to summer precipitation at continental scale – A comparison between Europe and West Africa with WRF-Hydro-tag ensembles. *Hydrological Processes*, 35(5), e14183. `https://doi.org/10.1002/hyp.14183`

Abstract: It is well accepted that summer precipitation can be altered by soil moisture condition. Coupled land surface – atmospheric models have been routinely used to quantify soil moisture – precipitation feedback processes. However, most of the land surface models (LSMs) assume a vertical soil water transport and neglect lateral terrestrial water flow at the surface and in the subsurface, which potentially reduces the realism of the simulated soil moisture – precipitation feedback. In this study, the contribution of lateral terrestrial water flow to summer precipitation is assessed in two different climatic regions, Europe and

West Africa, for the period June–September 2008. A version of the coupled atmospheric-hydrological model WRF-Hydro with an option to tag and trace land surface evaporation in the modelled atmosphere, named WRF-Hydro-tag, is employed. An ensemble of 30 simulations with terrestrial routing and 30 simulations without terrestrial routing is generated with random realizations of turbulent energy with the stochastic kinetic energy backscatter scheme, for both Europe and West Africa. The ensemble size allows to extract random noise from continental-scale averaged modelled precipitation. It is found that lateral terrestrial water flow increases the relative contribution of land surface evaporation to precipitation by 3.6% in Europe and 5.6% in West Africa, which enhances a positive soil moisture – precipitation feedback and generates more uncertainty in modelled precipitation, as diagnosed by a slight increase in normalized ensemble spread. This study demonstrates the small but non-negligible contribution of lateral terrestrial water flow to precipitation at continental scale.

(c) ***Potential and limitations of filling gaps in commercial microwave link data stemming from complete loss of signal during heavy rainfall***

Graf, M., Blettner, N., Polz, J., Chwala, C. (2023). Potential and Limitations of Filling Gaps in Commercial Microwave Link Data Stemming From Complete Loss of Signal During Heavy Rainfall. *2023 IEEE International Conference on Acoustics, Speech, and Signal Processing Workshops (ICASSPW)*, 1–5. `https://doi.org/10.1109/ICASSPW59220.2023.10193696`

Rainfall estimates from commercial microwave links (CML) can be impaired by the total loss of signal during heavy rainfall events. This implies that the highest rainfall intensities may not be observed by CMLs during these so-called blackouts. As CML rainfall estimation approaches an operational state, this issue has to be studied and potential mitigation strategies have to be developed. Therefore, we investigate three methods that fill blackout gaps detected by a filter established in previous work. The methods we developed consisted of a linear and a cubic interpolation as well as the infilling of the values at the detection limit of each CML. In general, the linear interpolation was underestimated and the cubic interpolation overestimated rainfall intensities compared to a reference. The physically motivated infilling at the detection limit performed best. In conclusion, blackout gaps should be mitigated with one proposed method to improve the quality of rainfall estimates derived from CMLs.

(d) ***Expert flagging of commercial microwave link signal anomalies: Effect on rainfall estimation and ambiguity of flagging***

Polz, J., Glawion, L., **Graf, M.**, Blettner, N., Lasota, E., Schmidt, L., Kunstmann, H., Chwala, C. (2023). Expert Flagging of Commercial Microwave Link Signal Anomalies: Effect on Rainfall Estimation and Ambiguity of Flagging. *2023 IEEE International Conference on Acoustics, Speech, and Signal Processing Workshops (ICASSPW)*, 1–5. `https://doi.org/10.1109/ICASSPW59220.2023.10193654`.

Accurate detection of signal anomalies in the attenuation time-series from commercial microwave links (CMLs) is crucial for high quality rainfall estimates. Example causes of such

anomalies include dew or ice on the antenna and multi-path propagation. In a first effort to catalog examples of CML signal anomalies, four experts flagged suspicious segments in the time-series of 20 CMLs in Germany. The results show that the agreement between experts depends on the definition of the anomaly class. Removing the flagged anomalies increased the Pearson correlation coefficient between CML and radar rainfall estimates from 0.61 to 0.70 and reduced the BIAS by 40%. An implication of our study is that expert uncertainty is an important factor for the quality control of environmental sensor data.

(e) ***High-resolution rainfall maps from commercial microwave links for a data-scarce region in West Africa***

Djibo, M., Chwala, C., **Graf, M.**, Polz, J., Kunstmann, H., Francoius, Z. (2023). High-resolution rainfall maps from commercial microwave links for a data-scarce region in West Africa. *Journal of Hydrometeorology*, 1(aop). `https://doi.org/10.1175/JHM-D-23-0015.1`.

We present high-resolution rainfall maps from commercial microwave link (CML) data in the city of Ouagadougou, Burkina Faso. Rainfall was quantified based on data from 100 CMLs along unique paths and interpolated to achieve rainfall maps with a 5-minute temporal and 0.55km spatial resolution for the monsoon season of 2020. Established processing methods were combined with newly developed filtering methods, minimizing the loss of data availability. The rainfall maps were analyzed qualitatively both at a five-minute and aggregated daily scale. We observed high spatio-temporal variability on the five-minute scale which cannot be captured with any existing measurement infrastructure in West Africa. For the quantitative evaluation only one rain gauge with a daily resolution was available. Comparing the gauge data with the corresponding CML rainfall map pixel showed a high agreement with a Pearson correlation coefficient of over 0.95 and an underestimation of the CML rainfall maps of around ten percent. Because the CMLs closest to the gauge have the largest influence on the map pixel at the gauge location, we thinned out the CML network around the rain gauge synthetically in several steps and repeated the interpolation. The performance of these rainfall maps dropped only when a radius of 5 km was reached and around half of all CMLs were removed. We further compared ERA5 and GPM-IMERG data to the rain gauge and found that they show much lower correlation than data from the CML rainfall maps. This clearly highlights the large benefit that CML data can provide in the data scarce but densely populated African cities.

Non-peer reviewed articles

Two additional non-peer-reviewed articles closely related to this thesis were published with contributions from the author in German. In Graf et al. (2021c), given in (f), the general principle of CML-based rainfall estimation is described. Additionally, results from the country-wide evaluation of these rainfall estimates in Germany are presented. The second article in (g) from Bárdossy et al. (2022) is an application using OS-derived rainfall for analysis of the Ahrtal flooding in July

2021. The main result was that OS rainfall products from PWSs and CMLs lead almost twice the areal precipitation compared to rain gauge and radar products. It also featured the first results from hydrological simulations with LARSIM, the operational product of the state agency for the environment of Rhineland-Palatinate, using OS rainfall data as input and comparing it to traditional rainfall products as input. The combination of rain gauges and PWSs as input thereby led to almost 50% more discharge at the gauge Altenahr than RADOLAN-RW as input.

(f) ***Regenmessung im Mobilfunknetz***

Graf, M., Polz, J., & Chwala, C. (2021). Regenmessung im Mobilfunknetz. *Physik in unserer Zeit*, 52(2), 88–93. https://doi.org/10.1002/piuz.202001602

Abstract: Das möglichst exakte Erfassen des Niederschlags ist ein grundlegender Bestandteil der Klima- und Umweltforschung sowie für verschiedene Anwendungen, beispielsweise in der Landwirtschaft. Eine neue Art der Niederschlagsmessung ermöglicht das Mobilfunknetz in Deutschland mittels Richtfunkstrecken (Commercial Microwave Link, CML). Der große Vorteil dieser Methode liegt in der potenziell weltweit nutzbaren Infrastruktur. Die Qualität der Niederschlagserfassung mit etwa 4000 CML in Deutschland weist eine hohe Übereinstimmung mit dem offiziellen Messnetz des Deutschen Wetterdienstes auf.

(g) ***Verbesserung der Abschätzung von Gebietsniederschlägen mittels opportunistischer Niederschlagsmessungen am Beispiel des Ahr-Hochwassers im Juli 2021***

Bardossy, A., Seidel, J., Eisele, M., El Hachem, A, Kunstmann, H., Chwala, C., **Graf, M.**, Demut, N., Gerlach, N. (2022) Verbesserung der Abschätzung von Gebietsniederschlägen mittels opportunistischer Niederschlagsmessungen am Beispiel des Ahr-Hochwassers im Juli 2021. Projektbericht HW 66. 2022, 208-214

Abstract: Am 14. und 15. Juli 2021 haben sich infolge starker und langanhaltender Niederschläge in mehreren Flusseinzugsgebieten im Westen Deutschlands katastrophale Hochwasser ereignet. Besonders betroffen war das Ahrtal, wo zahlreiche Todesopfer zu beklagen waren und große Schäden entstanden (LfU, 2022). Am durch das Hochwasser zerstörten Ahr-Pegel Altenahr (Einzugsgebiet 746 km^2) lag der anhand von Hochwassermarken rekonstruierte Höchststand am 15. Juli gegen 2:00 Uhr bei etwa 10 m. Der bis dahin höchste gemessene Wert im Messzeitraum von 1946 bis 2020 betrug 3,71 m. Auch an weiteren Pegeln an der Ahr kam es zu Ausfällen. Die Ursachen für die Unsicherheiten in der Abschätzung der Maximalabflüsse an den ausgefallenen Pegeln sind vielfältig. Die Pegel Müsch/Ahr, Altenahr/Ahr und Kreuzberg/Sahrbach im Ahr-Einzugsgebiet (Abb. 4) wurden während des Hochwasserereignisses zerstört, Verklausungen an Brückendurchlässen sowie der Zusammenbruch von Brücken führten zum Rückstau der Wassermassen bzw. zu vermuteten Schwallwellen. Des Weiteren war der aus Stationsmessdaten abgeschätzte Gebietsniederschlag nach derzeitiger Einschätzung mindestens 15 % zu niedrig, jener aus den Radarprodukten sogar bis etwa 30 %. Zur Ermittlung der Maximalabflüsse an den Pegeln im Ahr-Einzugsgebiet wurden

im Landesamt für Umwelt in Rheinland-Pfalz (LfU RLP) verschiedene Ansätze verfolgt, u. a. wurde das Hochwasser mit dem Wasserhaushaltsmodell LARSIM (LEG, 2021) mit unterschiedlichen, nachträglich erstellten Niederschlagsprodukten (u. a. unter Verwendung von privaten Wetterstationen) und mit unterschiedlichen Modelleinstellungen nachgerechnet. Die Herleitung der Scheitelabflüsse ist derzeit noch Gegenstand von Untersuchungen, nach vorläufigen Berechnungen wird der Maximalabfluss am Pegel Altenahr auf 750 bis 1.000 m^3/s geschätzt (Berkler et al., 2022)

Chapter 2

Rainfall estimation from a German-wide commercial microwave link network: Optimized processing and validation for one year of data (Graf et al., 2020a)

Graf, M., Chwala, C., Polz, J., and Kunstmann, H.: Rainfall estimation from a German-wide commercial microwave link network: optimized processing and validation for 1 year of data, *Hydrol. Earth Syst. Sci.*, 24, 2931–2950, https://doi.org/10.5194/hess-24-2931-2020, 2020.

Abstract

Rainfall is one of the most important environmental variables. However, it is a challenge to measure it accurately over space and time. During the last decade commercial microwave links (CMLs), operated by mobile network providers, have proven to be an additional source of rainfall information to complement traditional rainfall measurements. In this study we present the processing and evaluation of a German-wide data set of CMLs. This data set was acquired from around 4000 CMLs distributed across Germany with a temporal resolution of one minute. The analyzed period of one year spans from September 2017 to August 2018. We compare and adjust existing processing schemes on this large CML data set. For the crucial step of detecting rain events in the raw attenuation time series, we are able to reduce the amount of miss-classification. This was achieved by a new approach to determine the threshold, which separates a rolling window standard deviation of the CMLs signal into wet and dry periods. For the compensation of wet antenna attenuation, we compare a time-dependent model with a rain-rate-dependent model and show that the rain-rate-dependent model performs better for our data set. As precipitation reference, we use RADOLAN-RW, a gridded gauge-adjusted hourly radar product of the German Meteorological Service (DWD), from which we derive the path-averaged rain rates along each CML path. Our data processing is able to handle CML data across different landscapes and seasons

very well. For hourly, monthly and seasonal rainfall sums we found a good agreement between CML-derived rainfall and the reference, except for the winter season with non-liquid precipitation. We discuss performance measures for different subset criteria and show, that CML derived rainfall maps are comparable to the reference. This analysis shows that opportunistic sensing with CMLs yields rainfall information with a good agreement to gauge-adjusted radar data during periods without non-liquid precipitation.

2.1 Introduction

Measuring precipitation accurately over space and time is challenging due to its high spatiotemporal variability. It is a crucial component of the water cycle and knowledge of the spatiotemporal distribution of precipitation is an important quantity in many applications across meteorology, hydrology, agriculture, and climate research.

Typically, precipitation is measured by rain gauges, ground-based weather radars or spaceborne microwave sensors. Rain gauges measure precipitation at the point scale. Errors can be caused for example by wind, solid precipitation or evaporation losses (Sevruk, 2006). The main disadvantage of rain gauges is their lack of spatial representativeness. Weather radars overcome this spatial constraint, but are affected by other error sources. They do not directly measure rainfall, but estimate it from related observed quantities, typically via the Z-R relation, which links the radar reflectivity "Z" to the rain rate "R". This relation, however, depends on the rain drop size distribution (DSD), resulting in significant uncertainties. Dual-polarization weather radars reduce these uncertainties, but still struggle with the DSD-dependence of the rain rate estimation (Berne and Krajewski, 2013). Additional error sources can stem from the measurement high above ground, from beam blockage or ground clutter effects.

Satellites can observe large parts of the earth, but their spatial and temporal coverage also has limits. Geostationary satellites can provide a high temporal sampling rate of a specific part of the earth. However rain rate estimates show large uncertainties because they have to be derived from measurements of visible and infra red channels, which were not meant for this purpose. Satellites in Low Earth orbits typically use dedicated sensors for rainfall estimation (microwave radiometers and radars), but their revisiting times are constraint by their orbits. Typical revisit times are in the order of hours to days. As a result, even merged multi-satellite products have a latency of several hours, e.g. the Integrated Multi-satellite Retrievals (IMERG) early run of the Global Precipitation Measurement Mission (GPM) has a latency of 6 hours, while it is limited to a spatial resolution of 0.1 degrees. The employed retrieval algorithms are highly sophisticated and several calibration and correction stages are potential error sources (Maggioni et al., 2016).

Additional rainfall information, for example derived from commercial microwave links (CMLs) maintained by cellular network providers, can be used to compare and complement existing rainfall data sets (Messer et al., 2006). In regions with sparse observation networks, they might even provide unique rainfall information.

The idea to derive rainfall estimates via the opportunistic usage of attenuation data from CML networks emerged over a decade ago independently in Israel (Messer et al., 2006) and the Netherlands (Leijnse et al., 2007). The main research foci in the first decade of dedicated CML research were the development of processing schemes for the rainfall retrieval and the reconstruction of rainfall fields. The first challenge for rainfall estimation from CML data is to distinguish between fluctuations of the raw attenuation data during rainy and dry periods. This was addressed by different approaches which either compared neighbouring CMLs using the spatial correlation of rainfall (Overeem et al., 2016a) or which focused on analyzing the time series of individual CMLs (Chwala et al., 2012; Polz et al., 2020; Schleiss and Berne, 2010; Wang et al., 2012). Another challenge is to estimate and correct the effect of wet antenna attenuation. This effect stems from the attenuation caused by water droplets on the covers of CML antennas, which leads to rainfall overestimation (Fencl et al., 2019; Leijnse et al., 2008; Schleiss et al., 2013).

Since many hydrological applications require spatial rainfall information, several approaches have been developed for the generation of rainfall maps from the path-integrated CML measurements. Kriging was successfully applied to produce countrywide rainfall maps for the Netherlands (Overeem et al., 2016b), representing CML rainfall estimates as synthetic point observation at the center of each CML path. More sophisticated methods can account for the path-integrated nature of the CML observations, using an iterative inverse distance weighting approach (Goldshtein et al., 2009), stochastic reconstruction (Haese et al., 2017) or tomographic algorithms (D'Amico et al., 2016; Zinevich et al., 2010).

CML-derived rainfall products were also used to derive combined rainfall products from various sources (Fencl et al., 2017; Liberman et al., 2014; Trömel et al., 2014). In parallel, first hydrological applications were tested. CML-derived rainfall was used as model input for hydrologic modelling studies for urban drainage modeling with synthetic (Fencl et al., 2013) and real world data (Stransky et al., 2018) or on run-off modeling in natural catchments (Brauer et al., 2016; Smiatek et al., 2017).

With the exception of the research carried out in the Netherlands, where more than two years of data from a country-wide CML network were analyzed (Overeem et al., 2016b), CML processing methods have only been tested on small data sets. We advance the state of the art by performing an analysis of rainfall estimates derived from a German-wide network of close to 4000 CMLs. In this study one CML is counted as the link along one path with typically two sub-links, for the communication in both directions. The temporal resolution of the data set is one minute and the analyzed period is one year from September 2017 until August 2018. The network covers various landscapes from the North German Plain to the Alps in the south, which feature individual precipitation regimes.

The objectives of this study are (1) to compare and adjust selected existing CML data processing schemes for the classification of wet and dry periods and for the compensation of wet antenna attenuation and (2) to validate the derived rain rates with an established rainfall product, namely

RADOLAN-RW, both on the country-wide scale of Germany.

2.2 Data

2.2.1 Reference data set

The *Radar-Online-Aneichung* data set (RADOLAN-RW) of the German Weather Service (DWD) is a radar-based and gauge adjusted precipitation data set. We use data from the archived real-time product RADOLAN-RW as reference data set throughout this work (DWD, 2019). It is a compiled radar composite from 17 dual-polarization weather radars operated by DWD and adjusted by more than 1000 rain gauges in Germany and 200 rain gauges from surrounding countries. RADOLAN-RW does not use dual-pol information, though. It is based on the reflectivity observations in horizontal polarization from each radar site, which are available in real-time every five minutes. This data is then used to compile a national composite of reflectivities, from which rain rates are derived. For the hourly rainfall information of the RADOLAN-RW product, the national composite of 5-minute radar rain rates is then aggregated and adjusted with the hourly rain gauge observations. A weighted mixture of additive and multiplicative corrections is applied. The rain gauges used for the adjustment have a spatial density of approximately one gauge per 300 km^2.

The gridded data set RADOLAN-RW has a spatial resolution of 1 km, covering Germany with 900 by 900 grid cells. The temporal resolution is one hour and the rainfall values are given with a quantization of 0.1 mm. RADOLAN-RW is available with a lag time of around 15 minutes. Detailed information on the RADOLAN processing and products is availabel from DWD (Bartels et al., 2004; Winterrath et al., 2012).

Kneis and Heistermann (2009) and Meissner et al. (2012) compared RADOLAN-RW products to gauge-based data sets for small catchments and found differences in daily, area averaged precipitation sums of up to 50 percent, especially for the winter season. Nevertheless, no data set with comparable temporal and spatial resolution, as well as extensive quality control is available.

In order to compare the path integrated rainfall estimates from CMLs and the gridded RADOLAN-RW product, RADOLAN-RW rain rates are resampled along the individual CML paths. For each CML, the weighted average of all intersecting RADOLAN-RW grid cells is calculated, with the weights being the lengths of the intersecting CML path in each cell. As result, one time series of the hourly rain rate is generated from RADOLAN-RW for each CML. The temporal availability of this reference is 100 percent but we excluded the CML and RADOLAN-RW pairs in the evaluation, when CML data is not available. We chose the RADOLAN-RW product, because it provides both a high temporal and spatial resolution for entire Germany. This resolution is the basis for a good evaluation of the path-averaged rain rates derived from CMLs. The rain gauge adjustments, while not perfect, assures that the RADOLAN-RW rainfall estimates have an increased accuracy compared to a radar-only data set.

2.2.2 Commercial microwave link data

We present data of 3904 CMLs operated by Ericsson in Germany. Their distribution over Germany is shown in Fig. 2.1. The CMLs are distributed country-wide over all landscapes in Germany, ranging from the North German Plain to the Alps in the south. The uneven distribution, with large gaps in the north east can be explained by the fact that we only access one subset of all installed CMLs, the Ericsson MINI-LINK Traffic Node systems operated for one cell phone provider.

CML data is retrieved with a real-time data acquisition system which we operate in cooperation with Ericsson (Chwala et al., 2016). Every minute, the current transmitted signal level (TSL) and received signal level (RSL) are requested from more than 4000 CMLs for both ends of each CML. The data is then immediately sent to and stored at our server. For the complete processing chain presented in this work, we used this 1-minute instantaneous data of TSL and RSL for the period from September 2017 to August 2018 for 3904 CMLs to derive rain rates with a temporal resolution of 1 minute. For comparison with the reference data, the 1-minute data is then aggregated. Due to missing, unclear or corrupted metadata we could not use all CML data. Furthermore, we only used data of one sub-link per CML. There was no specific criterion for selecting the sub-link. We simply used the pair of TSL and RSL that came first in our listing.

The available power resolution is 1 dB for TSL and 0.3 (with occasional jumps of 0.4 dB) for RSL. The TSL is constant for 25 percent of the CMLs. An Automatic Transmit Power Control (ATCP), which is able to increase TSL by several dB to prevent blackouts due to heavy attenuation, is active at 75 percent of the CMLs. While the length of the CMLs ranges between a few hundred meters to almost 30 km, most CMLs have a length of 5 to 10 km. They are operated with frequencies ranging from 10 to 40 GHz, depending on their length. Figure 2.2 shows the distributions of path lengths and frequencies. For shorter CMLs higher frequencies are used.

To derive rainfall from CMLs, we used the difference between TSL and RSL, the transmitted minus received signal level (TRSL). An example of a TRSL time series is shown in Fig. 2.3a). To compare the rain rate derived from CMLs with the reference rain rate, we resampled it from a minutely to an hourly resolution after the processing

In our CML data set 2.2 percent are missing time steps due to outages of the data acquisition systems. Additionally, 1.2 percent of the raw data show missing values (Nan) and 0.1 percent show default fill values (e.g. -99.9 or 255.0) of the CML hardware, which we excluded from the analysis. In order to increase the data availability, we linearly interpolated gaps in raw TRSL time series which were up to five minutes long. This increased the data availability by 0.5 percent. On the one hand, these gaps can be the result of missing time steps and missing values but we also found cases where we suspect very high rainfall to be the reason for short blackouts of a CML.

The size of the complete CML data set is approximately 100 GB in memory. The data set is continuously extended by the operational data acquisition, allowing also the possibility of near-realtime rainfall estimation.

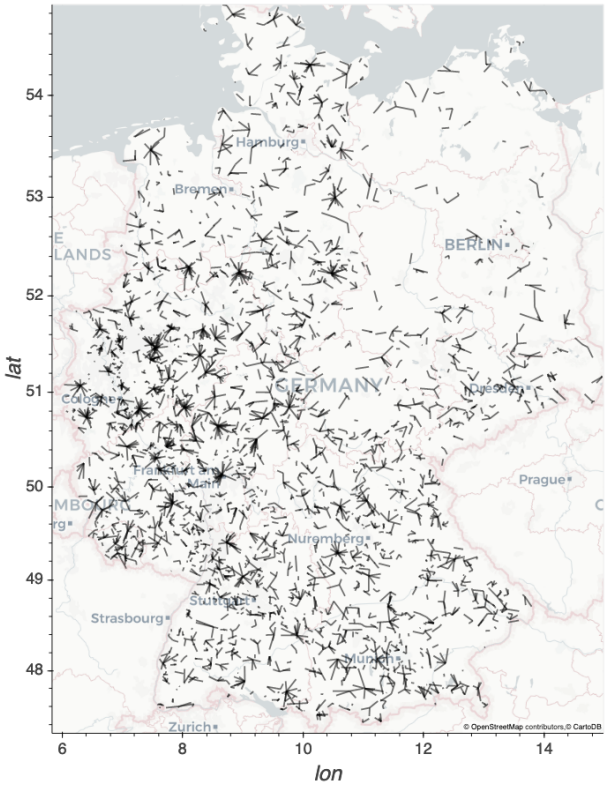

Figure 2.1: Map of the distribution of 3904 CMLs over Germany. © OpenStreetMap contributors 2019. Distributed under a Creative Commons BY-SA License.

Table 2.1: Adopted confusion matrix

		reference	
		wet	*dry*
CML	*wet*	true wet (TP)	false wet (FP)
	dry	missed wet (FN)	true dry (TN)

2.3 Methods

2.3.1 Performance measures

To evaluate the performance of the CML-derived rain rates against the reference data set, we used several measures which we calculated on an hourly basis. We defined a confusion matrix according to Tab. 2.1 where *wet* and *dry* refer to hours with and without rain, respectively. The Matthew's correlation coefficient (MCC) summarizes the four values of the confusion matrix in a single measure (2.1) and is typically used as measure of binary classification in machine learning. This measure is accounting for the skewed ratio of wet and dry events. It is high only if the classifier is performing well on both classes.

$$\mathrm{MCC} = \frac{\mathrm{TP} * \mathrm{TN} - \mathrm{FP} * \mathrm{FN}}{\sqrt{(\mathrm{TP}+\mathrm{FP})(\mathrm{TP}+\mathrm{FN})(\mathrm{TN}+\mathrm{FP})(\mathrm{TN}+\mathrm{FN})}} \tag{2.1}$$

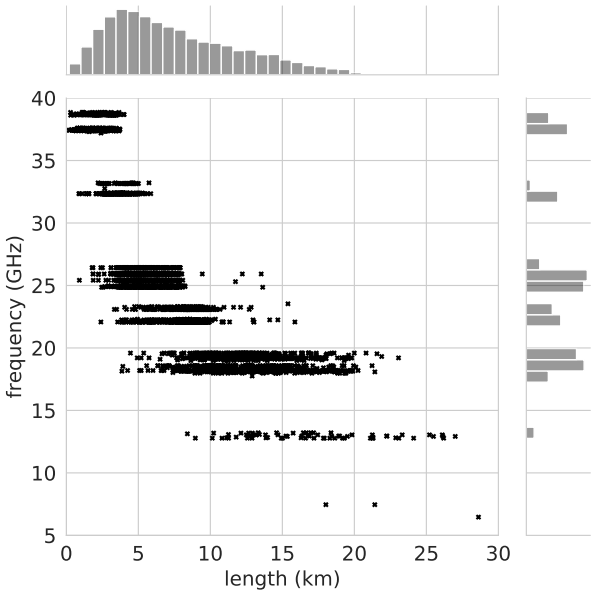

Figure 2.2: Scatterplot of the length against the microwave frequency of 3904 CMLs including the distribution of length and frequency.

The mean detection error (MDE) (2.2) is introduced as a further binary measure focusing on the miss-classification of rain events.

$$\mathrm{MDE} = \frac{\frac{\mathrm{FN}}{\mathrm{n(wet)}} + \frac{\mathrm{FP}}{\mathrm{n(dry)}}}{2} \tag{2.2}$$

It is calculated as the average of missed wet and false wet rates of the contingency table from Tab. 2.1.

The linear correlation between CML-derived rainfall and the reference is expressed by the Pearson correlation coefficient (PCC). The coefficient of variation (CV) in (2.3) gives the distribution of CML rainfall around the reference expressed by the ratio of residual standard deviation and mean reference rainfall,

$$\mathrm{CV} = \frac{\mathrm{std}\sum(\mathrm{R_{CML}} - \mathrm{R_{reference}})}{\overline{\mathrm{R_{reference}}}} \tag{2.3}$$

where R_{CML} and $R_{reference}$ are hourly rain rates of the respective data set. Furthermore, we computed the mean absolute error (MAE) and the root mean squared error (RMSE) to measure the accuracy of the CML rainfall estimates. The relative bias is given as

$$\mathrm{bias} = \frac{\overline{(\mathrm{R_{CML}} - \mathrm{R_{reference}})}}{\overline{\mathrm{R_{reference}}}} \tag{2.4}$$

Often, in studies comparing CML derived rainfall and radar data, a threshold is used as a lower boundary for rainfall. The performance measures, summarized in Tab. 2.2, were calculated with different subset criteria or thresholds. This gives insight on how CML derived rainfall compares

to the reference for different rain rates and on how the large number of data points without rain influence the performance measures. Another reason for listing the performance measures with several thresholds is the increased comparability with other studies on CML rainfall estimation, which do not uniformly use the same threshold, see e.g. Table A1 in de Vos et al. (2019b). Therefore, we defined a selection of subset criteria and thresholds and show performance measures for data without any thresholds (*none*), for the data set with R_{CML} and $R_{reference} < 0.1$ mm/h set to 0 mm/h, for two thresholds where at least R_{CML} or $R_{reference}$ must be > 0 and $>= 0.1$ mm/h and two thresholds where $R_{reference}$ must be $>= 0.1$ and $>= 1$ mm.

2.3.2 From raw signal to rain rate

As CMLs are an opportunistic sensing system rather than part of a dedicated measurement system, data processing has to be done with care. Most of the CML research groups developed their own methods tailored to their needs and data sets. Overviews of these methods are summarized by Chwala and Kunstmann (2019), Messer and Sendik (2015) and Uijlenhoet et al. (2018).

The size of our data set is a challenge itself. As TRSL can be attenuated by rain or other sources, described in Sect. 2.3.2.1 and only raw TSL and RSL data is provided, the large size of the data set is of advantage but also a challenge. Developing and evaluating methods was significantly sped up by the use of an automated processing workflow, which we implemented as a parallelized workflow on a HPC system using the Python packages *xarray* and *dask* for data processing and visual exploration. The major challenges which arose from the processing of raw TRSL data into rain rates and the selected methods from literature are described in the following sections. We use parameters in this processing which are either based on literature, modified from the literature or which we developed in this study. An overview of all used parameters is given in Appendix 2.A1.

2.3.2.1 Erratic behavior

Rainfall is not the only source of attenuation of microwave radio along a CML path. Additional attenuation can be caused by atmospheric constituents like water vapor or oxygen, but also by refraction, reflection or multi-path propagation of the beam (Upton et al., 2005). In particular, refraction, reflection and multi-path propagation can lead to strong attenuation in the same magnitude as from rain. CMLs that exhibit such behavior have to be omitted due to their noisiness.

We excluded erratic CML data which was extremely noisy or which showed drifts and jumps from our analysis on a monthly basis. To deal with this erratic data, we applied the following sanity checks: We exclude individual CMLs if 1) the five hour moving window standard deviation exceeds the threshold 2.0 for more then ten percent of a month, which typically is the case for CMLs with either a strong diurnal cycle or very noisy periods during a month, or if 2) a one hour moving window standard deviation exceeds the threshold 0.8 more than 33 percent of the time in a month. This filter is based on the approach for detecting rain events in TRSL time series from Schleiss and Berne (2010), which we also use later on in our processing. For the filter, a fairly high threshold was used, which should only be exceeded for fluctuations stemming from real rain events. The reasoning of our filter is, that if the threshold is exceeded too often, here 33 percent

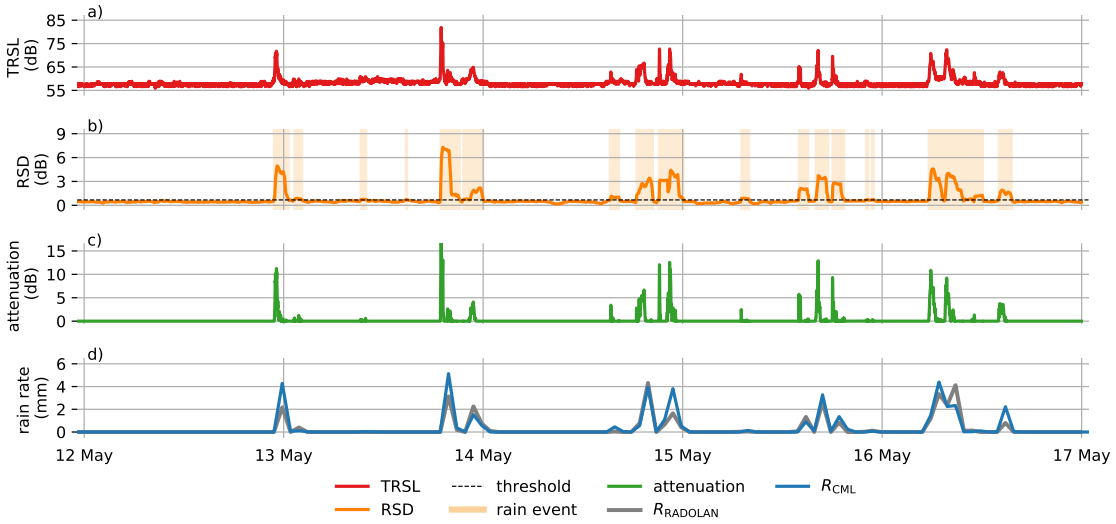

Figure 2.3: Processing steps from the TRSL to rain rate. a) The TRSL is the difference of TSL - RSL, the raw transmitted and received signal level of a CML. b) The RSD (rolling standard deviation) of the TRSL with an exemplary threshold shows the resulting wet and dry periods. c) The Attenuation is the difference between the baseline and the TRSL during wet periods. d) The derived rain rate is resampled to an hourly scale in order to compare it to the reference RADOLAN-RW.

of the time per month, the CML data shows an unreasonably high amount of strong fluctuation. In total, the two sanity checks removed 1.1 percent from our CML data set. Together with the missing values that remain after interpolating data gaps of maximum five minutes in the TRSL time series, 4.2 percent of our data set are not available or not used for processing.

Jumps in data are mainly caused by single default values in the TSL which are described in Sect. 2.2.2. When we removed these default values, we are able to remove the jumps. TRSL can drift and fluctuate on daily and yearly scale (Chwala and Kunstmann, 2019). We could neglect the influence of these drifts in our analysis, because we dynamically derived a baseline for each rain event, as explained in Sect. 2.3.2.2. We also excluded CMLs having a constant TRSL over a whole month.

2.3.2.2 Rain event detection and baseline estimation

The TRSL during dry periods can fluctuate over time due to ambient conditions as mentioned in the previous section. Rainfall produces additional attenuation on top of the dry fluctuation. In order to calculate the attenuation from rainfall, a baseline level of TRSL during each rain event has to be determined. We derived the baseline from the precedent dry period. During the rain event, this baseline was held constant, as no additional information on the evolution of the baseline level is available. The crucial step for deriving the baseline is to separate the TRSL time series into wet and dry periods, because only then the correct reference level before a rain event is used.

By subtracting the baseline from TRSL, we derived the attenuation caused by rainfall which is shown in Fig. 2.3c).

The separation of wet and dry periods is essential, because the errors made in this step will impact the performance of rainfall estimation. Missing rain events will result in rainfall underestimation. False detection of rain events will lead to overestimation. The task of detecting rain events in the TRSL time series is simple for strong rain events, but challenging when the attenuation from rain is approaching the same order of magnitude as the fluctuation of TRSL data during dry conditions.

There are two essential concepts to detect rain events. One compares the TRSL of a certain CML to neighbouring CMLs (Overeem et al., 2016a) and the other investigates the time series of each CML separately (Chwala et al., 2012; Schleiss and Berne, 2010; Wang et al., 2012). We choose the latter one and used a rolling standard deviation (RSD) with a centered moving window of 60 minutes length as a measure for the fluctuation of TRSL as proposed by Schleiss and Berne (2010).

It is assumed that RSD is high during wet periods and low during dry periods. Therefore, an adequate threshold can be defined, which differentiates the RSD time series in wet and dry periods. An example of an RSD time series and a threshold is shown in Fig. 2.3b) where all data points with RSD values above the threshold are considered as wet.

Schleiss and Berne (2010) proposed the use of a RSD threshold derived from rainfall climatology e.g. from nearby rain gauges. For our data set we assumed that it is raining 5 percent of all minutes in Germany, as proposed by Schleiss and Berne (2010) for their CMLs in France. Therefore, we used the 95 percent quantile of RSD as a threshold, assuming that the 5 percent of highest fluctuation of the TRSL time series refer to the 5 percent of rainy periods. We refer to this threshold as the climatologic threshold. We compared it to two new definitions of thresholds. We are aware that this threshold does not reflect the real climatology at each CML location, nevertheless this method is a rather robust and a simple approach which provides a first rain event detection.

For the first new definition, we derived the optimal threshold for each CML based on our reference data for the month of May 2018. We used the same approach as for the climatologic threshold, but for each CML we tested a range of possible thresholds and calculated the binary measure MCC for each. For each CML we picked the threshold which produced the highest MCC in May 2018 and used it over the whole analysis period.

The second new definition to derive a threshold is based on the quantiles of the RSD, similarly to the climatologic threshold describe above. However, we propose to not focus on the fraction of rainy periods for finding the optimal threshold, since a rainfall climatology is likely not valid for individual years and not easily transferable to different locations. We took the 80th quantile of the RSD of each CML, which can be interpreted as a measure of the strength of the TRSL fluctuation during dry periods, and multiplied it by a constant factor to derive the individual threshold. The 80th quantile can be assumed to be more robust against missclassification than the climatologic threshold, because this quantile represents the general notion of each TRSL time

series to fluctuate, rather than the percentage of time in which it is raining. We chose the 80th quantile, since it is very unlikely that it is raining more than 20 percent of the time in a month in Germany.

To find the right factor, we selected the month of May 2018 and fitted a linear regression between the optimal threshold for each CML and the 80th quantile. The optimal threshold was derived beforehand with a MCC optimization from the reference. We then used this factor for all other months in our analysis. Additional, we found it to be similar for all months of the analyzed period.

2.3.2.3 Wet antenna attenuation

Wet antenna attenuation is the attenuation caused by water on the cover of a CML antenna. With this additional attenuation, the derived rain rate overestimates the true rain rate (Schleiss et al., 2013; Zinevich et al., 2010). The estimation of WAA is complex, as it is influenced by partially unknown factors, e.g. the material of the antenna cover. van Leth et al. (2018) found differences in WAA magnitude and temporal dynamics due to different sizes and shapes of the water droplets on hydrophobic and normal antenna cover materials. Another unknown factor for the determination of WAA is the information whether both, one or none of the antennas of a CML is wetted during a rain event. We selected and compared two parametric WAA correction schemes which do not rely on the use of auxiliary data like near-by rain gauges.

Schleiss et al. (2013) measured the magnitude and dynamics of WAA with one CML in Switzerland and derived a time-dependent WAA model. In this model, WAA increases at the beginning of a rain event to a defined maximum in a defined amount of time. From the end of the rain event on, WAA decreases again, as the wetted antenna is drying off. We ran this scheme with the proposed 2.3 dB of maximal WAA for both antennas together. This is also similar to the WAA correction value of 2.15 dB, which Overeem et al. (2016b) derived over a 12-day period in their data set. For τ, which determines the increase rate with time we chose 15 minutes. The decrease of WAA after a rain event is not explicitly modelled, because this WAA scheme is only applied for time steps, which are considered wet from the rain event detection, which has to be carried out in a previous step.

Leijnse et al. (2008) proposed a physical approach where the WAA depends on the microwave frequency, the antenna cover properties (thickness and refractive index) and the rain rate. A homogeneous water film is assumed on the antenna, with its thickness having a power law dependence on the rain rate. Higher rain rates cause a thicker water film and hence higher WAA. A factor γ scales the thickness of the water film on the cover and a factor δ determines the non-linearity of the relation between rain rate and water film thickness. We adjusted the thickness of the antenna cover to 4.1 mm which we measured from one antenna provided by Ericsson. We are aware of the fact, that antenna covers have different thicknesses. But since we do not have this information for the actual antennas that are used by the CMLs of our data, we use this value, as the best one available. We further adjusted γ to 1.47E-5 and δ to 0.36 in such a way, that the increase of WAA with rain rates is less steep for small rain rates compared to the originally proposed

parameters. The original set of parameters suppressed small rain events too much because the WAA compensation attributed all attenuation in the TRSL to WAA. For strong rain events (>10 mm/h), the maximum WAA that is reached with our set of parameters is in the same range as the 2.3 dB used as maximum in the approach of Schleiss et al. (2013).

We want to note that several recent methods quantifying the WAA were developed using auxiliary information such as rain gauge data. This is the reason we did not consider these approaches, as we wanted our CML data processing to be as applicable to new regions as possible. The transferability of WAA estimation methods remains an open scientific question, though.

Fencl et al. (2019) quantified the influence of WAA for eight very short (length < 500 m) CMLs using cumulative distribution functions from attenuation and rain gauge data. Their approach is not applicable to new CMLs as it requires calibration for each individual CML based on the local rainfall and attenuation statistics. Ostrometzky et al. (2018) used a rain gauge to estimate the WAA of an E-band CML. They calculated both the (dry, constant during rain events) baseline and the theoretical attenuation using rain gauge data and attributed the residual attenuation as WAA. Moroder et al. (2020) developed a model based on the dynamic antenna parameters reflectivity, efficiency and directivity based on a full-wave simulation and applied it on a dedicated experimental setup with CML antennas (Moroder et al., 2019). To apply this method it is required to continuously collect the individual properties of the CML antennas, which might only be possible in future CML hardware generations.

2.3.2.4 Derivation of rain rates

The estimation technique of rainfall from the WAA-corrected attenuation is based on the well known relation between specific path attenuation k in dB/km and rain rate R in mm/h

$$k = aR^b \tag{2.5}$$

with a and b being constants depending on the frequency and polarization of the microwave radiation (Atlas and Ulbrich, 1977). In the currently most commonly used CML frequency range between 15 GHz and 40 GHz, the constants only show a low dependence on the rain drop size distribution. Using the k-R relation, rain rates can be derived from the path integrated attenuation measurements that CMLs provide as shown in Fig. 2.3 d). We used values for a and b according to ITU-R (2005) which show good agreement with calculations from disdrometer data in southern Germany (Chwala and Kunstmann, 2019, Fig. 3).

2.4 Results and Discussion

2.4.1 Comparison of rain event detection schemes

The separation of wet and dry periods has a crucial impact on the accuracy of the rainfall estimation. We compared an approach from Schleiss and Berne (2010) to three modifications on their success in classifying wet and dry events as explained in Sect. 2.3.2.2.

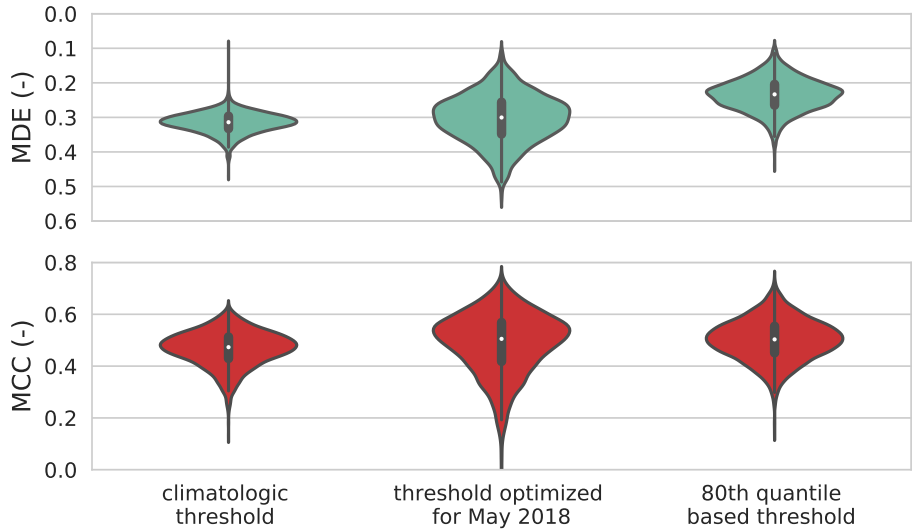

Figure 2.4: Mean detection error (MDE) and Matthews correlation coefficient (MCC) for three rain event detection schemes for the whole analysis period.

The climatologic approach by Schleiss and Berne (2010) worked well for CMLs with moderate noise and when the fraction of times with rainfall over the analyzed periods did correspond to the climatological value. The median MDE was 0.33 and the median MCC of 0.43. The distribution of MDE and MCC values from all CMLs of this climatologic threshold were compared with the performance of the two extensions, displayed in Fig. 2.4.

When we optimized the threshold for each CML for May 2018 and then applied these thresholds for the whole period, the performance increased with a median MDE of 0.32 and median MCC of 0.46. The better performance of MDE and MCC values highlights the importance of a specific threshold for each individual CML, accounting for their individual notion to fluctuate. The range of MDE and MCC values is wider than with the climatologic threshold, though. The wider range of MDE and MCC values, however, indicates that there is also a need for adjusting the individual thresholds over the course of the year.

The 80th quantile-based method had the lowest median MDE with 0.27 and highest median MCC with 0.47. Therefore it miss-classified the least wet and dry periods compared to the other methods.

The threshold, which is based on the 80th quantile, is independent from climatology and depends on the individual notion of a CML to fluctuate. Although the factor used to scale the threshold was derived from comparison to the reference data set as described in Sect. 2.3.2.2, it was stable over all seasons and for CMLs in different regions of Germany. Validating the scaling factor with other CML data sets could be a promising method for data scarce regions, as no external information is needed.

For single months, the MDE was below 0.20 as shown in Tab. 2.2, which still leaves room for an improvement of this rain event detection method. Enhancements could be achieved by adding information of nearby CMLs, if available. Also data from geostationary satellite could be used. Schip et al. (2017) found improvements of the rain event detection when using rainfall information from Meteosat Second Generation (MSG) satellite, which carries the Spinning Enhanced Visible and InfraRed Imager (SEVIRI) instrument.

All further processing, presented in the next sections, uses the method based on the 80th quantile.

2.4.2 Performance of wet antenna attenuation schemes

Two WAA schemes are tested and adopted for the present CML data set. Both are compared to uncorrected CML data and the reference in Fig. 2.5. Without a correction scheme, the CML-derived rainfall overestimated the reference rainfall by a factor of two when considering mean hourly rain rates, as displayed in Fig. 2.5a).

The correction by Schleiss et al. (2013) produced comparable mean hourly rain rates with regard to the reference data set. Despite its apparent usefulness to compensate for WAA, this scheme worked well only for stronger rain events. The mean detection error is higher than for the uncorrected data set, because small rain events are suppressed completely throughout the year. The discrepancy can also be a result of the path length of 7.6 km in our data set which is four times the length of the CML Schleiss et al. (2013) used. This might have an impact, since shorter CMLs have a higher likeliness that both antennas get wet. Furthermore, the type of antenna and antenna cover impacts the wetting during rain, as discussed in section Sect. 2.3.2.3.

With the method of Leijnse et al. (2008) the overestimation of the rain rate was also compensated well. It incorporates physical antenna characteristics and, what is more important, depends on the rain rate. The higher the rain rate, the higher the WAA compensation. This leads to less suppression of small events. The MDE is close to the uncorrected data sets and the PCC is higher, as displayed in 2.5b) and c). Recent results from Fencl et al. (2019) also favor a dynamic, rain intensity depended WAA model, instead of a constant value for WAA compensation. Therefore, the scheme from Leijnse et al. (2008) is used for the evaluation of the CML-derived rain rates in the following sections.

Both methods are parameterized, neglecting known and unknown interactions between WAA and external factors like temperature, humidity, radiation and wind. Current research aims to close this knowledge gap, but the feasibility for large scale networks like the one presented in this study is going to be a challenge as only TSL and RSL are available. A possible solution is the WAA model based on the reflectivityy, efficiency and directivity of the antenna proposed by Moroder et al. (2020), which would have to be measured by future CML hardware. Another approach could be to extend the analysis with meteorological model reanalysis products to be able to better understand WAA behavior in relation to meteorologic parameters like wind, air temperature, humidity and solar radiation.

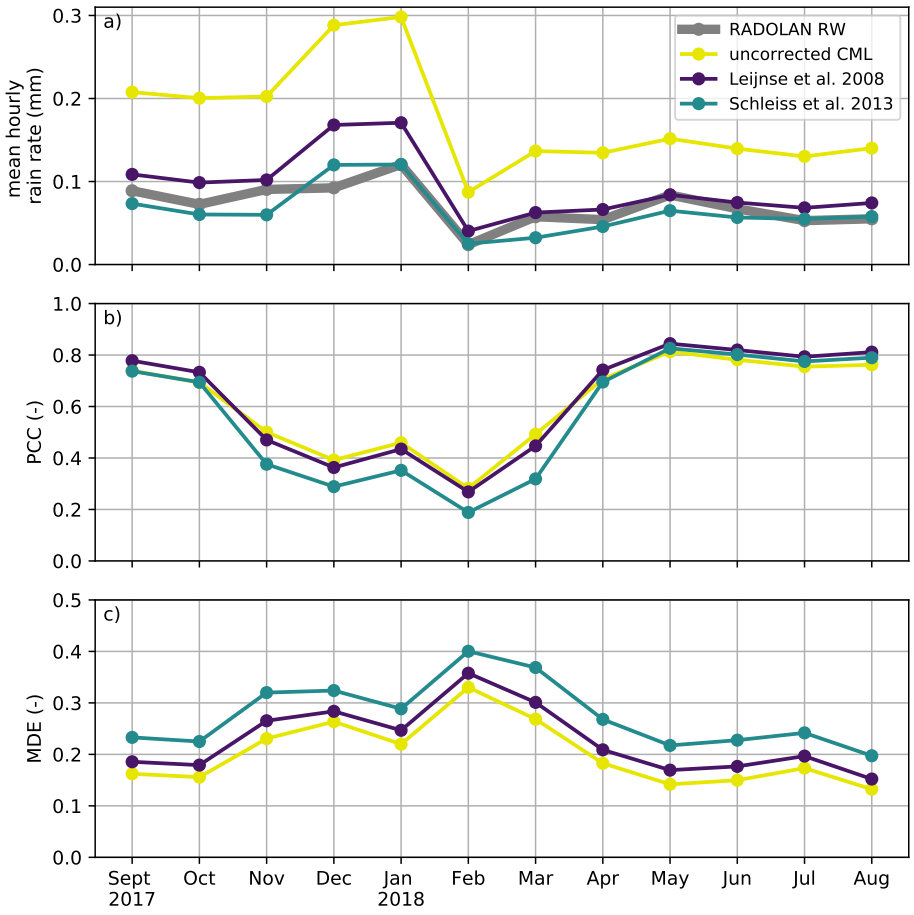

Figure 2.5: WAA compensation schemes compared on their influence on the a) mean hourly rain rate, b) the correlation between the derived rain rates and the reference and c) the mean detection error between the derived rain rates and the reference.

2.4.3 Evaluation of CML derived rainfall

Path-averaged rainfall information obtained from almost 4000 CMLs is evaluated against a reference data set, RADOLAN-RW. In Fig. 2.6 we show scatter density plots of path averaged hourly rain rates, daily rainfall sums and seasonal sums of each CML with the respective performance measures. Furthermore, scatter density plots of hourly, path-averaged rain rates and rain rates from interpolated rainfall maps are compared for each month in Fig. 2.8 and Fig. 2.9.

Looking at the differences between the seasons in 2.6, it is evident, that CMLs are prone to produce significant rainfall overestimation during the cold season (DJF). This can be attributed to precipitation events with melting snow, occurring mainly from November to March. Melting snow can potentially cause as much as four times higher attenuation than a comparable amount of liquid precipitation (Paulson and Al-Mreri, 2011). Snow, ice and their melt water on the covers of the antennas can also cause additional attenuation. A decrease of the seasonal performance measures

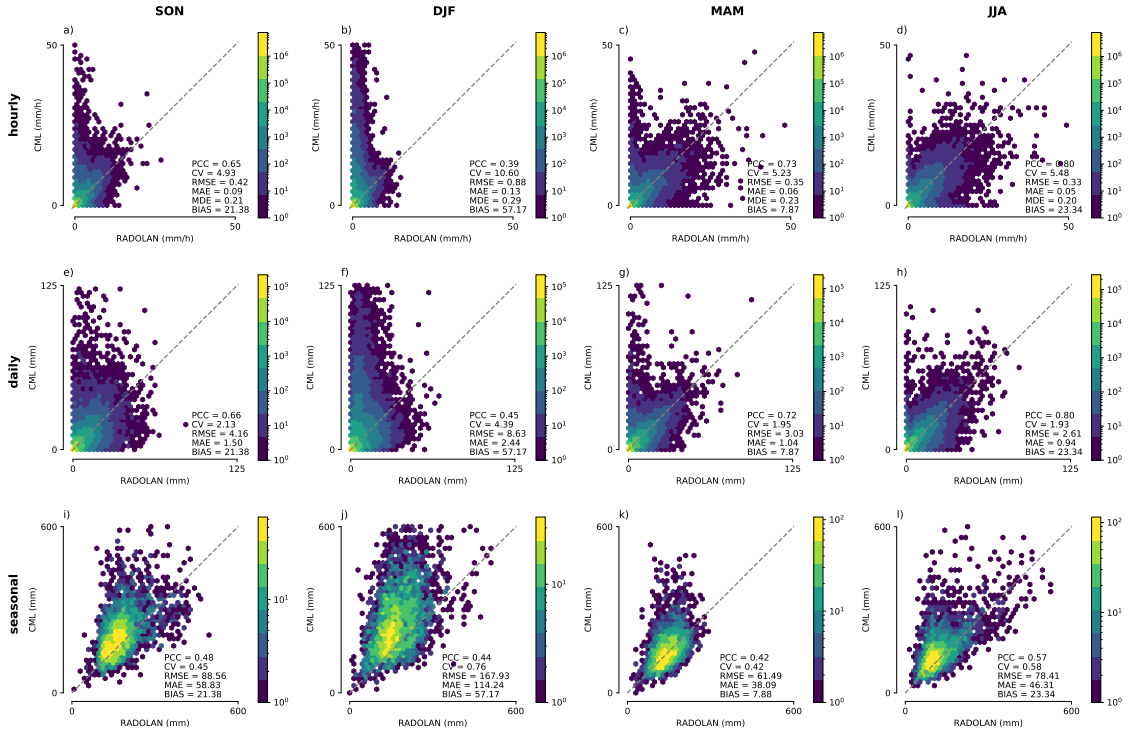

Figure 2.6: Seasonal scatter density plots of CML-derived rainfall and path-averaged RADOLAN-RW data for hourly, a) - d), daily, e) - h) and seasonal, i) - l) aggregations with respective performance metrics calculated from all available data pairs.

also reflects this effect, as the lowest values for PCC and highest for CV, MAE, RMSE, BIAS and MDE are found for DJF. The largest overestimation occurs at low rain rates of the reference. At higher reference rain rates, which most likely are those stemming from liquid precipitation, there is far less overestimation. In spring (MAM) and fall (SON), overestimation by CML rainfall is still visible, but less frequent. This can be explained by the fact, that in the Central German Upland and the Alps, snowfall can occur from October to April. Best agreement between CML-derived rainfall and RADOLAN-RW is found for summer (JJA) months.

The temporal aggregation to daily rainfall sums and the respective performance measures are shown in 2.6e)-h). The general relation between CML derived rainfall and the reference is similar on both the hourly and daily scale. The BIAS is identical for the daily aggregation. The RMSE and MAE are higher due to the higher rain sums. The overestimation during the winter month is unchanged.

The accumulated rainfall sums of individual CMLs are compared against the reference rainfall accumulation for each season in Fig 2.6i) - l). The overestimation of the CML derived rainfall sums in DJF, and partly SON and MAM, can again be attributed to the presence of non-liquid precipitation. This overestimation is larger for higher rainfall sums. This could be the result

Table 2.2: Monthly performance measures between path averaged, hourly CML-derived rainfall and RADOLAN-RW as reference for subset criteria and thresholds.

	subset criteria		**2017**				**2018**							
	(mm)	**mean**	**Sept**	**Oct**	**Nov**	**Dec**	**Jan**	**Feb**	**Mar**	**Apr**	**May**	**Jun**	**Jul**	**Aug**
PCC (-)	none	**0.62**	0.78	0.73	0.46	0.36	0.43	0.27	0.45	0.74	0.85	0.81	0.79	0.81
	light rain to 0	**0.62**	0.78	0.73	0.46	0.36	0.43	0.27	0.45	0.74	0.85	0.81	0.79	0.81
	cml or ref > 0	**0.58**	0.74	0.68	0.38	0.28	0.35	0.20	0.37	0.71	0.83	0.80	0.78	0.79
	cml or ref >= 0.1	**0.54**	0.70	0.64	0.34	0.23	0.31	0.13	0.32	0.68	0.81	0.78	0.76	0.77
	ref >= 0.1	**0.58**	0.73	0.71	0.38	0.28	0.35	0.22	0.39	0.73	0.82	0.79	0.80	0.80
	ref >= 1	**0.51**	0.65	0.64	0.32	0.17	0.27	0.12	027	0.67	0.75	0.73	0.73	0.74
CV (-)	none	**7.01**	3.80	4.40	6.09	11.4	7.62	18.5	6.82	5.20	3.98	5.17	5.88	5.33
	light rain to 0	**7.19**	3.88	4.51	6.23	11.64	7.75	18.28	7.06	5.33	4.03	5.23	5.96	5.40
	cml or ref > 0	**3.03**	1.73	2.00	2.96	5.59	3.85	6.82	3.09	2.19	1.60	2.04	2.36	2.10
	cml or ref >= 0.1	**2.42**	1.40	1.64	2.51	4.78	3.35	5.19	2.53	1.67	1.18	1.50	1.71	1.54
	ref >= 0.1	**1.69**	1.05	1.06	1.92	3.61	2.67	3.25	1.90	1.11	0.88	1.01	0.96	0.92
	ref >= 1	**1.11**	0.73	0.69	1.24	2.27	1.73	2.18	1.14	0.70	0.63	0.72	0.67	0.65
MAE (mm/h)	none	**0.08**	0.08	0.08	0.11	0.17	0.17	0.05	0.07	0.05	0.06	0.06	0.05	0.05
	light rain to 0	**0.08**	0.08	0.07	0.11	0.17	0.16	0.05	0.07	0.05	0.05	0.05	0.05	0.05
	cml or ref > 0	**0.41**	0.38	0.36	0.46	0.71	0.64	0.37	0.35	0.30	0.34	0.36	0.33	0.33
	cml or ref >= 0.1	**0.64**	0.58	0.53	0.64	0.97	0.86	0.66	0.53	0.49	0.61	0.64	0.60	0.58
	ref >= 0.1	**0.72**	0.64	0.57	0.70	1.02	0.91	0.68	0.55	0.54	0.73	0.83	0.74	0.69
	ref >= 1	**1.40**	1.16	1.05	1.40	2.02	1.73	1.73	1.25	1.09	1.30	1.51	1.39	1.22
RMSE (mm/h)	none	**0.48**	0.34	0.33	0.56	1.08	0.94	0.46	0.41	0.29	0.36	0.35	0.32	0.30
	light rain to 0	**0.48**	0.35	0.33	0.56	1.08	0.94	0.46	0.41	0.29	0.34	0.35	0.32	0.30
	cml or ref > 0	**1.06**	0.75	0.71	1.16	2.18	1.84	1.25	0.90	0.68	0.84	0.89	0.78	0.75
	cml or ref >= 0.1	**1.34**	0.94	0.87	1.38	2.58	2.14	1.70	1.12	0.90	1.14	1.22	1.08	1.02
	ref >= 0.1	**1.45**	1.01	0.90	1.47	2.66	2.22	1.68	1.15	0.96	1.33	1.52	1.31	1.18
	ref >= 1	**2.33**	1.59	1.43	2.36	4.02	3.33	3.48	1.97	1.61	1.99	2.32	2.04	1.78
BIAS (%)	none	**30**	20	34	11	79	39	67	7	21	0	10	30	35
	light rain to 0	**29**	20	34	11	80	40	67	7	20	-2	8	27	32
	cml or ref > 0	**30**	20	34	11	79	39	67	7	21	0	10	30	35
	cml or ref >= 0.1	**29**	20	33	11	80	40	67	7	20	-2	8	27	32
	ref >= 0.1	**-4**	-1	-1	-15	36	14	-6	-20	-10	-16	-15	-13	-3
	ref >= 1	**-9**	-4	-9	-24	22	2	-16	-21	-12	-15	-17	-13	-5
MDE	none	**0.23**	0.20	0.19	0.24	0.27	0.23	0.35	0.29	0.22	0.19	0.19	0.22	0.17

of more extensive snowfall in the mountainous parts of Germany, which are also the areas with highest precipitation year round. Rainfall sums close to zero can be the result from the quality control that we have applied. Periods with missing data in CML time series are consequently not counted in the reference rainfall data set. Therefore, the rainfall sums in Fig. 2.6 are not representative for the rainfall sum over Germany for the shown period. The PCC for the four seasons shown in Fig. 2.6i)-l) range from 0.42 in MAM to 0.57 in JJA.

2.4.4 Performance measures for different subset criteria

Tab. 2.2 gives an overview of monthly performance measures for different subsets of CML-derived and path-averaged reference rainfall. In the following, we will discuss the effects of the different subset criteria and then compare our results to previous CML rainfall estimation studies.

For all subset criteria, best performance measures are found during late spring, summer and early fall. Highest PCC values are reached when all data pairs, including true dry events, are used to

Table 2.3: Comparison of the performance measures to similar CML validation studies (only link-based comparisons) with respective thresholds

Study and Dataset	Comparison	Threshold	Bias (%)	CV (-)	PCC (-)
de Vos et al. (2019b)					
Average of 1451 CMLs over 7 months (18 Feb–16 Oct 2016), 15 min instantaneously sampled	Link-based comparison with gauge-adjusted radar, 15 min	CML or ref > 0 mm	23	3.43	0.52
Rios Gaona et al. (2015)					
Average of 1514 CMLs over 12 rainy days (June to September 2011), min-max sampled	CML-based comparison with gauge-adjusted ref, 15 min	CML or ref > 0.1 mm	-13	1.44	0.66
This study					
Average of 3904 CMLs over one year (September 2017 - August 2018), one min instantaneously sampled	CML-based comparison with gauge-adjusted radar, hourly	CML or ref > 0 mm	30	3.03	0.58
		CML or ref >= 0.1 mm	19	2.42	0.54

calculate the measures. When very light rain (< 0.1 mm/h) is set to zero on an hourly basis, the performance measures stay very similar, with the exception of CV and BIAS, which show a slight increase in performance. This means that, even when very small rain rates < 0.1 mm are produced, they do not change rainfall sums too much.

When either R_{CML} or $R_{reference}$ have to exceed 0 mm/h, the performance measures are worse than with all data, because all 0 mm/h pairs are removed. When the same subset criterion is set to 0.1 mm/h, a good agreement in the range of very small rain rates below 0.1 mm/h between both data becomes apparent, because the performance measures get worse without them.

To examine the performance of the CML derived rainfall during rain events detected by the reference, two thresholds are selected, where the reference must be above 0.1 and 1 mm/h, respectively, for the period to be considered rainy. With these thresholds, all false wet classifications are removed before the calculation of the performance measures. The PCC with this thresholds is still high for the non-winter months. The CV is reduced, while MAE and RMSE are higher due to higher mean rain rates. The biggest differences can be observed in the bias, where the influence of false wet detection and the overestimation of CMLs over 0.1 and 1 mm/h reduce the bias.

Therefore, when discussing these performance measures in relation to previous studies on CML rainfall estimation, the selection of the threshold is of great importance. de Vos et al. (2019b) showed a collection of dutch CML-studies in Table A1. In Tab. 2.3 we compare our performance measures to those of studies from de Vos et al. (2019b) table which are similar to our study. 'Similar' in this context means considering the size and temporal aggregation of the CML data set as well as the use of radar data as a reference for path-averaged (link-based) rain rates from CMLs. The performance measures from our results with the respective thresholds are in the same range as the performance measures from de Vos et al. (2019b) and Rios Gaona et al. (2015). The results thus should not be compared in a purely quantitative way, because both use different sampling strategies and span different time periods.

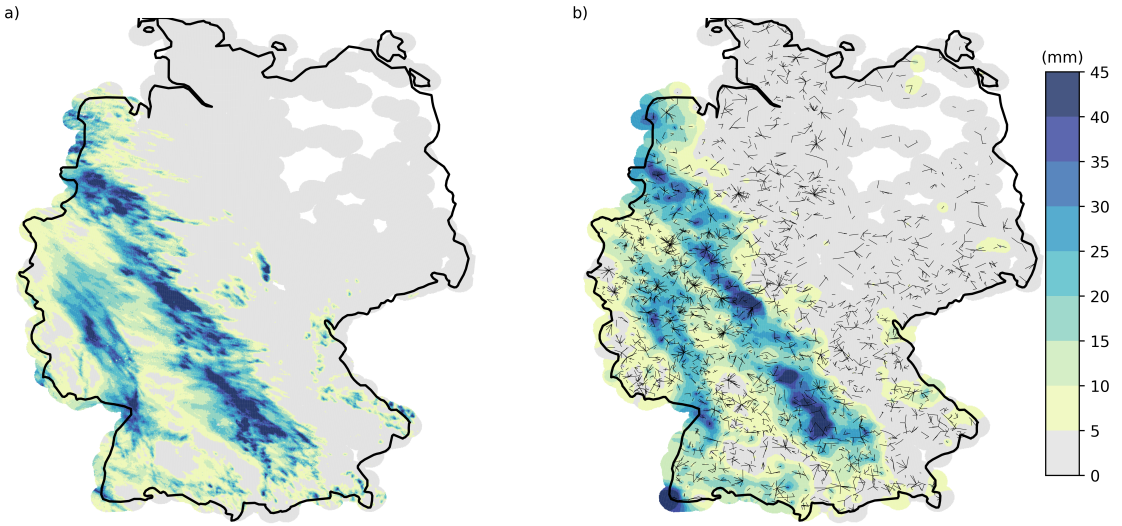

Figure 2.7: Accumulated rainfall for a 48 hour showcase from 12.05.2018 until 14.05.2018 for a) RADOLAN-RW and b) CML-derived rainfall. CML-derived rainfall is interpolated using a simple inverse distance weighting interpolation. A coverage mask of 30 km around CMLs is used.

2.4.5 Rainfall maps

Interpolated rainfall maps of CML-derived rainfall compared to RADOLAN-RW are shown in Fig. 2.7, Fig. 2.8 and Fig. 2.9. The respective CML maps have been derived using inverse distance weighting (IDW) with the RADOLAN-RW grid as target grid and on an hourly basis. Each CML rainfall value is represented as one synthetic point observation at the center of the CML path. For each pixel of the interpolated rainfall field the nearest 12 synthetic CML observation points are taken into account. Weights decrease with the distance d in km, according to d^{-2}. After the interpolation, we masked out grid cells further away than 30 km from a CML path, for each individual time step. Hence, hourly rainfall maps derived from CMLs are only produced for areas with data coverage. We applied the same mask to the reference data set on an hourly basis to increase the comparability between both data sets. For the aggregated rainfall maps, we summed up the interpolated, individually masked, hourly rainfall fields.

As an example, Fig. 2.7 shows 48 hours of accumulated rainfall in May 2018. The general distribution of CML-derived rainfall reproduces the pattern of the reference very well and the rainfall sums of both data sets are similar. Individual features of the RADOLAN-RW rainfall field are, however, missed due to the limited coverage by CMLs in certain regions. A video of this 48 hour showcase with hourly time steps is published alongside this study (Graf et al., 2020b).

A qualitative comparison of monthly aggregation of the hourly rainfall maps is shown in Fig. 2.8 and Fig. 2.9. The CML-derived rainfall fields resemble the general patterns of the RADOLAN-RW rainfall fields. Summer months show a better agreement than winter months. This is a direct

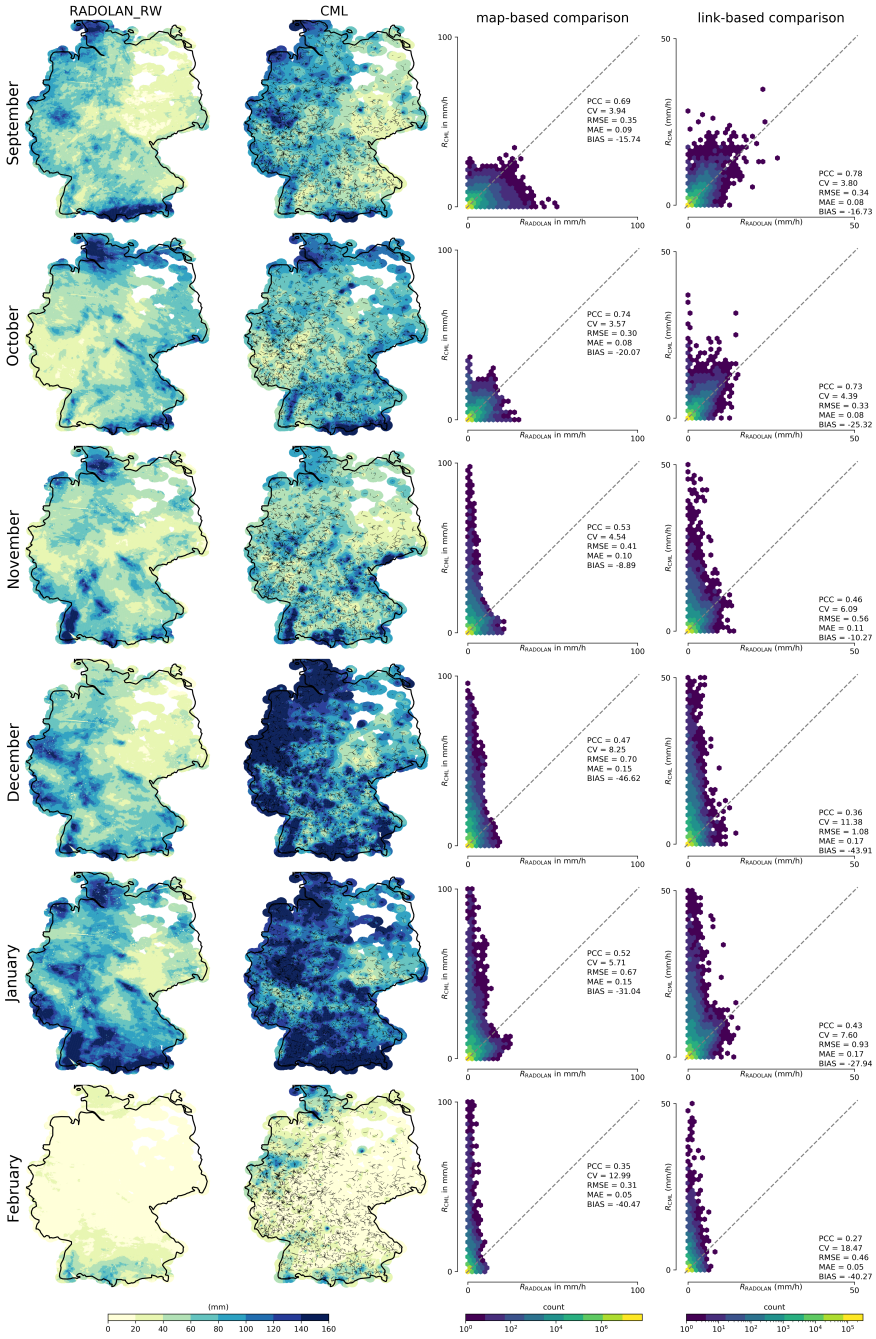

Figure 2.8: Monthly aggregations of hourly rainfall maps from CMLs compared to RADOLAN-RW from September 2017 until February 2018. For each month two scatter density plots are shown, one for pixel-by-pixel comparison of the hourly maps (map-based comparison), and one for the comparison of the hourly path-averaged rainfall along the individual CMLs (link-based comparison).

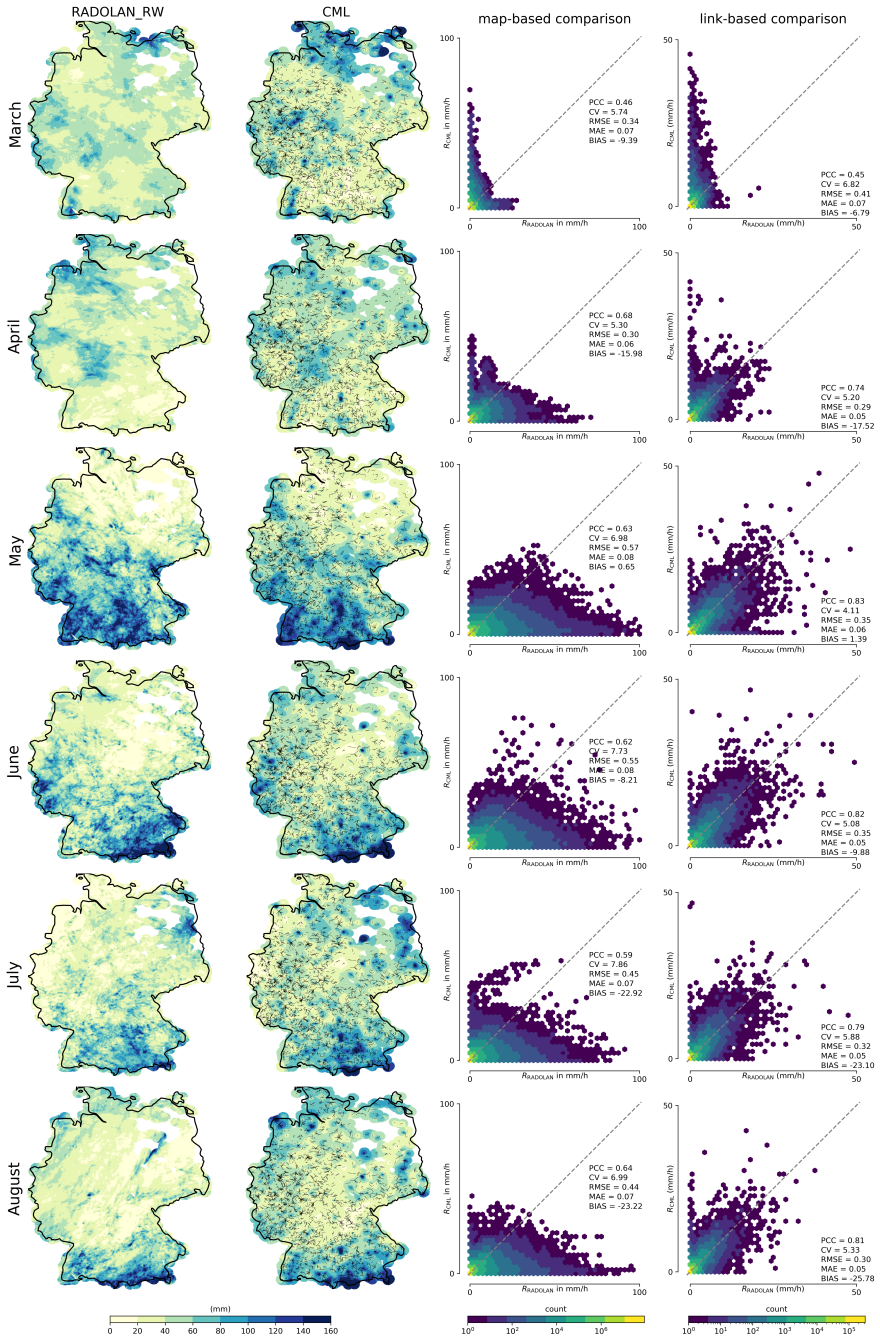

Figure 2.9: Monthly aggregations of hourly rainfall maps from CMLs compared to RADOLAN-RW from March until August 2018. For each month two scatter density plots are shown, one for pixel-by-pixel comparison of the hourly maps (map-based comparison), and one for the comparison of the hourly path-averaged rainfall along the individual CMLs (link-based comparison).

result of the decreased performance of CML-derived rain rates during the winter season, explained in Sect. 2.4.3. Strong overestimation is also visible year round for a few individual CMLs, for which the filtering of erratic behavior was not successful.

A quantitative comparison of the CML-derived rainfall maps to the reference is shown in the third column of Fig. 2.8 and Fig. 2.9. For these scatter density plots we used all hourly pixel values of the respective month within the 30 km coverage mask. During the winter month, CMLs show strong overestimation. This is a direct result of non-liquid precipitation as described in Sect. 2.4.3. From May to August 2018 the reference shows very high rain intensities between 50 and 100 mm/h, which are not produced by the CML rainfall maps. This can be attributed to several reasons. First, CML-derived rainfall, which serves as basis for the interpolation, is path-averaged, with a typical path length in the range of 3-15 km. This means, that the rainfall estimation of a single CML represents an average of several RADOLAN-RW grid cells which smoothes out the extremes. Second, due to the interpolation, rainfall maxima in the CML rainfall maps can only occur at the synthetic observation points at the center of each CML. Third, rainfall is only observed along the path of CMLs and even with almost 4000 CMLs across Germany, the spatial variation of rainfall cannot be fully resolved. In particular in summer, small convective rainfall events might not intersect with CML paths and hence cannot appear in the CML-derived IDW interpolated rainfall fields.

Considering this, the effect of different coverage ranges around the CMLs has to be taken into account. For the map based comparison in Fig. 2.8 and Fig. 2.9 we tested several distances from 10 to 50 km. For the presented results we choose 30 km as a trade off between minimizing the uncertainty of the spatial interpolation and the goal to reach country wide coverage with the produced rainfall maps. van de Beek et al. (2012) found an averaged range of around 30 km for summer semi-variograms of 30 years of hourly rain gauge data in the Netherlands, which can be used to justify/enforce our choice. With a 10 km coverage range, the performance measures are better than the ones for 30 km, which are shown in Fig. 2.8 and Fig. 2.9. Monthly PCC values show an increase of around 0.05 and the bias is reduced by 3 to 5 percent. Nevertheless, with a coverage of 10 km around the CMLs, coverage gaps emerge not only in the north-eastern part of Germany, but also in the south eastern part. Vice versa, with a 50 km coverage range, the country wide coverage is almost given, while the performance measures are worse compared to 30 km (PCC shows a decrease between 0.03 and 0.05). Overall, the difference of the performance measures of the 10 and 50 km coverage mask is limited in most parts of Germany by the high density of CMLs, which already lead to an almost full coverage with the 10 km mask.

In order to highlight the differences between a map-based and link-based comparison Fig. 2.8 and Fig. 2.9 also show hourly link-based scatter density plots for each month. The differences in the performances measures for the warm months support the qualitative impression, that the map-based comparison perform worse. The interpolation is prone to introduce an underestimation for areas which are more distant to the CML observations. During the winter months, this underestimation compensates the overestimation of the individual CMLs which is due to wet snow and ice covered antennas. Hence, because the two errors compensate each other by chance, this

results in slightly better map-based performance measures compared to the link-based measures for the winter months. Nevertheless, rainfall estimation with CMLs for months with non-liquid precipitation is considerably worse than for summer months in all spatial and temporal aggregations.

The derivation of spatial information from the estimated path-averaged rain rates could be improved by applying more sophisticated techniques as described in Sect. 2.1. We have already carried out several experiments using Kriging, to test one of these potential improvements over IDW. We followed the approach of Overeem et al. (2016b) and adjusted the semivariogram parameters on a monthly basis based on the values from van de Beek et al. (2012). We also tried fixed semivariogram parameters and parameters estimated from the individual CML rainfall estimates for each hour. In conclusion, we, however, only found marginal or no improvements of the performance metrics of the CML rainfall maps. Combined with the drawback of Kriging that the required computation time is significantly increased (approximately 10 to 100 times slower than IDW, depending e.g. on the number of neighboring points used by a moving kriging window), we thus decided to keep using the simple, yet robust and fast IDW interpolation. Furthermore, it is important to note that the errors in rain rate estimation for each CML contribute most to the uncertainty of CML-derived rainfall maps (Rios Gaona et al., 2015). Hence, within the scope of this work, we focused on improving the rainfall estimation at the individual CMLs.

Taking into account that we compare to a reference data set derived from 17 C-band weather radars combined with more than 1000 rain gauges, the similarity with the CML-derived maps, which solely stem from the opportunistic usage of attenuation data, is remarkable.

2.5 Conclusion

German wide rainfall estimates derived from CML data compared well with RADOLAN-RW, a hourly gridded gauge-adjusted radar product of the DWD. The methods used to process the CML data showed promising results over one year and several thousand CMLs across all landscapes in Germany, except for the winter season.

We presented the data processing of almost 4000 CMLs with a temporal resolution of one minute from September 2017 until August 2018. We developed a parallelized processing work flow, which could handle the size of this large data set. This workflow enabled us to test and compare different processing methods over a large spatiotemporal scale.

A crucial processing step is the rain event detection from the TRSL, the raw attenuation data recorded for each CML. We used a scheme from (Schleiss and Berne, 2010) which uses the 60 minute rolling standard deviation RSD and a threshold. We derived this threshold from a fixed multiple of the 80th quantile of the RSD distribution of each TRSL. Compared to the original threshold using the 95th quantile, which is based on rainfall climatology, the 80th quantile reflects the general notion of each CML's TRSL to fluctuate. We were able to reduce the amount of

miss-classification of wet and dry events, reaching a yearly mean MDE of 0.27, with an average of the MDE for summer months below 0.20. Potential approaches for further decreasing the amount of miss-classifications could be the use of additional data sets. For example, cloud cover information from geostationary satellites could be employed to reduce false wet classification, by, as a first simple approach, defining periods without clouds as dry. Another opportunity would be, to additionally implement algorithms exploiting information of neighboring CMLs.

For the compensation of WAA, the attenuation caused by water droplets on the cover of CML antennas, we compared and adjusted two approaches from literature. In order to evaluate WAA compensation approaches, we used the reference data set. We were able to reduce the overestimation caused by WAA, while maintaining the detection of small rain events, using an adjustment of the approach introduced by Leijnse et al. (2008). The compensation of WAA without an evaluation with a reference data set is not feasible with the CML data set we use.

Compared to the reference data set RADOLAN-RW, the CML-derived rainfall performs well for periods with only liquid precipitation. For winter months, the performance of CML-derived rainfall is limited. Melting snow and snowy or icy antenna covers can cause additional attenuation resulting in overestimation of precipitation, while dry snow cannot be measured at the frequencies and the TRSL quantizations the CMLs in our data set use. We found high correlations for hourly, monthly and seasonal rainfall sums between CML-derived rainfall and the reference. To increase the comparability of our analysis with existing and future studies on CML rainfall estimation we calculated all performance metrics for different subset criteria, e.g. requiring that either CML or reference rainfall is larger than 0 mm.

We found the performance measures of this study to be in accordance with similar CML studies, although the comparability is limited due to differences of the CML and reference data sets. CML-derived rainfall maps calculated with a simple, yet robust inverse distance weighting interpolation showed the plausibility of CMLs as an stand-alone rainfall measurement system.

With the analysis presented in this study, the need for reference data sets in the processing routine of CML data is reduced, so that the opportunistic sensing of country-wide rainfall with CMLs is at a point, where it should be transferable to (reference) data scarce regions. Especially in Africa, where water availability and management are critical, this task should be challenged as Doumounia et al. (2014) did already. The high temporal resolution of the presented data set can be used in future studies, e.g. for urban water management. In addition, CML derived rainfall can also complement other rainfall data sets, e.g. to improve the radar data adjustment in RADOLAN in regions with high CML density and regions, like mountain ranges, where radar data is often compromised. Thus, CMLs can contribute substantially to improve the spatiotemporal estimations of rainfall.

Code availability

Code used for the processing of CML data can be found in the Python package pycomlink (pycomlink, 2021).

Data availability

CML data was provided by Ericsson Germany and is not publicly available. RADOLAN-RW is publicly available through the Climate Data Center of the German Weather Service

Acknowledgements

We thank Ericsson for the support and cooperation in the acquisition of the CML data. This work was funded by the Helmholtz Association of German Research Centres within the Project *Digital Earth*. We also like to thank the German Research Foundation for funding the projects *IMAP* and *RealPEP* and the Bundesministerium für Bildung und Forschung for funding the project *HoWa-innovativ*. We further thank the three anonymous reviewers for their valuable comments improving this paper.

Appendix A

Table 2.A1: Comprehensive overview of used parameters, a short description and their reference from literature if applicable. Parameters with enumeration in parentheses are not used in the final processing.

	description	**parameter value**	**source**
parameters used in final processing routine			
1. Erratic behavior of CMLs (section 3.2.1)			
1.1	sanity check to remove CMLs with strong duirnal cycle or which have noisy periods	5 hour RSD >2 for at lest 10% per month	this study
1.2	sanity check to remove CMLs with high fluctuation over large parts of or the complete month	1 hour RSD >0.8 for at least 33% per month	this study
2. Rain event detection (section 3.2.2)			
2.1	RSD window length	60 min	Schleiss and Berne (2010)
2.2	scaled q80 threshold	1.12 * 80% quantile of RSD	this study
3. WAA compensation (section 3.2.3)			
3.1	thickness of antenna cover	4.1 cm	measured from one antenna cover
3.2	scale for water film thickness γ	1.47E-5	modified after Leijnse et al. (2008)
3.3	factor for the relation between	0.36	modified after Leijnse et al. (2008)
parameters used in alternative processing steps			
(2.3)	climatologic threshold	95% quantile of RSD	Schleiss and Berne (2010)
(3.4)	time for WAA to reach maximum τ	15 min	Schleiss et al. (2013)
(3.5)	maximal value of WAA	2.3 dB	Schleiss et al. (2013)

Chapter 3

Rain event detection in commercial microwave link attenuation data using convolutional neural networks (Polz et al., 2020)

Polz, J., Chwala, C., Graf, M., and Kunstmann, H.: Rain event detection in commercial microwave link attenuation data using convolutional neural networks, *Atmos. Meas. Tech.*, 13, 3835–3853, https://doi.org/10.5194/amt-13-3835-2020, 2020.

Abstract

Quantitative precipitation estimation with commercial microwave links (CMLs) is a technique developed to supplement weather radar and rain gauge observations. It is exploiting the relation between the attenuation of CML signal levels and the integrated rain rate along a CML path. The opportunistic nature of this method requires a sophisticated data processing using robust methods. In this study we focus on the processing step of rain event detection in the signal level time series of the CMLs, which we treat as a binary classification problem. This processing step is particularly challenging, because even when there is no rain the signal level can show large fluctuations similar to that during rainy periods. False classifications can have a high impact on falsely estimated rainfall amounts. We analyze the performance of a convolutional neural network (CNN), which is trained to detect rainfall specific attenuation patterns in CML signal levels, using data from 3904 CMLs in Germany. The CNN consists of a feature extraction and a classification part with, in total, 20 layers of neurons and 1.4×10^5 trainable parameters. With a structure, inspired by the visual cortex of mammals, CNNs use local connections of neurons to recognize patterns independent of their location in the time-series. We test the CNNs ability to generalize to CMLs and time periods outside the training data. Our CNN is trained on four months of data from 800 randomly selected CMLs and validated on two different months of data,

once for all CMLs and once for the 3104 CMLs not included in the training. No CMLs are excluded from the analysis. As a reference data set we use the gauge adjusted radar product RADOLAN-RW provided by the German meteorological service (DWD). The model predictions and the reference data are compared on an hourly basis. Model performance is compared to a state of the art reference method, which uses the rolling standard deviation of the CML signal level time series as a detection criteria. Our results show that within the analyzed period of April to September 2018, the CNN generalizes well to the validation CMLs and time periods. A receiver operating characteristic (ROC) analysis shows that the CNN is outperforming the reference method, detecting on average 76% of all rainy and 97% of all non-rainy periods. From all periods with a reference rain rate larger than 0.6 mmh^{-1}, more than 90% were detected. We also show that the improved event detection leads to a significant reduction of falsely estimated rainfall by up to 51%. At the same time, the quality of the correctly estimated rainfall is kept at the same level in regard to the Pearson correlation with the radar rainfall. In conclusion, we find that CNNs are a robust and promising tool to detect rainfall induced attenuation patterns in CML signal levels from a large CML data set covering entire Germany.

3.1 Introduction

Rainfall is the major driver of the hydrologic cycle. Accurate rainfall observations are fundamental for understanding, modeling and predicting relevant hydrological phenomena, e.g. flooding. Data from commercial microwave link (CML) networks have proven to provide valuable rainfall information. Given the high spatio-temporal variability of rainfall, they are a welcome complement to support traditional observations with rain gauges and weather radars; particularly in regions where radar is hampered by beam blockage or ground clutter. In regions with sparse rainfall observation networks, like in developing countries, CMLs might even be the only source of small scale rainfall information.

Since the work of Messer et al. (2006) and Leijnse et al. (2007) more than a decade ago, several research groups have shown the potential of CML data for hydrometeorological usage. Prominent examples are the countrywide evaluations in the Netherlands (Overeem et al., 2016b) and Germany (Graf et al., 2020a), which demonstrated that CML-derived rainfall information corresponds well with gauge-adjusted radar rainfall products, except for the cold season with solid precipitation. CML-derived rainfall information was also successfully used for river runoff simulations in a pre-alpine catchment in Germany (Smiatek et al., 2017) and for pipe flow simulation in a small urban catchment in Czech Republic (Pastorek et al., 2019). A further important step was the first analysis of CML-derived rain rates in a developing country, carried out by Doumounia et al. (2014), with data from Burkina Faso.

In general, the number of CMLs available for research has increased significantly over the last years and researchers from several countries have gained access to CML attenuation data. Currently, data from 4000 CMLs over Germany is recorded continuously with a temporal resolution of one minute via a real-time data acquisition system (Chwala et al., 2016). The number of ex-

isting CMLs over Germany is 30 times higher (Bundesnetzagentur, 2017), amounting to 130.000 registered CMLs. Consequently, it is envisaged to increase the number of CMLs included in the data acquisition.

With this large number of CMLs available in Germany and with new data being retrieved continuously, there is a need for optimized and robust processing of these big data sets. Several studies address the details of the processing steps which are required for deriving rainfall information from CMLs. These steps involve, e.g. the detection of rain events in noisy raw data, the filtering of artifacts, correcting for bias due to wet antenna attenuation (WAA) and the spatial reconstruction of rainfall fields. Uijlenhoet et al. (2018) give a general overview of the required processing steps and the existing methods and Chwala and Kunstmann (2019) discuss and summarize the related current challenges.

3.1.1 On the importance of rain event detection

The first of these processing steps, called rain event detection, is the separation of rainy (wet) and non-rainy (dry) periods. A static signal level baseline to derive attenuation that can be attributed to rainfall has proven to be ineffective due to e.g. daily or annual cycles and unexpected jumps in the time series like for CML B in Fig. 3.1. Therefore, after the rain events are localized correctly, an event specific attenuation baseline can be determined and actual rain rates can be derived via the k-R power law which relates specific attenuation k in dB km^{-1} to rain rate R in mm h^{-1}.

Detecting rain events is challenging, because CML signal levels can show high fluctuations, even when there is no rain, e.g. due to multi-path propagation (e.g. Chwala and Kunstmann, 2019, Fig. 6). Therefore, the main difficulty is to distinguish between noise and signal fluctuations caused by rain along the CML path. As seen in Fig. 3.1, the differences in noise levels can vary significantly, depending on the CML that is used. When looking at the magnitude of these fluctuations, we can see that a misclassification of wet and dry periods can easily lead to a large over- or underestimation of rainfall. These missed or falsely estimated quantities are often overlooked in scatter density comparisons of rainfall products like Figure 3.9 a) and b) below, which shows our own results. But when absolute amounts are compared, they represent an obvious issue with up to 30% of the total CML rainfall that can be attributed to false positives. As these misclassifications generate a bias different from the bias corrected in later processing steps like the WAA correction it is important to optimize the rain event detection as an isolated processing step first and to optimize subsequent processing steps afterwards.

3.1.2 State of the art

So far, several methods for rain event detection with CMLs have been proposed. The main difference that divides these methods into two groups, is the type of CML data that can be used to estimate rainfall. Depending on the available data acquisition, CML signal levels are either instantaneously sampled at a rate ranging from a few seconds up to 15 minutes or they are stored as 15-minute minimum and maximum values derived from a high instantaneous sampling rate in the background. In almost all cases only one of the two sampling strategies is available due to

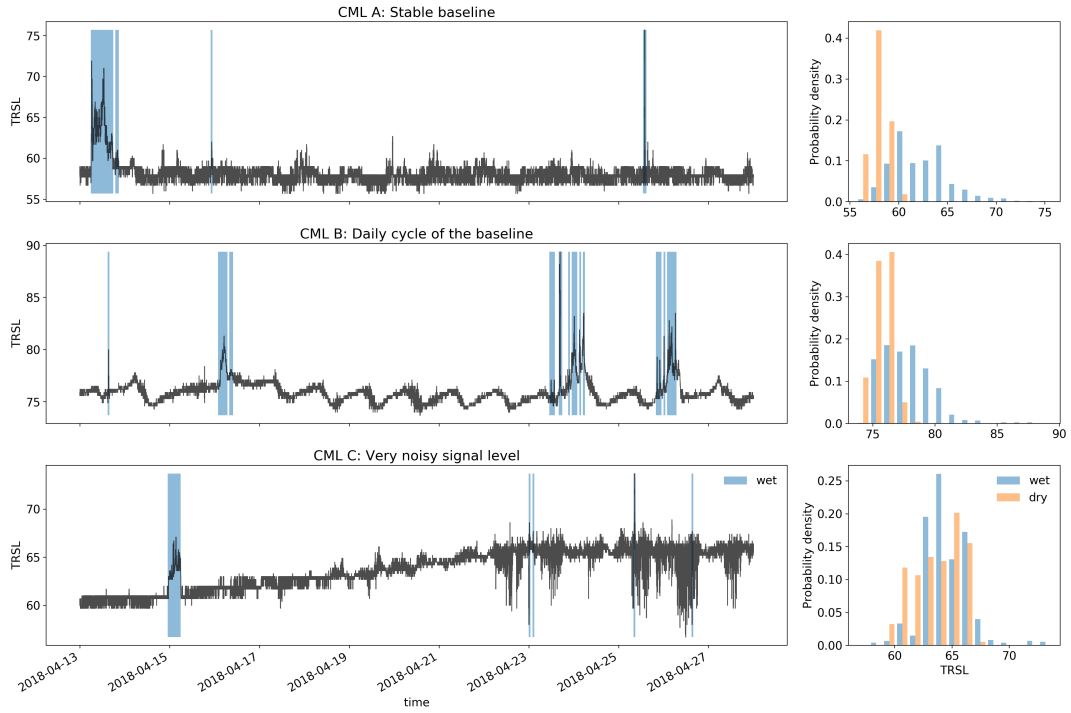

Figure 3.1: Three example signal level (TRSL) time series that illustrate the high variability in data quality when comparing different CMLs. The blue shaded periods indicate where the radar reference show rainfall along the CML paths. The challenge is to identify these periods by analysing the time series. Note that each attenuation event that is falsely classified as wet, will produce false rain rate estimates, which will lead to overestimation. The histograms show that for some CMLs the wet periods can be easily separated from the dry periods and for others the distribution of TRSL values is nearly identical for both classes. Fig. 3.2 below will show an example of how different detection methods deal with the challenging time series of CML C.

the type of data management through the network provider. The resulting rain event detection methods are highly optimized for one kind of sampling strategy and therefore in general incompatible with the other kind.

The following methods were developed for instantaneous measurements: Schleiss and Berne (2010) introduced a threshold for the rolling standard deviation (RSTD) of the attenuation time-series as a criteria to detect rain events. Despite being one of the first methods that were developed, a large part the method is still the most commonly used within the CML research community, as it was used in very recent studies from different working groups such as Kim and Kwon (2018), Graf et al. (2020a) or Fencl et al. (2020). Chwala et al. (2012) introduced Fourier transformations on a rolling window of CML signal levels to detect the pattern of rain events in the frequency domain. Wang et al. (2012) used a Markov switching model, which was calibrated and validated for a single CML test site. Kaufmann and Rieckermann (2011) have shown the applicability of random forest classifiers and Gaussian factor graphs and validated their approach using 14 CMLs. Đorđević et al. (2014) used a simple Multilayer Perceptron (MLP) which was trained and validated

on a single CML. Ostrometzky and Messer (2018) proposed a simple rolling mean approach to determine a dynamic baseline, also validated on a single CML. Most of these studies are based on a comparably low and sometimes pre-selected amount of CMLs ranging from one to a maximum of 50 devices, a number that is likely much larger in a possible operational setting.

As a detection scheme for 15 minute min/max sampled data with a 10 Hz background sampling rate Overeem et al. (2011) introduced the 'nearby link approach'. A period is considered wet if the increase of CML specific attenuation correlates with the attenuation pattern of nearby CMLs. They concluded that this is only applicable for dense CML networks with a high data availability. Later, they conducted the first evaluation of a rain event detection method on data from 2044 CMLs on a country scale Overeem et al. (2016b). Very recently the same approach was used in de Vos et al. (2019b), showing that this approach works better in combination with min/max sampling than with 15 minute instantaneous sampling. Habi and Messer (2018) tested the performance of Long Short-Term Memory (LSTM) networks to classify rainy periods from 15 minute min/max values of CML signal levels for 34 CMLs.

All rain event detection methods have to make a similar trade-off: A liberal detection of wet periods is more likely to recognize even small rain rates, while it will produce more false alarms during dry periods. On the other hand, a conservative detection will accurately classify dry periods, but is more likely to miss small rain events. One can address this by two means. First, by increasing detection rates on both wet and dry periods as much as possible and therefore decreasing the impact of the trade-off. Second, by allowing the flexibility to easily adjust the model towards liberal or conservative detection, e.g. by only changing a single parameter.

In conclusion, until now, there have been few studies analyzing the performance of rain event detection methods on large data sets. Overeem et al. (2016b) tested the nearby link approach using 2044 CMLs distributed over the Netherlands with a temporal coverage of 2.5 years of data. Graf et al. (2020a) extended the RSTD method and applied it to one year of data from 3904 CMLs to set a benchmark performance on the same data set used in this study. By optimizing thresholds for individual CMLs the full potential of the RSTD method for one year of data was explored, yielding good results for the warm season with liquid precipitation. While the RSTD method is simple to implement and has only two parameters (window length and threshold) to optimize, it is limited to measuring the amount of fluctuations, rather than the specific pattern. More room for optimization is expected using a data driven approach, such as machine learning techniques for pattern recognition.

3.1.3 Data driven optimization through deep learning

Deep learning is a rapidly evolving field that is becoming increasingly popular in the earth system sciences. A large field of application is remote sensing using artificial neural networks for image recognition (Zhu et al., 2017). Deep learning is also an established method in time-series classification (Ismail Fawaz et al., 2019). In both studies, convolutional neural networks (CNNs) are considered one of the leading neural network architectures for image and time-series classification.

CNNs are inspired by the visual cortex of mammals and they are designed to recognize objects or patterns, regardless of their location in images or time-series (Fukushima, 1980). They are characterized by local connections of neurons, shared weights and a large number of layers of neurons, involving pooling layers (LeCun et al., 2015). CNNs with one dimensional input data (1D-CNNs) have already been used for time-series classification, e.g. for classifying environmental sounds (Piczak, 2015). This makes 1D-CNNs a promising candidate for the task of rain event detection in CML signal levels.

3.1.4 Research gap and objectives

Due to the opportunistic use of CMLs, the variety of signal fluctuations and possible occurrences of errors naturally increase in a CML data set with its size. Separating rainy from non-rainy periods is therefore a crucial step for rainfall estimation from CMLs. Although applicable on a large scale, recently applied methods still struggle with falsely estimated rainfall as can be seen in the evaluations from Graf et al. (2020a) and de Vos et al. (2019b). Despite the amount of proposed methods, this processing step has not yet been investigated in detail using a large and diverse CML data set, especially for data driven approaches. Given their promising results in other applications, the usage of artificial neural networks (ANNs) for rain event detection in the CML attenuation time-series on a large scale provides a promising opportunity. It has been proven that in many cases ANNs allow for high-performance, fast and robust processing of a variety of suitable data sets. What is missing is a proof that they are applicable to a large and diverse CML data set. The question is, does a high variability of frequency, length and spatial distribution of the analyzed CMLs or a high variability of rain rates and event duration for a large amount of analyzed periods affect the performance of ANNs in this specific case or not? Additionally, the effect of rain event detection performance on the estimated rain rates has yet to be investigated.

The objective of this study is to evaluate the performance of 1D-CNNs to detect rainfall induced attenuation patterns in instantaneously measured CML signal levels and to investigate the effect of an improved temporal event localization on the CML-derived rainfall amounts. Furthermore, we test the CNNs ability to generalize to new CMLs and future time periods in order to provide a validated open source model, that can be used on other data sets. To provide the CML community with comprehensible results, we compare the CNN to the method of Schleiss and Berne (2010), which we consider state-of-the-art due to the amount of recent applications. We aim to provide a high statistical robustness of the derived performance measures by using the, to date, largest available CML data set consisting of data from 3904 CMLs distributed over entire Germany.

3.2 Methods

The following definition of rain event detection with CMLs is the basis of our methodology: Rain event detection is a binary classification problem. Given a time window $X_{t,w,i}$ of CML signal data, where t is the starting time, w is the window length and i is the index specifying a unique CML path, we have to decide if there is attenuation caused by rain (wet) or not (dry). A time window is assigned the label 1 if it is wet or 0 if it is dry. The available information to do this classification

depends on the used data acquisition and on which information is provided by the CML network operator. In the following, we describe how a CNN can be used as a binary classifier to succeed in this task.

3.2.1 Data set

We use a CML data set that has been collected in cooperation with Ericsson Germany through our custom CML data acquisition system Chwala et al. (2016). It covers 3904 CMLs across entire Germany. The CML path length ranges from 0.1 km to more than 30 km, with an average of around 7 km. CML frequencies range from 10 to 40 GHz. The acquired data consists of two sub-links per CML, transmitting their signal in opposite directions along the CML path. For each sub-link a received signal level (RSL) and a transmitted signal level (TSL) is recorded at a temporal resolution of 1 minute and a power resolution of 0.3 dB for RSL and 1.0 dB for TSL. The recorded period used in this study starts in April 2018 and ends in September 2018, to focus on the periods which are dominated by liquid precipitation, where CMLs perform better than during the cold season (Graf et al., 2020a). The data is available at 97.1% of all time steps and gaps are mainly due to outages of the data acquisition system.

As reference data we use the gauge adjusted radar product RADOLAN-RW provided by the German meteorological service (DWD). It has a spatial resolution of 1x1 km, covering entire Germany on 900x900 grid cells. The temporal resolution is 60 minutes and the resolution for the rain amount is 0.1 mm (Winterrath et al., 2012). To compare to this reference, the window length w is set to 60 minutes and therefore w is omitted in the notation below. Along each CML i, the path-averaged mean hourly rain rate $R_{t,i}$ is generated from the reference, using the weighted sum

$$R_{t,i} = \frac{\sum_k l_{k,i} r_{k,t}}{l_i}, \tag{3.1}$$

where k is indexing the RADOLAN grid cells intersected by the path of i. The rain rate of each grid cell is $r_{k,t}$. Furthermore, $l_{k,i}$ is the length of the intersect of k and i and l_i is the total length of i. A time window $X_{t,i}$ is considered wet if $R_{t,i} \geq 0.1$ mm h^{-1} and dry otherwise.

3.2.2 Pre-processing

Before training and testing an artificial neural network, the raw time-series data has to be pre-processed. We do this to sample time windows of a fixed size, which are normalized and labelled according to the reference.

First, the full data set, consisting of all available CMLs, is split into three subsets. One subset is used for training the CNN (TRG), one is used for validation and to optimize model hyper-parameters (VALAPR) and one is used for testing only (VALSEP). The data set TRG consists of data from 800 randomly chosen CMLs in the period from May to August 2018. VALAPR covers the remaining 3104 CMLs during April 2018 and VALSEP consists of data from all 3904 CMLs during September 2018. We used this splitting routine to avoid information leakage from the training to the validation data. There can be a high correlation of signal levels between CMLs

that are situated close to each other (Overeem et al., 2011). Therefore, the measurements contained in VALAPR or VALSEP can not be taken from the same time range as for TRG. Using only 20% of all available CMLs for training allows us to analyze the CNNs generalization to the remaining CMLs in the validation data set. No CMLs were excluded from this analysis.

For each of the two sub-links of a CML, we compute a transmitted minus received signal level (TRSL). Within one TRSL time-series, randomly occurring gaps of up to five minutes of missing data are linearly interpolated to be consistent with with the preprocessing used in Graf et al. (2020a). We assume that the temporal variability of rainfall is not high enough such that entire rain events can be hidden in such short gaps. The next step is to normalize the data. Normalization of training and validation data is a commonly used procedure in deep learning to enhance the model performance. We perform the normalization as a pre-processing step and outside the CNN. After testing various normalization techniques it turned out that the best performance of the CNN can be achieved by subtracting the median of all available data from the preceding 72 hours from each time step. In rare cases of larger gaps in the data acquisition, we set a lower limit for the data availability to 120 minutes.

The set of starting time-stamps of the hourly reference data set is denoted T_{rad}. For each CML i and each starting time $t \in T_{rad}$ a sample of data $\bar{X}_{t,i}$ is composed from 60+k minutes of TRSL from the two sub-links starting at $t - k$. The first k minutes serve as a reference to previous behaviour of the same CML and the last 60 minutes are the period $X_{t,i}$ that has to be classified. To investigate the impact of adding this additional information, we compare multiple setups with k ranging from 0 to 240 minutes. The results are given in Sect. 3. An example TRSL over a period of two weeks is shown in Fig. 3.2 (a).

After interpolating short gaps, as described above, we exclude all samples with missing values from the analysis. Since we loose up to five hours of data whenever there is a gap, the interpolation routine increases the number of available samples from 75% to 94%.

To train the CNN we have to balance the wet and dry classes in the data set (Hoens and Chawla, 2013). The under-sampling approach to achieve an equalized (50:50) class ratio is to randomly discard samples of the majority class, i.e. dry samples. This approach is chosen since we assume that dry periods mostly consist of redundant samples with only small fluctuations. Later, we check that there is no loss in performance by evaluating the unbalanced data. The initial percentage of wet samples is between 5-10%. We perform the balancing on TRG and VALAPR. The balanced version of VALAPR is denoted VALAPRB. VALAPR and VALSEP are kept as unbalanced data sets for validation. TRG already denotes the balanced data, since the original unbalanced training data set is not used in the analysis. In total, the number of samples is 2.3×10^5 for TRG, 3.9×10^5 for VALAPRB, 2.2×10^6 for VALAPR and 2.8×10^6 for VALSEP.

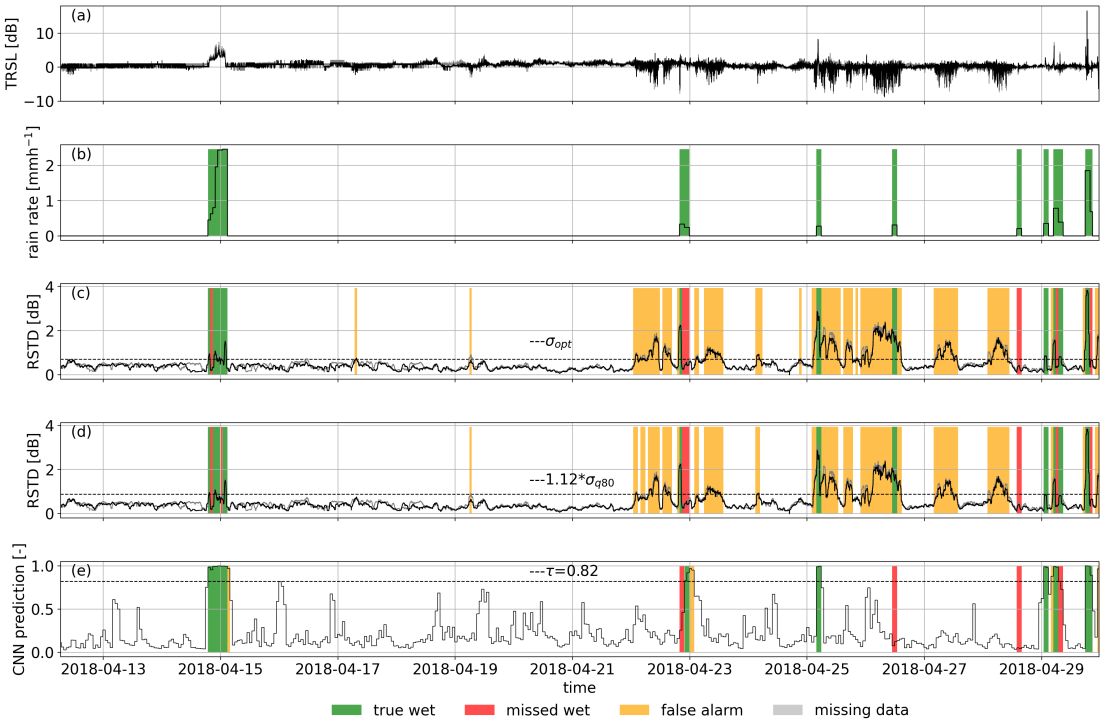

Figure 3.2: Performance of the CNN and the reference methods for the noisy example CML time-series from Fig. 3.1. a) shows the normalized TRSL time-series and b) is the radar reference. Predictions from the CNN (e) yield an MCC of 0.74. Predictions through σ_{opt} (c) and σ_{q80} (d), which are very similar in this case, both yield MCCs of 0.28. Note that the TRSL and RSTD time series of sub-link 2 are almost identical to those of sub-link 1 and are shown in light grey.

3.2.3 Neural Network

CNNs especially apply to time-series classification when patterns have to be recognized in longer sequences of data but the location of the occurring patterns is variable. They are therefore suitable classifiers for sensor data like the TRSL from CMLs. The expected advantage of the CNN over the reference method is that it is able to recognize the rainfall specific patterns, rather than just the amount of fluctuations. Like other neural network architectures they consist of a series of layers of neurons (Fig. 3.3). The first layer receives the input data and the last layer serves as an output for a prediction. The hidden layers in between are organized in two functional parts. The first part consists of a series of convolution and pooling layers and is used to extract features from the raw model input. Earlier convolution layers identify simple patterns in the data, which are used to identify more complex patterns in subsequent layers. The second part consists of fully connected layers of neurons and is used to classify the input based on the features extracted by the convolutional part.

Before a CNN can be used as a classifier, it has to be trained on data in a supervised learning

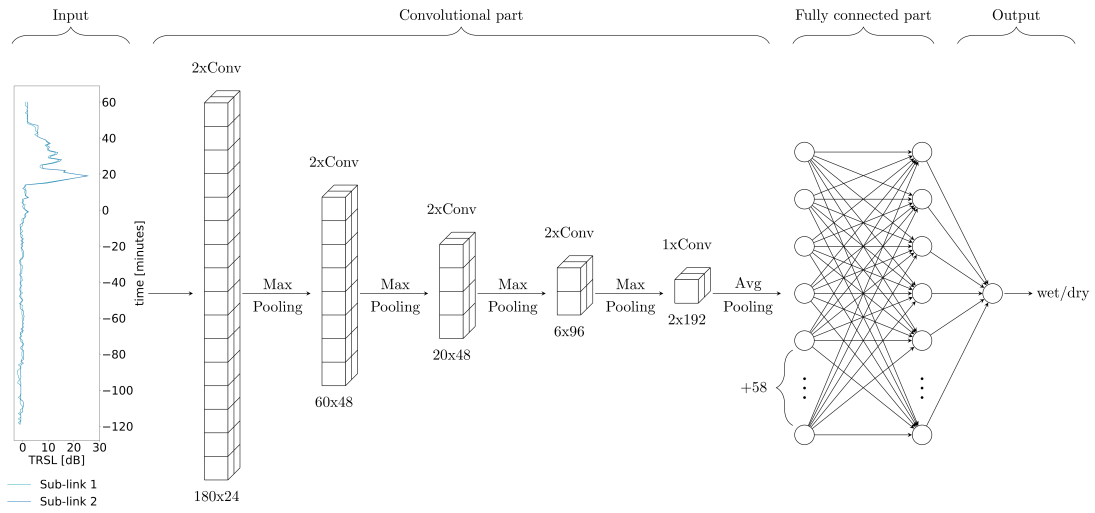

Figure 3.3: Graphical illustration of the CNNs architecture for $k = 120$. The Input shows one sample $\bar{X}_{t,i}$ of data consisting of 180 minutes of TRSL from the two sub-links of one CML. Convolutional and pooling layers reduce the input dimension from 180 to 2, while a total of 192 features are extracted. Numbers below convolutional layers are the layer output dimensions, i.e. input dimension times the number of filters. The size of the local patch in a convolutional layer is 3. Based on the extracted features, the fully connected layers predict a class, which is stored in the output layer.

process. All layers have a set of trainable parameters, so called weights, which are optimized during the training process according to a learning rule. To be able to monitor the model performance, a test data set is evaluated regularly during the training process. Training is stopped before the model starts to over-fit, i.e. the performance on the test data set either stagnates or drops, while it still rises for the training data.

3.2.3.1 Network architecture

We use a 1D-CNN, which has the same structure as the basic 2D-CNN, with alternating convolutional and pooling layers followed by fully connected layers. The only difference is that the input data of the convolutional layers is one dimensional. The specific architecture and parameterization was optimized experimentally. To give an intuitive description of our CNN, we follow the approach provided in (LeCun et al., 2015, p. 439):

The convolutional part of the CNN consists of four blocks of two convolutional layers followed by a max pooling layer and one block of one convolutional and one average pooling layer (see Fig. 3.3). Convolutional layers extract feature maps by passing local patches (3x1) of input from the preceding layer through a set of filters followed by a rectified linear unit. Each filter creates a different feature map. The pooling layer then combines semantically similar features by taking the maximum (resp. average) within one local patch. This way, the dimension of the input is

gradually reduced while, at the same time, the number of extracted features increases.

The fully connected part of the CNN consists of two layers with 64 neurons each and an output layer with one neuron. Its output is a prediction between zero and one, that can be interpreted as the likeliness for the input sample to be wet or dry. To avoid over-fitting to the training data two dropout layers are added, one after each fully connected layer, with a dropout ratio of 0.4 (Srivastava et al., 2014).

We implement the CNN in a Python framework using the Keras (version 2.3.1) backend for Tensorflow (version 2.1.0) (Chollet, 2022; Developers, 2022). For the model architecture, type, number and order of layers has to be chosen. There are several hyper-parameters that can be specified in the model setup. Each layer has a number of hyper-parameters that can be adjusted, e.g. the size of the local patch or the number of filters in a convolutional layer. We optimized all hyper-parameters iteratively by evaluating the performance of several reasonable configurations on the test data set VALAPRB, and by choosing the model with the best performance metrics (see 3.2.4). Depending on the length of the input time-series, which varies with k, the number of convolutional layers is different, i.e. $k < 60$ we omit the last two convolution layers. We trained one model for each value of k and one extra model, that additionally receives the CML meta-data consisting of the length and the frequency of both channels through parallel fully connected layers and an add-layer before the fully connected part. For k set to 120 minutes the final CNN consists of 20 functional layers with a total of 140,033 trainable parameters. The organization of those layers is shown in the network graph in Fig. 3.3. For all model versions, the detailed model and training specifications, all hyper parameters and the weights of the trained CNN can be retrieved from the code example at `https://github.com/jpolz/cnn_cml_wet-dry_example`.

3.2.3.2 Training setup

CNNs are feed-forward neural networks, which are trained by a supervised learning algorithm (Goodfellow et al., 2016). Batches of samples are passed through the network and the outputs are compared to the reference labels. After each batch a loss function is computed and the weights are updated according to a learning rule. Here, the learning rule is stochastic gradient descent with binary cross-entropy as a loss function and an initial learning rate of 0.008 (Bottou et al., 2018). The training data set TRG consists of 7 batches with 10^4 samples each and the validation data set is VALAPRB. One training epoch is finished when the whole data set is used once. After each epoch the training and validation data sets are evaluated to compute the training and validation loss and the learning rate is decreased slightly.

The training is stopped if the validation loss does not equal or surpass an earlier minimal value for 50 epochs (stopping criterion). Afterwards the model which achieves the best validation Matthews correlation (see MCC below) is selected from all versions, that existed after the individual training epochs (model selection criterion). This model is then used for classification on the validation data sets.

3.2.4 Validation

Our CNN is a probabilistic classifier. The raw model output $\bar{Y}_{t,i}$ is on a continuous scale from 0 to 1 (see Fig. 3.4), representing the estimated likeliness that a sample $\bar{X}_{t,i}$ is wet. A threshold $\tau \in [0,1]$ is then set to decide whether a sample is wet or not, leading to the prediction rule

$$\tilde{Y}_{t,i} = \begin{cases} 1, & \text{if } \bar{Y}_{t,i} > \tau \\ 0, & \text{otherwise} \end{cases} \tag{3.2}$$

Classification results, in the form of true positives (TP), false positives (FP), false negatives (FN) and true negatives (TN) are compared to the reference in a confusion matrix, shown in Table 3.B1, which is the basis for computing further metrics. The normalized version of the confusion matrix consists of the occurrence rates of TP, FP, FN and TN samples, defined as

$$TPR = \frac{TP}{TP + FN}, \tag{3.3}$$

$$FPR = \frac{FP}{FP + TN}, \tag{3.4}$$

$$FNR = \frac{FN}{TP + FN}, \tag{3.5}$$

and

$$TNR = \frac{TN}{FP + TN}. \tag{3.6}$$

As a first metric for validation we use the accuracy score, defined as

$$ACC = \frac{TP + TN}{\text{total population}} \in [0,1]. \tag{3.7}$$

It is a measure for the percentage of correct classifications being made. It is dependent on the class balance of the data set. The balance of wet and dry samples in the data set is directly related to the regional and seasonal climatology. Therefore, this metric is not climatologically independent. The second metric we use is the Matthews correlation coefficient (MCC), also known as ϕ-coefficient, which is a commonly used metric for binary classification (Baldi et al., 2000). It is acknowledging the possibly skewed ratio of the wet and dry periods and is high only if the classifier is performing good on both of those classes. It is defined as

$$MCC = \frac{TP \cdot TN - FP \cdot FN}{\sqrt{(TP + FP)(TP + FN)(TN + FP)(TN + FN)}} \in [-1,1], \tag{3.8}$$

where an MCC of 0 represents random guessing and an MCC of 1 represents a perfect classification. A strong correlation is given at values above 0.25 (Akoglu, 2018). The advantage of the MCC is, that it is a single number which we use to optimize the threshold for the CNN.

The third metric we use is the receiver operating characteristic (ROC), defined by the pair $(FPR, TPR) \in [0,1] \times [0,1]$ (Fawcett, 2006). The domain of the ROC is called ROC space. The point (0,1) represents a perfect classifier, while the [(0,0),(1,1)] diagonal represents random guessing. The ROC is independent of the ratio of wet and dry periods and therefore a climatologically independent measure for the classifier's performance on rain event detection. Each $\tau \in [0,1]$

leads to a ROC resulting in a ROC curve $\gamma \subset [0,1] \times [0,1]$ (e.g. Fig. 3.6). The performance of a classifier for different values of τ is measured by the area

$$AUC = \int_0^1 \gamma d\tau \in [0,1] \tag{3.9}$$

under the ROC curve. Since changing τ directly influences the prediction rule (Eq. 3.2), it can be adjusted causing the model to classify in a conservative (below [(0,1),(1,0)] diagonal in ROC space) or liberal (above diagonal) manner. We can therefore address the trade-off between true wet and true dry predictions as mentioned in the introduction. This way, the AUC becomes a measure of the flexibility of a classifier, i.e. the ability to show good performance with a more conservative or liberal threshold τ. The main purpose of the ROC is that we use it to compare different methods, e.g. different values of k, independent from a fixed threshold, by considering the ROC curve and the AUC.

3.2.5 Reference method

The reference method is a modification of Schleiss and Berne (2010) which is to date the most commonly used method to separate wet and dry periods as reviewed in the introduction. It is based on the following assumption: The standard deviation values of fixed-size windows of TRSL is bounded during dry periods, whereas it exceeds this boundary during wet periods and therefore allows for distinguishing the two classes. This assumption has proven to give good results on our data set, however there are known drawbacks. The method is limited to measuring the amount of signal fluctuations and there are multiple effects that can cause high signal fluctuations during dry periods, e.g. like for CML C in Fig. 3.1. Some of the factors are known, like multi-path propagation, but others are unknown and still need to be investigated.

The method is applied by computing a rolling standard deviation of the TRSL time-series. The normalization step is not necessary for this method. The window length is 60 minutes and the standard deviation value is written to the timestamp in the center of this window. A period $X_{t,i}$ is considered wet if at least one standard deviation value on one or both sub-links exceeds a threshold σ.

We compare two different thresholds σ, which are computed individually for each CML. The first one, denoted σ_{80}, is the 80th percentile of the 60-minute rolling standard deviation of one month for a certain CML multiplied by a scaling factor which is constant for all CMLs. In our case, the threshold is computed for VALAPR in April and VALSEP in September. The scaling factor of 1.12 is adopted from Graf et al. (2020a). The second one, denoted σ_{opt}, is optimized against the reference by maximizing the MCC. We computed it for April 2018 and then reapplied it to September 2018 to test its transferability to future time periods. To derive ROC curves, we applied a scaling factor τ_σ to each of the standard deviation thresholds. In the following we will refer to σ_{80} and σ_{opt} as both the resulting detection method and the threshold.

3.2.6 Rain rate estimation

In the same way as the rolling standard deviation, the CNN can be used in a rolling window approach, classifying the timestamp t as wet or dry by using the sample with starting timestamp $t - 30$ as model input. With the resulting rain event detection information from either the CNN or the two reference methods, rain rates are estimated in several steps. We use the exact same processing scheme as described in Graf et al. (2020a), which we refer the reader to for all the technical details. This processing includes erratic treatment of CMLs and WAA compensation to derive rain rates with a temporal resolution of one minute. For each detected rain event a constant baseline of the TRSL is calculated from the preceding dry period. The attenuation above this baseline level is attributed to rain but also to WAA. The WAA is compensated depending on the rain rate using a method modified after Leijnse et al. (2008). The remaining specific attenuation k is used to derive the path averaged rain rate R using the $k - R$ relation from Eq. 3.10. The constants a and b are taken from ITU-R (2005).

$$k = aR^b \tag{3.10}$$

For the CMLs used in this study this relation is close to linear, i.e. b is close to one. For a comparison to RADOLAN-RW the one minute rain rates are then aggregated by taking the hourly average.

Only from this analysis data from 45 CMLs (1.1 %) is discarded due to substantially erratic signal levels to be able to follow the same procedure as in Graf et al. (2020a). Additionally, we justify this procedure with the following observation: For the rain event detection we want periods of erratic behavior to be included in both training and validation data, since also CMLs that are not discarded by the erratic treatment can show periods of erratic behavior, such as CML C from Fig. 3.1. Each erratic training and validation sample contributes to the final statistics as one sample and the erratic CMLs do not distort the analysis. This is very different for the rainfall amount, since erratic links are prone to a very high overestimation of the final rain rates even when a low amount of time periods is detected wet. Since erratic CMLs are a small fraction of the available CMLs and they can be detected automatically, we decided to exclude their bias when analyzing the contribution of false positives to absolute rainfall amounts. An example of such a time series can be found in Fig. 3.A2.

3.3 Results

During training on TRG, the performance of the CNN was evaluated on VALAPRB after each epoch. The resulting graphs of loss, ACC, TPR and TNR during the training process are shown in Fig. 3.7. For all three variables the performance on TRG and VALAPRB were similar across all epochs with slightly higher performance on TRG. The threshold τ was optimized using VALAPR, by maximizing the MCC, with resulting values of τ shown in Tab. 3.B3. The results from that table and the ROC curves in Fig. 3.6 c) show that in general the performance of the CNN is increasing with higher values of k, but the performance gain was insignificant for raising the value higher than 120 minutes or adding meta data as model input. We therefore decided to set $k = 120$ and not to use added meta data for evaluating further results and comparing them to the reference

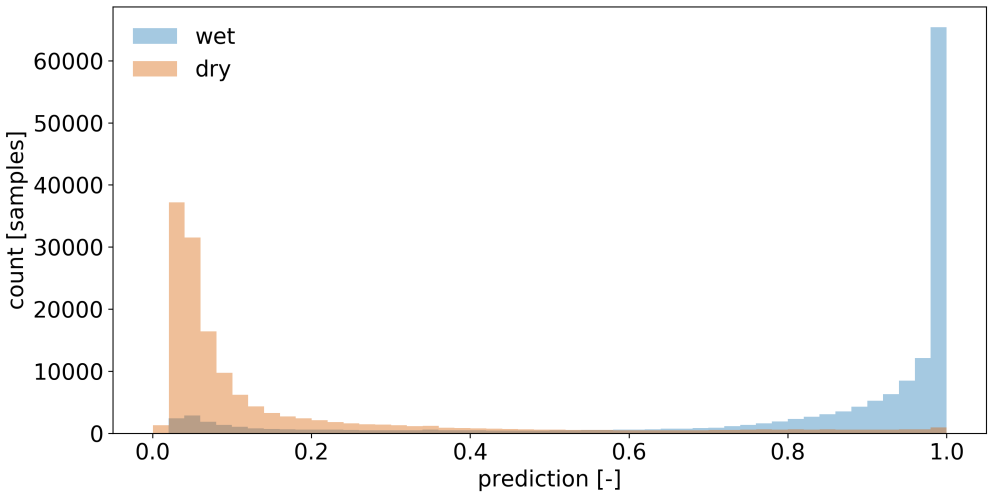

Figure 3.4: Raw CNN predictions on VALAPRB, coloured according to the reference.

methods.

Fig. 3.4 shows the distribution of the CNNs predictions on VALAPRB. The threshold τ is set to 0.82. The final number of training epochs was 248 and the model from epoch 212 was selected (see Fig. 3.7 (a)). On one Nvidia Titan Xp GPU the training time was 30 minutes. Classifying 3904 samples, i.e. a one minute time-step for all CMLs, took 20ms which can be considered extremely fast allowing for a real-time application of the method. For further verification, we repeated the training multiple times with a different randomization (selection of CMLs and balancing) of TRG and VALAPRB but no significant changes in performance could be observed.

We evaluated the performance of the CNN and both reference methods using the unbalanced data sets VALAPR and VALSEP. The complete list of the achieved performance metrics is presented in Table 3.B2. Applying the threshold τ to the CNN predictions yielded TPRs of 0.74 (VALAPR) and 0.77 (VALSEP) and TNRs of 0.97 (VALAPR and VALSEP) (see also Fig. 3.A1). On average, only 3% of the dry periods were falsely classified as wet and 24% of the wet periods were missed. With a scaling factor $\tau_{\sigma_{q80}}$ of 1.12, σ_{q80} achieved a balanced TPR and TNR with a value of around 0.79 for both rates in April and September. σ_{opt} on the other hand achieved similar TNRs than the CNN but at the cost of lower TPRs.

For both data sets, the CNN's ROC showed a higher TPR for any fixed FPR than the reference methods (see Fig. 3.6). As a consequence, the AUC was largest for the CNN. On VALAPR, σ_{opt} yielded a better ROC than σ_{q80}, but only for low FPR values. On VALSEP σ_{q80} achieved a better ROC than σ_{opt}. The ROC curves of the CNN and σ_{q80} had a very similar convex shape. Compared to the other two curves the ROC curve of σ_{opt} showed a higher asymmetry. The CNN

achieved the highest ACC and MCC scores with an average of 0.95 and 0.69 on both data sets. While σ_{opt} has the second highest ACC and MCC scores, the area below the ROC curve is lowest for both data sets.

We compare the ACC on detecting samples with a specific RADOLAN-RW rain rate of $x < R_{t,i} < x + 0.1$ in Fig. 3.5. From all rain events where $R_{t,i} \geq 0.6\ mm$ 90.4% were correctly detected by the CNN. On the other hand around 38.9% of all rain events with $R_{t,i} < 0.6\ mm$ were missed. All three methods have a lower ACC, the lower the rain rate is. While σ_{q80} shows an ACC for wet periods of different rain intensities, that is very similar to that of the CNN, σ_{opt} misses more small events. On the other hand σ_{q80} is producing more false wet classifications than the CNN or σ_{opt}.

The MCC was computed individually for each CML and each validation data set. Figure 3.8 shows scatter density plots comparing the individual MCC scores of the CNN and σ_{opt}. The CNN's MCC on VALAPR is higher for 95.9% of all CMLs and on VALSEP it is higher for 96.7% of all CMLs.

We focus our analysis on hourly rainfall rates from all non-erratic CMLs in September 2018. The resulting rain rates using either the CNN or the σ_{q80} detection scheme are shown in Fig. 3.9. For both methods the distribution of false positive and false negative samples is centered around 0.1 mmh^{-1} and the distribution of true positives is centered around 1 mmh^{-1}. While the percentage of CML derived rainfall estimated during false positive events is 29.9% for σ_{q80}, it is significantly less for the CNN (see Fig. 3.9 d) and f). This constitutes a reduction of 51% of falsely estimated rainfall for the month of September 2018. At the same time the amount of missed rainfall is reduced by 27.5%. The amount of rainfall in the true positive category could therefore be raised by 4.7%. The Pearson correlation for the hourly rainfall estimates between radar and CMLs is 0.83 using σ_{q80} and 0.84 using the CNN.

3.4 Discussion

3.4.1 Performance

We evaluate the performance of the CNN to detect rain events by two means. First, we compare it to the performance of a reference method. Second, we estimate if the model is performing in a near optimal state or if we expect that a higher performance could be achieved. The comparison to the results of previous studies, e.g. Overeem et al. (2016a), is difficult since the overall performance is depending on the distribution of the intensity of rain events (see Fig. 3.5) and since there is a large variability of performance between the CMLs (see Fig. 3.8).

Since the results on both validation data sets are very similar (see Table 3.B2) we further focus on VALSEP, which was not used to optimize the model hyper-parameters. With an ACC of 0.95 and an MCC of 0.69 the correlation between the CNN predictions and the reference data set RADOLAN-RW can be considered as very high. A TPR of 0.74 might not appear very good at

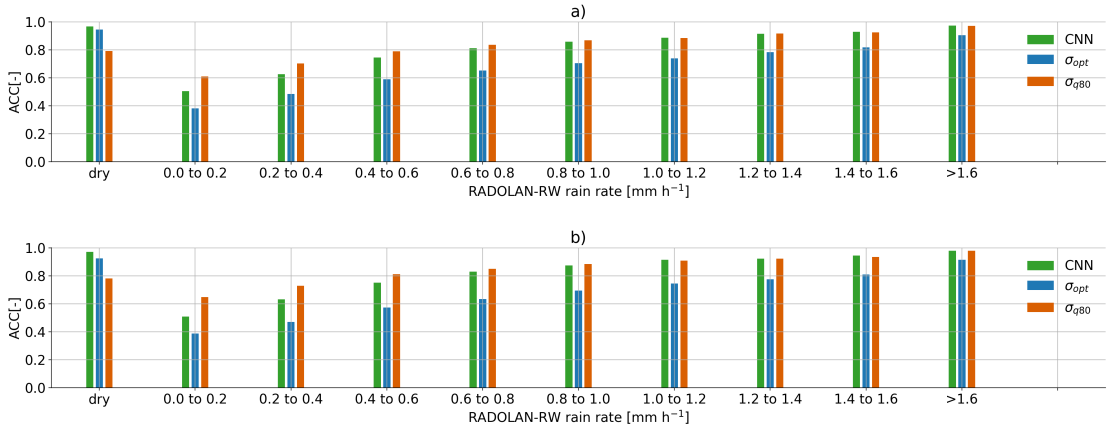

Figure 3.5: Each bar shows the ACC score on samples from a) VALAPR and b) VALSEP, grouped by the reference rain rate. An ACC of 0.5 represents random guessing.

first sight, but considering that the detection accuracy for samples with a rain rate of smaller than 0.6 mmh^{-1} is only 0.61, we actually achieve an accuracy of over 0.9 for all rain rates higher than 0.6 mmh^{-1}.

The CNN and the reference method σ_{opt} have a similar ACC value. At the same time the CNN's MCC is higher, despite the fact that σ_{opt} is MCC optimized for each CML. The high ACC of σ_{opt} is due to the high TNR and the fact that 95% of all samples are negative (dry). At a similar ACC and TNR we could increase the TPR, or rain event detection rate, by 0.13. This constitutes a major improvement by the CNN. As shown in Fig. 3.8 the improvement is higher for CMLs with lower MCC, making the whole CML data set more balanced in performance and therefore more trustworthy for quantitative precipitation estimation. The CNNs distribution of MCC values of individual CMLs is the same in April and September, while performance drops for σ_{opt}. The CNN's improvement in ACC and MCC over σ_{q80} was even higher with 0.17 and 0.32. While the TPR of σ_{q80} is slightly higher than the TPR of the CNN, the TNR is much lower for σ_{q80}. Thus the CNN shows substantial improvement in correctly classifying dry periods.

While the RSTD method can be set up to either have a high TPR (σ_{q80}) or a high TNR (σ_{opt}), the ROC curves show that CNN achieves both rates at the same time. Thus, the CNN shows a better overall performance than the reference methods and therefore improves on the trade-off as mentioned above. This observation is illustrated by the example in Fig. 3.2, which shows a very noisy CML time-series that produces a high amount of false positives for the reference method, while the CNN does not attribute these fluctuations to rainfall.

All three methods have limitations to detect events with rain rates smaller than 0.3mm. This is likely due to the detection limit of CMLs in our data set which is in the same range. The detection limit depends on frequency, length and signal quantization of a CML. For example, at a frequency

of <20 GHz and at a length of <10 km a path averaged rain rate of 1 mm h^{-1} creates a maximum of 1 dB of attenuation (Chwala and Kunstmann, 2019, Fig. 7). In some cases the quantization (0.3dB for RSL and 1dB for TSL) might therefore not allow for a detectable signal.

Differences in the performance on VALAPR and VALSEP can be traced back to a different distribution of occurring rain rates. While in April 35.5% of all events are in the critical range from 0.1mm to 0.3mm, there are only 32% in September. In both data sets the performance on higher rain rates (> 1.6 mm) and dry periods is almost identical. Therefore the loss of performance in April is due to the slightly worse performance of the CNN on smaller rain rates which occur more often in VALAPR than in VALSEP.

It should not be expected that the rain events detected through CMLs and the events detected by the radar coincide completely. Both methods produce artifacts that are mistaken as rainfall, or they miss events due to their detection limits. From all false classifications that the CNN makes on VALSEP there are 50% with a raw model output between 0.2 and 0.8. Here the CNN does not give a certain prediction. This is due to very similar signal patterns in noisy dry periods and small rain rates. The other 50% of those samples are, according to the CNN, very likely to belong to the falsely predicted class. Despite this being an issue for many CMLs about 10% have a ROC of $(> 0.97, < 0.1)$ and correlate very well with the RADOLAN reference. Therefore, we expect that less errors could be made when training with a perfect reference data set, but there would still be errors due to artifacts or insensitivity in CML measurements.

Despite those errors, which occur mostly for small rain rates, the correlation of wet and dry periods between RADOLAN-RW and our CML data set is very high. The performance boost in rain event detection gained through the CNN is very promising for future applications in quantitative precipitation estimation with CMLs.

3.4.2 Robustness

The CNNs ability to generalize to previously unknown CMLs is very high. As seen in the training results the learning curves for both training and validation show a similar dynamic (see Fig. 3.7). As expected the training data showed better performance, but the validation was close at all epochs.

Only 20% of all available CMLs were used for training. The remaining 80% were only used to prevent the model from over-fitting to the training data, to choose the model architecture and to optimize the single parameter τ. Thus no information about the validation data was given directly to the model. The resulting model architecture and hyper-parameters are not specific enough to store this information. The high performance in ACC, MCC and ROC on data set VALAPR, together with the learning curves in Fig. 3.7), therefore prove that the CNN was able to recognize the attenuation pattern in the signal levels of a large number of previously unknown CMLs.

The stability of the CNNs performance for future time periods is analyzed using the results on

VALSEP. While the training was done with TRG including the period of May to August 2018, the performance in September was similar. Compared to the results on VALAPR the CNN shows even higher performance on VALSEP, which can be explained by the lower percentage of samples with small rain rates in September, which are challenging to classify (see Fig. 3.5 a)). When we compare the CNNs accuracy per rain rate between VALAPR and VALSEP, we see that there are no major differences in the individual scores. Therefore the method can be considered as very stable throughout the analyzed time period, while differences in overall performance mostly stem from different distributions of the occurring rain rates. The reference method σ_{opt}, which was optimized in April, loses performance in September, where it is outperformed by the adaptive method σ_{q80}. The bootstrapping in Fig. 3.6 shows that all three methods perform almost equally well on small random subsets of the validation data. The CNN shows the lowest variability.

As a measure for the flexibility of a classifier we adopted the ROC analysis in Sect. 3.2.4. A model is called flexible if it has a high area below its ROC curve and if the curve is axis-symmetric with respect to the [(0,1),(1,0)] diagonal of the ROC space. As observed both the CNN and σ_{q80} show a symmetrical ROC curve. Therefore they perform almost equally well with a liberal or conservative threshold with a slight tendency to the conservative side. On the other hand σ_{opt} shows a skewed performance, with a strong tendency to the conservative side. The area AUC below the ROC curve was highest for the CNN, making it the most flexible classifier. We can adjust τ for a ROC of either $(0.03, 0.7)$ or $(0.3, 0.94)$ and a smooth, concave transition in between (see Fig. 3.6).

We conclude that within the analyzed period the CNN shows a temporally stable performance, with a good generalization to previously unknown CMLs. The σ_{opt} method performs well only if it is re-calibrated for different months and to individual CMLs, while σ_{q80} is by definition an adaptive method. Even with re-calibration or adaption, the reference methods are outperformed by the CNN.

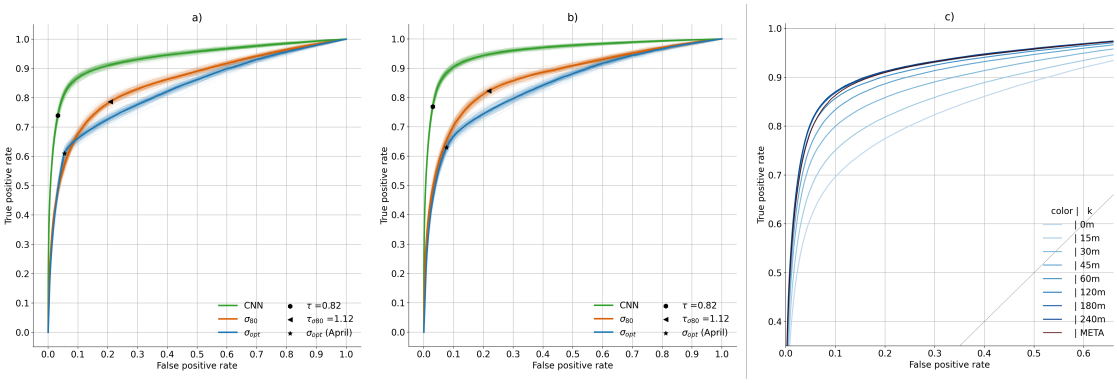

Figure 3.6: Receiver Operating Characteristic curves on VALAPR a) and VALSEP b). Fine lines are generated by 200 random selections (bootstrapping) of 1% of the samples and account for the variability of the model performance during a random short period ($\sim$ eight hours) of data. The performances of the CNN for different values of k and the added meta data are shown in c) and the AUC values are given in Table 3.B3

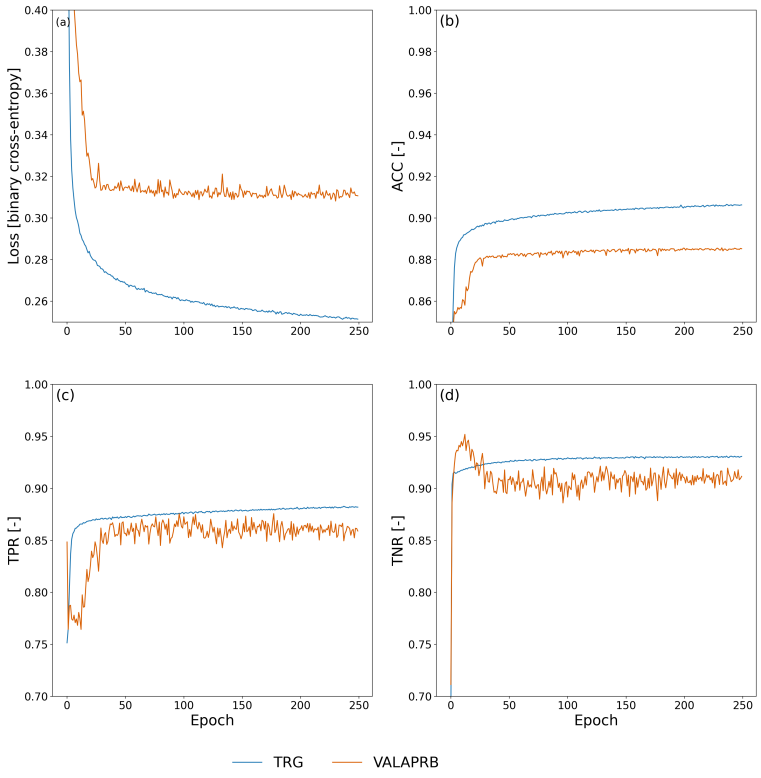

Figure 3.7: Statistics of variables that were monitored during the training process.

3.4.3 Impact of the detection scheme on the derived rainfall amounts

The difference between the scatter density plots in Fig. 3.9 a) and b) seems to be quite low at first sight. What this representation of the data is not stressing enough is the amount of rainfall generated by false positives. But they are an issue that is clearly visible from Fig. 3.9 c)-h). Considering that the amount of rainfall estimated during time periods falsely classified as wet can be reduced by 51.0% and that the amount of rainfall from missed events can be reduced by 27.4%, the CNN shows a major improvement over the reference method. The 4.1% of additional rainfall in the correctly classified wet periods stem from time periods that were originally harder to classify, i.e. from small rain events, and it should be expected, that the correlation between CML and radar rainfall drops. Instead, the Pearson correlation coefficient increased slightly showing that the quality of the estimated hourly rainfall could be improved. We omitted the same analysis for a comparison of the CNN and σ_{opt} for which, based on the ROC values in Fig 3.6, we anticipate a similar result, but with a higher pronunciation of missed rain events instead of the strong impact of false positives.

Overall, we could observe that the improvement in rain event detection has a considerable effect

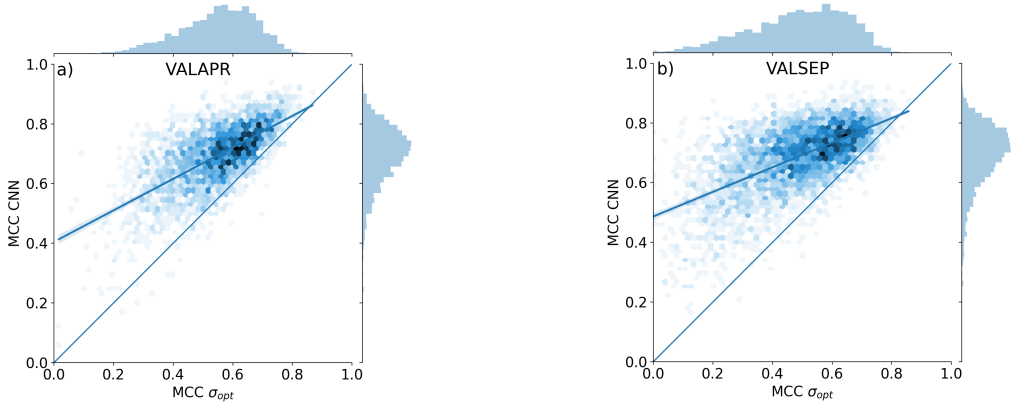

Figure 3.8: Scatter density plots of the MCC achieved by the CNN and σ_{opt} on data from individual CMLs. Both methods are MCC optimized for the unbalanced data from VALAPR, while the CNN keeps the optimized performance in September, the performance of σ_{opt} drops.

on the amount of over- or under estimation through falsely detected or missed rain events. The improvement on the trade-off between false positives and false negatives directly translates to the impact of their respective rainfall amounts. This is shown by the false positive and false negative distributions in Fig. 3.9 c)-f) which are centered around the same value, but are different in their amount depending on the used detection method.

3.5 Conclusion

In this study, we explore the performance and robustness of 1D-CNNs for rain event detection in CML attenuation time-series using a large and diverse data set, acquired from 3904 CMLs distributed over entire Germany. We prove that, compared to a reference method, we can minimize the trade-off between false wet and missed wet predictions. While the reference method needs to be adjusted for different months of the analyzed period to provide optimal results, the trained CNN generalizes very well to CMLs and time periods not included in the training data. On average, 76% of all wet and 97% of all dry periods were detected by the CNN. For rain rates higher than 0.6 mmh^{-1} more than 90% were correctly detected. This underlines the strong agreement between rain events that can be detected in the CML time-series and rain events in the RADOLAN-RW data set.

In future work, we plan to investigate the potential of using reference data with higher temporal resolution to improve the temporal localization of the rain events. Data with higher temporal resolution will, however, magnify the uncertainties that arise due to the different spatial and temporal coverage of the different rainfall observation techniques. In order to address these uncertainties, it will be important to further explore the relationship between weather radar and CML derived rainfall products. In the study presented here, we focused on the optimization of rain

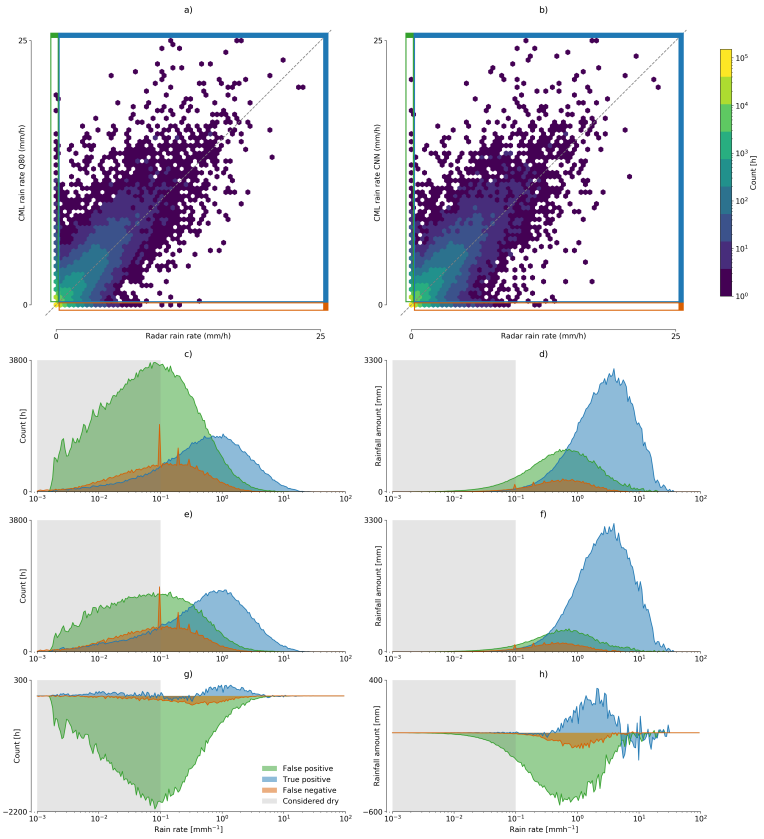

Figure 3.9: Scatter density comparison between hourly CML and radar rain rate estimates derived from a) σ_{q80} and b) the CNN. On the left hand side the amount of FP, TP and FN hours with a specific rain rate are compared for c) σ_{q80}, e) the CNN and g) their difference). On the right hand side the amount of rainfall these hours contribute are shown for d) σ_{q80}, f) the CNN and h) their difference. The rain rates for false positives and true positives are estimated by the CML, while the rain rates for false negatives are taken from the reference.

event detection as an isolated processing step, which provides the basis for a successful rain rate estimation. All subsequent processing steps, including WAA correction, k-R relation and spatial interpolation, have an effect on the CML derived rain rate, that can also lead to over or under-estimation. While 29.9% of the estimated rainfall through the reference method can be attributed to false positive classifications, the CNN reduces this amount by up to 51% and, at the same time, improves on true positive and false negatives. We anticipate, that this improvement will lead to new insights into other effects that may disturb the quality of this opportunistic sensing approach.

Our study shows that using data driven methods like CNNs in combination with the good coverage of the highly developed weather radar network in Germany can lead to robust CML data processing. We anticipate that this robustness enhances the chance that we can transfer processing methods to data from other CML networks, particularly in developing countries like Burkina Faso, where rainfall information is still scarce despite its high importance to the local population (Gosset et al., 2016).

Code availability

Interactive code to build the CNN and an example evaluation using the trained CNN are available at `https://github.com/jpolz/cnn_cml_wet-dry_example`. CML data was provided by Ericsson Germany and is not publicly available in its full extent. RADOLAN-RW is publicly available through the Climate Data Center of the German Weather Service (DWD) `https://opendata.dwd.de/climate_environment/CDC/grids_germany/hourly/radolan/`. We include a small example data set with modified CML locations, the trained model weights and the preprocessed RADOLAN-RW reference data together with the interactive code at `https://github.com/jpolz/cnn_cml_wet-dry_example`.

Acknowledgements

We thank Ericsson, especially Reinhard Gerigk, Michael Wahl and Declan Forde for their support and cooperation in the acquisition of the CML data. This work was funded by the German research foundation within the RealPEP research group. Furthermore, we like to thank the German Research Foundation for funding the project IMAP, the Helmholtz Association of German Research Centres for funding the project Digital Earth and the Bundesministerium für Bildung und Forschung for funding the project HoWa-innovativ. Special thanks are given to Bumsuk Seo for his valuable advice and for providing the Titan Xp GPU used for this research, which was donated by the NVIDIA Corporation.

Appendix A: Additional Figures

Fig. 3.A1; Fig. 3.A2

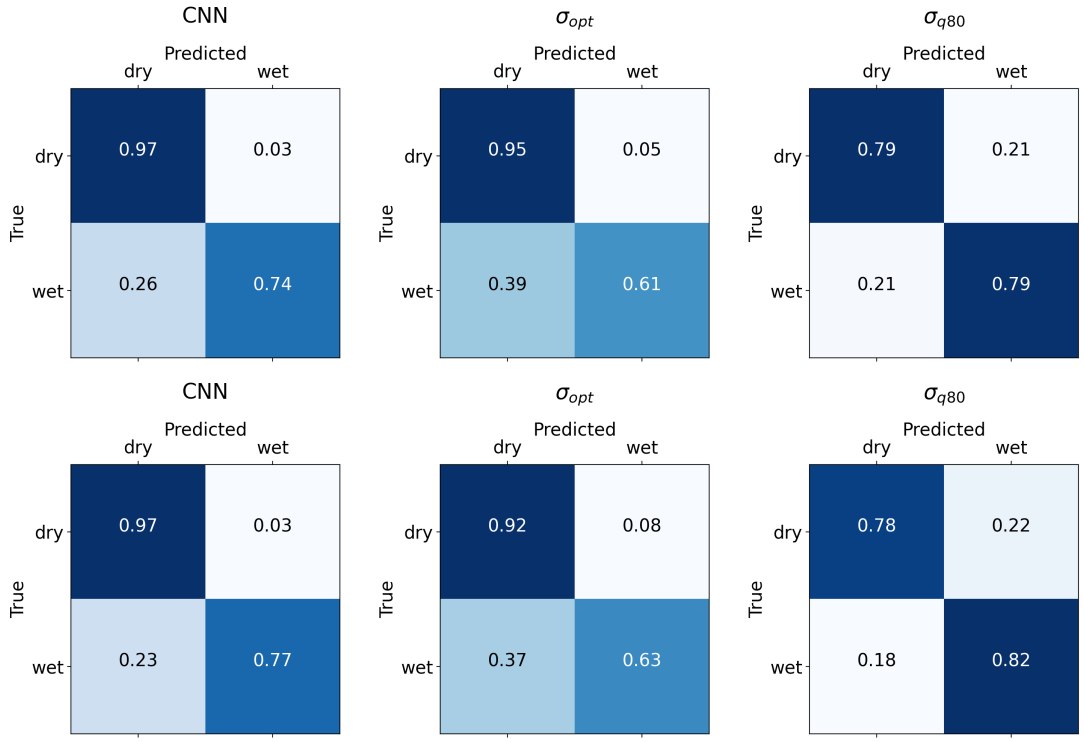

Figure 3.A1: Normalized confusion matrices of VALAPR (top) and VALSEP (bottom).

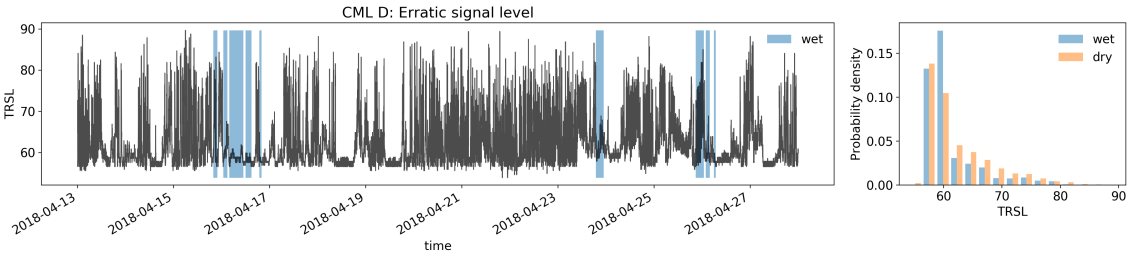

Figure 3.A2: Time series of a CML that is considered as erratic and is removed by the simple filter for erratic CML data introduced in Graf et al. (2020a). There are no time periods, where a reasonable rainfall estimation would be possible.

Appendix B: Additional Table

Table 3.B1: Confusion matrix

		reference *wet*	**reference** *dry*
prediction	*wet*	True wet (TP): #{ detected wet| reference wet}	False wet (FP): #{ detected wet| reference dry}
	dry	Missed wet (FN): #{ detected dry| reference wet}	True dry (TN): #{ detected dry| reference dry}

Table 3.B2: Performance metrics of rain event detection methods on VALAPR and VALSEP

	Method	TPR	TNR	ACC	MCC	AUC
VALAPR	CNN	0.74	**0.97**	**0.95**	**0.69**	**0.94**
	σ_{q80}	**0.79**	0.79	0.79	0.38	0.85
	σ_{opt}	0.61	0.95	0.91	0.52	0.83
VALSEP	CNN	0.77	**0.97**	**0.96**	**0.69**	**0.96**
	σ_{q80}	**0.82**	0.78	0.78	0.35	0.87
	σ_{opt}	0.63	0.92	0.90	0.44	0.84

Table 3.B3: Number of training epochs, MCC optimized threshold and resulting metrics for different values of k, evaluated on VALAPR.

Method	k	Training epochs	Threshold τ	TPR	TNR	ACC	MCC	AUC
CNN	0	269	0.77	0.53	0.97	0.93	0.55	0.86
	15	158	0.78	0.59	0.97	0.94	0.60	0.88
	30	274	0.79	0.64	0.97	0.94	0.64	0.91
	45	271	0.79	0.67	0.97	0.94	0.66	0.92
	60	128	0.84	0.71	0.97	0.95	0.68	0.93
	120	212	0.85	0.72	0.97	0.95	0.69	0.94
	180	211	0.86	0.72	0.97	0.95	0.69	0.94
	240	170	0.84	0.73	0.97	0.95	0.69	0.94
CNN+Meta	180	321	0.79	0.70	0.97	0.95	0.68	0.93
σ_{q80}	-	-	-	0.79	0.79	0.79	0.38	0.85
σ_{opt}	-	-	-	0.61	0.95	0.91	0.51	0.83

Chapter 4

Missing rainfall extremes in commercial microwave link data due to total loss of signal (Polz et al., 2023b)

Polz, J., Graf, M. (shared first authorship), Chwala, C.: Missing rainfall extremes in commercial microwave link data due to total loss of signal, *ESS*, 10(2), e2022EA002456. https://doi.org/10.1029/2022EA002456, 2023

Abstract

An important aspect of rainfall estimation is to accurately capture extreme events. Commercial microwave links (CMLs) can complement weather radar and rain gauge data by estimating path-averaged rainfall intensities near ground. Our aim with this paper was to investigate attenuation induced total loss of signal (blackout) in the CML data. This effect can occur during heavy rain events and leads to missing extreme values. We analyzed three years of attenuation data from 4000 CMLs in Germany and compared it to a weather radar derived attenuation climatology covering 20 years. We observed that the average CML experiences 8.5 times more blackouts than we would have expected from the radar derived climatology. Blackouts did occur more often for longer CMLs (e.g. $>$ 10 km) despite their increased dynamic range. Therefore, both the hydrometeorological community and network providers can consider our analysis to develop mitigation measures.

Plain Language Summary

Commercial microwave links (CMLs) are used to transmit information between towers of cellphone networks. If there is rainfall along the transmission path, the signal level is attenuated. By comparing the transmitted and received signal levels, the average rainfall intensity along the path can be estimated. If the attenuation is too strong, no signal is received, no information can be transmitted and no rainfall estimate is available. This is unfavorable both for network stability

and rainfall estimation. In this study, we investigated the frequency of such blackouts in Germany. How many blackouts per year are observed in a three year CML dataset covering around 4000 link paths and how many are expected from 20 years of weather radar data? We observed that the average CML experiences 8.5 times more blackouts than we would have expected from the radar derived climatology. Blackouts did occur more often for long CMLs, which was an unexpected finding. While only one percent of the annual rainfall amount is missed during blackouts, the probability that a blackout occurs was very high for high rain rates. Both, the hydrometeorological community and network providers can consider our analysis to develop mitigation measures.

4.1 Introduction

Microwave radiation is attenuated by hydrometeors through scattering and absorption processes. For raindrops an advantageous relationship between specific attenuation k in dB/km and rainfall rate R in mm h^{-1} exists. This power law known as the k-R relation is close to linear at frequencies between 20 and 35 GHz (Chwala and Kunstmann, 2019). Commercial microwave links (CMLs) use frequencies from 7 to 80 GHz and thus can be used to derive path averaged rainfall intensities by comparing transmitted and received signal levels (TSL and RSL) (Uijlenhoet et al., 2018). In theory, the k-R relation is valid for arbitrary rainfall intensities occurring in the underlying drop size distribution simulations. In practice, the measurement of high attenuation values at a given transmitted signal level has an upper bound when the signal cannot be distinguished from the receiver's background noise.

CML rainfall estimates were derived for many countries around the globe, e.g. the Netherlands (Overeem et al., 2016b), Sri Lanka (Overeem et al., 2021), Burkina Faso (Doumounia et al., 2014) and Germany (Graf et al., 2020a). CML-derived rainfall information can be used for applications like streamflow prediction, urban drainage modeling, agricultural purposes and rainfall nowcasting (Fencl et al., 2013; Brauer et al., 2016; Stransky et al., 2018; Imhoff et al., 2020). Especially for flash flood prediction, precise precipitation maxima are of great importance (Cristiano et al., 2017). While rainfall estimates from weather radars are known to underestimate high intensities (Schleiss et al., 2020), rain gauges lack spatial representativeness (Sevruk, 2006). CMLs can fill this information gap by estimating path averaged intensities at path lengths of a few kilometres.

Recent studies on the quality of CML rainfall estimates suggest a good agreement with radar and rain gauge estimates (Graf et al., 2021b; Overeem et al., 2021). However, missing periods in the signal level time series might be excluded e.g. when comparing CML time series against a path-averaged radar reference or rain gauges. Such periods can occur due to hardware failure, maintenance or outages in the data acquisition. Additionally, network providers usually design the hardware in such a way that transmission outages due to high attenuation (blackouts) are allowed to occur for a certain amount of time per year. The International Telecommunication Union (ITU) recommends a minimum availability of 99.99% which would allow up to 52 minutes of total loss of signal per year (ITU-R, 2017).

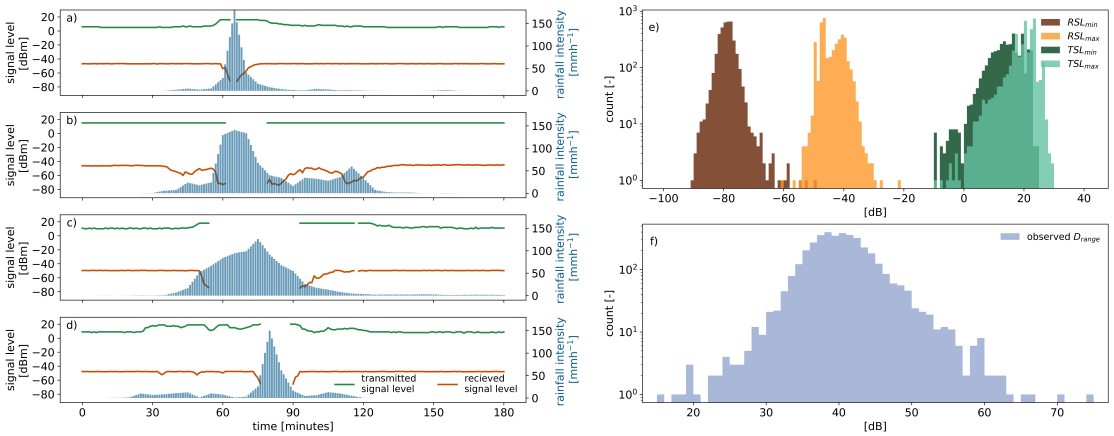

Figure 4.1: a)-d) show TSL and RSL time series during blackout gaps from four CMLs. Rainfall intensities are derived from RADKLIM-YW along the CML's paths. e) gives the minimal and maximal TSL and RSL values of all 3904 CMLs for the analysed period of three years. f) shows the distribution of the dynamic range directly calculated from CML signal levels with Equation 4.1.

Rainfall is the prevalent reason for CML signal attenuation. Hence, the amount of missing data is in a close relationship with the local rainfall climatology. Because of blackouts rainfall estimates from CMLs miss peak intensities, an error which propagates to further applications. Figure 4.1 shows examples of such blackouts in CML attenuation time series and the rainfall intensity according to a weather radar reference. To date, it is unclear to what extent rain events are missed due to blackouts.

Our aim is to answer two questions related to CML blackouts using a country-wide CML network in Germany. The first question is how many blackouts each CML is experiencing in practice and how this affects rainfall estimates. The second question is how much blackout time is expected considering 20 years of high-resolution weather radar rainfall climatology and how this expectation compares to the results derived from the CML data.

4.2 Data and Methods

Our analysis was based on observed blackouts within CML data collected in Germany and a comparison to the expected frequency derived from weather radar climatology (Sec. 4.2.1). We detected gaps in CML data that are assumed to be caused by attenuation (Sec. 4.2.2) and derived path integrated attenuation values from path averaged weather radar rain rates (Sec. 4.2.3). Note that all calculations were repeated for each CML individually.

4.2.1 Data

CML data has been collected in cooperation with Ericsson Germany. The data acquisition system described by (Chwala et al., 2016) has been used to record three years of instantaneously measured RSL and TSL of 3904 CMLs distributed over Germany (2018 to 2020). The temporal resolution is one minute and the power resolution is 0.3 or 0.4 dBm for RSL and 1 dBm for TSL. 25% of the CMLs have a constant TSL value (e.g. Figure 4.1b). The other 75% use an automatic transmit power control (ATPC), which can increase TSL if RSL decreases due to attenuation (e.g. Figure 4.1a,c,d). The CML path lengths range from 0.1 to 30 kilometers with frequencies from 7 to 40 GHz as shown in Figure 4.2d). In the context of rainfall estimation, CMLs are characterized by two main features. First, the signal level sensitivity to rainfall, see e.g. Fig. 7 in Chwala and Kunstmann (2019), which depends on the frequency, polarization and path length. Second, the dynamic range of the signal level D_{range}, i.e. the difference between clear sky attenuation and maximum measurable attenuation. The communication along a CML requires (de-)modulation of information onto the carrier frequency. Different modulation schemes are used. In case of increased attenuation along their path, the CMLs switch to more simple modulation. This decreases the usable bandwidth but increases the robustness against transmission errors stemming from the lower signal-to-noise ratio during attenuation events (Bao et al., 2015). If the RSL is too low, i.e. close to the noise floor of the receiver, the error rate for demodulation becomes too large and communication is cut off. Datasheets of CML hardware (e.g. from Ericsson (2012)) guarantee a certain error rate at defined low RSL values rather than a fixed lower RSL limit where this cutoff happens. Therefore, we need to estimate the empirical D_{range} of each CML as

$$D_{range} = TSL_{max} - RSL_{min} - TSL_{min} + RSL_{max}. \tag{4.1}$$

We removed TSL and RSL outliers outside the intervals [-20 dBm, 50 dBm] and [-99 dBm, 0 dBm] respectively. TSL_{max} and RSL_{min} were the highest (lowest) values which occurred during heavy attenuation events representing the strongest observed attenuation event for each single CML (see Fig 4.1a)- d) as examples). Contrarily, we can assume that TSL_{min} and RSL_{max} are occurring frequently during clear sky conditions. To account for individual outliers we removed values for TSL_{min} and RSL_{max} when they occurred less often than approximately one hour in total during the three years, i.e. using the 99.995% quantile. Without this filter D_{range} would be overestimated for about half of all CMLs because there are individual rarely occurring high RSL_{max} or low TSL_{min} values.

With the potentially abrupt onset of heavy rainfall causing a complete loss of signal, RSL_{min} may have been undersampled by the 1-minute instantaneous data sampling. Therefore, the derived D_{range} can be assumed to be the minimal dynamic range a CML has.

As reference we used RADKLIM-YW (Winterrath et al., 2018) from the German Meteorological Service (DWD) which we linearly interpolated from a 5- to a 1-minute resolution to match the CML resolution. RADKLIM-YW is a gauge-adjusted, climatologically corrected radar product with a temporal resolution of five minutes and a spatial resolution of 1 km. The underlying radar precipitation scans have been carried out every five minutes. Therefore, the radar rainfall

intensities can be considered to be instantaneous measurements without temporal averaging. The product is composed of 17 weather radars and adjusted by more than 1000 rain gauges with additive and multiplicative corrections. The climatological correction accounts for range-dependent underestimation and radar spokes caused by beam blockage, among others. RADKLIM-YW was considered the best and highest resolved rainfall reference for this analysis and was available from 2001 to 2020. Following Graf et al. (2020a) we derived the path averaged rain rate R for each CML as the sum of radar grid cell rainfall intensities r_i weighted by their lengths of intersection l_i with a given CML path of total length L as described by Eq. 4.2.

$$R = \frac{1}{L} \sum_i r_i l_i \tag{4.2}$$

To be able to investigate a potential temperature dependence of observed blackouts we used the 2 meter temperature from the ERA5 analysis dataset provided by the European Centre for Medium-Range Weather Forecasts Muñoz-Sabater et al. (2021). The temporal resolution is instantaneous at a one hour frequency and the spatial resolution is 9 kilometers. Similar to Eq. 4.2 an average along the CML path was computed by a weighted sum of ERA5-land grid cells intersected by the CML path.

4.2.2 Detecting blackouts in CML data

Gaps in CML signal level time series can have various causes. In this analysis we were interested in gaps caused by strong attenuation during heavy rainfall and therefore excluded periods which could be attributed to one of the following causes. Gaps longer than 24 hours were assumed not to be caused by heavy rain events. When more than 400 CMLs exhibited a gap at the same time, we excluded this time step. The reasoning behind this value is that we assumed a partial or complete outage of our data acquisition system which polls the data in several batches of 400 to 500 CMLs every minute. Gaps occurring during a period where a seven-day rolling mean of the RSL was below -60 dBm were removed. This was done, because we can assume that there is a long-term transmission disturbance, i.e. partial beam blockage due to a growing tree or due to ice cover on the antenna during consecutive winter days with temperatures below freezing point, since none of the CMLs in our dataset has a 3-year median RSL below -60 dBm. That is, all our CMLs have their long-term baseline RSL level during clear sky conditions above -60 dBm. Around 0.2% of all RSL values are removed from the analysis by filtering data acquisition gaps and long term transmission disturbances.

The actual detection of blackout gaps is done with the remaining CML data based on the following rule. A gap is defined as a blackout gap if either the last valid RSL before, the first valid RSL after this gap, or both values were below -65 dBm. Examples of such automatically detected gaps are shown in Figure 4.1a-d). The median RSL levels within our dataset are well above -65 dBm. Therefore, we chose this threshold to select only events with attenuation typical of heavy rain events. The thresholds we chose for filtering the data and detecting the blackout gaps proved to be robust when applied to our dataset where the CML hardware and data acquisition

are homogeneous Chwala et al. (2016). However, they might need adjustment if our method is applied for CML datasets with different characteristics.
We grouped observed blackouts into reference rainfall intensity bins and computed the average amount of observed blackout minutes n_{obs} per year for each CML. In addition, n_{obs} was normalized by applying the factor

$$f_{avail} = \frac{\#\{\ minutes\ in\ observation\ period\}}{\#\{\ minutes\ with\ valid\ observations\}} \tag{4.3}$$

for each CML to account for missing time steps in the CML data.

4.2.3 Deriving a blackout climatology from radar data

In theory, a blackout due to heavy rainfall should be expected whenever the path integrated attenuation (PIA) exceeds the CML's dynamic range D_{range}. We estimated a blackout climatology using 20 years of instantaneous radar measurements. A radar derived PIA was calculated by individually applying the k-R relation to the rain rate r_i of the i-th radar grid cell intersected by a CML path. This procedure was chosen over applying the k-R relation to the path averaged rain rate to minimize errors due to the spatial variability of rainfall along the path as explored by Berne and Uijlenhoet (2007). Hence, we calculated

$$PIA = \frac{1}{L} \sum_i a r_i^b l_i + w_{aa} \tag{4.4}$$

using coefficients a and b, derived from the ITU recommendation ITU-R (2005), which depend on the CMLs frequency and polarization. The intersection length of CML path and radar grid cell i is denoted l_i. Additionally, a constant w_{aa} =3 dB accounting for the wet antenna attenuation (WAA) caused by rain drops on the cover of the CML antennas was added (van Leth et al., 2018). We chose a value similar to Leijnse et al. (2008); Schleiss et al. (2013). We assumed a high constant value which is reasonable for peak rainfall intensities. Whenever PIA was larger than D_{range}, the CML was expected to show a blackout gap. Thus, we derived the cumulative number of expected blackout minutes $n_{exp}(D_{range})$ as the average number of timestamps per year where PIA> D_{range} multiplied by five due to the radar's instantaneous sampling rate of five minutes. We applied Eq. 4.3 to n_{exp} according to the radar availability along CML paths. Due to RSL_{min} undersampling, D_{range} might be higher in reality than estimated. In turn, n_{exp} should be lower than estimated, i.e. we would expect n_{obs} to be smaller than n_{exp}.

4.3 Results

4.3.1 CML signal levels and dynamic ranges

The distribution of TSL_{min} and TSL_{max} is defined by hardware configuration. The distribution of RSL_{min} and RSL_{max} depends on TSL, path length and path loss. The spread of observed RSL_{max} is lower than the spread of observed RSL_{min}. The distribution of the dynamic range estimate is shown in Figure 4.1f). The observed D_{range} was on average 40.5 dB with a minimum of 15.2 dB and a maximum of 74.3 dB.

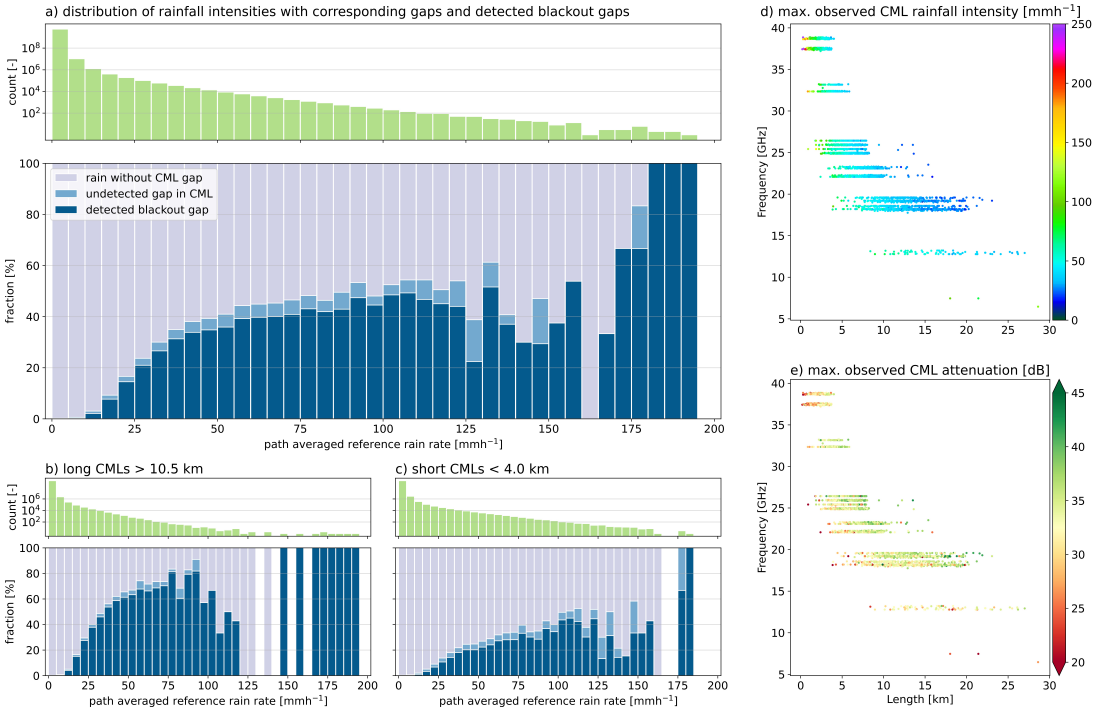

Figure 4.2: a) shows the distribution of the reference rainfall intensities in green. For each bin the fraction of gaps in the CMLs *RSL* time series and the fraction of the detected blackout gaps are shown in light and dark blue. b) and c) show the same for the longest ($>$ 10.5 km) and shortest ($<$ 4.0 km) quartile of all CMLs, respectively. Note that gaps that were attributed to, e.g. failure of the data acquisition, have been removed as described in Sec. 2.1 for a), b) and c). d) shows the maximal rainfall intensity derived from the CMLs estimated with the rainfall retrieval methodology from Graf et al. (2020a) and Polz et al. (2020). e) shows the respective maximal attenuation observed at each CML during the analysed three years.

4.3.2 Observed CML blackout gaps

Figure 4.2a) shows a histogram of path-averaged radar rainfall intensities. The higher the path-averaged rainfall intensity the less frequently it occurred. For each bin the fraction of CML data gaps which were detected as blackout gaps are shown (dark blue). In addition, the fraction of all gaps that have not been detected as blackout are shown (light blue). Note that gaps that were attributed to, e.g. failure of the data acquisition, have been removed as described in Sec. 4.2.1. The fraction of gaps is increasing quickly until 50 $\mathrm{mm\,h^{-1}}$ and then less steep up to 125 $\mathrm{mm\,h^{-1}}$. For very high intensities above 125 $\mathrm{mm\,h^{-1}}$ the sample size was less than 50 minutes per bin. Therefore, the fraction of all gaps, including detected blackout gaps, was becoming sensitive to the occurrence of individual events and hence the statistics were less robust. Overall, around 95% of the gaps during rainfall in the radar reference were detected as blackout gaps. This fraction varied for the highest observed rainfall intensities due to the small sample size. Based on the statistics from Figure 4.2a), CMLs missed on average 1% of the yearly rainfall sum during blackout gaps.

The quartile of long CMLs, i.e. longer than 10.5 km, in 4.2b) showed a higher fraction of (blackout) gaps. Additionally, path-averaged rainfall intensities are lower on average as longer paths average out peak intensities. The quartile of short CMLs , i.e. shorter than 4.0 km, shows fewer (blackout) gaps and higher rainfall intensities. This pattern is also visible in 4.2d) and e) where the maximum instantaneous rainfall intensity and attenuation from each CMLs observations are shown. While the maximum attenuation increased with length, the maximum observed path-averaged rainfall intensity decreased. The maximum observed rainfall intensity from CMLs with 600 $\mathrm{mm\,h^{-1}}$ (and several events above 250 $\mathrm{mm\,h^{-1}}$ all beyond the figures colorscale) is well above the maximum intensity of the path averaged reference product. Overall, shorter CMLs show fewer blackouts during heavy rainfall.

4.3.3 Expected blackout gaps derived from radar based attenuation climatology

Expected PIA values along each CML path were derived using Equation 4.4 and 20 years of RADKLIM-YW data. Figure 4.3 shows path-averaged rain rate and PIA percentiles of the full 20-year dataset corresponding to the highest 60, five or one minutes per year and the 20-year maximum for individual CMLs (i.e. 60 minutes per year corresponds to the highest 0.011415526 percent in the data). The expected PIA was increasing with CML length, while the path averaged rain rate was decreasing. The five-minute PIA exceedance level (see Figure 4.3 second column) was between 10 dB (1st percentile), occurring mostly for shorter CMLs, and 53 dB (99th percentile), occurring mostly for longer CMLs. On average, a path-average rain rate of 42.8 $\mathrm{mm\,h^{-1}}$ and a PIA of 32.7 dB were exceeded for five minutes per year and a path-averaged rain rate of 17.9 $\mathrm{mm\,h^{-1}}$ and a PIA of 13.5 dB were exceeded for 60 minutes per year.

The decrease of path-averaged rain rate exceedance levels with CML length was similar for all frequency bins, while the increase of PIA was higher for higher frequencies. For all frequencies, the respective de- or increase was higher for more extreme values, i.e. comparing the 20 year

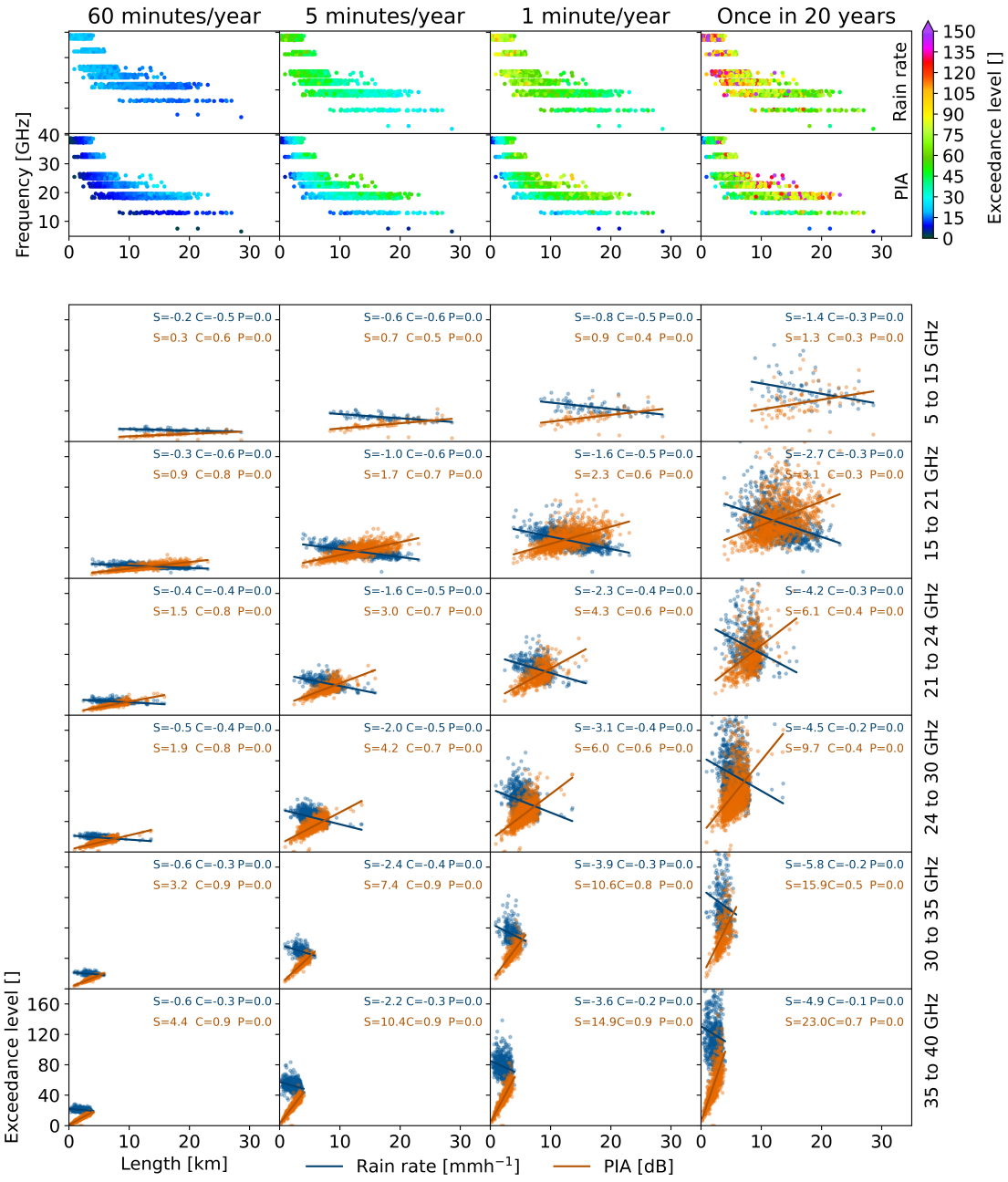

Figure 4.3: Rainfall and attenuation climatology for individual CMLs based on 20 years of RADKLIM-YW. The exceeded path-averaged rain rate and PIA along each CML path of a given length and frequency for at least 60, five and one minutes per year and the maximum rain rate occurring once in 20 years are shown in the four columns. The top two rows show rain rate and PIA (same color scale) as length against frequency scatterplots. Below, the same rain rate and PIA exceedance levels are compared to the CML length data points are shown for six frequency bins. The respective linear regression lines are shown with values for slope (S), correlation (C) and p-value (P).

maximum to 60 minutes per year, while the correlation was decreasing. The p-value was close to zero in all cases showing very high statistical significance.
Using the expected PIA values and our estimates of D_{range} we calculated n_{exp} which is shown in the second column of Figure 4.4). The majority of D_{range} was between 30dB and 50dB with higher values for longer CMLs (Figure 4.4 first column). Even though D_{range} was increasing with length, n_{exp} was also increasing with length.

4.3.4 Comparison of observed and expected blackouts

D_{range} and the number of observed (n_{obs}) and expected n_{exp} blackout minutes per year are shown in Figure 4.4 for the individual CMLs length and frequencies and shown for each length in six frequency bins. D_{range} was increasing with CML length for all frequency bins except for 5 GHz to 10 GHz. We observed that n_{exp} and n_{obs} increased with CML length. However, n_{exp} showed a smaller slope than n_{obs}. The correlation between length and n_{obs} was low, but significant. The slope was strictly positive and increasing with higher frequencies, though.

Longer CMLs missed a higher percentage of of high rainfall intensities than shorter CMLs (see Figure 4.2b) and c). According to n_{exp} a 99.99% availability margin (as recommended by the ITU which is less than 60 minutes of blackouts per year) should have been observed for all CMLs. In practice, i.e. for n_{obs}, the 99.99% margin (60 minutes) was exceeded for the longest CMLs in each frequency band. We found this to be true throughout all frequency bins except 5 GHz to 15 GHz.

In Figure 4.5, n_{exp} is directly compared to n_{obs}. The mean of n_{obs} was 6 times higher than the mean of n_{exp}. The 99th percentiles of n_{obs} and n_{exp} were 207.2 and 17.5 minutes. Higher values are considered as outliers. On average n_{obs} was twelve times higher than n_{exp} for all CMLs where $n_{exp} > 0$ and 8.5 times higher if outliers were excluded. Taking the median instead of the mean, the value is 4.6 independent of outliers included or not. The average n_{obs} for CMLs where $n_{exp} = 0$ was 19.4 minutes and the median was 3.2 minutes. 95.0% of all CMLs showed more observed blackout minutes than expected, i.e. $\frac{n_{obs}}{n_{exp}} > 1$. For 47.6% of the CMLs we observed more than five times more blackouts than expected and for 22.8% we observed more than 10 times more blackouts. A linear regression excluding outliers shows an additive increase of 11 minutes and a multiplicative increase of a factor 2. However, the correlation of 0.29 was low.

4.4 Discussion

4.4.1 Effects of CML length on blackout gaps and network design

The result that short CMLs have a lower likeliness to experience a blackout gap than longer CMLs was unexpected, because we expected the dynamic range to increase with CML length to account for the increasing PIA. Our empirical dynamic range estimates indeed show an increase with length, but it is not sufficient to compensate the even larger increase of PIA. Also, the path-averaging effect results in lower peak intensities of the path-averaged rain rates which decreases the attenuation per kilometer of CML length.

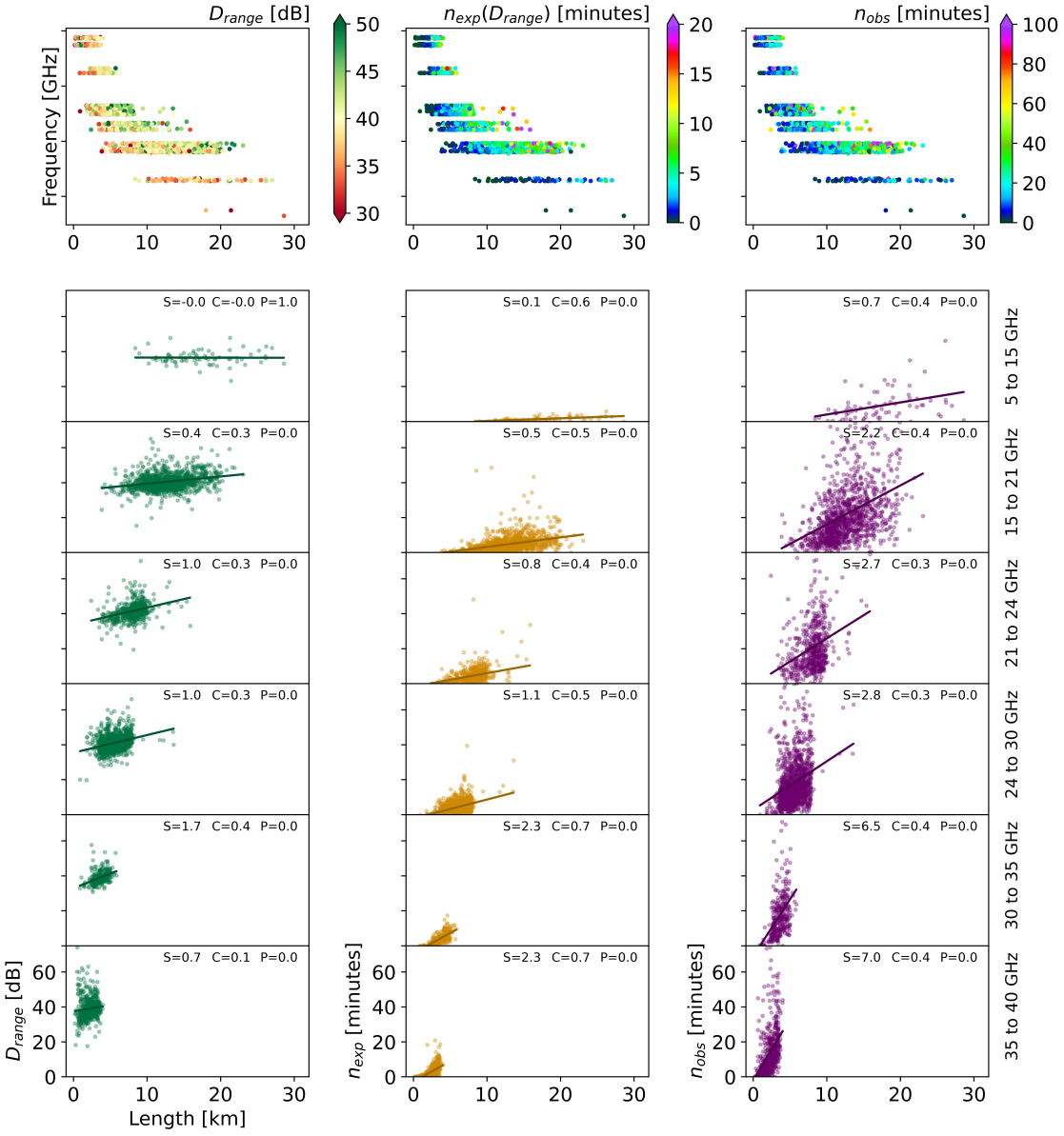

Figure 4.4: In the three columns D_{range} (left), n_{obs} (middle) and n_{exp} (right) are compared for each CML. The top row shows the respective variable on the color scale of a length against frequency scatterplot. Below, the three variables are shown against the CMLs length for six different frequency bins. A linear regression line and its values for slope (S), correlation (C) and p-value (P) is given for each of the scatter plots.

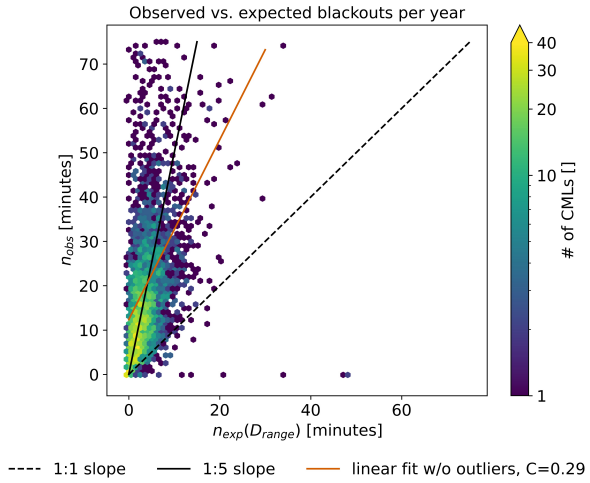

Figure 4.5: The observed number of blackout minutes per CML shown is compared to the number of expected blackout minutes in the scatter density plot, where the dashed black line corresponds to a 1:1 relation and the solid black line corresponds to a 5:1 relation. The orange line shows the best linear regression fit with a slope of 2.0 and a correlation (C) of 0.29. Outliers above the 99th percentile, i.e. $n_{obs} > 207.2$ or $n_{exp} > 17.5$, are excluded from the linear regression.

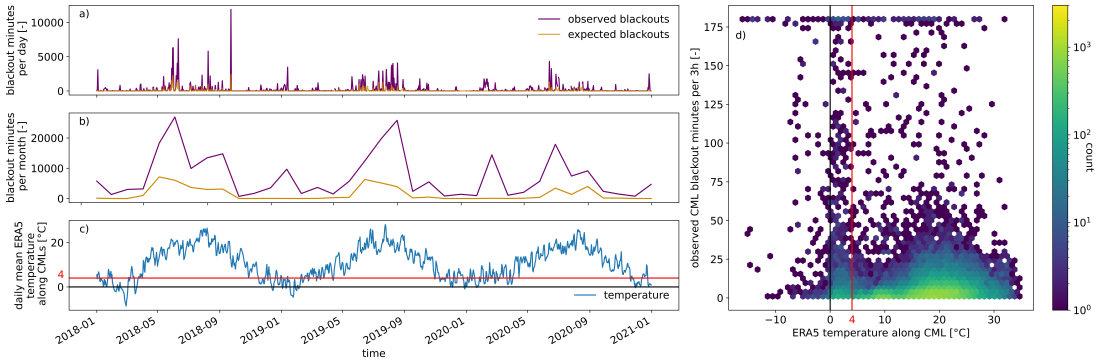

Figure 4.6: a) and b) show the observed and expected number of blackouts per day and month between 2018 and 2020. c) shows the mean 2 meter temperature along all CMLs derived from ERA-5-land. d) shows the observed number of blackout minutes per CML per 3 hours compared to the average ERA5-land 2 meter temperature along the link path during the same period. The red line in c) and d) indicates the 4°C threshold below which mixed type precipitation is more likely. 17.7% of all observed blackouts occurred below this threshold.

We found this difference between short and long CMLs in both our CML dataset and our radar-based attenuation climatology. Since observed and expected blackouts are based on independent methodological assumptions, we are confident that the effect is real. One potential explanation is that the path-averaging effect of peak intensities is overestimated during planning of the CMLs availability, so that longer CMLs experience more PIA than expected.

Our findings show potential to improve planning for future CML installations. Most prominently, our results suggest to increase the dynamic range of long CMLs. ITU recommends that the actual path length is multiplied by a so-called *distance factor* when calculating long-term statistics of rain attenuation (ITU-R, 2021). This factor significantly reduces the effective length (which is used for the calculation of path attenuation exceedance levels from rain rate exceedance statistic) of longer CMLs, e.g. the factor is approximately 0.5 for a 10 km CML with 20 GHz. Our findings, that longer CMLs experience more blackouts then shorter ones, suggest that this reduction of effective length of a CML for the calculation of path attenuation statistics is too strong, resulting in longer CMLs being planned with a too low D_{range}. Our radar-based exceedance probability can be used to estimate the potential increase of blackouts with CML length on the one hand. The total number of blackouts should be expected to be much higher on the other hand, which requires an additional increase of the dynamic range for all CMLs. As the ITU-recommended 99.99% availability was satisfied in most cases, this recommendation may be more urgent for hydrometeorological applications than network stability.

4.4.2 Implications of blackouts on CML rainfall estimation

Previous studies which compared CML rainfall information against reference data, naturally considered blackouts as missing values and little attention was payed to their implication on CML rainfall estimation. Our results confirmed that their impact on annual precipitation sums is in fact low with around 1% .

However, blackout gaps do impact CML-derived rainfall maps on shorter time scales and extreme value statistics in general, because extreme values are lost. The importance of this effect is illustrated by Figure 4.2 which shows the occurrence of blackouts during certain radar rainfall rates. The probability of a blackout at path-averaged rainfall intensities beyond 100 $\mathrm{mm\,h^{-1}}$ is higher than 40%. To interpret such maximum observable path-averaged rainfall rates the path-averaging effect of the CML observation needs to be taken into account, which is different from point-like observations.

Since we observed that shorter CMLs have a much lower probability of blackout gaps, there cannot be a general conclusion about the capability of a CML network to capture rainfall extremes. We suggest several possibilities to deal with blackouts associated with higher rainfall estimates. For applications requiring estimates of rainfall maxima with high temporal resolution, only short CMLs could be used. Another solution could be to fill RSL during detected blackout gaps with the minimal observable RSL value. Although the true maxima cannot be recovered, this could be a

reasonable first step to reduce the considerable underestimation of high rain rates in CML-derived rainfall maps.

4.4.3 Underestimation of blackouts through radar-based attenuation climatology

Our results also have potential implications for radar rainfall estimates. We observed that the average CML experienced 8.5 times more blackouts than expected from the radar-based climatology. The underestimation occurs even though our dynamic range estimate is lower than in reality due to undersampling of RSL_{min} and the consideration of 3dB WAA. Although false positive blackout detection can not be excluded with certainty, manual checks of the blackout gap detection (see Graf et al. (2022a)) confirmed the correct magnitude of observed blackouts for the vast majority of CMLs.

Therefore, there is evidence that radar-derived path-averaged rain rates and the related PIA could underestimate extreme values. This is supported by studies reporting that gauge-adjusted radar products often underestimate heavy rainfall (e.g. Schleiss et al. (2020)). This underestimation could be explained by the different spatial integration characteristic of CML and radar. Another reason for the underestimation are effects that occur in combination with rainfall, e.g. hail, that may lead to unexpected high attenuation values, but they may not lead to high weather radar rainfall estimates due to quality control and attenuation of the radar signal.

Melting hydrometeors like wet snow or sleet cause attenuation of CML signal larger than their rainfall equivalent (e.g.Tjelta and Bacon (2010)). We tested whether this effect influenced the number of observed blackouts by comparing blackout occurrences to the temperature along the CML paths derived from ERA5-land. Figure 4.6 shows the three-year time series of daily and monthly observed and expected blackouts with the daily mean temperature from ERA5 as well as a scatter density comparison of temperature and observed blackouts occurring in 3-hour periods. Similar to van Leth et al. (2018) we assumed that almost all precipitation above 4°C is liquid. We found that 17.7% of all observed blackouts occurred below 4°C, while the majority was centered around 20 degrees. This shows that the contribution of melting hydrometeors at temperatures below 4°C is not high enough to fully explain the underestimation of blackouts through weather radar data. It could also be observed that, as expected, blackouts rarely occur at negative temperatures. We conclude that despite the high spatial and temporal resolution, the weather radar data is not sufficient to fully explain CML blackouts.

4.5 Conclusions

During extreme heavy rain events, CMLs may experience blackouts, i.e., complete loss of signal. Our objectives were to determine the impact on rainfall estimation, the occurrence of blackouts in a country-wide network of 3904 CMLs and to determine if these numbers were consistent with the theoretical number of occurrences of blackouts derived from a 20-year climatology of a high-resolution weather radar product. On average, CMLs experienced 20 minutes of blackout

per year and the average CML experienced 8.5 times more blackouts than the radar climatology suggested. Shorter CMLs showed fewer blackouts in both the observed and theoretically derived data. Although the amount of rainfall missed was small compared to annual sums, the observed probability of blackouts during path-averaged radar rainfall intensities beyond 100 $\mathrm{mm\,h^{-1}}$ was more than 40%, which impacts CML rainfall estimates of individual heavy rainfall events on short timescales. Especially surprising was the increase of blackouts with CML length. Therefore, we suggest that the CML research community should be aware of this limitation and the proposed mitigation measures. Finally, this study fills a knowledge gap on the distribution of blackouts in CML data and weather radar derived attenuation climatology which can be considered in future CML infrastructure planning.

Acknowledgments

We thank Ericsson, especially Reinhard Gerigk, Michael Wahl, and Declan Forde for their support in the CML data acquisition. This research has been supported by the Helmholtz Association (grant ZT-0025), the German Research Foundation (grant CH-1785/1-2) and the Federal Ministry of Education and Research (grant 13N14826). We acknowledge support by the KIT-Publication Fund of the Karlsruhe Institute of Technology.

Open research

Software for the blackout gap detection routine (Graf et al., 2022a) is available within the CML rainfall retrieval Python-package pycomlink (Chwala et al., 2022) under BSD-3-Clause License. The CML data supporting this research was provided to the authors by Ericsson, restricting the distribution of this data due to their commercial interest. In order to obtain CML data for research purposes a separate and individual agreement with the network provider has to be established. To allow for an independent evaluation of our methodology we published data from 500 CMLs over ten days and two CMLs for the full period of this study (Chwala et al., 2022; Graf et al., 2022b) under CC BY 4.0. The RADKLIM-YW dataset used in this research is publicly available and can be downloaded from Winterrath et al. (2018).

Chapter 5

Rainfall estimates from opportunistic sensors in Germany across spatio-temporal scales (Graf et al., 2021b)

Graf, M., El Hachem, A., Eisele, M., Seidel, J., Chwala, C., Kunstmann, H., Bárdossy, A:. Rainfall estimates from opportunistic sensors in Germany across spatio-temporal scales, *J. Hydrol. Reg. Stud.*, 37, 100883. https://doi.org/10.1016/j.ejrh.2021.100883, 2021.

Abstract

Study Region: The study region is Germany and two sub-regions in Germany, i.e. the state of Rhineland-Palatinate and the city of Reutlingen.

Study Focus: Opportunistic rainfall sensors, namely personal weather stations and commercial microwave links, together with rain gauge data from the German Weather Service, were used in different combinations to derive rainfall maps with a geostatistical interpolation framework for Germany. This kriging type framework considered the uncertainty of opportunistic sensors and the line structure of commercial microwave links. The resulting rainfall maps were compared to two gauge-adjusted radar products and evaluated to three reference gauge datasets in the respective study regions on both a daily and hourly basis.

New Hydrological Insights for the Region: The interpolated rainfall products from opportunistic sensors provided good agreement to the reference rain gauges. The dataset combinations including information from the opportunistic sensors performed best. The addition of rain gauges from the German Weather Service did not consistently lead to an improvement of the interpolated rainfall maps. On the country-wide, daily scale the interpolated rainfall maps performed well, but the

gauge-adjusted radar products were closer to the reference. For the regional and local scale in Rhineland-Palatinate and Reutlingen with an hourly resolution, the interpolated rainfall maps outperformed the interpolated product from DWD rain gauges and showed a similar agreement to the reference as the radar products.

5.1 Introduction

The reliable measurement of rainfall is crucial for monitoring and understanding the hydrologic cycle and climate variability. It delivers important information for water-resource management, agriculture, urban planning, as well as for weather, climate, and hydrological modelling. Several measurement devices for rainfall observations were developed in the past. While rain gauges of different types are used since the nineteenth century, weather radar observations are operated for the past decades. The spatial and temporal coverage of such measurement networks are unevenly distributed over the globe. Compared to other regions, the rain gauges and weather radars in Germany form a dense observation network (Lorenz and Kunstmann, 2012). Still, depending on the spatial and temporal scale of a rainfall event, rainfall estimates can still be uncertain. For example, small convective events can be underestimated by weather radars or even missed completely by a network of rain gauges. The respective disadvantages of the individual measurement systems are the reason behind potentially uncertain estimates of the spatio-temporal distribution of rainfall (Cristiano et al., 2017). Quantitative precipitation estimates (QPE) from weather radars suffer from an uncertain Z-R relationship, beam blockage and ground clutter amongst others (Berne and Krajewski, 2013). Rain gauges can underestimate rainfall due to wind but more importantly the spatial and temporal variability of rainfall is not fully captured by point observations (Pollock et al., 2018).

New opportunities of measuring meteorological data are emerging with the increasing number and availability of opportunistic sensors in the last years (Zheng et al., 2018). Clark et al. (2018) used humidity, temperature and air pressure from personal weather stations (PWSs) to track the path of a hailstorm. The same variables from PWSs together with air pressure, temperature, and radiation from cell phones as well as rainfall estimates from commercial microwave links (CMLs) were used to examine a frontal system and the urban heat island effect over Amsterdam (de Vos et al., 2020).

Various different opportunistic rainfall sensors have already been investigated: the attenuation along satellite TV link path due to rainfall was exploited (Barthès and Mallet, 2013; Mercier et al., 2015). Windshield wiper frequency regulated by the optical rainfall sensor of a car were used to derive binary rainfall information (Mahoney and O'Sullivan, 2013; Rabiei et al., 2013). Rainfall estimates were derived from camera footage of rain (Allamano et al., 2015; Jiang et al., 2019). With the emerging 5G network and the growing number of devices connected to the Internet of Things, the number of potential sensors will further increase (Balsamo et al., 2018; McCabe et al., 2017; Tauro et al., 2018). In this study we use rainfall data from PWSs and commercial

microwave links (CMLs).

The nearly linear relationship between rainfall and the attenuation of microwave link signals operating with frequencies between 10 and 40 GHz is known for several decades (Atlas and Ulbrich, 1977). With the growth of modern telecommunication infrastructure, for which CMLs provide a large portion of the backhaul network, an increasing number of microwave links became available and CMLs were introduced as opportunistic rainfall sensor almost 15 years ago (Messer et al., 2006; Leijnse et al., 2007). Deriving rainfall estimates from CMLs can be challenging because of several issues. Erratic signal behavior due to refraction, reflection, or multipath propagation as well as unknown relation to meteorologic variables cause fluctuation of the signal (Upton et al., 2005; van Leth et al., 2018). Likewise, wet CML antennas can cause additional attenuation during and also after rainfall events until they are dry again (Fencl et al., 2019). Rainfall estimates from CMLs were derived for diverse regions in the world mainly in Europe (e.g. Andersson et al., 2017; Fencl et al., 2017; Overeem et al., 2016b; Roversi et al., 2020; van de Beek et al., 2020), but also for other countries as for example Israel (Ostrometzky and Messer, 2018), Brasil (Rios Gaona et al., 2018), West Africa (Doumounia et al., 2014) and, China (Song et al., 2020). An overview of the background and challenges in rainfall estimation from CMLs was given by Chwala and Kunstmann (2019) and Uijlenhoet et al. (2018), respectively. Rainfall maps were derived from CMLs, often neglecting the path-integrated nature of the estimated rain rate but rather using the center of each CML as a theoretical point measurement (Graf et al., 2020a; Overeem et al., 2016b). Some dedicated mapping algorithms were introduced but not analyzed on a larger scale (Liberman et al., 2014; van de Beek et al., 2020; Haese et al., 2017)

The potential and challenges using rainfall data from PWSs were first shown by de Vos et al. (2017). PWSs also provide other meteorological information (Bell et al., 2013; Jenkins, 2014), but for our study, from here on, PWSs will only refer to personal weather stations measuring rainfall. PWSs are rain gauges which are set up by individual citizens. Data from PWSs are prone to numerous error sources ranging from calibration issues to poor maintenance and unfavourable positioning. Therefore, a thorough quality check of PWSs data is necessary. An intrinsic approach using information of neighboring PWSs was tested in the Netherlands (de Vos et al., 2019a). The Norwegian Meteorological Institute deployed an automatic data quality control for their meteorological station data which is supplemented by opportunistic data e.g. for temperature (Båserud et al., 2020). Another approach presented by Bárdossy et al. (2021) used data from a trustworthy primary network and a geostatistical method combined with rank statistics. This approach is also used in our study to remove and bias correct suspicious PWSs and CML data with modifications of the filtering approach to account for the line characteristic of the CML data.

This study aims to provide 1) a large scale evaluation of rainfall estimates from two types of opportunistic rainfall sensors, 2) a geostatistical interpolation framework and 3) a related performance analysis of the derived rainfall maps using data from opportunistic sensors, official rain gauges and various combinations of these datasets. The performance analysis is carried out on different spatial and temporal scales. The interpolation framework takes the specific characteristics and uncertainties of the sensors into account and combines rainfall information from point

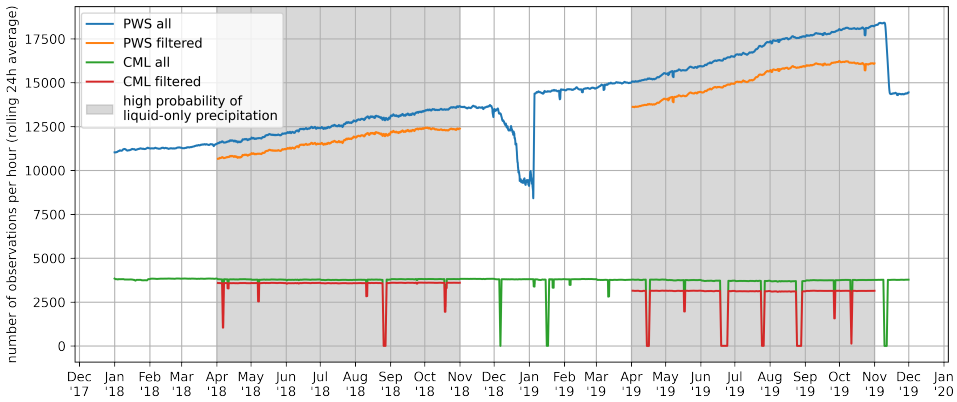

Figure 5.1: Availability of PWS and CML data for the years 2018 and 2019 before and after the processing and filtering.

and line sources with individual weights. These sensors are official rain gauges from the German Meteorological Service (DWD), PWSs data obtained from Netatmo, and CML data obtained from Ericsson, in Germany. The question we raise is, how accurate can opportunistic sensors measure rainfall on a country wide, regional, and local scale? Specifically: in Germany, the federal state of Rhineland-Palatinate, and the city of Reutlingen, respectively?

5.2 Study region and data

5.2.1 Study region

The study region is Germany and our analysis was carried out on a national scale for the whole of Germany with 357,386 km^2, on a regional scale for the state of Rhineland-Palatinate with 19,847 km^2 and on a local scale for the city of Reutlingen with 87 km^2. Rainfall in Germany is falling year-round with a peak during the summer months. The driest regions are located in the northeast with mean rainfall amounts of 450 mma^{-1} year. Highest rainfall amounts occur in the Central German Uplands with over 1,000 mma^{-1} and in the Alps with up to 2,000 mma^{-1}. Rainfall in the northern part of Germany is mostly influenced by synoptic driven processes while convective events become more frequent southwards. Rhineland-Palatinate is situated in the mid-west of Germany with yearly rainfall amounts between 500 and 800 mm between the Rhine Valley and the low mountain ranges of Taunus and Hunsrück. The city of Reutlingen is located in the south-western state of Baden-Wuerttemberg approximately 30 km south of the state capital Stuttgart.

The density of hydro-meteorologic measurements over Germany, and therefore also for Rhineland-Palatinate and Reutlingen, is high compared to most other parts of the world (Lorenz and Kunstmann, 2012). The German Weather Service (DWD) operates a weather radar network and roughly 2,000 rain gauges with daily and hourly temporal resolution. Several state agencies and

private companies additionally operate hundreds of rain gauges, which are partly used in rainfall products of the DWD. The continuous measurement of precipitation in Germany started more than a hundred of years ago with many gauge locations being sampled for multiple decades (Hellmann, 1907). Therefore, the measurement of precipitation with additional opportunistic sensors and the generation of interpolated products from these sensors would not seem to be of primary importance in Germany.

Yet, the spatio-temporal variability of rainfall cannot be captured completely with common products derived from rain gauges and weather radars. This is especially the case for short duration and high intensity rainfall which can cause flash floods (Berne et al., 2004; Emmanuel et al., 2012; Ochoa-Rodriguez et al., 2015). A striking example is the devastating flash flood in the city of Braunsbach in 2016. In a 10 km radius around Braunsbach, only one rain gauge with a daily resolution is located. Radar data underestimated the rainfall measured from the rain gauge by 30 percent, therefore it is uncertain whether the radar measurements of the peak rainfall several kilometers away from the gauge was estimated correctly (Bronstert et al., 2018). With the increasing density of opportunistic sensor networks, like the ones used in this study, the probability that such sensors detect small scale events and their variability is also increasing. We use the opportunity of having several independent rain gauge networks in Germany to evaluate the rainfall maps derived from opportunistic rainfall sensors with our mapping approach on three different scales: On the country-wide scale for the whole of Germany, on the regional scale for Rhineland-Palatinate and on the local scale for Reutlingen. We expect the higher network density of the opportunistic sensors to be beneficial especially on the regional and local scale.

5.2.2 Opportunistic rainfall data

We use two types of opportunistic rainfall data, namely PWS data from the Netatmo network (https://weathermap.netatmo.com) and CML data from Ericsson. Netatmo is a company selling PWSs among other smart-home devices. Their basic PWS system (which provides measurements of temperature, humidity, air pressure) can be extended with an unheated tipping bucket gauge for rainfall measurement. These rain gauges have a collecting area of 125 cm^2 and a temporal resolution of five minutes. de Vos et al. (2019a) gives further technical details to Netatmo PWSs. If the owner agrees, data from the PWSs is uploaded to Netatmo's weather map. Data is then available via an API in temporal resolutions down to five minutes. The used dataset consists of all freely available PWSs data from Netatmo in Germany in 2018 and 2019. Fig. 5.1 shows their continuously growing number of up to 15,000 by the end of our study period. The reason for the decreasing numbers during winter was not investigated. A possible explanation could be battery failure due to cold temperatures. The spatial distribution of PWSs in Germany follows roughly the population density with most PWSs situated in urban areas as for example shown in the map in Fig. 5.4.

CML data are typically not publicly available but need to be provided by telecommunication providers. We receive data from 3,904 CMLs from Ericsson in Germany via a near-real time data acquisition system (Chwala et al., 2016). The CML lengths range from 0.3 to 30 km and their

frequencies from 10 to 40 GHz. The spatial distribution of CMLs is highly unbalanced throughout Germany. We currently only have access to a subset of CMLs which is only a small part of the more than 100,000 CMLs installed in Germany (Bundesnetzagentur, 2017). The distribution of the CMLs in this subset is not representative for the general distribution of CMLs in Germany. More information on the characteristics of this CML dataset are available from Graf et al. (2020a).

The analyzed periods are the summer season from April to October 2018 and 2019 as shown in Fig. 5.1. For previous years, the availability of PWSs was significantly lower and our country-wide data acquisition for CMLs in Germany started in August 2017. We excluded months with high probability of snow, since performance for both sensors decreases in winter. PWSs are not heated and CML suffer from snow and ice on their antennas as well as from large uncertainties of the relation between attenuation and snow and melting snow. Melting sown for example causes a many times higher attenuation than rain resulting in large overestimation of the precipitation event. An overview of all used datasets and their respective usage is given in Tab. 5.1.

5.2.3 Gauge and radar data

We use two different gauge datasets operated by the DWD. The first gauge dataset consists of 968 automatic pluviometers. We use the hourly and quality checked data from these rain gauges (referred to as $\mathrm{DWD_{auto}}$ from here onwards) in the interpolation framework (Sec. 5.3.3). The second gauge dataset (referred to as $\mathrm{DWD_{man}}$) consists of 1,062 manual rain gauges with a daily resolution. The collection diameter is 200 cm^2 and the gauges are heated. This dataset is used as a reference for the country-wide evaluation as it is independent of the $\mathrm{DWD_{auto}}$ data. Both DWD gauge datasets have a density of roughly one gauge per 300 km^2. A network of 169 hourly rain gauges in Rhineland-Palatinate is used for the evaluation on a higher temporal resolution. These gauges are operated by the State Agrometeorological Agency of Rhineland-Palatinate. This dataset has a spatial density of roughly one gauge per 100 km^2. For the evaluation on the local scale we use hourly data from ten rain gauges situated in the city of Reutlingen. The OTT pluviometers form a dense network of one gauge per 9 km^2.

We use two radar datasets in this study, namely, RADOLAN-RW and RADKLIM-YW provided by the DWD. RADOLAN-RW is a near-real time product with an hourly resolution. It is updated with 30 minutes lag time. The gridded dataset covers Germany with 900 by 900 grid cells with a 1 km resolution. It is a composite of 17 weather radars adjusted via a weighted combination of additive and multiplicative corrections from the $\mathrm{DWD_{auto}}$ gauge network (Bartels et al., 2004; Winterrath et al., 2012). RADKLIM-YW is based on the same radar and gauge data as RADOLAN-RW but undergoes climatological adjustments, accounting for e.g. range-dependent underestimation and radar spokes due to beam blockage (Winterrath et al., 2018). The adjustments are carried out with hourly data (RADKLIM-RW), but are also applied to the 5-minute data (RADKLIM-YW) which we use here. The performance of radar and rain gauge products from the DWD were already analysed. While especially during winter and in small catchments the differences in daily, areal rainfall could exceed 50% (Kneis and Heistermann, 2009; Meissner et al., 2012), the mean yearly rainfall sums of DWD rain gauges and radar products compare well

(Kreklow et al., 2019).

Table 5.1: Overview of used datasets: a) input data for the interpolation framework, b) radar datasets used for comparison, and c) reference rain gauge datasets used for the evaluation

Name	Number of sensors	Resolution	Operator
a) Rain gauge and opportunistic data used in the interpolation framework			
DWD_{auto}	968	hourly	DWD
(filtered) PWSs	10,500 - 16,200	hourly	private/Netatmo
(filtered) CMLs	3,150 - 3,600	hourly	Ericsson
b) Radar datasets used for comparison			
RADOLAN-RW	900x900 grid	hourly	DWD
RADKLIM-YW	1,100x900 grid	hourly	DWD
c) Reference gauge datasets			
DWD_{man}	1,062	daily	DWD
RLP	169	hourly	State Agrometeorological Agency Rhineland-Palatinate
RT	10	hourly	City of Reutlingen

5.3 Methods

5.3.1 CML and PWS data preparation and processing

CML data cannot be converted to a rainfall estimate directly. Several processing steps are required to obtain rain rates from raw CML data. We use the processing routine described in Graf et al. (2020a) with the exception of the classification of wet and dry periods where we use an improved method presented by Polz et al. (2020): First, CMLs with erratic data (e.g. from drifts, jumps or high levels of noise) are removed from the dataset using two filters based on monthly statistics of the CML raw data. Data gaps shorter than 5 minutes are interpolated linearly. Then, wet and dry periods are classified by a convolutional neural network trained to that specific task. For each identified rain event the baseline of the signal is derived from the precedent dry period. Using this event-specific baseline, attenuation values are calculated which are then corrected for the additional attenuation caused by raindrops on the CML antennas. From the final rain-induced attenuation the rain rate can be calculated using the $k - R$ relation, where k is the specific path attenuation (in $dBkm^{-1}$) and R is the rain rate (in mmh^{-1}). A detailed description of these steps as well as a large scale analysis can be found in Graf et al. (2020a). We chose the new classification of wet and dry periods from Polz et al. (2020) because it reduces the false-positive rate (FPR) while keeping the false-negative rate (FNR) constant which is shown along with an evaluation of the combination of both methods for one month for the whole of Germany in Fig. 9 of Polz et al. (2020). All introduced CML processing routines can be found in the software package pycomlink (2021). The resulting data consists of rain rates averaged along the CMLs path with one minute temporal resolution. This data is then aggregated to an hourly resolution except for hours with gaps longer than 5 minutes which were not interpolated in the first step.

The reason for the five-minute interpolation, besides rare connection problems of the data acquisition system, is the engineering requirements of the CML network. For each CML the combination of a given path length with a microwave frequency is chosen so that, on average, the path attenuation due to heavy rain leads to a complete signal loss at the receiver only for some minutes per year. Because the choice of the frequency and the path length are constrained - only certain frequency bands are available, high frequencies are desired to allow more bandwidth, and path length is determined by the locations of CML towers - the maximum rain rate before signal loss is different for all CMLs. It can be as low as 40 mmh^{-1} but also above 150 mmh^{-1} e.g. for very short CMLs (1 km or shorter) or for short CMLs (< 5 km) with low frequencies (< 20 GHz). Therefore, for heavy rainfalls some CMLs do not provide accurate rainfall information.
The PWS data have been acquired via the Netatmo API in time steps of variable length of typically 5 minutes and aggregated to hourly resolution. Additional information regarding the Netatmo data acquisition can be found in de Vos et al. (2020). Compared to the hourly data of the Netatmo API, which accepts up to eleven missing five-minute values, we have removed all hours with more than one missing five minute value.

5.3.2 Indicator correlation filter, event based filter and bias correction

The filtering and bias correction approach introduced by Bárdossy et al. (2021) was the basis for filtering and bias correcting the PWS data in this study. The CML data was also treated with this approach even though they already were pre-processed with pycomlink which removed the worst performing CMLs from the dataset. Problems we still encountered in the CML derived rain rates were strong overestimation of melting snow (evident in April and October) and other false positive events caused by attenuation which is not induced by rain which rather liberal filtering of pycomlink did not remove.

The main assumption behind the indicator correlation filter is that the specific PWS or CML values might be wrong but their ranks are correct, especially for the most intense events. Using a reference network such as the $\mathrm{DWD_{auto}}$ rain gauges, which are installed according to the WMO guidelines, the dependence between the nearest neighboring stations is investigated. For each location, the correlation value of the indicator series between the pairs of $\mathrm{DWD_{auto}}$-PWS or $\mathrm{DWD_{auto}}$-CML is compared to the values between the $\mathrm{DWD_{auto}}$ stations for similar separation distances and time periods. Hereby, information on how precipitation varies in space is acquired and PWS or CML locations with unreliable observations for high precipitation intensities are identified. For the CML data we used an extended version of the indicator correlation filter to account for the geometric line structure of the CMLs which is described in Appendix 5.6.2 while the basic principle of the filter was unchanged.

The indicator correlation filter is applied on a yearly basis for all hourly PWS and CML data. Figure 5.2 shows the results for the year 2019. After applying the filter, around 92% of the PWSs and of the CMLs remained. The number of PWSs in Fig. 5.2 refers to the overall number of PWSs providing data during 2019 while Fig. 5.1 shows the availability of PWS measurements at

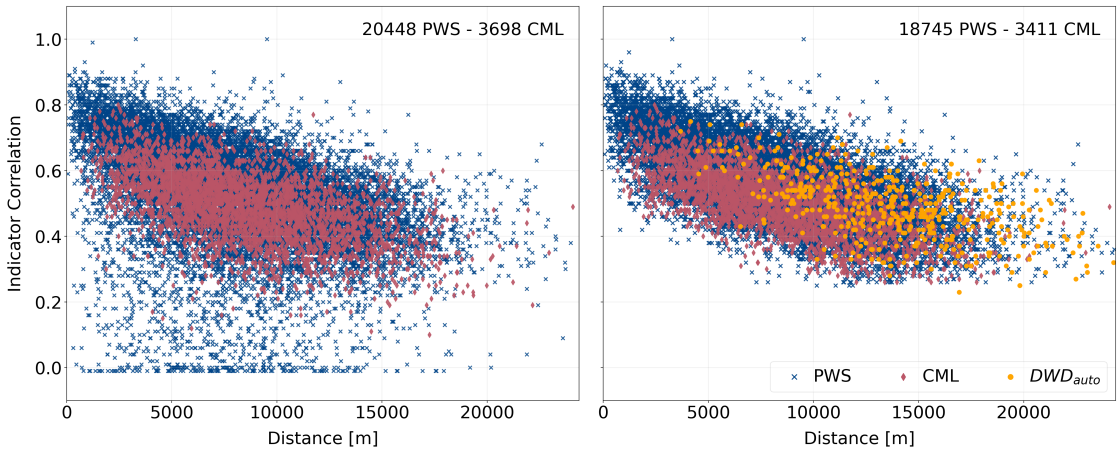

Figure 5.2: Indicator correlations for 1h temporal resolution and a quantiles level of 0.99 between the PWS and CML networks and the nearest $\mathrm{DWD}_{\mathrm{auto}}$ (the reference network in this case) stations before (left) and after (right) applying the filter for the year 2019. The orange dots refer to the indicator correlation between the $\mathrm{DWD}_{\mathrm{auto}}$ network stations.

each point in time which causes the different values.

Even though the order of the values is assumed to be correct, the PWS and CML values remaining after the indicator correlation filter might have an unknown bias. The bias varies individually for each location and each observation. Therefore, the real precipitation amounts need to be estimated. This is done for the observed hourly data. For this purpose, the precipitation distribution functions of the $\mathrm{DWD}_{\mathrm{auto}}$ stations are used. For a target location and a given time step, using the observed quantiles (PWS or CML), the corresponding $\mathrm{DWD}_{\mathrm{auto}}$ quantiles are derived and the corresponding precipitation amount is interpolated. Through this procedure the possible bias available at the PWS and CML locations is reduced. The resulting time series are used further on in this study. A more detailed description of both the indicator correlation filter and bias correction for the CML data can be found in Appendix 5.6.2.

While the indicator correlation filter removes opportunistic sensors for a whole year some remaining sensors can suffer from erratic measurements for individual events. Possible reasons can be low battery or clogged funnels for PWSs as well as outages in the data acquisition or attenuation induced by other sources than rain for CMLs. We applied an event based filter after the bias correction which uses the variogram of the next 30 $\mathrm{DWD}_{\mathrm{auto}}$ stations to cross-validate each sensor in order to remove faulty values. If a sensors' rainfall value differs too much from the value estimated by the variogram of the 30 stations (here three times the kriging standard deviation) it was rejected. In order to preserve higher rainfall values and to focus more on discarding false zeros, this filter used the square root of the rainfall sum. This was the only modification of the event based filter which first was shown in Bárdossy et al. (2021). Overall, this filter removed around 0.6% of the PWS data and 1.5% of the CML data.

5.3.3 Geostatistical interpolation framework

We developed a geostatistical interpolation framework which allows a combination of different data sources and their specific features and geometric properties. Let $\{x_1, \ldots, x_n\}$ be the locations of the DWD_{auto} observation points, $\{y_1, \ldots, y_m\}$ the locations of the PWSs (after filtering) and $\{L_1, \ldots, L_k\}$ be the line segments of the CMLs (after filtering). The estimation of the precipitation amounts Z at a given location x^* is done by a combined kriging approach in which both the increased uncertainty of the PWS and CML based precipitation is taken into account, and the CML's line structure is considered by using a block kriging type approach. The estimation is obtained in the form

$$Z(x^*) = \sum_{i=1}^{n} \lambda_i Z(x_i) + \sum_{i=1}^{m} \alpha_i Z(y_i) + \sum_{i=1}^{k} \beta_i Z(L_i) \tag{5.1}$$

With the additional condition of unbiasedness

$$\sum_{i=1}^{n} \lambda_i + \sum_{i=1}^{m} \alpha_i + \sum_{i=1}^{k} \beta_i = 1 \tag{5.2}$$

The weights $\mathbf{w}^T = (\lambda_1, \ldots, \lambda_n, \alpha_1, \ldots, \alpha_m, \beta_1, \ldots, \beta_k, \mu)$ can be obtained by solving the linear equation system

$$\mathbf{A}\mathbf{w} = \mathbf{c} \tag{5.3}$$

μ is the Lagrange multiplier introduced to ensure the fulfilment of the unbiasedness condition (5.2).
The matrix $\mathbf{A}$ is

$$\mathbf{A} = \begin{pmatrix}
\gamma(x_1,x_1) & \cdots & \gamma(x_1,x_n) & \gamma(x_1,y_1) & \cdots & \gamma(x_1,y_m) & \bar{\gamma}(x_1,L_1) & \cdots & \bar{\gamma}(x_1,L_k) & 1 \\
\vdots & \ddots & \vdots & \vdots & \ddots & \vdots & \vdots & \ddots & \vdots & \vdots \\
\gamma(x_n,x_1) & \cdots & \gamma(x_n,x_n) & \gamma(x_n,y_1) & \cdots & \gamma(x_n,y_m) & \bar{\gamma}(x_n,L_1) & \cdots & \bar{\gamma}(x_n,L_k) & 1 \\
\gamma(y_1,x_1) & \cdots & \gamma(y_1,x_n) & \gamma(y_1,y_1)+\varepsilon_y & \cdots & \gamma(y_1,y_m) & \bar{\gamma}(y_1,L_1) & \cdots & \bar{\gamma}(y_1,L_k) & 1 \\
\vdots & \ddots & \vdots & \vdots & \ddots & \vdots & \vdots & \ddots & \vdots & \vdots \\
\gamma(y_m,x_1) & \cdots & \gamma(y_m,x_n) & \gamma(y_m,y_1) & \cdots & \gamma(y_m,y_m)+\varepsilon_y & \bar{\gamma}(y_m,L_1) & \cdots & \bar{\gamma}(y_m,L_k) & 1 \\
\bar{\gamma}(L_1,x_1) & \cdots & \bar{\gamma}(L_1,x_n) & \bar{\gamma}(L_1,y_1) & \cdots & \bar{\gamma}(L_1,y_m) & \bar{\gamma}(L_1,L_1)+\varepsilon_L & \cdots & \bar{\gamma}(L_1,L_k) & 1 \\
\vdots & \ddots & \vdots & \vdots & \ddots & \vdots & \vdots & \ddots & \vdots & \vdots \\
\bar{\gamma}(L_k,x_1) & \cdots & \bar{\gamma}(L_k,x_n) & \bar{\gamma}(L_k,y_1) & \cdots & \bar{\gamma}(L_k,y_m) & \bar{\gamma}(L_k,L_1) & \cdots & \bar{\gamma}(L_k,L_k)+\varepsilon_L & 1 \\
1 & \cdots & 1 & 1 & \cdots & 1 & 1 & \cdots & 1 & 0
\end{pmatrix} \tag{5.4}$$

and the right hand side of the equation is

$$\mathbf{c}^T = (\gamma(x^*,x_1), \ldots, \gamma(x^*,x_n), \gamma(x^*,y_1), \ldots, \gamma(x^*,y_m), \bar{\gamma}(x^*,L_1), \ldots, \bar{\gamma}(x^*,L_k), 1) \tag{5.5}$$

Here for any pair of points, $\gamma(x_i, y_j)$ is the variogram value corresponding to the vector $x_i - y_j$. The combination of a point and a line segment requires a mean variogram value over the segment

$$\bar{\gamma}(x_i, L_j) = \frac{1}{|L_j|} \int_{L_j} \gamma(x_i, u)\, du \tag{5.6}$$

and for the consideration of pairs of line segments L_i and L_j one has to calculate the corresponding mean value:

$$\bar{\gamma}(L_i, L_j) = \frac{1}{|L_i||L_j|} \int_{L_i} \int_{L_j} \gamma(u, v)\, du\, dv \tag{5.7}$$

The ε_y and the ε_L values in the diagonal of the matrix represent the uncertainty of measurements of the PWSs and the CMLs respectively. In our approach we selected a 10 % error. Experimental variograms were calculated for each one hour time step using the DWD_{auto} only and the filtered bias corrected PWS data only. The variograms were subsequently normalized, and a k-means clustering algorithm was used to divide them into 4 different groups. Theoretical variograms were fitted to each center of the cluster. The fitted variograms differed mainly in the range which was between 12.5 and 40.0 km. The variograms based on the DWD_{auto} data showed no nugget effect, while the PWS based variograms had a nugget of about 10 %. This was the reason why the ε was selected as 10 % of the sill. The consideration of the length and orientation of the line segments is fully respected in this equation. If one would replace each line segment with its central point (as done e.g. in Overeem et al., 2016a) the weights would be significantly different (see 5.A1 for an example). All combinations of datasets and the respective interpolated products are given in Tab. 5.2

Table 5.2: Interpolated rainfall products and their input data

Abbreviation	Input data
DWD_{int}	DWD_{auto}
PWS_{int}	PWS
CML_{int}	CML
DWD_CML_{int}	DWD_{auto}, CML
DWD_PWS_{int}	DWD_{auto}, PWS
PWS_CML_{int}	PWS, CML
$DWD\_PWS\_CML_{int}$	DWD_{auto}, PWS, CML

5.4 Results and Discussion

5.4.1 Cross validation of the interpolated rainfall products

A leave one out cross validation is used to compare the performance between the interpolated products among each other at the location of the DWD_{auto} stations for temporal aggregations between one hour and 30 days. For the cross validation the target stations were removed for the whole procedure, the filtering, the assessment of the distribution function and for the interpolation of the precipitation amounts. This allows us to evaluate the performance of the different interpolation products at the location of each DWD_{auto} independently. As diagnostic measures, the Pearson's correlation coefficient (PCC), the coefficient of variation (CV) and the Kling-Gupta efficiency (KGE) as well as the false positive (FPR) and false negative rate (FPR) are used. Their definitions can be found in Appendix 5.6.3. Because DWD_{auto} was also used in four of the seven interpolation products, the validation was carried out as a leave-one-out cross validation. The results are shown in Fig. 5.3 a) to c) for all DWD_{auto} stations as validation stations and in d) to f) for a selection of ten percent of DWD_{auto} stations defined by the density of opportunistic sensors in close vicinity which we call selected validation stations from here on.

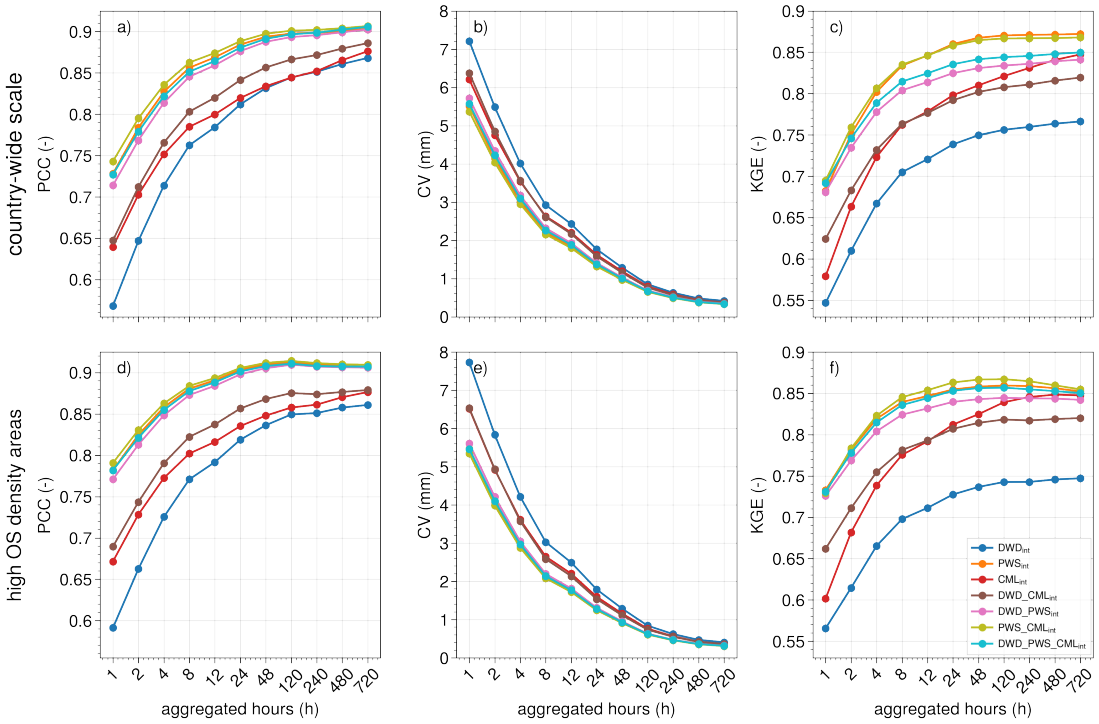

Figure 5.3: Performance measures of the cross validation from the interpolation framework for different temporal aggregations. a) to c) show PCC, CV and KGE for all country-wide $\mathrm{DWD_{auto}}$ validation stations and d) to f) show PCC, CV and KGE for validation stations with more than 80 PWSs or CMLs in 20 *km* vicinity which have data available for the whole analysed period. Those are the 10 percent of the validation stations which are surrounded by the most opportunistic sensors.

Two groups of interpolation products are visible for all measures and both selections of stations. This distinction was larger for the selected validation stations. One group contained $\mathrm{PWS_{int}}$ and the other combinations with PWSs, whereas the other group contained $\mathrm{DWD_{int}}$, $\mathrm{CML_{int}}$ and their combination. $\mathrm{PWS_{int}}$ and the other combinations with PWSs performed better for all three performance measures. The interpolated products with opportunistic sensors had higher performance measures for the selected validation stations. $\mathrm{DWD_{int}}$ showed the worst performance for both all and selected validation stations. The performance of opportunistic sensors increased when only validations stations surrounded by many PWSs and CMLs were considered. We think that the heterogeneous distribution of opportunistic sensor networks of CMLs and PWSs shown in the map in Fig. 5.4 is the reason for this better performance. $\mathrm{DWD_{auto}}$ with its more homogeneous distribution performed similar between both validation station sets.

With increasing temporal aggregation the performance of all interpolated products increased. The difference between all and selected validation stations was highest at short aggregations of one to 12 hours for PCC and KGE. For the aggregations over days, they were similar. This emphasizes

the influence of quality and amount of sampling points when interpolating rainfall on sub-daily temporal scales.

Overall, the combinations with PWSs had the highest performance values while the interpolation product which used all three possible datasets (DWD_PWS_CML$_{\text{int}}$) was not the overall best performing one, even though it contained the highest number of sampling points. A potential explanation is that DWD$_{\text{int}}$ measurements are considered more reliable and hence have a higher weight in the block kriging, however their spatial density is the lowest on average. We conclude that the large number and the accuracy of the opportunistic sensors lead to a better interpolation.

The block kriging approach in the interpolation framework accounts for the integral characteristic of the CMLs. The comparison to kriging with the center of each CML as point measurement (CML_point$_{\text{int}}$) done in the same manner as in Fig. 5.3 shows a higher PCC for the block kriging approach (see Fig. 5.A2). For temporal aggregations, of one and two hours CML_point$_{\text{int}}$ leads to higher KGE values. With the variance directly affecting KGE values, we assume that the reduced variance in CML$_{\text{int}}$ of block kriging is the reason for the lower KGE values.

5.4.2 Performance of interpolated rainfall products compared to gauge datasets on different scales

The performance of the interpolated datasets is analyzed for the whole of Germany, a regional, and a local subset with different, independent reference datasets. Additionally, two radar datasets from the DWD are compared analogously to the reference data.

5.4.2.1 Country-wide, daily scale for Germany

For the country-wide scale we used data from manual rain gauges with a daily resolution from the DWD (DWD$_{\text{man}}$). The interpolated rainfall maps and radar product values for this evaluation are taken at the respective grid cell of the locations of DMD$_{\text{man}}$ gauges. An overview of the DWD$_{\text{man}}$ gauges, PWSs locations and CMLs is given in the map of Fig. 5.4 together with results of the evaluation for this scale.

In general, the radar products match the reference data better than the interpolated products. They have slightly higher PCC and KGE as well as a lower FPR. The comparison is not quite fair, though. The radar products are based on measurements directly at each reference station's location while the interpolated rainfall fields have to rely on observation at a certain distance, a distance that varies from hundreds of meters to tens of kilometers in the north-eastern part of Germany. Nevertheless, the performance measures of the interpolated products are good. Looking at the two radar products, RADKLIM-YW outperformed RADOLAN-RW except for FPR. This leads to the assumption that the climatological adjustments of RADKLIM-YW, e.g. seasonal correction of range dependent underestimation, improve this radar product not only for longer aggregations times, from which the climatological corrections are derived, but also on a daily scale.

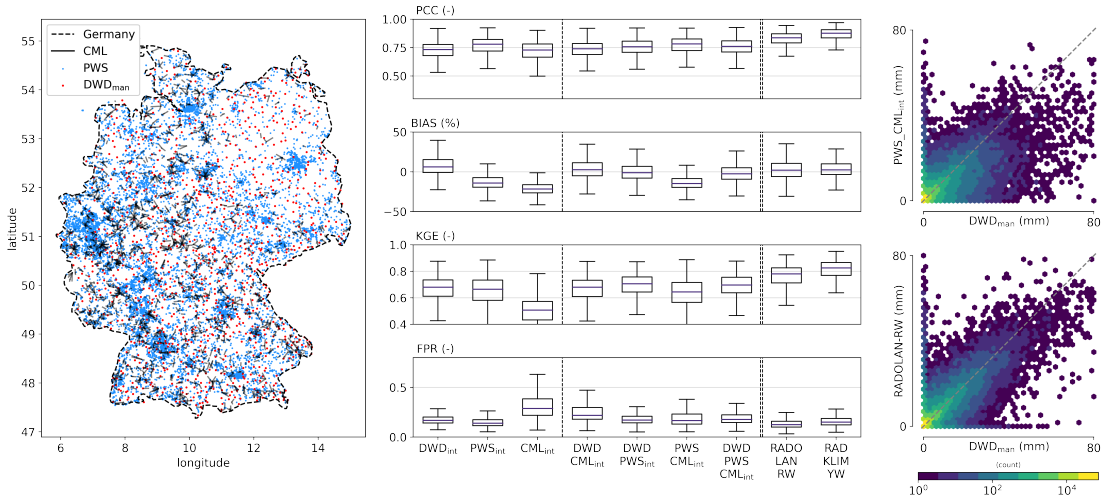

Figure 5.4: Map of Germany with DWD_{man} gauges (reference), PWS locations and CML paths, boxplots of performance measures for the seven interpolated products as well as RADOLAN-RW and RADKLIM-YW against the reference. The vertical dashed line separates the interpolated products which are based on a single data set from the combined products and the double dashed line separates the radar products. On the right, scatter density plots of daily PWS-CML and RADOLAN-RW rainfall sums are compared to the reference

Among the interpolated products, the ones including PWSs compared better to the reference than the others. The worst performance was obtained by the CML_{int}. These results are in accordance with the cross validation. The scatter density plots show all daily rainfall values for PWS_CML_{int} and RADOLAN-RW against DWD_{man}. The number of missed rainy days (false negative rate: FNR) from the reference, visible along the x-axis in Fig. 5.4, was lower for the interpolated product than for the radar product.

The performance of PWS_{int} and the other combinations with PWSs is better compared to the DWD_{auto} product. The reason for this is the high spatial density resulting from the high number of OS. This is true even though the OS are heterogeneously distributed in contrast to the more homogeneously distributed DWD_{man}. This means that hydrological modeling studies, which often use data from rain gauge networks, can benefit from rainfall information derived from opportunistic sensors. Requirements for such applications are the availability of opportunists sensors, the acquisition of their data and a thorough quality control.

Similar to the cross validation, the subset of DWD_{man} surrounded by the densest opportunistic network were examined separately (see 5.A3). The results differ only slightly from the country-wide analysis of Fig. 5.4. The range of the individual performance measures are more narrow and PWS_{int} and CML_{int} have a small improvement, similar to what was observed for the daily aggregation results of the cross validation. This means that the density of opportunistic sensors is sufficient for rainfall mapping in almost all parts of Germany except for the north-eastern part

of Germany.

5.4.2.2 Regional, hourly scale for Rhineland-Palatinate

As reference on a regional scale 169 rain gauges with an hourly resolution operated by the State Agrometeorological Agency of Rhineland-Palatinate (RLP) are used. An overview of the Rhineland-Palatinate gauges, PWS locations and CMLs is given in the map of Fig. 5.5 together with results of the evaluation for this scale. For the PCC all interpolated products with opportunistic sensors outperformed the DWD_{int} product. PWS_{int} and the other combinations with PWSs performed almost as good as the radar products. The combination PWS_CML_{int} reached marginally higher PCC values than PWS_{int}. CML_{int} has the highest (negative) bias. This can be caused for example by the integral character of the CML underestimating the highest rainfall events and the heterogeneous distribution of the CMLs. The FPR (not shown in the plot for the evaluation at this scale) of all products is 5 times smaller than FNR, with the best performance for PWS_{int} and PWS_CML_{int}. RADOLAN-RW shows more over- and underestimation of the highest hourly rainfall events which can be seen in the scatter plot. The PWS_CML_{int} product underestimates the highest rainfall events, which could be caused by a combination of the effect of the integral character of the CML measurement and the smoothing of the field caused by the 10 % nugget that is used in Kriging to represents the uncertainty of the opportunistic sensors. Moreover, despite the thorough PWSs quality check, there could still be some stations that were not filtered and that recorded false zeros for the intense events affecting the performance of the interpolation products.

The biggest difference to the country-wide DWD_{man} reference evaluation is that the comparison to RLP is based on hourly data. On this temporal resolution, rainfall shows more variability than on a daily scale. Hence, on the hourly scale all interpolated and radar products have lower values for PCC and KGE. Nevertheless, the agreement of the best performing interpolation products with the reference data is high. It can be assumed that for all regions with similar distribution and density of opportunistic sensors in Germany, similar results as for Rhineland-Palatinate could be achieved. That means, opportunistic sensors can provide rainfall estimates with a good quality for most parts of Germany, with the exception of north-eastern regions where their network density is low.

5.4.2.3 Local, hourly scale for the city of Reutlingen

Ten rain gauges operated by the city of Reutlingen (RT) are used to evaluate the performance of the interpolated products and radar datasets on local scale with a temporal resolution of one hour. An overview of the RT gauges, PWS locations and CMLs is given in the map of Fig. 5.6 together with results of the evaluation for this scale. The network of 10 rain gauges in and around Reutlingen has a significantly higher density than the previous gauge datasets used as reference. On this small scale, the high number of PWSs in this urban area becomes apparent, with around thirty stations in Reutlingen. PWS_{int} and the combinations with PWSs compared best to the ref-

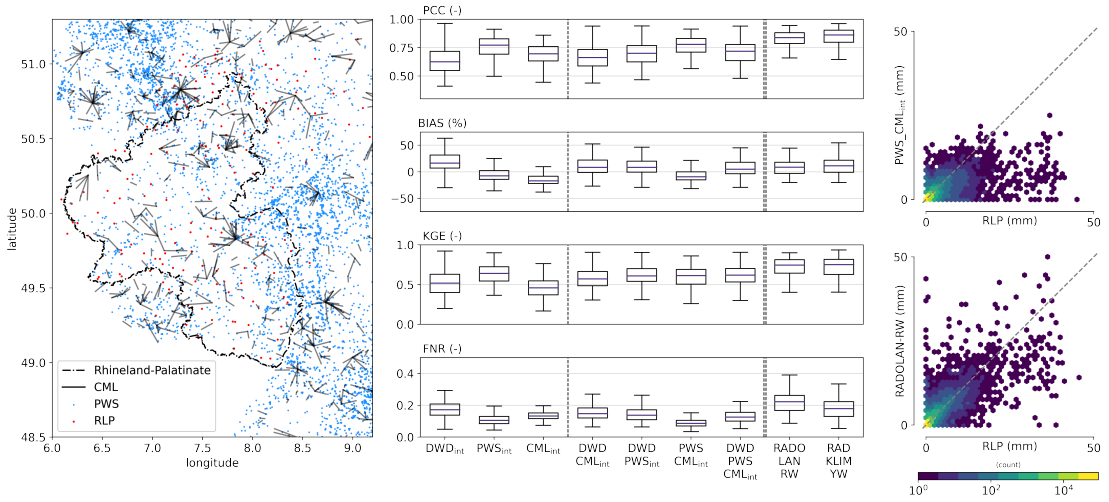

Figure 5.5: Map of Rhineland-Palatinate and surroundings with Rhineland-Palatinate gauges (reference), PWS locations and CML paths, boxplots of performance measures for the seven interpolated products as well as RADOLAN-RW and RADKLIM-YW against the reference. Dashed lines are similar to Fig. 5.4. On the right, scatter density plots of hourly PWS_CML$_{\text{int}}$ and RADOLAN-RW rain sums are compared to the reference.

erence with a high PCC. CML$_{\text{int}}$ and combinations reproduce the reference rainfall values slightly better than DWD$_{\text{int}}$. DWD$_{\text{int}}$ as well as the radar products show a positive bias. The reason could be the large distance of the next rain gauge which is also used to adjust the radar products. The next rain gauges on this local scale are more than 15 km away and not located in the area shown by Fig. 5.6. This could make a difference in the rather complex terrain at the border of the Swabian Alps. For the OS products the bias is almost zero. For the most intense events shown in the scatter plot of PWS_CML$_{\text{int}}$ the opportunistic sensors are underestimated by the interpolated product. Upon closer inspection all reference rainfall points above 20 mm were from an event on the 12th of June 2018 lasting 3 hours. While some of the PWSs resembled the reference gauges rainfall almost perfectly, others underestimated this event by a factor of ten. The two CMLs also underestimated the peak rainfall due to a complete loss of signal for a total of 12 and 21 minutes, respectively. We currently do not interpolate or fill gaps of this size in our processing. The rainfall sum of the hour with this data gap is treated as missing value. Hence, the one hour with the peak rainfall sum is missing from the CML data. This rainfall event is an interesting opportunity to study the ability and required processing steps to measure intense events with PWSs and CMLs in the future. First steps in this direction could be the improvement of the event based filter for PWS or filling CML outages caused by rain with the maximum of measurable rainfall at this CML.

Apart from the city of Reutlingen, there are few cities which operate such a dense and high quality network of rain gauges. Only with such a dense network of conventional rain gauges, we were able to evaluate the performance of opportunistic sensors on such a small scale. The opportunistic sensors show very good results in estimating rainfall on this local scale, therefore we conclude

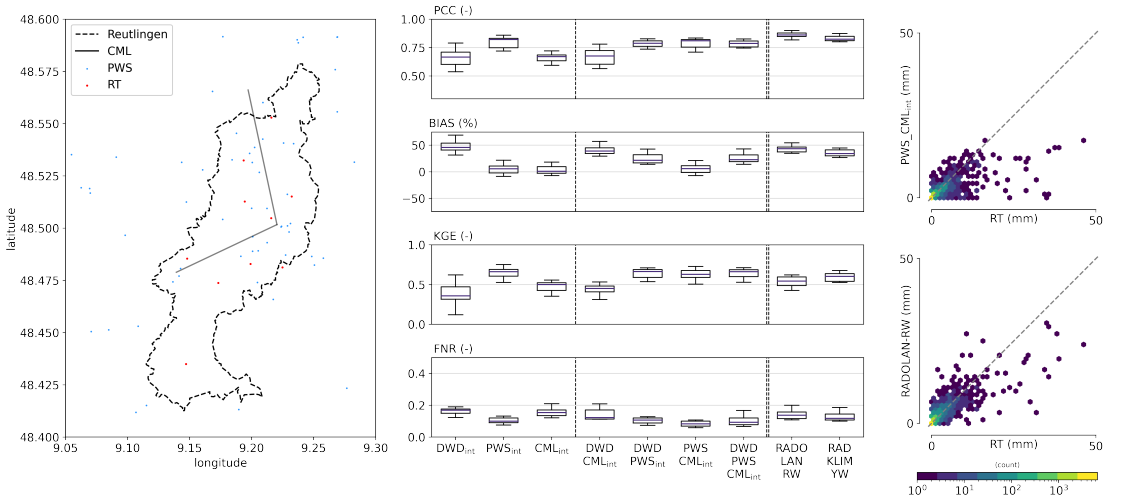

Figure 5.6: Map of Reutlingen with Reutlingen gauges (reference), PWS locations and CML paths, boxplots of performance measures for the seven interpolated products as well as RADOLAN-RW and RADKLIM-YW against the reference. Dashed lines are similar to Fig. 5.4. On the right, scatter density plots of hourly PWS_CML$_{int}$ and RADOLAN-RW rain sums are compared to the reference.

that rainfall information from PWSs and CMLs are highly valuable for the rainfall estimation in other urban areas with few or no conventional rain gauges. This opens the possibility to use opportunistic rainfall sensors for applications in urban hydrology for all cities with a similar sensor density.

5.4.3 Performance for high intensity rainfall

We investigated the potential of opportunistic sensors in capturing the most intense rain events with the leave one out cross validation results. We performed the same analysis as in Sec. 5.4.1 but only considered rain events above the 0.99 quantile level of each aggregation interval. The results in Fig. 5.7 show PCC, Spearman's rank correlation coefficient (SCC) and CV. The SCC defined in Appendix 5.6.3 is used here because it credits the skewed distribution of rainfall. For the PCC and CV the results are similar to the cross validation results for all rain events. PWS$_{int}$ and combinations with PWSs performed best, while the combination with CML was the overall best. CML$_{int}$ also outperformed DWD$_{int}$ for these two measures. Considering the SCC, the best results were obtained from PWS$_{int}$ without further combination. Both CML and DWD data could not add further information to increase the SCC. One reason for this might be the increased distance between CML and especially DWD sensors opposed by the high density of PWSs. For the SCC, DWD and CML performed similarly for one hour while DWD reaches higher values for aggregations between two and 120 hours.

For an analysis of the performance of the interpolated products and radar datasets for high in-

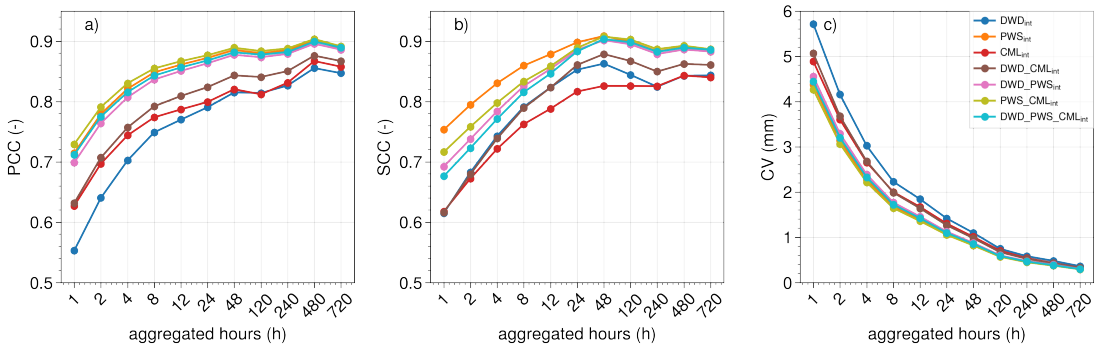

Figure 5.7: Performance measures of the cross validation for the 0.99 quantile of rain events for each temporal aggregation.

tensity rainfall for the regional and local scale we show the SCC hourly rainfall sums in Fig. 5.8. The German-wide scale is not shown as it is only available with a daily temporal resolution and an hourly evaluation for the whole of Germany is already covered by Fig. 5.7.
The three individual interpolated products show similar results, on both scales. As in Fig. 5.7, PWS_{int} shows the overall highest SCC while DWD_{int} reaches slightly higher values than CML_{int}. The combined interpolated products show a similar SCC as the radar products, except for DWD-CML_{int}. This again highlights the potential of exploiting dense opportunistic sensor networks on both regional and urban scales for hydrometeorologic purposes. For the radar products, the climatological adjustment seems to increase the SCC marginally.

The lower SCC values for CML_{int} on both scales could be caused by several reasons. One reason for this is the engineering requirements of the CML network which allows an outage of the systems during the strongest rainfall events for some minutes. This results in a maximum rain rate before signal loss between 40 mmh^{-1} and more than 150 mmh^{-1}, depending on the exact CML configuration (length, frequency, transmit power, antenna gain). Thus, for heavy rainfalls, CMLs do not always provide accurate rainfall information. Consequently, the rank correlation for high rain intensities is decreased for CMLs. Another reason is the integral character of the CMLs measurement which gives the path-averaged rain rate independently of the distribution of rain rates along the CMLs path. This leads to an underestimation of the highest rain rates along the path. Finally, the effect of the classification of rainy and dry periods in the CMLs processing has to be considered. Every wrong classification which can be caused by non-rain induced attenuation, multi-path propagation or others, will influence the FPR and FNR which ultimately have a large influence on the SCC. Considering all this, the hourly SCC of CML_{int} is still close to the one of the conventional rain gauge product DWD_{int}.

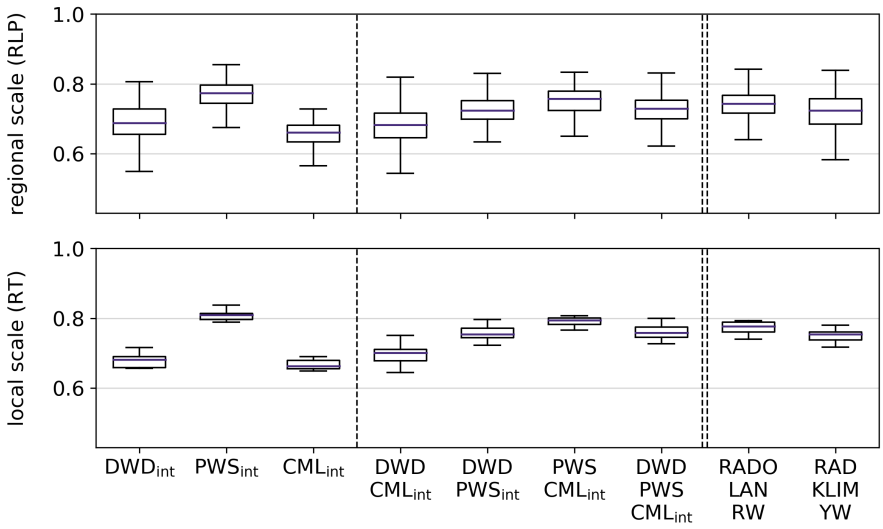

Figure 5.8: Spearman's rank correlation coefficient of interpolated products and radar products against the hourly references of Rhineland-Palatinate (regional scale), and Reutlingen (local scale).

5.4.4 Rain event example in Rhineland-Palatinate

To illustrate the interpolation framework results for the different datasets we show an example for several interpolated rainfall maps from different combinations and RADOLAN-RW in Rhineland-Palatinate in Fig. 5.9. On 12 July 2019 at 12:00 several rain cells are visible for all interpolation products and RADOLAN-RW. For some regions, the DWD_{auto} network misses rainfall because the station density is too sparse. This can be seen in the map showing the opportunistic sensors and DWD_{auto} stations locations. For DWD_{int} the underlying structure of the network is clearly visible. In comparison, PWS_CML_{int} shows more variability in the rainfall field and with most features related to several opportunistic sensors. The opportunistic sensors miss the most intense feature measured by the DWD_{auto} gauges in the north of Rhineland-Palatine, while PWS_{int} has the highest intensities further south. We presume that the increased variability due to the larger number of measurements should be closer to the true spatio-temporal distribution of rainfall. Most features and structures detected by RADOLAN-RW are visible in PWS_CML_{int}, while the radar product produces higher rainfall values. It seems that more (opportunistic) sensors lead to higher spatial variability in the interpolated rainfall fields, which could potentially improve hydrological applications.

5.5 Conclusion

The study region of Germany with two sub-regions, namely the state of Rhineland-Palatinate and the city of Reutlingen, are hydrometeorologically well monitored compared to most locations in the world and therefore provide a suitable testing ground to evaluate opportunistic rainfall sensors. In this study, we demonstrate the use of two different types of such opportunistic sensors.

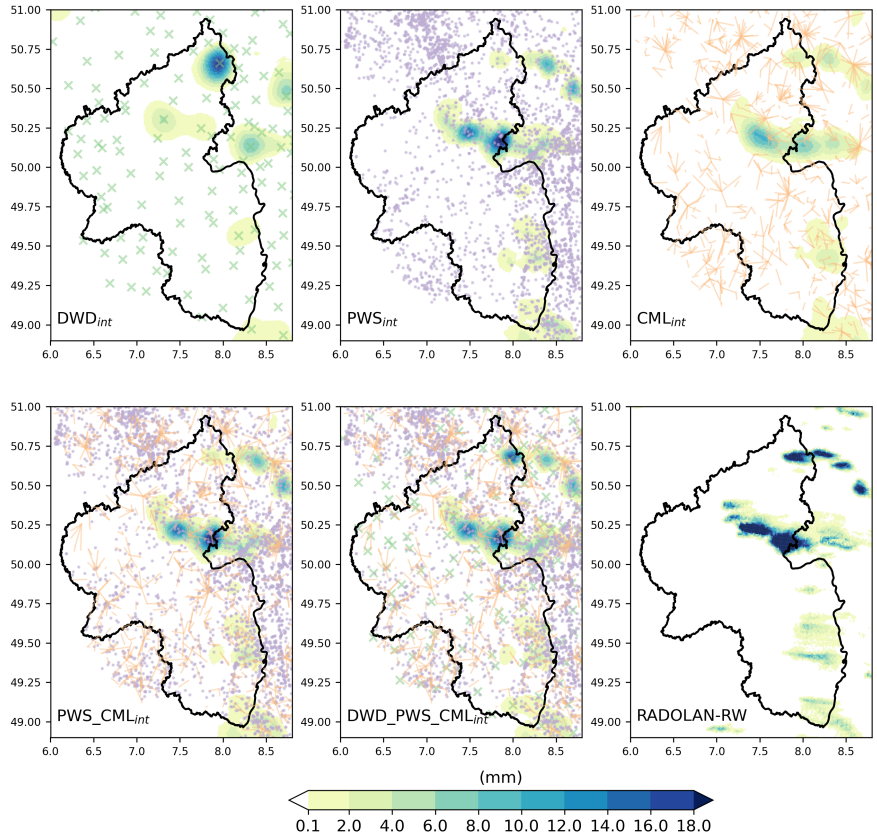

Figure 5.9: Rainfall example maps for one hour accumulated rainfall at 12.07.2019 12:00 CET for three different interpolation products, a radar product and their differences between each other.

We obtain rainfall fields, using a geostatistic interpolation framework incorporating block kriging, from point information of PWSs and line information of CMLs. Seven combinations of CML, PWS and official hourly rain gauge data from the DWD are evaluated for three different reference datasets in the respective study regions. Two radar products from the DWD were evaluated in the same manner as the interpolated datasets to further quantify the performance of the interpolated rainfall maps.

Both PWS and CML data come with individual drawbacks, e.g. unfavorable locations of PWSs or erratic fluctuations in the raw CML data. After the respective data retrieval and the rainfall estimation for the CMLs, both datasets are filtered with an indicator correlation and event based method and are bias corrected. Only then, they are used in different combinations with and without hourly rain gauge data from the DWD for interpolation. While the presented indicator correlation filter approach relies on a primary station network, the data from this network could potentially come from another period as the rain rates are compared and adjusted only by their

distribution functions. Besides very high rainfall events, i.e. with return periods of several years, the rainfall distribution for individual years as used in this study might not change this distribution too much. Hence, this approach could be usable for opportunistic sensors in areas where the number of rain gauges was reduced over the last decades because only their distribution function is needed. To use the indicator correlation filter, event based filter and the bias correction for data with higher temporal resolution than one hour, upcoming issues like the increasing number of zero precipitation events and the filtering of small-scaled extreme events which were not observed by the primary network (i.e. DWD gauges), have to be addressed. Potential solutions could be the usage of advection vectors or the mutual filtering of PWS and CML where one opportunistic sensor can serve as primary network for the other and vice versa. In this study, reliable CMLs were identified using the indicator correlation and event based filter and their values were corrected using the bias correction method. These methods accounted for the line characteristic of the CMLs measurement.

A cross validation shows the ability of CMLs and especially PWSs for rainfall mapping. This is true for hourly as well as for multi-day aggregations. The opportunistic sensors are able to produce reasonable rainfall maps with increased spatial variability compared to rainfall maps derived from conventional rain gauge data. These rainfall maps were evaluated country-wide for Germany with independent daily gauge data as reference and for Rhineland-Palatinate and Reutlingen with hourly gauge data as reference. To set the results of the evaluation in a perspective we used the official gauge adjusted radar datasets RADOLAN-RW and RADKLIM-YW from the DWD.

On the country-wide daily scale the radar products had a better agreement with the reference than the interpolated products. For the two sub-regions with an hourly resolution, the interpolated products performed similarly good as the radar products. The high number of opportunistic sensors might be the most import reason for this. Differences between the interpolated and radar products can be found especially for the highest rainfall amounts. Overall, interpolations incorporating PWS data performed best while the usage of CMLs resulted in better performance metrics as product from hourly DWD rain gauges. Similar results were found for the most intense rain events with the exception of CMLs which performed worse than the DWD product for temporal aggregations of several hours.

The results show the accuracy and increased spatial variability of rainfall maps from opportunistic sensors, especially on smaller spatial and temporal scales. Numerous hydrometeorological applications can potentially benefit from this information. The quick data availability could be used to access real-time rainfall information. Applications in urban hydrology could therefore benefit both from the potential real-time accessibility and the often dense opportunistic sensor network in this urban areas. Nevertheless, some of the presented methods, e.g. the indicator correlation filter, cannot readily be used for real-time applications but rather provide a baseline for such developments. Another opportunity is the combination with traditional gauge or radar datasets to derive a further improved joint product that leverages the individual advantages of all individual sensors.

Acknowledgements

We are grateful to Ericsson providing the CML data, and especially to Reinhard Gerigk, Michael Wahl, and Declan Forde for their ongoing support and cooperation. We would like to thank the State Agrometeorological Agency Rhineland-Palatinate, the State Environmental Agency Rhineland-Palatinate and the SER Reutlingen for providing the corresponding precipitation data. We also would like to thank the German Weather Service for providing rain gauge and radar data. This work was co-funded by the Helmholtz Association of German Research Centres within the "Digital Earth" project. We acknowledge support by the KIT-Publication Fund of the Karlsruhe Institute of Technology. We further want to thank two reviewers for their thorough work.

5.6 Appendices

5.6.1 Additional Figures

Fig. 5.A1; Fig. 5.A2; Fig. 5.A3

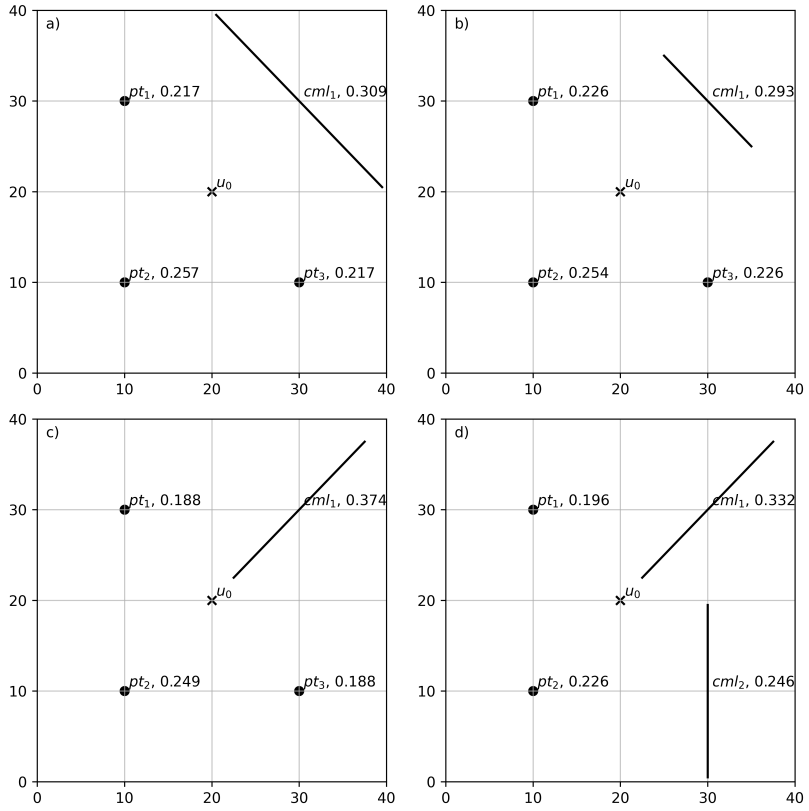

Figure 5.A1: Different weights $\mathbf{w}^T$ for points (pt_i) and line segments (cml_i) depending on their length and orientation for estimating the precipitation amount at a given location u_0. If the center of the CMLs in each of these four examples (a-d) were assumed to be point information, the weights of all points would be equal (here: 0.25). However, if the length and orientation of the CMLs are taken into account, different weights are obtained.

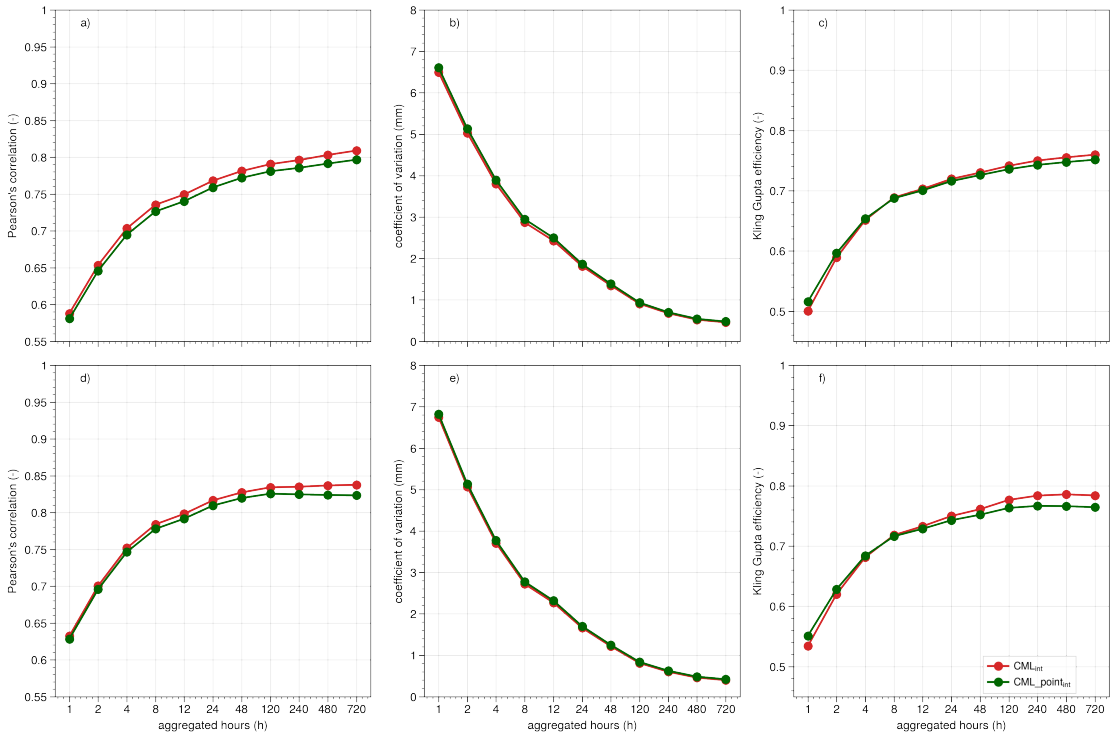

Figure 5.A2: Performance measures of the cross validation results from the interpolation framework for different temporal aggregations. Here CML_{int} and CML_point_{int} are shown. For CML_point_{int} the points at the center of each CML were used as point information in the interpolation framework. a) to c) show PCC, CV and KGE for country-wide validation stations and d) to f) show PCC, CV and KGE for validation stations with more than 80 PWSs or CMLs in 20 *km* vicinity. Those are the 10 percent of the validation station which are surrounded by the most opportunistic sensors.

5.6.2 Consideration of the CML length for the indicator correlation filter and bias correction

It is well known that the length, area or volume of an observation or measurement has an effect on the statistical properties of this observation. This so-called support effect has been intensively studied in geostatistics, mainly for mining applications. There are several approaches which can be used to calculate the change of variance as a function of the support size and the variogramm. Block Kriging, as applied in this paper is also taking the support size into account.

The different lengths of the CMLs have to be taken into account for the application of the indicator correlation filter and the bias correction. The classical geostatistical formulas cannot be used, as we consider the distribution of the values and not only their variances. Therefore, the following simulation based approach is considered.

The indicator correlation between the CML and a primary station is partly influenced by the orientation and the length of the CML. As the indicator correlation is independent of the marginal

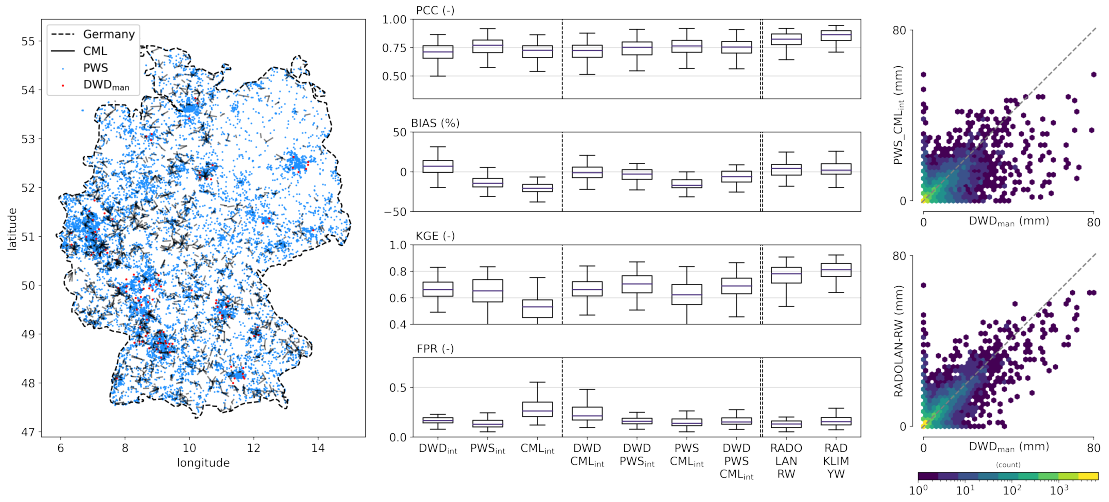

Figure 5.A3: Map of Germany with a subset of $\mathrm{DWD}_{\mathrm{man}}$ gauges (reference), PWS locations and CML paths, boxplots of performance measures for the seven interpolated products as well as RADOLAN-RW and RADKLIM-YW against the reference, and scatter density plots of daily PWS-CML and RADOLAN-RW rain sum compared to the reference. The subset of $\mathrm{DWD}_{\mathrm{man}}$ gauges compromises the 10 % of gauges which are surrounded by the most opportunistic sensors.

distribution only the dependence structure is of importance.
It is assumed that the spatial dependence of precipitation follows a normal copula. This is a frequent assumption, however not often stated explicitly.
This means that precipitation $Z(x,t)$ can be obtained from the realization of a spatially stationary normal process $Y(x,t)$ by a transformation:

$$Z(x,t) = F_x^{-1}\left(\Phi(Y(x,t))\right)$$

where $F_x()$ is the distribution function of precipitation for location x and $\Phi()$ is the distribution function of the standard normal distribution.

$$Z(L,t) = \frac{1}{|L|}\int_L Z(y,t)\,dy$$

From the point observations the spatial correlation function of the indicators can be calculated. This can be transformed to a correlation function of a normal Y $C_Y(h)$. With this correlation function realizations of Y can be simulated, and with the local distributions $F_y()$ realizations of $Z(x,t)$ and $Z(L,t)$ can be derived. Thereafter, the indicator correlations, and the distribution functions $F_L()$ of $Z(L,t)$ can be calculated. These distribution function can also be used for bias correction of the CMLs.
For the indicator correlations a good approximation can be obtained by replacing the line L by a specific point u, such that:

$$C_I(x,L) = C_I(x,u)$$

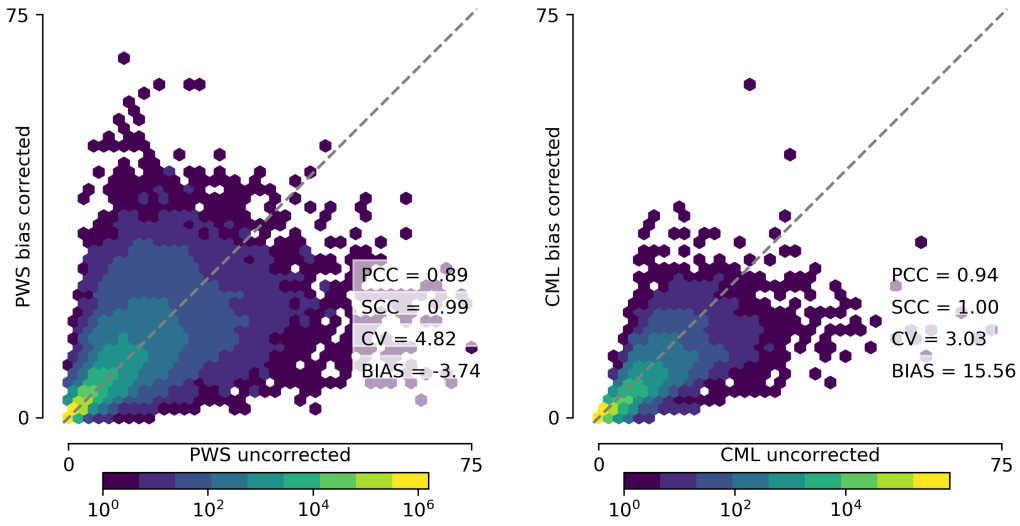

Figure 5.B1: Comparison of uncorrected and bias corrected hourly PWS and CML rain rates.

where

$$d(x,u) = d(x,L) = \frac{1}{L}\int_L d(x,y)\ dy$$

This means that for the indicator correlation filter which for CMLs with a primary network the CMLs have to be considered as $d(x,L)$ and not as the central point along its path L.
The same assumption can be used for the bias correction. To calculate the distribution of $Z(L,t)$ as a first step the distribution functions of the precipitation observations at the primary observations are interpolated for each point y of the line L. (In practice L is discretized to a few points.) This is done the same way as for the PWSs. Using these simulations the line averages can be calculated as follows:

$$Z(L,t) = \frac{1}{|L|}\int_L Z(y,t)\ dy = \frac{1}{|L|}\int_L F_y^{-1}\left(\Phi(Y(y,t))\right)\ dy$$

So a Monte Carlo simulation of Y can be used to obtain the distribution function of $Z(L,t)$. Due to the averaging procedure this distribution is different from the point distributions. For example, the probability of high values is reduced. Fig. 5.B1 shows the result of the bias correction for hourly rain rates.

5.6.3 Diagnostic values considered in this study

Here all used diagnostic values are described. The values which are evaluated (e.g. interpolated values from DWD_PWS_CML$_{\text{int}}$) are denoted as *pred* while the values from the references are denoted as ref. *std* refers to the standard deviation.

Pearson's correlation coefficient (PCC)

$$PCC = \frac{\sum_{i=1}^{n}(pred_i - \overline{pred})(ref_i - \overline{ref})}{\sqrt{\sum_{i=1}^{n}(pred_i - \overline{pred})^2 (ref_i - \overline{ref})^2}}$$

Coefficient of variation (CV)

$$CV = \frac{std \sum (pred - ref)}{\overline{ref}}$$

Kling-Gupta efficiency (KGE)

$$KGE = 1 - \sqrt{(r-1)^2 + (\alpha - 1)^2) + (\beta - 1)^2)}$$

where

$$\alpha = \frac{std(pred))}{std(ref))}$$

and

$$\beta = \frac{\overline{pred}}{\overline{ref}}$$

Spearman's rank correlation coefficient

$$SCC = 1 - \frac{6 \sum d_i^2}{n(n^2 - 1)}$$

where

$$d_i = rg(pred_i) - rg(obs_i)$$

and n is the number of considered time steps.

Bias

$$\text{bias} = \frac{\overline{(\text{pred} - \text{ref})}}{\overline{\text{ref}}}$$

Chapter 6

Synthesis

6.1 Summary

Rainfall affects many different aspects of human security. Estimating rainfall accurately in space and time is crucial for applications ranging from long-term water management decisions to short-term flash flood forecasting. However, traditional measurement systems such as rain gauges, weather radars, and satellite instruments are not always sufficient to capture rainfall accurately because of their individual limitations. Additionally, rain gauges and especially weather radars are not distributed evenly across the land surface. OS, such as CMLs and PWSs, can serve as additional sources of rainfall information. The number of these sensors has grown rapidly over the last decades exceeding that of traditional sensors many times over. The inconsistent quality of OS-derived rainfall estimates is a major scientific challenge and one of the main reasons why there is no widespread use of OS data in hydrological applications. To bridge this gap, this thesis aims to derive rainfall estimates from OS in a quality similar to operational rainfall products. Therefore, methods for quality control, rainfall estimation, and the merging of different sensors into one product were developed.

CMLs, which are a part of the cellular backhaul network, can be used to derive rainfall information through the relationship between rainfall and the attenuation of their microwave signal. In **Chapter 2:** *Rainfall estimation from a German-wide commercial microwave link network: Optimized processing and validation for one year of data* (Graf et al., 2020a) more than 4000 CMLs in Germany were used to develop, optimize and evaluate a range of CML processing methods over one year. Two filters removing erratic CMLs were developed and for the crucial processing step of rain event detection, an existing method was extended using a rolling standard deviation approach with a threshold dynamically adjusting to each CMLs behavior. This led to a reduction of misclassified time steps. To compensate for the wet antenna attenuation, a comparison and optimization of existing methods was conducted, which revealed that a rain-rate-dependent model performed best. All processing steps were combined in a parallelized, flexible processing framework, which was integrated into the open software package *pycomlink* (Chwala et al., 2022). Overall, this framework was able to provide rainfall estimates in good quality throughout Ger-

many for all seasons when compared to a reference, except for the winter season with non-liquid precipitation. As a reference, the rain gauge-adjusted weather radar product RADOLAN-RW from the Germany Weather Service (DWD) was chosen. To increase the comparability of the results to other studies, the evaluation was conducted for various subsets of rainfall intensities. Additionally, the first CML-derived rainfall maps covering Germany were produced using IDW interpolation.

While this large-scale evaluation of CMLs overall provided good results, some individual CMLs still showed large over- or underestimation. This motivated the further development of CML processing methods like in **Chapter 3:** *Rain event detection in commercial microwave link attenuation data using convolutional neural networks* (Polz et al., 2020). A convolutional neural network was trained to detect the patterns in the CML time series that were caused by rain. The model was trained with 800 CMLs over four months and validated using two different months for all 4000 CMLs. While increasing the amount of true negative classifications significantly, the number of true positive classifications only decreased slightly compared to the reference methods. By showing a similar performance for new CMLs and time periods the model could prove its ability to generalize to previously unseen data. When incorporating this rain event detection in the previously developed processing chain, a reduction of the amount of falsely classified rainfall by over 50% was shown. The CNN model proved to be a robust method for rain event detection for CML attenuation data.

Besides the improvement of CML processing steps, limitations of the CML attenuation observations have to be considered. **Chapter 4:** *Missing rainfall extremes in commercial microwave link data due to total loss of signal* (Polz et al., 2023b) investigated such a drawback which has implications on the usage of CML rainfall estimates in hydrological applications. CMLs can experience the total loss of signal caused by the strong attenuation of high rainfall intensities which ultimately leads to missing rainfall information. These so-called blackouts were investigated with three years of CML-based attenuation data and compared to a 20-year weather radar-based attenuation climatology. About 1% of rainfall was missing in the CML rainfall data due to blackouts. The number of blackouts observed from CML data exceeded the climatologically expected values by a magnitude which is explained by radar underestimation, high attenuation from hail or wet snow, and the difference in sampling volume. An unexpected finding was that blackouts occurred more often for longer CMLs despite the fact that these CMLs have a higher dynamic range to compensate for higher path-integrated attenuation. Both researchers and network providers can benefit from these findings by considering blackouts in CML rainfall estimation and network planning.

PWSs are another source of opportunistically sensed rainfall information. They are investigated in combination with CMLs and rain gauges in **Chapter 5:** *Rainfall estimates from opportunistic sensors in Germany across spatio-temporal scale* (Graf et al., 2021b). Data from around 20,000 PWSs were combined with 4,000 CMLs and 1,000 rain gauges from DWD to a total of seven rainfall products. The CML rainfall estimates were derived with the processing methods developed in this thesis. The data quality of the rainfall estimates from both OS was further ensured by a

set of filters previously used for PWSs and now extended for the usage with CMLs. The three datasets were combined by an interpolation framework accounting for the geometric properties of the CMLs which also considered the uncertainty of the two opportunistic sensors. The seven products were evaluated against three rain gauge datasets with different spatial scales and daily and hourly resolutions. Overall, products consisting of OS performed better than the ones containing DWD rain gauges. When OS-based and two radar products were compared against three rain gauge-based references, the OS-based products performed worse on a country-wide scale with a daily resolution but reached a similar performance as the radar products on a local and regional scale with an hourly resolution.

Overall, this thesis shows the development of methods for filtering, processing, and combining CML and PWS data. These developments were evaluated on large scales in Germany against different reference datasets. It could be proven that CML and PWS rainfall estimates and combined rainfall products can reach a similar quality as operational rainfall products.

6.2 Answers to the research questions

1. How do state-of-the-art processing methods perform, and how can they be optimized to provide high-quality CML rainfall estimates?

In Graf et al. (2020a) it was proven that it is possible to obtain rainfall estimates of good quality from CMLs throughout Germany with a single optimized processing routine. An important finding was that each CML needed an individual threshold for the rain event detection. This was solved by an adaptive threshold. Erratic CMLs were filtered out from the analysis in a similar manner and several methods for the compensation for wet antenna attenuation were compared to find the best one. As a result, the optimized processing routine provided CML rainfall estimates which compared well to the gauge-adjusted radar product used as a reference with Pearson's correlation coefficients of 0.75 to 0.85 at an hourly resolution. The CMLs performed similarly in all regions of Germany in spring, summer, and fall. During winter months, a strong overestimation was found which was likely caused by melting snow, which leads to significantly more attenuation than its rainfall equivalent. For the other seasons, a good agreement between the CML-derived rainfall sums and the reference was found for hourly, monthly, and seasonal aggregations. This one-year analysis proved the applicability of CMLs for rainfall estimation on a country-wide scale. Additionally, using a simple IDW interpolation scheme, country-wide rainfall maps could be shown. These maps showed plausible rainfall patterns and qualitatively compared well to the reference. Nevertheless, they also showed limitations caused by individual CMLs which under- or overestimated rainfall systematically and therefore motivated further improvements of the processing routine.

2. Can an artificial neural network for rain event detection improve CML derived rainfall estimates?

The reliable detection of rain events is an important CML processing step, as it defines the periods for which rainfall is estimated. Nevertheless, available methods are limited by either their need for neighboring observations and auxiliary data or do not consider signal patterns. Using a data-driven approach, Polz et al. (2020) overcame these limitations. The trained model was able to classify individual CML time series without the need for auxiliary or reference data. It showed a high success rate at separating actual rainfall patterns from noise. The CNN-based model was trained on a temporal and spatial subset of the available CML data but could classify data from new CMLs and time periods similarly well. This implies the robustness of the developed method. The quality of the rainfall estimates using the CNN rain event detection method combined with the processing framework of Graf et al. (2020a) led to an increase in the quality of rainfall estimates compared to previous methods and provided evidence that the CNN event detection improves the quality of CML rainfall estimates.

3. How many blackouts from heavy rainfall can be observed in CML data and how does this affect rainfall estimation?

Around 1% of yearly rainfall was missed by blackouts from an average of 20 minutes of missing signal at each CML. This loss of signal of a CML due to heavy rainfall is a consequence of CML network planning and predefined receiver capacity. The CML rainfall community did not consider this effect at all until Polz et al. (2023b) showed the influence of blackouts on rainfall estimates over three years of CML and 20 years of synthetic CML data derived from weather radar data in Germany. The number of blackout minutes per year depended heavily on the length of the CML in both real and synthetic CML data: The longer the CML, the more blackouts occurred. In the comparison of real and synthetic data, it was observed that the real CML data had around 8.5 times more blackouts than expected from synthetic data. When considering the effect on rainfall estimation, it was found that around 1 % of yearly rainfall was missed by the CMLs due to blackouts. Despite this marginal underestimation, it is highly relevant for the hydrometeorological community as this 1 % contains the most intense rainfall events.

4. How good is the performance of PWS and combined CML and PWS rainfall estimates considering various spatial scales in a large-scale evaluation?

Rainfall maps from PWSs and from combinations of PWSs and CMLs reached a quality similar to that of gauge-adjusted radar products on a regional (the state of Rhineland-Palatinate) and local (the city of Reutlingen) scale. To achieve this, robust quality control was imperative, as the data quality of PWSs relied on the correct setup and maintenance of private users, while rainfall estimates from individual CMLs suffered from fluctuations caused by factors other than rain that were not filtered by processing steps from previous chapters. Additionally, the fact that PWSs measure rainfall at the point scale and CMLs as path integral had to be taken into account during the spatial reconstruction of rainfall fields. Therefore, a filtering and bias correction routine, as well as a spatial reconstruction approach were developed in Graf et al. (2021b). As a result, German-wide rainfall maps with a resolution of one hour and 1 km could be evaluated

against different reference datasets on three spatial scales. On the country-wide scale with a daily resolution, operational gauge-adjusted radar products from DWD showed a better performance than OS-derived rainfall maps due to missing coverage in some parts and the advantage of the radar to measure over the whole of Germany. For both the regional and local scale with an hourly resolution, the OS-derived products achieved similar good performance measures as the operational radar products. PWSs, with their large number, contributed more to the good performance than CMLs which still outperformed the network of automated rain gauges from DWD. In conclusion, OS data could be used to derive rainfall products with high quality, especially on finer scales.

6.3 Rainfall estimation with opportunistic sensors: Discussion and conclusions

This thesis has shown that CMLs and PWS can offer robust rainfall estimates. Therefore, they offer the possibility to either increase the density of existing observation networks or deliver unique rainfall information in previously unobserved regions. The latter is more relevant for CMLs as they are available in most inhabited areas of the world, while PWSs can be found more frequently in developed countries. The main challenge in deriving robust rainfall information from OS lies in understanding and ensuring data quality and the improvement of processing routines. Two large-scale evaluations of CML and combined CML and PWS-derived rainfall estimates using five different reference datasets covering various scales gave evidence of reliable, high-quality OS-based rainfall estimates derived using methods developed in this thesis. This section discusses the methods used and the main findings to draw conclusions about the advantages and limitations of rainfall estimation with OS.

With the development of an appropriate processing routine, it could be shown that CMLs can provide robust rainfall estimates throughout the whole of Germany for one year in **Chapter 2**. One of the main goals for the development and optimization of this processing routine for CML rainfall estimation was to be independent, both of reference data and of the density of the CML network. This means that an individual time series of a CML without nearby reference data had to be sufficient to derive rainfall information from attenuation data. Such a situation is typical for regions like West Africa where CML data is available in an otherwise data-scarce environment. In the case when reference data is available, independently processed CMLs can provide rainfall estimates which are typically denser than the ones from a network of traditional ground observations. Additionally, due to individual network topology and the issues related to deriving CML attenuation data in the first place, one can not expect a certain density of a CML network which is necessary for processing methods like the "nearby link approach" published in the software package RAINLINK (e.g. Overeem et al., 2016a).

This motivated the goal of an independent processing routine which was achieved in **Chapter 2** and **3** and led to a good quality of the CML rainfall estimates. However, the usage of information from nearby CMLs or rainfall information from other sensors can certainly be of an advantage. This was shown, for example, in the indicator correlation filter and bias correction in **Chapter**

5, which compared CML and PWS data against DWD rain gauge data, further improving the quality of the OS rainfall estimates. Another possible application, where the use of additional rainfall information for the CML processing might be beneficial, can be found in the adjustment of weather radar data using CML data. The radar data can be used as a rain event classifier resulting in CML rainfall values for the adjustment only during periods where the radar observes rain.

The first step to derive high-quality CML rainfall estimates in an independent manner was to remove erratic CML data. Fluctuations not caused by rainfall were considered as the main source of false rainfall estimates in **Chapter 2**. Not filtering these anomalies decreased the performance of CML rainfall estimates due to overestimation and was especially noticeable through positive outliers in interpolated rainfall maps. A limitation of the developed filters is that they removed CMLs on a monthly basis and thus potentially removed more data than necessary, but at the same time, the filters are easy to apply and do not have a large computational demand.

The processing step of rain event detection is necessary for rainfall estimation in general, but can also remove erratic periods by not classifying them as rain. The method from Schleiss and Berne (2010) proved to be robust when combined with a dynamic threshold that was automatically adjusted by the general amount of fluctuation of each CML. Without this dynamical threshold, it would have been necessary to run one global optimization for all CMLs. A resulting global threshold used for each CML would have been too conservative for CMLs with very stable signal levels, resulting in missing small events, while for more noisy CMLs, too many false positive rain events would have been detected.

The finding that a better WAA compensation was achieved by methods using the rainfall intensity as a parameter was further reinforced by Pastorek et al. (2022) who compared five different methods and reached the same conclusion. Nevertheless, WAA remains a source of uncertainty as all methods are highly parameterized and the actual processes are not fully understood. Results from WAA-CML experiments observing multiple variables of the antenna and transmission properties are set up to better understand this phenomenon, but their results suggest even more chaotic behavior as Tiede et al. (2023) showed recently. It remains an open challenge to use information derived from such experiments to improve existing WAA models.

The comparison of CML rainfall estimates with the rain gauge adjusted weather radar product RADOLAN-RW along the CML paths generally showed good agreement, except for winter months. The weighted averaging of the radar reference along the CML paths' was an important methodological step. Only with such a direct comparison the advantages of radar data as a reference can be fully used and CMLs can be evaluated individually. This was not considered in the only other country-wide study conducted prior to the work from **Chapter 2** in the Netherlands (Overeem et al., 2016b). Also, previous CML studies often only considered one or a maximum of two (Overeem et al., 2016b) subset criteria when evaluating CML rainfall estimates against a reference (e.g. reference ≥ 0.1 mm, CML or reference ≥ 1 mm, ..). de Vos et al. (2019b) criticized the fact that different subset criteria were chosen by authors, which ultimately limits the

comparability between studies. Therefore, hourly CML and reference rainfall estimates were compared for five different subset criteria which resulted in remarkably different performance metrics, especially for the bias. This allowed for a better quantitative comparison to other studies which in turn showed the high quality of the results produced in **Chapter 2**. Recently, Wolff et al. (2022) followed our example and evaluated their CML rainfall estimates from a Dutch dataset using almost the same subset criteria. For future studies, it would be desirable to have common evaluation criteria, albeit the comparability between different methods will always be limited by the sampling strategies of different CML data acquisitions which have a direct influence on the design of these processing methods.

With a baseline for the whole processing chain provided in **Chapter 2**, the focus in **Chapter 3** was set on a single processing step, the rain event detection which separates a CML time series in rainy and dry periods. The data-driven method was able to outperform the reference method from **Chapter 2** and significantly increased the true negative rate while keeping the true positive rate almost constant. One reason for this success was the consideration of the imbalance in the model's training process, which was caused by the fact that rainfall in Germany only occurs between 5 and 10% of the time. Without manually balancing the number of wet and dry training samples equally, the CNN model would have classified too many wet samples as dry. The improvement of the classification method had a direct influence on the resulting rainfall estimates. It led to a reduction of the rainfall amount caused by time steps falsely classified wet by more than half and reduced the rainfall amount from missed events by more than a quarter. For rain rates above 1 mm/h the difference between the CNN-based classification and the dynamic threshold from **Chapter 2** was small, as the signal of strong rain events is easier to detect, independently of the used method. For rain rates below 0.5 mm/h, the performance of the CNN-based method was better. Still, both methods performed worse than for higher rain rates as the detection limit of each CML was reached. These detection limits depend on the TSL and RSL quantization, length, and frequency of each CML. The CNN performed better in this range because it could differentiate between the patterns caused by rain and the ones caused by other factors.

An important step in gaining confidence in the robustness of the CNN was to test its ability to correctly classify previously unknown CMLs and time periods. The ability of data-driven methods to interpret unseen data or predict results not present in the training data is subject to a long-term discussion in hydrological sciences (Klemeš, 1983; Todini, 2007). But there are many use cases for various problems that prove the ability of deep learning methods like long short-term memory (LSTM) networks and CNNs to deal with this issue (e.g. Reichstein et al., 2019; Frame et al., 2022) and extrapolate to e.g. previously unprecedented maxima. With the presented rain event detection method it could be shown that for previously unseen CMLs and new periods, only minor differences in performance were found compared to the performance of the model with the training data. These differences could be explained by the different distribution of rain rates in the respective datasets, where a larger amount of small rain rates near the detection limit of the CMLs in a given month resulted in a decreased performance of the model. Hence, the trust in the model was further strengthened. Another advantage of the CNN-based classification is its probabilistic nature. By altering the threshold for the probability of a time step to be rainy, a rather

conservative or liberal behavior of the classification can be chosen, depending on the intended use.

The development of the CNN, which included iterative training and validation, was computed on a Nvidia Titan Xp GPU. The final training took 30 minutes on that GPU. In direct comparison to the dynamic threshold method from **Chapter 2**, the CNN method increased the processing time for the rain event detection by a factor of ten, which was not a big issue when it was incorporated into the parallelized workflow developed in **Chapter 2**. The processing steps from **Chapter 2**, often together with the rain event detection method from **Chapter 3**, were used in the subsequent chapter of this thesis, by publications of our CML group (e.g. Blettner et al. (2022, 2023); Djibo et al. (2023b); Wagner et al. (2023)) and also by others e.g. Bubniak et al. (2022) using *pycomlink*.

A behavior not considered in **Chapters 2** and **3** was the absence of some of the more intense rainfall peaks observed in the radar reference. The reason for this was that only times steps where both CML and radar observations were available were evaluated. In a detailed analysis of individual events, it was later found, that heavy rainfall can lead to a total loss of signal and hence missing values in the CML rainfall series. This effect was investigated in detail in **Chapter 4**, which focused on the technical ability of CMLs to observe heavy rainfall rather than on improving the CML processing as in the previous chapters. Understanding this limitation is essential when using CMLs as rainfall sensors for hydrological applications, as the most intense rainfall events often have the most impact.

In most CML rainfall studies, blackouts were treated as missing values and therefore excluded from the evaluation (**Chapters 2** and **3** of this thesis, but also e.g. by Andersson et al. (2017); Fencl et al. (2014); Overeem et al. (2013a), or Wolff et al. (2022). Based on the results from **Chapter 4**, it can be concluded that on the one hand, the influence of blackouts on annual precipitation with around 1% is, in fact, neglectable, but on the other hand, this 1% consisted of the highest rainfall intensities. The surprising fact that there were 8.5 times more blackout minutes in the CML data than expected from the radar could not be explained completely with the available data. This difference was considered as an underestimation by radar which can be caused by several reasons: The different spatial integration characteristics of CML and radar could lead to different observations of heavy rainfall events, similar to the underestimation of rainfall extremes from radar in comparison to rain gauges (Peleg et al., 2018). For example, the average CML in the dataset has a length of 7 km which was compared to around 10 radar pixels covering 10 km^2 of radar data along its path. For the longer CMLs in the dataset, this area increased to over 30 km^2. Also, Radar products, even gauge-adjusted or polarimetric ones are reportedly prone to underestimate high rainfall intensities (Schleiss et al., 2020). An open question is how hydrometeors like hail lead to unexpected high attenuation of the CML signal while melting snow could be ruled out as the reason for the underestimation based on the analysis of the ambient temperature during blackouts.

From the perspective of mobile network operators, rainfall is just an unwanted source of attenuation, which has to be considered in network planning. The ITU recommends that a CML should be available for more than 99.9 % per year and gives instructions on how to calculate maximal rainfall intensities for given temporal aggregations and return periods from rain gauge data as

the basis for the CMLs' layout (ITU-R, 2017). While this 99.9 % availability was met by almost all CMLs in our dataset, from a hydrometeorologists point of view, a larger dynamic range for all and especially longer CMLs would be desirable. The finding that longer CMLs suffered more often from blackouts can either be interpreted as a shortcoming of the suggested calculations for planning the layout of CMLs from the ITU or as a miscalculation in the actual planning done by the mobile network operator.

The results of this chapter have an influence on the future development, application, and evaluation of the methods presented in **Chapters 2** and **3** of this thesis. The mitigation approach proposed in **Chapter 4** which estimates a minimum rain rate during blackouts based on their highest measured attenuation, was investigated in Graf et al. (2023). It led to an overall improvement of rainfall estimates compared to no mitigation measures and to a more consistent time series of CML-derived rainfall estimates for evaluation. The information of a minimum rainfall amount could also be used by probabilistic methods like the stochastic reconstruction approach random mixing (Hörning and Haese, 2021) that could use this information as a constraint in the spatial reconstruction of rainfall maps.

PWSs are another type of OS that have not been evaluated quantitatively on a large until **Chapter 5** combined data from PWS, CMLs, and rain gauges for a two-year period covering Germany to generate high-resolution rainfall maps. In addition to the CML processing developed in **Chapters 2** and **3**, a three-step filtering and bias correction routine and an interpolation framework were developed. By evaluating the rainfall maps on three spatial and two temporal scales over two years it was found that the combination of CML and PWS data was able to reach similar high quality as rain gauged-adjusted weather radar products from DWD in Germany.

Compared to the filtering methods from **Chapter 2**, which were developed to work without reference data and achieved good results on the comparison to reference data on a link path base, rain gauge data was used for the filtering routine in this case. The reason for this was that for CMLs erratic fluctuations from individual CMLs and during short periods were not filtered by the previous methods which sometimes resulted in sharp outliers in the hourly rainfall maps. We, therefore, used an additional filtering routine first developed for PWSs in Bárdossy et al. (2021) and adopted it to account for the line characteristic of the CML rainfall estimates. This was an important step as the statistical properties of a measurement change with the sampling volume. While for PWS the filtering and bias correction was necessary due to non-conform setup or calibration, for CMLs the bias correction served as an adjustment of the parameterized steps of the CML processing, mainly WAA compensation, for each individual CML. A limitation of these proposed methods for quality control is that it is limited to an area with a fairly dense network of reference observations.

One of the main reasons for the good performance of OS and especially PWS-based rainfall maps and one of their major advantages, in general, is their vast number. After filtering out unreliable OS, between 14,000 and 18,000 individual sensors were available. This number is a magnitude higher than the number of rain gauge stations operated by the DWD. After combining these

three sensor types in the seven possible combinations, it was interesting to find that the best performance was not achieved by the combination of all three sensors, but by PWS and the combinations with either CML or DWD rain gauges. It might be that the rain gauges from DWD, being the most reliable sensors and therefore receiving the highest weight in the interpolation framework, lack the spatial density to improve the overall performance. Therefore, the weights of the rain gauges might not be justified and thus, similar to the OS, an uncertainty factor based on the relation between sill and nugget could be considered to derive variograms from the rain gauges.

For the generation of rainfall maps, previous CML studies often used the center of a CML as point information for IDW or kriging, which does not give justice to the sampling volume of a CML. Other methods like random mixing (Haese et al., 2017) or tomographic reconstruction (D'Amico et al., 2016) are computationally demanding or highly underdetermined. To overcome these limitations, a combination of ordinary and block kriging was developed which is able to consider the line characteristic of the CMLs in the block kriging type approach and which accounts for the uncertainty of individual sensors.

While radar products showed a better performance than OS products in the evaluation on the country-wide scale with a daily resolution, the OS products performed similarly well on the regional and local scale with an hourly resolution. A reason for the worse performance of OS on the country-wide scale was that especially in the northeastern part of Germany the OS density is quite low. An interpolated product from $\mathrm{DWD}_{\mathrm{auto}}$, despite being the most precise measurement device, achieved the worst performance caused by its limited spatial representativeness on the regional and local scale. As a consequence, applications like hydrological modeling which often rely on traditional rain gauge datasets as input could benefit from the use of OS which can deliver more accurate rainfall estimates and have an increased spatial variability which is considered a main driver for hydrological modeling (Cristiano et al., 2017).

One of the main limitations of the two OS considered here is that non-liquid precipitation cannot be measured accurately. For PWSs, this is because they are not heated. The readings therefore either can be misplaced in time when snow melts in the orifice of the device or underestimate the true precipitation amount due to wind removing snow from the orifice. For CMLs, the $k - R$ relation for solid and mixed-type precipitation is different from the one for rainfall. While dry snow leads to almost no attenuation, melting snow, hail, or sleet cause very strong attenuation and therefore overestimation of these events. This was the main reason why only months without solid precipitation were analyzed in **Chapters 3** and **5**.

As the article of **Chapter 5** was published before the work for **Chapter 4** was conducted, blackouts were not considered. Therefore, the underestimation of CMLs, both for the three different scales, as well as for the consideration of high-intensity rainfall, can be partly attributed to the occurrence of blackouts. In the performance analysis for high-intensity rainfall, only rain events above the 0.99 quantile level were considered. This corresponded well to the 1% of missing rainfall due to blackouts. Considering this and that the CMLs correlation to the reference for high-intensity rainfall is only slightly worse than that of the DWD rain gauges, the uncertainty of the

CML rainfall estimates is partly compensated by their larger number. In summary, it could be shown that reliable rainfall estimates can be derived from the combination of CML and PWS data.

The key to products of such quality was the development of methods for filtering, processing, and combining CML and PWS data. This summarizes the main findings of this thesis. CMLs and PWS can be used alone or in combination with traditional rainfall observations in any region where they are available. This was proved by first-of-its-kind evaluations across Germany which were able to show the high quality of OS rainfall products can achieve. Overall it can be concluded that CMLs and PWSs can be used to obtain rainfall products with a quality similar to operational gauge-adjusted weather radar products when their data is treated with care.

6.4 Outlook

Applications of the developed methods

This thesis mainly built on data from 4000 CMLs and 20,000 PWSs to develop and evaluate new methods for filtering, processing, and interpolating these OS. These datasets are among the largest of their kind, hence certain robustness of the methods can be assumed. Additionally, other datasets are already used to further evaluate these methods covering a region around Gothenburg with the openMRG dataset from Andersson et al. (2022) and in Burkina Faso within the BMBF-funded project AgRAIN (`https://www.agrain.eoc.dlr.de/`).

The openMRG dataset is used for a comparison of different CML processing frameworks within the EU Cost Action OPENSENSE which started in 2021 (`https://opensenseaction.eu/`). This project consists of OS experts, stakeholders, and national meteorological services from over 30 countries with a focus on the opportunistic sensing of rainfall. The first results of the comparison between the approach developed in this thesis and the nearby link approach from Overeem et al. (2016a) further confirm the robustness of these methods. Other activities of OPENSENSE that use methods and knowledge from this thesis include the definition of data formats and standards, a training school on *Software and methods on data processing from opportunistic rainfall sensors* (`https://indico.scc.kit.edu/event/3645/`), the comparison of merging techniques of OS and traditional rainfall sensors, and the preparation of dissemination material (`https://www.youtube.com/watch?v=yJXft_V1ky4`).

In AgRAIN, 300 CMLs in Ouagadougou, the capital of Burkina Faso, were processed successfully with the routine developed in **Chapter 2** resulting in 5-minute rainfall maps over the city. The only adaption needed was to filter out spikes (strong positive outliers at individual time steps) and steps (sudden change in the baseline of a CML) which are likely caused by the local data acquisition system. The validation of the CML rainfall maps is rather difficult with just one rain gauge with a daily resolution available in Ouagadougou, a situation typical for this region of the world. The aggregated rainfall maps correlated highly (>0.95) with the rain gauges' values on a daily basis. The timing of rainfall in the CML rainfall maps matched the timing of GPM-IMERG products which have a 30-minute resolution. These results were published recently in

Djibo et al. (2023b) an animated example of a rain event with a 5-minute resolution can be found here: `https://zenodo.org/record/8032918`.

In a further application the rain event detection methods from **Chapter 2** and **3** are combined with MSG SEVIRI satellite data. Rainfall probabilities from MSG SEVIRIS and the rain event detection methods are combined in such a way that highly likely classifications from each of the three rain event detection methods are trusted most. Overall, this leads to a slight increase of the MCC compared to a radar reference, but more importantly, the classification for CMLs with problematic signal time series, i.e., strong fluctuations during wet and dry periods, could be improved significantly. A pre-print summarizing this combination of rain event detection methods and results is currently under review (Wagner et al., 2023).

Future improvements of filtering and processing methods

CML and PWS data are on the verge of being used operationally in different hydrometeorological applications as robust methods like the ones developed in this thesis are used to ensure their data quality. Nevertheless, quality issues are still encountered when checking individual rain events. Therefore, such methods have to be tested and improved continuously as OS data will always be more challenging to handle than data from traditional rainfall sensors. All filtering and processing steps can potentially be improved by combining information from CML and PWS data, or by using traditional rainfall observations For instance, the filters relying on a primary network of trustworthy rain gauges (indicator correlation filter, on-event filter, and bias correction from **Chapter 5**) could be tested with CML rainfall estimates instead of rain gauge data from DWD. Another possibility would be the classification of rain events in CML time series with the help of nearby PWSs. Further improvements could be achieved when focusing on OS processing on very short time scales i.e. sub-hourly scales. This will require an adjustment of filters to incorporate advection and to account for zero-inflated problems which increase with temporal resolution. To use these filters in real-time applications, some of the developed methods e.g. the indicator correlation filter must be modified. Here again, the mutual use of CMLs and PWSs as primary and secondary networks could be a possible solution due to their timely availability.

Another pathway to improve OS rainfall estimates is the use of multivariate meteorological information. This information could stem from OS, like PWSs themselves, but also from station or remote sensing data. As an example, local convective events could be investigated by using temperature and air pressure data of the PWSs to detect so-called cold pools (temperature drops and air pressure spikes due to heavy rainfall). For CMLs, a relation between erratic signal fluctuations and a range of meteorological parameters was already noted (Chwala and Kunstmann, 2019) but these influences are yet to be quantified. Examples are the influence of temperature and radiation from the sun on the antenna as well as oscillations of cellular towers due to wind. With a better knowledge of the interactions between CML signal strength and meteorological variables, the number of false-positive rainfall estimates could be reduced.

CMLs used in weather radar adjustment

The opportunity to combine OS with traditional rainfall sensors like rain gauges or weather radars should be investigated in more detail. First experiments were already conducted to combine CML-derived rainfall information with rain gauges (Fencl et al., 2017) and weather radar (Liberman et al., 2014; Trömel et al., 2014). The vast number of OS and the fact that CMLs and PWSs provide rainfall information on the ground offer great potential in the adjustment and validation of weather radar and satellite measurements.

National weather services from France, Sweden, Norway, and Germany are in the early phases of using OS operationally. A first analysis from Mapiam et al. (2022) showed that a bias correction using PWSs could increase the performance of the weather radar data compared to using operational rain gauges alone. Further, improved joint products can leverage the individual advantages of OS through their vast number, spatial representation, and timely availability. On a larger scale, a pre-print from Overeem et al. (2023) showed that PWS are able to reduce the underestimation of a pan-European weather radar product over one year.

A further advantage of CMLs and PWS is their potential to deliver rainfall estimates in near-real time as shown by Chwala et al. (2016) for CMLs and by a number of websites presenting real-time PWS data (e.g. Netatmo or weather underground). This allows for timely merging with weather radar data and hence, faster access to rainfall information valuable in flood warnings especially in small catchments. The first steps towards operationalization of a CML and rain gauge-adjusted weather radar were undertaken in Germany within the BMBF project HoWa-innovativ which could show the improvement through the adjustment radar rainfall fields with CMLs. An operationalized merging routine is being developed in the successor project HoWa-PRO right now and the evaluation of the results is underway (`https://www.wasser.sachsen.de/howa-pro.html`). A case study for the severe flooding in the Arhtal, Germany in 2021 could already show that a CML-adjusted radar product outperforms a gauge-adjusted radar product. This shows that the main goal of this thesis was reached. OS now overcome the phase where their potential has to be proven and reach a degree of trustworthiness, with respect to their actual limitations, that was only given to traditional rainfall observations before. When treated with care, opportunistically sensed rainfall data from CMLs and PWSs can be used successfully in real-world applications.

Bibliography

R. F. Adler, C. Kidd, G. Petty, M. Morissey, and H. M. Goodman. Intercomparison of Global Precipitation Products: The Third Precipitation Intercomparison Project (PIP-3). Bulletin of the American Meteorological Society, 82(7), July 2001. doi: 10.1175/1520-0477(2001)082⟨1377:IOGPPT⟩2.3.CO;2.

H. Akoglu. User's guide to correlation coefficients. Turkish Journal of Emergency Medicine, 18 (3), Sept. 2018. doi: 10.1016/j.tjem.2018.08.001.

P. Allamano, A. Croci, and F. Laio. Toward the camera rain gauge. Water Resources Research, 51(3), 2015. doi: https://doi.org/10.1002/2014WR016298.

J. Andersson, P. Berg, J. Hansryd, A. Jacobsson, J. Olsson, and J. Wallin. Microwave Links Improve Operational Rainfall Monitoring in Gothenburg, Sweden. In Proc. CEST, Aug. 2017.

J. C. M. Andersson, J. Olsson, R. C. Z. . van de Beek, and J. Hansryd. OpenMRG: Open data from Microwave links, Radar, and Gauges for rainfall quantification in Gothenburg, Sweden. Earth System Science Data, 14(12), Dec. 2022. doi: 10.5194/essd-14-5411-2022.

J. Arnault, B. Fersch, T. Rummler, Z. Zhang, G. M. Quenum, J. Wei, M. Graf, P. Laux, and H. Kunstmann. Lateral terrestrial water flow contribution to summer precipitation at continental scale – A comparison between Europe and West Africa with WRF-Hydro-tag ensembles. Hydrological Processes, 35(5), 2021. doi: https://doi.org/10.1002/hyp.14183.

D. Atlas and C. W. Ulbrich. Path- and Area-Integrated Rainfall Measurement by Microwave Attenuation in the 1–3 cm Band. Journal of Applied Meteorology, 16(12), Dec. 1977. doi: 10.1175/1520-0450(1977)016⟨1322:PAAIRM⟩2.0.CO;2.

P. Baldi, S. Brunak, Y. Chauvin, C. A. F. Andersen, and H. Nielsen. Assessing the accuracy of prediction algorithms for classification: an overview. Bioinformatics, 16(5), May 2000. doi: 10.1093/bioinformatics/16.5.412.

G. Balsamo, A. Agusti-Panareda, C. Albergel, G. Arduini, A. Beljaars, J. Bidlot, E. Blyth, N. Bousserez, S. Boussetta, A. Brown, R. Buizza, C. Buontempo, F. Chevallier, M. Choulga, H. Cloke, M. F. Cronin, M. Dahoui, P. De Rosnay, P. A. Dirmeyer, M. Drusch, E. Dutra, M. B. Ek, P. Gentine, H. Hewitt, S. P. E. Keeley, Y. Kerr, S. Kumar, C. Lupu, J.-F. Mahfouf, J. McNorton, S. Mecklenburg, K. Mogensen, J. Muñoz-Sabater, R. Orth, F. Rabier, R. Reichle,

B. Ruston, F. Pappenberger, I. Sandu, S. I. Seneviratne, S. Tietsche, I. F. Trigo, R. Uijlenhoet, N. Wedi, R. I. Woolway, and X. Zeng. Satellite and In Situ Observations for Advancing Global Earth Surface Modelling: A Review. Remote Sensing, 10(12), Dec. 2018. doi: 10.3390/rs10122038.

L. Bao, J. Hansryd, T. Danielson, G. Sandin, and U. Noser. Field trial on adaptive modulation of microwave communication link at 6.8GHz. In 2015 9th European Conference on Antennas and Propagation (EuCAP), Apr. 2015.

H. Bartels, E. Weigl, T. Reich, P. Lang, A. Wagner, O. Kohler, and N. Gerlach. Routineverfahren zur Online-Aneichung der Radarniederschlagsdaten mit Hilfe von automatischen Bodenniederschlagsstationen(Ombrometer). Technical report, DWD, 2004.

L. Barthès and C. Mallet. Rainfall measurement from the opportunistic use of an Earth–space link in the Ku band. Atmospheric Measurement Techniques, 6(8), Aug. 2013. doi: https://doi.org/10.5194/amt-6-2181-2013.

S. Bell, D. Cornford, and L. Bastin. The state of automated amateur weather observations. Weather, 68(2), 2013. doi: https://doi.org/10.1002/wea.1980.

S. Berkler, T. Bettman, M. Böhm, N. Demuth, N. Gerlach, and A. Hengst. Hochwasser im Juli 2021. Technical report, Landesamt für Umwelt Rheinland-Pfalz, 2022.

A. Berne and W. F. Krajewski. Radar for hydrology: Unfulfilled promise or unrecognized potential? Advances in Water Resources, 51, Jan. 2013. doi: 10.1016/j.advwatres.2012.05.005.

A. Berne and R. Uijlenhoet. Path-averaged rainfall estimation using microwave links: Uncertainty due to spatial rainfall variability. Geophysical Research Letters, 34(7), 2007. doi: 10.1029/2007GL029409.

A. Berne, G. Delrieu, J.-D. Creutin, and C. Obled. Temporal and spatial resolution of rainfall measurements required for urban hydrology. Journal of Hydrology, 299(3), Dec. 2004. doi: 10.1016/j.jhydrol.2004.08.002.

V. Blauhut, M. Stoelzle, L. Ahopelto, M. I. Brunner, C. Teutschbein, D. E. Wendt, V. Akstinas, S. J. Bakke, L. J. Barker, L. Bartošová, A. Briede, C. Cammalleri, K. C. Kalin, L. De Stefano, M. Fendeková, D. C. Finger, M. Huysmans, M. Ivanov, J. Jaagus, J. Jakubínský, S. Krakovska, G. Laaha, M. Lakatos, K. Manevski, M. Neumann Andersen, N. Nikolova, M. Osuch, P. van Oel, K. Radeva, R. J. Romanowicz, E. Toth, M. Trnka, M. Urošev, J. Urquijo Reguera, E. Sauquet, A. Stevkov, L. M. Tallaksen, I. Trofimova, A. F. Van Loon, M. T. H. van Vliet, J.-P. Vidal, N. Wanders, M. Werner, P. Willems, and N. Živković. Lessons from the 2018–2019 European droughts: a collective need for unifying drought risk management. Natural Hazards and Earth System Sciences, 22(6), June 2022. doi: 10.5194/nhess-22-2201-2022.

N. Blettner, C. Chwala, B. Haese, S. Hörning, and H. Kunstmann. Combining Commercial Microwave Link and Rain Gauge Observations to Estimate Countrywide Precipitation: A Stochastic Reconstruction and Pattern Analysis Approach. Water Resources Research, 58(10), 2022. doi: 10.1029/2022WR032563.

N. Blettner, M. Fencl, V. Bareš, H. Kunstmann, and C. Chwala. Transboundary Rainfall Estimation Using Commercial Microwave Links. Earth and Space Science, 10(8), 2023. doi: 10.1029/2023EA002869.

J. Bliefernicht, S. Salack, M. Waongo, T. Annor, P. Laux, and H. Kunstmann. Towards a historical precipitation database for West Africa: Overview, quality control and harmonization. International Journal of Climatology, 2021. doi: 10.1002/joc.7467.

L. Bottou, F. E. Curtis, and J. Nocedal. Optimization Methods for Large-Scale Machine Learning. SIAM Review, 60(2), Jan. 2018. doi: 10.1137/16M1080173.

C. C. Brauer, A. Overeem, H. Leijnse, and R. Uijlenhoet. The effect of differences between rainfall measurement techniques on groundwater and discharge simulations in a lowland catchment. Hydrological Processes, 30(21), 2016. doi: 10.1002/hyp.10898.

A. Bronstert, A. Agarwal, B. Boessenkool, I. Crisologo, M. Fischer, M. Heistermann, L. Köhn-Reich, J. A. López-Tarazón, T. Moran, U. Ozturk, C. Reinhardt-Imjela, and D. Wendi. Forensic hydro-meteorological analysis of an extreme flash flood: The 2016-05-29 event in Braunsbach, SW Germany. Science of The Total Environment, 630, July 2018. doi: 10.1016/j.scitotenv.2018.02.241.

M. Bubniak, P. Musil, P. Mlýnek, L. Benesl, and M. Rusz. Design and Evaluation of the Application for a Measurement of Rainfall via Microwave Links. In 2022 14th International Congress on Ultra Modern Telecommunications and Control Systems and Workshops (ICUMT), Oct. 2022. doi: 10.1109/ICUMT57764.2022.9943528.

Bundesnetzagentur. Bundesnetzagentur: Tätigkeitsbericht Telekommunikation 2016/2017, Tech. rep., Report 2016/2017, Bundesnetzagentur für Elektrizität, Gas, Telekommunikation, Post und Eisenbahnen, Bonn, 2017.

A. Bárdossy and G. Pegram. Combination of radar and daily precipitation data to estimate meaningful sub-daily point precipitation extremes. Journal of Hydrology, 544, Jan. 2017. doi: 10.1016/j.jhydrol.2016.11.039.

A. Bárdossy, J. Seidel, and A. El Hachem. The use of personal weather station observations to improve precipitation estimation and interpolation. Hydrology and Earth System Sciences, 25 (2), Feb. 2021. doi: https://doi.org/10.5194/hess-25-583-2021.

A. Bárdossy, J. Seidel, M. Eisele, A. El Hachem, H. Kunstmann, C. Chwala, M. Graf, N. Demuth, and N. Gerlach. Verbesserung der Abschätzung von Gebietsniederschlägen mittels opportunistischer Niederschlagsmessungen am Beispiel des Ahr-Hochwassers im Juli 2021. Projektbericht HyWa, 66, 2022.

L. Båserud, C. Lussana, T. N. Nipen, I. A. Seierstad, L. Oram, and T. Aspelien. TITAN automatic spatial quality control of meteorological in-situ observations. In Advances in Science and Research, volume 17, July 2020. doi: 10.5194/asr-17-153-2020.

K. Calvin, D. Dasgupta, G. Krinner, A. Mukherji, P. W. Thorne, C. Trisos, J. Romero, P. Aldunce, K. Barrett, G. Blanco, W. W. Cheung, S. Connors, F. Denton, A. Diongue-Niang, D. Dodman, M. Garschagen, O. Geden, B. Hayward, C. Jones, F. Jotzo, T. Krug, R. Lasco, Y.-Y. Lee, V. Masson-Delmotte, M. Meinshausen, K. Mintenbeck, A. Mokssit, F. E. Otto, M. Pathak, A. Pirani, E. Poloczanska, H.-O. Pörtner, A. Revi, D. C. Roberts, J. Roy, A. C. Ruane, J. Skea, P. R. Shukla, R. Slade, A. Slangen, Y. Sokona, A. A. Sörensson, M. Tignor, D. Van Vuuren, Y.-M. Wei, H. Winkler, P. Zhai, Z. Zommers, J.-C. Hourcade, F. X. Johnson, S. Pachauri, N. P. Simpson, C. Singh, A. Thomas, E. Totin, P. Arias, M. Bustamante, I. Elgizouli, G. Flato, M. Howden, C. Méndez-Vallejo, J. J. Pereira, R. Pichs-Madruga, S. K. Rose, Y. Saheb, R. Sánchez Rodríguez, D. Ürge Vorsatz, C. Xiao, N. Yassaa, A. Alegría, K. Armour, B. Bednar-Friedl, K. Blok, G. Cissé, F. Dentener, S. Eriksen, E. Fischer, G. Garner, C. Guivarch, M. Haasnoot, G. Hansen, M. Hauser, E. Hawkins, T. Hermans, R. Kopp, N. Leprince-Ringuet, J. Lewis, D. Ley, C. Ludden, L. Niamir, Z. Nicholls, S. Some, S. Szopa, B. Trewin, K.-I. Van Der Wijst, G. Winter, M. Witting, A. Birt, M. Ha, J. Romero, J. Kim, E. F. Haites, Y. Jung, R. Stavins, A. Birt, M. Ha, D. J. A. Orendain, L. Ignon, S. Park, Y. Park, A. Reisinger, D. Cammaramo, A. Fischlin, J. S. Fuglestvedt, G. Hansen, C. Ludden, V. Masson-Delmotte, J. R. Matthews, K. Mintenbeck, A. Pirani, E. Poloczanska, N. Leprince-Ringuet, and C. Péan. IPCC, 2023: Climate Change 2023: Synthesis Report. Contribution of Working Groups I, II and III to the Sixth Assessment Report of the Intergovernmental Panel on Climate Change [Core Writing Team, H. Lee and J. Romero (eds.)]. IPCC, Geneva, Switzerland. Technical report, Intergovernmental Panel on Climate Change (IPCC), July 2023.

G. Cazzaniga, C. De Michele, M. D'Amico, C. Deidda, A. Ghezzi, and R. Nebuloni. Hydrological response of a peri-urban catchment exploiting conventional and unconventional rainfall observations: the case study of Lambro Catchment. Hydrology and Earth System Sciences, 26(8), Apr. 2022. doi: 10.5194/hess-26-2093-2022.

A. B. Chen, M. Behl, and J. L. Goodall. Trust me, my neighbors say it's raining outside: ensuring data trustworthiness for crowdsourced weather stations. In Proceedings of the 5th Conference on Systems for Built Environments, BuildSys '18, New York, NY, USA, Nov. 2018. ISBN 978-1-4503-5951-1. doi: 10.1145/3276774.3276792.

D. Cherkassky, J. Ostrometzky, and H. Messer. Precipitation Classification Using Measurements From Commercial Microwave Links. IEEE Transactions on Geoscience and Remote Sensing, 52 (5), May 2014. doi: 10.1109/TGRS.2013.2259832.

F. Chollet. Keras: Deep Learning for humans, Jan. 2022. URL `https://github.com/keras-team/keras`. [last access: 26.01.2022].

C. Chwala and H. Kunstmann. Commercial microwave link networks for rainfall observation: Assessment of the current status and future challenges. Wiley Interdisciplinary Reviews: Water, 6(2), 2019. doi: 10.1002/wat2.1337.

C. Chwala, A. Gmeiner, W. Qiu, S. Hipp, D. Nienaber, U. Siart, T. Eibert, M. Pohl, J. Seltmann, J. Fritz, and H. Kunstmann. Precipitation observation using microwave backhaul links in the

alpine and pre-alpine region of Southern Germany. Hydrology and Earth System Sciences, 16 (8), Aug. 2012. doi: 10.5194/hess-16-2647-2012.

C. Chwala, F. Keis, and H. Kunstmann. Real-time data acquisition of commercial microwave link networks for hydrometeorological applications. Atmospheric Measurement Techniques, 9 (3), Mar. 2016. doi: 10.5194/amt-9-991-2016.

C. Chwala, J. Polz, M. Graf, D. Sereb, N. Blettner, F. Keis, and Y. Boose. pycomlink/pycomlink: v0.3.4, Jan. 2022. URL `https://zenodo.org/record/5832991`. [last acess: 27.01.2023].

M. R. Clark, J. D. C. Webb, and P. J. Kirk. Fine-scale analysis of a severe hailstorm using crowd-sourced and conventional observations. Meteorological Applications, 25(3), 2018. doi: https://doi.org/10.1002/met.1715.

E. Cristiano, M.-C. ten Veldhuis, and N. van de Giesen. Spatial and temporal variability of rainfall and their effects on hydrological response in urban areas – a review. Hydrology and Earth System Sciences, 21(7), July 2017. doi: https://doi.org/10.5194/hess-21-3859-2017.

L. E. G. de Vasconcelos, E. C. M. dos Santos, M. L. F. Neto, N. J. Ferreira, and L. G. de Vasconcelos. Using Tweets for Rainfall Monitoring. In S. Latifi, editor, Information Technology: New Generations, Advances in Intelligent Systems and Computing, Cham, 2016. doi: 10.1007/978-3-319-32467-8_100.

L. W. de Vos, H. Leijnse, A. Overeem, and R. Uijlenhoet. The potential of urban rainfall monitoring with crowdsourced automatic weather stations in Amsterdam. Hydrology and Earth System Sciences, 21(2), Feb. 2017. doi: https://doi.org/10.5194/hess-21-765-2017.

L. W. de Vos, H. Leijnse, A. Overeem, and R. Uijlenhoet. Quality Control for Crowdsourced Personal Weather Stations to Enable Operational Rainfall Monitoring. Geophysical Research Letters, 46(15), 2019a. doi: https://doi.org/10.1029/2019GL083731.

L. W. de Vos, A. Overeem, H. Leijnse, R. Uijlenhoet, A. Overeem, H. Leijnse, and R. Uijlenhoet. Rainfall Estimation Accuracy of a Nationwide Instantaneously Sampling Commercial Microwave Link Network: Error Dependency on Known Characteristics. Journal of Atmospheric and Oceanic Technology, July 2019b. doi: 10.1175/JTECH-D-18-0197.1.

L. W. de Vos, A. M. Droste, M. J. Zander, A. Overeem, H. Leijnse, B. G. Heusinkveld, G. J. Steeneveld, and R. Uijlenhoet. Hydrometeorological Monitoring Using Opportunistic Sensing Networks in the Amsterdam Metropolitan Area. Bulletin of the American Meteorological Society, 101(2), Feb. 2020. doi: 10.1175/BAMS-D-19-0091.1.

T. Developers. TensorFlow, Jan. 2022. URL `https://zenodo.org/record/5898685`. [last access: 26.01.2022].

M. Djibo, C. Chwala, M. Graf, J. Polz, H. Kunstmann, and F. Zougmoré. High-resolution rainfall maps from commercial microwave links for a data-scarce region in West Africa. Journal of Hydrometeorology, -1(aop), Aug. 2023a. doi: 10.1175/JHM-D-23-0015.1.

M. Djibo, C. Chwala, M. Graf, J. Polz, H. Kunstmann, and F. Zougmoré. Rainfall maps from commercial microwave link data for Ouagadougou, Burkina Faso, June 2023b.

A. Doumounia, M. Gosset, F. Cazenave, M. Kacou, and F. Zougmore. Rainfall monitoring based on microwave links from cellular telecommunication networks: First results from a West African test bed. Geophysical Research Letters, 41(16), 2014. doi: 10.1002/2014GL060724.

C. D. C. DWD. Historische stündliche RADOLAN-Raster der Niederschlagshöhe (binär), 2019. URL `https://opendata.dwd.de/climate_environment/CDC/grids_germany/hourly/radolan/historical/bin/`. [last access: 04.10.2023].

M. D'Amico, A. Manzoni, and G. L. Solazzi. Use of Operational Microwave Link Measurements for the Tomographic Reconstruction of 2-D Maps of Accumulated Rainfall. IEEE Geoscience and Remote Sensing Letters, 13(12), Dec. 2016. doi: 10.1109/LGRS.2016.2614326.

I. Emmanuel, H. Andrieu, E. Leblois, and B. Flahaut. Temporal and spatial variability of rainfall at the urban hydrological scale. Journal of Hydrology, 430-431, Apr. 2012. doi: 10.1016/j.jhydrol.2012.02.013.

Ericsson. Receiver performance; receiver thresholds rau1 - Ericsson MINI-LINK E Technical Description [Page 136] | ManualsLib, 2012. URL `https://www.manualslib.com/manual/1620197/Ericsson-Mini-Link-E.html?page=136#manual`. [last access: 09.02.2022].

Ericsson. Microwave outlook 2016, 2016. URL `https://www.ericsson.com/4adebb/assets/local/reports-papers/microwave-outlook/2016/ericsson-microwave-outlook-report-2016.pdf`. [last access: 03.05.2022].

Ericsson. Microwave outlook 2021, Oct. 2021. URL `https://www.ericsson.com/4a8c50/assets/local/reports-papers/microwave-outlook/2021/microwave-report-2021-wind-impact-on-e-band.pdf`. [last access: 31.01.2022].

A. Eshel, H. Messer, H. Kunstmann, P. Alpert, and C. Chwala. Quantitative Analysis of the Performance of Spatial Interpolation Methods for Rainfall Estimation Using Commercial Microwave Links. Journal of Hydrometeorology, -1(aop), Jan. 2021. doi: 10.1175/JHM-D-20-0164.1.

T. Fawcett. An introduction to ROC analysis. Pattern Recognition Letters, 27(8), June 2006. doi: 10.1016/j.patrec.2005.10.010.

M. Fencl, J. Rieckermann, M. Schleiss, D. Stránský, and V. Bareš. Assessing the potential of using telecommunication microwave links in urban drainage modelling. Water Science and Technology, 68(8), Oct. 2013. doi: 10.2166/wst.2013.429.

M. Fencl, J. Rieckermann, P. Sýkora, D. Stránský, and V. Bareš. Commercial microwave links instead of rain gauges: fiction or reality? Water Science and Technology, 71(1), Nov. 2014. doi: 10.2166/wst.2014.466.

M. Fencl, M. Dohnal, J. Rieckermann, and V. Bareš. Gauge-adjusted rainfall estimates from commercial microwave links. Hydrology and Earth System Sciences, 21(1), Jan. 2017. doi: https://doi.org/10.5194/hess-21-617-2017.

M. Fencl, P. Valtr, M. Kvičera, and V. Bareš. Quantifying Wet Antenna Attenuation in 38-GHz Commercial Microwave Links of Cellular Backhaul. IEEE Geoscience and Remote Sensing Letters, 16(4), Apr. 2019. doi: 10.1109/LGRS.2018.2876696.

M. Fencl, M. Dohnal, P. Valtr, M. Grabner, and V. Bareš. Atmospheric observations with E-band microwave links – challenges and opportunities. Atmospheric Measurement Techniques, 13(12), Dec. 2020. doi: 10.5194/amt-13-6559-2020.

F. Fenicia, L. Pfister, D. Kavetski, P. Matgen, J.-F. Iffly, L. Hoffmann, and R. Uijlenhoet. Microwave links for rainfall estimation in an urban environment: Insights from an experimental setup in Luxembourg-City. Journal of Hydrology, 464-465, Sept. 2012. doi: 10.1016/j.jhydrol.2012.06.047.

J. M. Frame, F. Kratzert, D. Klotz, M. Gauch, G. Shalev, O. Gilon, L. M. Qualls, H. V. Gupta, and G. S. Nearing. Deep learning rainfall–runoff predictions of extreme events. Hydrology and Earth System Sciences, 26(13), July 2022. doi: 10.5194/hess-26-3377-2022.

K. Fukushima. Neocognitron: A self-organizing neural network model for a mechanism of pattern recognition unaffected by shift in position. Biological Cybernetics, 36(4), Apr. 1980. doi: 10.1007/BF00344251.

O. Goldshtein, H. Messer, and A. Zinevich. Rain Rate Estimation Using Measurements From Commercial Telecommunications Links. IEEE Transactions on Signal Processing, 57(4), Apr. 2009. doi: 10.1109/TSP.2009.2012554.

V. R. Golroudbary, Y. Zeng, C. M. Mannaerts, and Z. B. Su. Urban impacts on air temperature and precipitation over The Netherlands. Climate Research, 75(2), May 2018. doi: 10.3354/cr01512.

I. Goodfellow, Y. Bengio, and A. Courville. Deep Learning. Adaptive Computation and Machine Learning series. MIT Press, Cambridge, MA, USA, Nov. 2016. ISBN 978-0-262-03561-3.

M. Gosset, H. Kunstmann, F. Zougmore, F. Cazenave, H. Leijnse, R. Uijlenhoet, C. Chwala, F. Keis, A. Doumounia, B. Boubacar, M. Kacou, P. Alpert, H. Messer, J. Rieckermann, and J. Hoedjes. Improving Rainfall Measurement in Gauge Poor Regions Thanks to Mobile Telecommunication Networks. Bulletin of the American Meteorological Society, 97(3), Mar. 2016. doi: 10.1175/BAMS-D-15-00164.1.

M. Graf, C. Chwala, J. Polz, and H. Kunstmann. Rainfall estimation from a German-wide commercial microwave link network: optimized processing and validation for 1 year of data. Hydrology and Earth System Sciences, 24(6), June 2020a. doi: https://doi.org/10.5194/hess-24-2931-2020.

M. Graf, C. Chwala, J. Polz, and H. Kunstmann. Showcase video of hourly RADOLAN and CML rainfall maps, Apr. 2020b. URL `https://zenodo.org/record/3759208`. [last access: 21.04.2020].

M. Graf, J. Arnault, B. Fersch, and H. Kunstmann. Is the soil moisture precipitation feedback enhanced by heterogeneity and dry soils? A comparative study. Hydrological Processes, 35(9), Dec. 2021a. doi: 10.1002/hyp.14332.

M. Graf, A. El Hachem, M. Eisele, J. Seidel, C. Chwala, H. Kunstmann, and A. Bárdossy. Rainfall estimates from opportunistic sensors in Germany across spatio-temporal scales. Journal of Hydrology: Regional Studies, 37, 2021b. doi: 10.1016/j.ejrh.2021.100883.

M. Graf, J. Polz, and C. Chwala. Regenmessung im Mobilfunknetz. Physik in unserer Zeit, 52 (2), Jan. 2021c. doi: https://doi.org/10.1002/piuz.202001602.

M. Graf, J. Polz, and C. Chwala. Blackout gap detection example notebook [Software], Mar. 2022a. URL `https://github.com/pycomlink/pycomlink/blob/12fc302539851b19f7656cf7e2438c0ddbaa48bf/notebooks/Blackout%20gap%20detection%20examples.ipynb`. [last access: 16.03.2022].

M. Graf, J. Polz, and C. Chwala. Data for a CML blackout gap detection example [Dataset], Mar. 2022b. URL `https://zenodo.org/record/6337557`. [last access: 09.03.2022].

M. Graf, N. Blettner, J. Polz, and C. Chwala. Potential and Limitations of Filling Gaps in Commercial Microwave Link Data Stemming From Complete Loss of Signal During Heavy Rainfall. In 2023 IEEE International Conference on Acoustics, Speech, and Signal Processing Workshops (ICASSPW), June 2023. doi: 10.1109/ICASSPW59220.2023.10193696.

B. Guo, Y. Ouyang, T. Guo, L. Cao, and Z. Yu. Enhancing Mobile App User Understanding and Marketing With Heterogeneous Crowdsourced Data: A Review. IEEE Access, 7, 2019. doi: 10.1109/ACCESS.2019.2918325.

H. V. Habi and H. Messer. Wet-Dry Classification Using LSTM and Commercial Microwave Links. In 2018 IEEE 10th Sensor Array and Multichannel Signal Processing Workshop (SAM), July 2018. doi: 10.1109/SAM.2018.8448679.

B. Haese, S. Hörning, C. Chwala, A. Bárdossy, B. Schalge, and H. Kunstmann. Stochastic Reconstruction and Interpolation of Precipitation Fields Using Combined Information of Commercial Microwave Links and Rain Gauges. Water Resources Research, 53(12), 2017. doi: 10.1002/2017WR021015.

G. Hellmann. Die Niederschläge in den norddeutschen Stromgebieten. Nature, 75(1954), Apr. 1907. doi: 10.1038/075556a0.

K. S. Hintz, H. Vedel, and E. Kaas. Collecting and processing of barometric data from smartphones for potential use in numerical weather prediction data assimilation. Meteorological Applications, 26(4), 2019. doi: https://doi.org/10.1002/met.1805.

T. R. Hoens and N. V. Chawla. Imbalanced Datasets: From Sampling to Classifiers. In Imbalanced Learning. John Wiley & Sons, Ltd, 2013. ISBN 978-1-118-64610-6.

D. C. Hogg. Millimeter-Wave Communication through the Atmosphere. Science, 159(3810), Jan. 1968. doi: 10.1126/science.159.3810.39.

J. Howe. The Rise of Crowdsourcing. Wired, June 2006. URL `https://www.wired.com/2006/06/crowds/`. [last access: 06.07.2023].

G. J. Huffman, D. T. Bolvin, and E. J. Nelkin. Integrated Multi-satellitE Retrievals for GPM (IMERG) Technical Documentation, 2015.

S. Hörning and B. Haese. RMWSPy (v 1.1): A Python code for spatial simulation and inversion for environmental applications. Environmental Modelling & Software, 138, Apr. 2021. doi: 10.1016/j.envsoft.2021.104970.

R. O. Imhoff, A. Overeem, C. C. Brauer, H. Leijnse, A. H. Weerts, and R. Uijlenhoet. Rainfall Nowcasting Using Commercial Microwave Links. Geophysical Research Letters, 47(19), 2020. doi: 10.1029/2020GL089365.

H. Ismail Fawaz, G. Forestier, J. Weber, L. Idoumghar, and P.-A. Muller. Deep learning for time series classification: a review. Data Mining and Knowledge Discovery, 33(4), July 2019. doi: 10.1007/s10618-019-00619-1.

ITU-R. Specific attenuation model for rain for use in prediction methods (Recommendation P.838-3). Geneva, Switzerland: ITU-R. Retrieved from https:// www.itu.int/rec/R-REC-P.838-3-200503-I/en, 2005.

ITU-R. Characteristics of precipitation for propagation modelling (Recommendation P.837-7). Geneva, Switzerland: ITU-R. Retrieved from https://www.itu.int/rec/R-REC-P.837/en, 2017.

ITU-R. P.530 : Propagation data and prediction methods required for the design of terrestrial line-of-sight systems, Sept. 2021.

G. Jenkins. A comparison between two types of widely used weather stations. Weather, 69(4), 2014. doi: https://doi.org/10.1002/wea.2158.

S. Jiang, V. Babovic, Y. Zheng, and J. Xiong. Advancing Opportunistic Sensing in Hydrology: A Novel Approach to Measuring Rainfall With Ordinary Surveillance Cameras. Water Resources Research, 55(4), 2019. doi: https://doi.org/10.1029/2018WR024480.

J. Joss and A. Waldvogel. Ein Spektrograph für Niederschlagstropfen mit automatischer Auswertung. pure and applied geophysics, 68(1), Dec. 1967. doi: 10.1007/BF00874898.

M. Kaufmann and J. Rieckermann. Identification of dry and rainy periods using telecommunication microwave links. In 12nd International Conference on Urban Drainage, Porto Alegro, Brazil, Sept. 2011.

M. Kharadly and R. Ross. Effect of wet antenna attenuation on propagation data statistics. IEEE Transactions on Antennas and Propagation, 49(8), Aug. 2001. doi: 10.1109/8.943313.

C. Kidd, A. Becker, G. J. Huffman, C. L. Muller, P. Joe, G. Skofronick-Jackson, and D. B. Kirschbaum. So, How Much of the Earth's Surface Is Covered by Rain Gauges? Bulletin of the American Meteorological Society, 98(1), Jan. 2017. doi: 10.1175/BAMS-D-14-00283.1.

C. Kidd, G. Huffman, V. Maggioni, P. Chambon, and R. Oki. The Global Satellite Precipitation Constellation: Current Status and Future Requirements. Bulletin of the American Meteorological Society, 102(10), Oct. 2021. doi: 10.1175/BAMS-D-20-0299.1.

M.-S. Kim and B. H. Kwon. Rainfall Detection and Rainfall Rate Estimation Using Microwave Attenuation. Atmosphere, 9(8), Aug. 2018. doi: 10.3390/atmos9080287.

V. Klemeš. Conceptualization and scale in hydrology. Journal of Hydrology, 65(1), Aug. 1983. doi: 10.1016/0022-1694(83)90208-1.

D. Kneis and M. Heistermann. Bewertung der Güte einer Radar-basierten Niederschlagsschätzung am Beispiel eines kleinen Einzugsgebiets. Hydrologie und Wasserbewirtschaftung. Hydrologie und Wasserbewirtschaftung, 53(3), 2009.

J. Kreklow, B. Tetzlaff, G. Kuhnt, and B. Burkhard. A Rainfall Data Intercomparison Dataset of RADKLIM, RADOLAN, and Rain Gauge Data for Germany. Data, 4(3), Sept. 2019. doi: 10.3390/data4030118.

Y. LeCun, Y. Bengio, and G. Hinton. Deep learning. Nature, 521(7553), May 2015. doi: 10.1038/nature14539.

H. Leijnse, R. Uijlenhoet, and J. N. M. Stricker. Rainfall measurement using radio links from cellular communication networks. Water Resources Research, 43(3), 2007. doi: 10.1029/2006WR005631.

H. Leijnse, R. Uijlenhoet, and J. N. M. Stricker. Microwave link rainfall estimation: Effects of link length and frequency, temporal sampling, power resolution, and wet antenna attenuation. Advances in Water Resources, 31(11), Nov. 2008. doi: 10.1016/j.advwatres.2008.03.004.

Y. Liberman and H. Messer. Accurate reconstruction of rain field maps from Commercial Microwave Networks using sparse field modeling. In 2014 IEEE International Conference on Acoustics, Speech and Signal Processing (ICASSP), May 2014. doi: 10.1109/ICASSP.2014.6854914.

Y. Liberman, R. Samuels, P. Alpert, and H. Messer. New algorithm for integration between wireless microwave sensor network and radar for improved rainfall measurement and mapping. Atmospheric Measurement Techniques, 7(10), Oct. 2014. doi: https://doi.org/10.5194/amt-7-3549-2014.

C. Lorenz and H. Kunstmann. The Hydrological Cycle in Three State-of-the-Art Reanalyses:: Intercomparison and Performance Analysis. Journal of Hydrometeorology, 13(5), 2012. doi: 10.1175/JHM-D-11-088.1.

L. E. Madaus and C. F. Mass. Evaluating Smartphone Pressure Observations for Mesoscale Analyses and Forecasts. Weather and Forecasting, 32(2), Apr. 2017. doi: 10.1175/WAF-D-16-0135.1.

V. Maggioni, P. C. Meyers, and M. D. Robinson. A Review of Merged High-Resolution Satellite Precipitation Product Accuracy during the Tropical Rainfall Measuring Mission (TRMM) Era. Journal of Hydrometeorology, 17(4), Feb. 2016. doi: 10.1175/JHM-D-15-0190.1.

W. P. Mahoney and J. M. O'Sullivan. Realizing the Potential of Vehicle-Based Observations. Bulletin of the American Meteorological Society, 94(7), July 2013. doi: 10.1175/BAMS-D-12-00044.1.

P. P. Mapiam, M. Methaprayun, T. Bogaard, G. Schoups, and M.-C. Ten Veldhuis. Citizen rain gauges improve hourly radar rainfall bias correction using a two-step Kalman filter. Hydrology and Earth System Sciences, 26(3), Feb. 2022. doi: 10.5194/hess-26-775-2022.

J. S. Marshall and W. M. K. Palmer. THE DISTRIBUTION OF RAINDROPS WITH SIZE. Journal of the Atmospheric Sciences, 5(4), Aug. 1948. doi: 10.1175/1520-0469(1948)005⟨0165:TDORWS⟩2.0.CO;2.

M. F. McCabe, M. Rodell, D. E. Alsdorf, D. G. Miralles, R. Uijlenhoet, W. Wagner, A. Lucieer, R. Houborg, N. E. C. Verhoest, T. E. Franz, J. Shi, H. Gao, and E. F. Wood. The future of Earth observation in hydrology. Hydrology and Earth System Sciences, 21(7), July 2017. doi: https://doi.org/10.5194/hess-21-3879-2017.

D. Meissner, S. Gebauer, A. H. Schumann, and S. Rademacher. Analyse radarbasierter Niederschlagsprodukte als Eingangsdaten verkehrsbezogener Wasserstandsvorhersagen am Rhein. Hydrologie und Wasserbewirtschaftung, 1(02), 2012. doi: DOI10.5675/HyWa_2012,1_2.

F. Mercier, L. Barthès, and C. Mallet. Estimation of Finescale Rainfall Fields Using Broadcast TV Satellite Links and a 4DVAR Assimilation Method. Journal of Atmospheric and Oceanic Technology, 32(10), Oct. 2015. doi: 10.1175/JTECH-D-14-00125.1.

B. Merz, G. Blöschl, S. Vorogushyn, F. Dottori, J. C. J. H. Aerts, P. Bates, M. Bertola, M. Kemter, H. Kreibich, U. Lall, and E. Macdonald. Causes, impacts and patterns of disastrous river floods. Nature Reviews Earth & Environment, 2(9), Sept. 2021. doi: 10.1038/s43017-021-00195-3.

H. Messer and O. Sendik. A New Approach to Precipitation Monitoring: A critical survey of existing technologies and challenges. IEEE Signal Processing Magazine, 32(3), May 2015. doi: 10.1109/MSP.2014.2309705.

H. Messer, A. Zinevich, and P. Alpert. Environmental Monitoring by Wireless Communication Networks. Science, 312(5774), May 2006. doi: 10.1126/science.1120034.

W. Met Office and Netatmo. EUMETNET Sandbox: surface observations from Met Office WOW and Netatmo networks, Dec. 2021. URL `http://catalogue.ceda.ac.uk/uuid/37d6ea7956a74af0bef827b94e0fb602`. [last access: 13.12.2022].

C. Moroder, U. Siart, C. Chwala, and H. Kunstmann. Microwave Instrument for Simultaneous Wet Antenna Attenuation and Precipitation Measurement. IEEE Transactions on Instrumentation and Measurement, 2019. doi: 10.1109/TIM.2019.2961498.

C. Moroder, U. Siart, C. Chwala, and H. Kunstmann. Modeling of Wet Antenna Attenuation for Precipitation Estimation From Microwave Links. IEEE Geoscience and Remote Sensing Letters, 17(3), Mar. 2020. doi: 10.1109/LGRS.2019.2922768.

J. Muñoz-Sabater, E. Dutra, A. Agustí-Panareda, C. Albergel, G. Arduini, G. Balsamo, S. Boussetta, M. Choulga, S. Harrigan, H. Hersbach, B. Martens, D. G. Miralles, M. Piles, N. J. Rodríguez-Fernández, E. Zsoter, C. Buontempo, and J.-N. Thépaut. ERA5-Land: a state-of-the-art global reanalysis dataset for land applications. Earth System Science Data, 13(9), Sept. 2021. doi: 10.5194/essd-13-4349-2021.

Netatmo. Smart Home Weather Station and accessories - Smart Rain Gauge – Physical installation and precautions | Netatmo Helpcenter, 2022. URL https://helpcenter.netatmo.com/en-us/smart-home-weather-station-and-accessories/setup-installation/smart-rain-gauge-physical-installation-and-precautions. [last access: 21.07.2022].

S. Ochoa-Rodriguez, L.-P. Wang, A. Gires, R. D. Pina, R. Reinoso-Rondinel, G. Bruni, A. Ichiba, S. Gaitan, E. Cristiano, J. van Assel, S. Kroll, D. Murlà-Tuyls, B. Tisserand, D. Schertzer, I. Tchiguirinskaia, C. Onof, P. Willems, and M.-C. ten Veldhuis. Impact of spatial and temporal resolution of rainfall inputs on urban hydrodynamic modelling outputs: A multi-catchment investigation. Journal of Hydrology, 531, Dec. 2015. doi: 10.1016/j.jhydrol.2015.05.035.

J. Ostrometzky and H. Messer. Dynamic Determination of the Baseline Level in Microwave Links for Rain Monitoring From Minimum Attenuation Values. IEEE Journal of Selected Topics in Applied Earth Observations and Remote Sensing, 11(1), Jan. 2018. doi: 10.1109/JSTARS.2017.2752902.

J. Ostrometzky, R. Raich, L. Bao, J. Hansryd, and H. Messer. The Wet-Antenna Effect—A Factor to be Considered in Future Communication Networks. IEEE Transactions on Antennas and Propagation, 66(1), Jan. 2018. doi: 10.1109/TAP.2017.2767620.

A. Overeem, H. Leijnse, and R. Uijlenhoet. Measuring urban rainfall using microwave links from commercial cellular communication networks. Water Resources Research, 47(12), 2011. doi: 10.1029/2010WR010350.

A. Overeem, H. Leijnse, and R. Uijlenhoet. Country-wide rainfall maps from cellular communication networks. Proceedings of the National Academy of Sciences, 110(8), Feb. 2013a. doi: 10.1073/pnas.1217961110.

A. Overeem, J. C. R. Robinson, H. Leijnse, G. J. Steeneveld, B. K. P. Horn, and R. Uijlenhoet. Crowdsourcing urban air temperatures from smartphone battery temperatures. Geophysical Research Letters, 40(15), 2013b. doi: https://doi.org/10.1002/grl.50786.

A. Overeem, H. Leijnse, and R. Uijlenhoet. Retrieval algorithm for rainfall mapping from microwave links in a cellular communication network. Atmospheric Measurement Techniques, 9 (5), June 2016a. doi: 10.5194/amt-9-2425-2016.

A. Overeem, H. Leijnse, and R. Uijlenhoet. Two and a half years of country-wide rainfall maps using radio links from commercial cellular telecommunication networks. Water Resources Research, 52(10), Oct. 2016b. doi: 10.1002/2016WR019412.

A. Overeem, H. Leijnse, T. C. v. Leth, L. Bogerd, J. Priebe, D. Tricarico, A. Droste, and R. Uijlenhoet. Tropical rainfall monitoring with commercial microwave links in Sri Lanka. Environmental Research Letters, 16(7), July 2021. doi: 10.1088/1748-9326/ac0fa6.

A. Overeem, H. Leijnse, G. van der Schrier, E. van den Besselaar, I. Garcia-Marti, and L. W. de Vos. Merging with crowdsourced rain gauge data improves pan-European radar precipitation estimates. Hydrology and Earth System Sciences Discussions, June 2023. doi: 10.5194/hess-2023-122.

J. Pastorek, M. Fencl, J. Rieckermann, and V. Bareš. Commercial microwave links for urban drainage modelling: The effect of link characteristics and their position on runoff simulations. Journal of Environmental Management, 251, Dec. 2019. doi: 10.1016/j.jenvman.2019.109522.

J. Pastorek, M. Fencl, J. Rieckermann, and V. Bareš. Precipitation Estimates From Commercial Microwave Links: Practical Approaches to Wet-Antenna Correction. IEEE Transactions on Geoscience and Remote Sensing, 60, 2022. doi: 10.1109/TGRS.2021.3110004.

K. Paulson and A. Al-Mreri. A rain height model to predict fading due to wet snow on terrestrial links. Radio Science, 46(4), 2011. doi: 10.1029/2010RS004555.

N. Peleg, F. Marra, S. Fatichi, A. Paschalis, P. Molnar, and P. Burlando. Spatial variability of extreme rainfall at radar subpixel scale. Journal of Hydrology, 556, Jan. 2018. doi: 10.1016/j.jhydrol.2016.05.033.

G. B. Physical Society and G. B. Royal Meteorological Society, editors. Meteorological factors in radio-wave propagation: report of a conference held on 8 April 1946 at the Royal Institution, London. Publisher: Physical Society, Great Britain and Royal Meteorological Society, Great Britain, London, 1947.

B. S. Pickering, R. R. Neely III, and D. Harrison. The Disdrometer Verification Network (DiVeN): a UK network of laser precipitation instruments. Atmospheric Measurement Techniques, 12(11), Nov. 2019. doi: 10.5194/amt-12-5845-2019.

K. J. Piczak. Environmental sound classification with convolutional neural networks. In 2015 IEEE 25th International Workshop on Machine Learning for Signal Processing (MLSP), Sept. 2015. doi: 10.1109/MLSP.2015.7324337.

M. D. Pollock, G. O'Donnell, P. Quinn, M. Dutton, A. Black, M. E. Wilkinson, M. Colli, M. Stagnaro, L. G. Lanza, E. Lewis, C. G. Kilsby, and P. E. O'Connell. Quantifying and Mitigating Wind-Induced Undercatch in Rainfall Measurements. Water Resources Research, 54(6), 2018. doi: https://doi.org/10.1029/2017WR022421.

J. Polz, C. Chwala, M. Graf, and H. Kunstmann. Rain event detection in commercial microwave link attenuation data using convolutional neural networks. Atmospheric Measurement Techniques, 13(7), July 2020. doi: https://doi.org/10.5194/amt-13-3835-2020.

J. Polz, L. Glawion, M. Graf, N. Blettner, E. Lasota, L. Schmidt, H. Kunstmann, and C. Chwala. Expert Flagging of Commercial Microwave Link Signal Anomalies: Effect on Rainfall Estimation and Ambiguity of Flagging. In 2023 IEEE International Conference on Acoustics, Speech, and Signal Processing Workshops (ICASSPW), June 2023a. doi: 10.1109/ICASSPW59220.2023.10193654.

J. Polz, M. Graf, and C. Chwala. Missing Rainfall Extremes in Commercial Microwave Link Data Due To Complete Loss of Signal. Earth and Space Science, 10(2), Feb. 2023b. doi: 10.1029/2022EA002456.

M. Prohom, M. Barriendos, and A. Sanchez-Lorenzo. Reconstruction and homogenization of the longest instrumental precipitation series in the Iberian Peninsula (Barcelona, 1786–2014). International Journal of Climatology, 36(8), 2016. doi: 10.1002/joc.4537.

pycomlink, 2021.

E. Rabiei, U. Haberlandt, M. Sester, and D. Fitzner. Rainfall estimation using moving cars as rain gauges – laboratory experiments. Hydrology and Earth System Sciences, 17(11), Nov. 2013. doi: https://doi.org/10.5194/hess-17-4701-2013.

M. Reichstein, G. Camps-Valls, B. Stevens, M. Jung, J. Denzler, N. Carvalhais, and Prabhat. Deep learning and process understanding for data-driven Earth system science. Nature, 566 (7743), Feb. 2019. doi: 10.1038/s41586-019-0912-1.

C. Reller, H.-A. Loeliger, and J. P. Marín Díaz. A model for quasi-periodic signals with application to rain estimation from microwave link gain. In 2011 19th European Signal Processing Conference, Aug. 2011.

M. F. Rios Gaona, A. Overeem, H. Leijnse, and R. Uijlenhoet. Measurement and interpolation uncertainties in rainfall maps from cellular communication networks. Hydrology and Earth System Sciences, 19(8), Aug. 2015. doi: https://doi.org/10.5194/hess-19-3571-2015.

M. F. Rios Gaona, A. Overeem, T. H. Raupach, H. Leijnse, and R. Uijlenhoet. Rainfall retrieval with commercial microwave links in São Paulo, Brazil. Atmospheric Measurement Techniques, 11(7), July 2018. doi: 10.5194/amt-11-4465-2018.

G. Roversi, P. P. Alberoni, A. Fornasiero, and F. Porcù. Commercial microwave links as a tool for operational rainfall monitoring in Northern Italy. Atmospheric Measurement Techniques, 13(11), Oct. 2020. doi: 10.5194/amt-13-5779-2020.

T. I. v. h. Schip, A. Overeem, H. Leijnse, R. Uijlenhoet, J. F. Meirink, and A. J. v. Delden. Rainfall measurement using cell phone links: classification of wet and dry periods using geostationary satellites. Hydrological Sciences Journal, 62(9), July 2017. doi: 10.1080/02626667.2017.1329588.

M. Schleiss and A. Berne. Identification of Dry and Rainy Periods Using Telecommunication Microwave Links. IEEE Geoscience and Remote Sensing Letters, 7(3), July 2010. doi: 10.1109/LGRS.2010.2043052.

M. Schleiss, J. Rieckermann, and A. Berne. Quantification and Modeling of Wet-Antenna Attenuation for Commercial Microwave Links. IEEE Geoscience and Remote Sensing Letters, 10(5), Sept. 2013. doi: 10.1109/LGRS.2012.2236074.

M. Schleiss, J. Olsson, P. Berg, T. Niemi, T. Kokkonen, S. Thorndahl, R. Nielsen, J. Ellerbæk Nielsen, D. Bozhinova, and S. Pulkkinen. The accuracy of weather radar in heavy rain: a comparative study for Denmark, the Netherlands, Finland and Sweden. Hydrology and Earth System Sciences, 24(6), June 2020. doi: https://doi.org/10.5194/hess-24-3157-2020.

B. Sevruk. Rainfall Measurement: Gauges. In Encyclopedia of Hydrological Sciences. John Wiley & Sons, Ltd, 2006. ISBN 978-0-470-84894-4.

B. E. Sheppard and P. I. Joe. Comparison of Raindrop Size Distribution Measurements by a Joss-Waldvogel Disdrometer, a PMS 2DG Spectrometer, and a POSS Doppler Radar. Journal of Atmospheric and Oceanic Technology, 11(4), Aug. 1994. doi: 10.1175/1520-0426(1994)011⟨0874:CORSDM⟩2.0.CO;2.

G. Smiatek, F. Keis, C. Chwala, B. Fersch, and H. Kunstmann. Potential of commercial microwave link network derived rainfall for river runoff simulations. Environmental Research Letters, 12 (3), Mar. 2017. doi: 10.1088/1748-9326/aa5f46.

K. Song, X. Liu, M. Zou, D. Zhou, H. Wu, and F. Ji. Experimental Study of Detecting Rainfall Using Microwave Links: Classification of Wet and Dry Periods. IEEE Journal of Selected Topics in Applied Earth Observations and Remote Sensing, 13, 2020. doi: 10.1109/JSTARS.2020.3021555.

N. Srivastava, G. Hinton, A. Krizhevsky, I. Sutskever, and R. Salakhutdinov. Dropout: A Simple Way to Prevent Neural Networks from Overfitting. Journal of Machine Learning Research, 15 (56), 2014.

I. Strangeways. A history of rain gauges. Weather, 65(5), 2010. doi: 10.1002/wea.548.

D. Stransky, M. Fencl, and V. Bares. Runoff prediction using rainfall data from microwave links: Tabor case study. Water Science and Technology, 2017(2), Apr. 2018. doi: 10.2166/wst.2018.149.

F. Tauro, J. Selker, N. v. d. Giesen, T. Abrate, R. Uijlenhoet, M. Porfiri, S. Manfreda, K. Caylor, T. Moramarco, J. Benveniste, G. Ciraolo, L. Estes, A. Domeneghetti, M. T. Perks, C. Corbari, E. Rabiei, G. Ravazzani, H. Bogena, A. Harfouche, L. Brocca, A. Maltese, A. Wickert, A. Tarpanelli, S. Good, J. M. L. Alcala, A. Petroselli, C. Cudennec, T. Blume, R. Hut, and S. Grimaldi. Measurements and Observations in the XXI century (MOXXI): innovation and multi-disciplinarity to sense the hydrological cycle. Hydrological Sciences Journal, 63(2), Jan. 2018. doi: 10.1080/02626667.2017.1420191.

J. Tiede, C. Chwala, and U. Siart. New Insights into the Dynamics of Wet Antenna Attenuation Based on In-Situ Estimations Provided by the Dedicated Field Experiment ATTRRA2. IEEE Geoscience and Remote Sensing Letters, 2023. doi: 10.1109/LGRS.2023.3320755.

T. Tjelta and D. Bacon. Predicting Combined Rain and Wet Snow Attenuation on Terrestrial Links. IEEE Transactions on Antennas and Propagation, 58(5), May 2010. doi: 10.1109/TAP.2010.2044316.

E. Todini. Hydrological catchment modelling: past, present and future. Hydrology and Earth System Sciences, 11(1), Jan. 2007. doi: 10.5194/hess-11-468-2007.

S. Trömel, M. Ziegert, A. V. Ryzhkov, C. Chwala, and C. Simmer. Using Microwave Backhaul Links to Optimize the Performance of Algorithms for Rainfall Estimation and Attenuation Correction. Journal of Atmospheric and Oceanic Technology, 31(8), June 2014. doi: 10.1175/JTECH-D-14-00016.1.

R. Uijlenhoet, J. A. Smith, and M. Steiner. The Microphysical Structure of Extreme Precipitation as Inferred from Ground-Based Raindrop Spectra. Journal of the Atmospheric Sciences, 60(10), May 2003. doi: 10.1175/1520-0469(2003)60⟨1220:TMSOEP⟩2.0.CO;2.

R. Uijlenhoet, A. Overeem, and H. Leijnse. Opportunistic remote sensing of rainfall using microwave links from cellular communication networks. Wiley Interdisciplinary Reviews: Water, 5(4), July 2018. doi: 10.1002/wat2.1289.

UNFCCC. Sharm el-Sheikh Implementation Plan. Revised draft decision - cma.4 UNFCCC, Nov. 2022. URL `https://unfccc.int/documents/621908`. [last access: 24.11.2022].

G. Upton, A. Holt, R. Cummings, A. Rahimi, and J. Goddard. Microwave links: The future for urban rainfall measurement? Atmospheric Research, 77(1-4), Sept. 2005. doi: 10.1016/j.atmosres.2004.10.009.

P. Valtr, M. Fencl, and V. Bareš. Excess Attenuation Caused by Antenna Wetting of Terrestrial Microwave Links at 32 GHz. IEEE Antennas and Wireless Propagation Letters, 18(8), Aug. 2019. doi: 10.1109/LAWP.2019.2925455.

R. C. Z. van de Beek, H. Leijnse, P. J. J. F. Torfs, and R. Uijlenhoet. Seasonal semi-variance of Dutch rainfall at hourly to daily scales. Advances in Water Resources, 45, Sept. 2012. doi: 10.1016/j.advwatres.2012.03.023.

R. C. Z. van de Beek, J. Olsson, and J. Andersson. Optimal grid resolution for precipitation maps from commercial microwave link networks. In Advances in Science and Research, volume 17, June 2020. doi: https://doi.org/10.5194/asr-17-79-2020.

T. C. van Leth, A. Overeem, H. Leijnse, and R. Uijlenhoet. A measurement campaign to assess sources of error in microwave link rainfall estimation. Atmospheric Measurement Techniques, 11(8), Aug. 2018. doi: 10.5194/amt-11-4645-2018.

G. Villarini and W. F. Krajewski. Review of the Different Sources of Uncertainty in Single Polarization Radar-Based Estimates of Rainfall. Surveys in Geophysics, 31(1), Jan. 2010. doi: 10.1007/s10712-009-9079-x.

A. Wagner, C. Chwala, M. Graf, J. Polz, L. Lliso, J. A. Lahuerta, and H. Kunstmann. Improved rain event detection in Commercial Microwave Link time series via combination with MSG SEVIRI data. Atmospheric Measurement Techniques Discussions, pages 1–24, Oct. 2023. doi: 10.5194/amt-2023-175.

Z. Wang, M. Schleiss, J. Jaffrain, A. Berne, and J. Rieckermann. Using Markov switching models to infer dry and rainy periods from telecommunication microwave link signals. Atmospheric Measurement Techniques, 5(7), July 2012. doi: 10.5194/amt-5-1847-2012.

T. Winterrath, W. Rosenow, and E. Weigl. On the DWD quantitative precipitation analysis and nowcasting system for real-time application in German flood risk management. IAHS Publ., 351, 2012.

T. Winterrath, C. Brendel, M. Hafer, T. Junghänel, A. Klameth, K. Lengfeld, E. Walawender, E. Weigl, and A. Becker. Radar climatology (RADKLIM) version 2017.002: Reprocessed quasi gauge-adjusted radar data, 5-minute precipitation sums (YW) [Dataset]. Deutscher Wetterdienst (DWD), 2018. doi: 10.5676/DWD/RADKLIM_YW_V2017.002.

W. Wolff, A. Overeem, H. Leijnse, and R. Uijlenhoet. Rainfall retrieval algorithm for commercial microwave links: stochastic calibration. Atmospheric Measurement Techniques, 15(2), Jan. 2022. doi: 10.5194/amt-15-485-2022.

F. Zheng, R. Tao, H. R. Maier, L. See, D. Savic, T. Zhang, Q. Chen, T. H. Assumpção, P. Yang, B. Heidari, J. Rieckermann, B. Minsker, W. Bi, X. Cai, D. Solomatine, and I. Popescu. Crowdsourcing Methods for Data Collection in Geophysics: State of the Art, Issues, and Future Directions. Reviews of Geophysics, 56(4), 2018. doi: https://doi.org/10.1029/2018RG000616.

X. X. Zhu, D. Tuia, L. Mou, G.-S. Xia, L. Zhang, F. Xu, and F. Fraundorfer. Deep Learning in Remote Sensing: A Comprehensive Review and List of Resources. IEEE Geoscience and Remote Sensing Magazine, 5(4), Dec. 2017. doi: 10.1109/MGRS.2017.2762307.

A. Zinevich, H. Messer, and P. Alpert. Prediction of rainfall intensity measurement errors using commercial microwave communication links. Atmospheric Measurement Techniques, 3(5), Oct. 2010. doi: 10.5194/amt-3-1385-2010.

V. Đorđević, O. Pronic-Rancic, Z. Marinković, M. Milijić, V. Markovic, U. Siart, C. Chwala, and H. Kunstmann. New Method for Detection of Precipitation Based on Artificial Neural Networks. Microwave Review, 19(2), 2014.

A. Špačková, V. Bareš, M. Fencl, M. Schleiss, J. Jaffrain, A. Berne, and J. Rieckermann. A year of attenuation data from a commercial dual-polarized duplex microwave link with concurrent disdrometer, rain gauge, and weather observations. Earth System Science Data, 13(8), Aug. 2021. doi: 10.5194/essd-13-4219-2021.

Danksagung

Ich möchte mich bei Allen die mich auf der Reise zu dieser Arbeit begleitet haben bedanken.
Harald, für die Möglichkeit mich überhaupt mit diesem spannende Thema beschäftigen zu können, danke für deine Betreuung und für das in mich gesetzte Vertrauen.
Christoph, danke für die Übernahme des Zweitgutachtens und die Zeit und Arbeit die du dafür aufgewendet hast.
Christian, danke für den meiner Meinung nach gelungenen Balanceakt zwischen guidance und freedom und für das Forschungs(um)feld das du am IFU bereitet hast. Es macht viel Spaß mit dir zusammenzuarbeiten und von dir zu lernen. Julius, danke für die Freundschaft. Danke für Gespräche zu jeder Uhrzeit und zu jedem Thema und für Motivationsschübe, wenn sie nötig waren.
Danke Nico, Jonas, Luca, Ela, Rebecca, Moumouni und allen, die Teil des CML-Teams sind oder waren, für die zahllosen Diskussion und Einblicke in eure spannenden Forschungsthemen. Mein Start in den Montag wäre ohne eure Gesichter und Geschichten deutlich langweiliger gewesen.
Mein Dank gilt allen Kollegen und Kolleginnen am Lehrstuhl in Augsburg, Andi, Barbara, Jan, Manu, Manu, Sally, Souleymane, Thomas und Windmanagda. Ihr habt den täglichen Wahnsinn mitgemacht, danke für Hilfe durch Rat und Tat, die Zeit mit euch war immer sehr angenehm. Dasselbe gilt für Benni, Joel, Tanja, Verena und allen anderen aus der AG, die mich an meinem - zum Ende hin selten genutzten - Zweit-Schreibtisch in Garmisch begleitet haben.
Das Erfolgsteam aka die PhD-Selbsthilfegruppe mit Kathi, Annette und Basti tat vor allem in den Coronawintern unglaublich gut und es ist schön zu sehen wie nach und nach alles zusammenkommt.
Projektarbeit und -treffen haben mich mal mehr und mal weniger stark in Anspruch genommen, aber es gab immer viele freundliche Gesichter, die meine Arbeit vor allem zu Beginn und Ende der Diss stark geprägt haben. Ich durfte mit euch Hochzeitssuiten teilen und in der hippen Dresdener Neustadt abhängen. Danke dafür Christian S., Dani, Tanja, Christian V. und Malte.
Danke Meinolf, Christina und Saskia, dass ihr mich vor vielen Jahren zum ersten Mal wissenschaftliche Luft schnuppern habt lassen.
Děkuji, Dankjewel, Grazie, Takk und Toda an alle die in Opensense ihr Interesse an opportunistischen Niederschlagssensoren mit mir geteilt haben, besonders Martin, Aart, Anna, Bas, Christina, Erlend, Greta, Joni, Linda, Luuk, Remko, Remco und Vojtěch.
Danke all den Menschen die mein Leben in der Zeit neben der Arbeitszeit bereichert haben. Egal wo ihr euch wiederfindet, ihr wisst Bescheid: Ein fettes Baci geht an die Pizzabande, Dalaas mit Spaß, Promille Brüder, Abridden Fart Field, Gis my Ass, Augusta Bikepolo, 4er-Kette, coole Kids, geoconnection, 6-Laufende und die famose Fachschaft, eure Namen würden hier den Rahmen sprengen und das ist gut so. Schön das es euch gibt.
Der größte Dank geht an meine Familie und Partnerin, an meine Eltern Cornelia und Johann, und meinen Bruder Kilian, ihr habt schon immer den Tiefseetaucher unterstützt, mir beigebracht das bei Gogol nicht Schluss ist und immer an mich geglaubt. Danke Ronja, fürs Aushalten und da sein, fürs zum laufen schicken und in den Arm nehmen, du gibst mir so viel Ruhe und Lebensenergie. Ohne euch wäre das hier nicht passiert.

Augsburg, 3.10.2023